

CERN-THESIS-2009-231

# **Study of GMSB models with photon final states using the ATLAS detector**

Dissertation  
zur Erlangung des Doktorgrades  
des Department Physik  
der Universität Hamburg

vorgelegt von  
Diplom-Physiker Mark Terwort  
aus Haltern

Hamburg  
September 2009

Gutachter der Dissertation: JProf. Dr. Johannes Haller  
Prof. Dr. Peter Schleper

Gutachter der Disputation: JProf. Dr. Johannes Haller  
Prof. Dr. Joachim Mnich

Datum der Disputation: 07. Oktober 2009

Vorsitzender des Prüfungsausschusses: Dr. Georg Steinbrück  
Vorsitzender des Promotionsausschusses: Prof. Dr. Robert Klanner

Leiter des Departments Physik: Prof. Dr. Joachim Bartels  
Dekan der MIN-Fakultät: Prof. Dr. Heinrich Graener

## Abstract

Models with gauge mediated supersymmetry breaking (GMSB) provide a possible mechanism to mediate supersymmetry breaking to the electroweak scale. In these models the lightest-supersymmetric particle is the gravitino, while the next-to-lightest supersymmetric particle is either the lightest neutralino or a slepton. In the former case final states with large missing transverse energy from the gravitinos, multiple jets and two hard photons are expected in  $pp$ -collisions at the LHC. Depending on the lifetime of the neutralino the photons might not point back to the interaction vertex, which requires dedicated search strategies. Additionally, this feature can be used to measure the neutralino lifetime using either the timing information from the electromagnetic calorimeter or the reconstructed photon direction. Together with the measurements of kinematic endpoints in invariant mass distributions, the lifetime can be used as input for fits of the GMSB model and for the determination of the underlying parameters.

The signal selection and the discovery potential for GMSB models with photons in the final state are discussed using simulated data of the ATLAS detector. In addition, the measurement of supersymmetric particle masses and of the neutralino lifetime as well as the results of the global GMSB fits are presented.



## **Zusammenfassung**

Supersymmetriebrechung kann durch die Eichwechselwirkungen des Standardmodells zur elektroschwachen Skala vermittelt werden. In diesen sogenannten GMSB Modellen ist das Gravitino das leichteste supersymmetrische Teilchen, während das zweit leichteste supersymmetrische Teilchen entweder das leichteste Neutralino oder ein Slepton ist. Im Falle des leichtesten Neutralinos erwartet man in  $pp$ -Kollisionen am LHC Endzustände mit hohen Werten der fehlenden Transversalenergie, Jets mit hoher Multiplizität und zwei harte Photonen. In Abhängigkeit der Neutralinolebensdauer weisen diese Photonen möglicherweise nicht zum Primärvertex, was entsprechend optimierte Suchstrategien erfordert. Außerdem kann diese Eigenschaft der Photonen genutzt werden, um die Neutralinolebensdauer mit Hilfe der Zeitmessung des elektromagnetischen Kalorimeters oder der rekonstruierten Photonenrichtung zu bestimmen. Zusammen mit Messungen von Endpunkten in Verteilungen invariante Massen kann die gemessene Lebensdauer als Observable für eine Anpassung eines GMSB Modells an die Messungen verwendet werden, um die zugrundeliegenden Parameter des Modells zu bestimmen.

Die Signalselektion und das Entdeckungspotential von ATLAS für GMSB Modelle mit Photonen im Endzustand werden unter Verwendung simulierter Daten des ATLAS Detektors diskutiert. Außerdem werden sowohl die Bestimmung der Massen supersymmetrischer Teilchen und der Neutralinolebensdauer als auch die Resultate der Modellanpassung vorgestellt.



# Contents

<b>1</b>	<b>Introduction</b>	<b>1</b>
<b>2</b>	<b>The Standard Model and supersymmetric extensions</b>	<b>3</b>
2.1	The Standard Model . . . . .	3
2.1.1	Main building blocks . . . . .	3
2.1.2	Problems of the Standard Model . . . . .	9
2.2	Supersymmetry . . . . .	12
2.2.1	Introduction and theoretical basis . . . . .	12
2.2.2	The MSSM . . . . .	14
2.3	Supersymmetry breaking . . . . .	16
2.3.1	Soft-breaking and gaugino mixing . . . . .	17
2.3.2	General theoretical description . . . . .	19
2.3.3	Gauge mediated supersymmetry breaking . . . . .	21
2.3.4	Experimental results . . . . .	24
<b>3</b>	<b>The LHC and the ATLAS detector</b>	<b>27</b>
3.1	The Large Hadron Collider . . . . .	27
3.2	The ATLAS detector . . . . .	28
3.2.1	The coordinate system . . . . .	29
3.2.2	The magnet system . . . . .	30
3.2.3	Inner detector . . . . .	31
3.2.4	Calorimetry . . . . .	33
3.2.5	The muon spectrometer . . . . .	38
3.2.6	Trigger and data acquisition . . . . .	40
<b>4</b>	<b>Monte Carlo generation and detector simulation</b>	<b>45</b>
4.1	Generation of simulated events . . . . .	45
4.2	Detector Simulation . . . . .	48
4.2.1	Full GEANT4 simulation . . . . .	48
4.2.2	Fast simulation approach . . . . .	49
4.3	Event data model . . . . .	51
<b>5</b>	<b>Object reconstruction and identification</b>	<b>53</b>
5.1	Photon identification . . . . .	53
5.1.1	Trigger strategy . . . . .	53
5.1.2	Cluster reconstruction . . . . .	55
5.1.3	Identification . . . . .	56
5.1.4	Electron/photon discrimination and electron identification . . . . .	58

5.2	Photon conversions . . . . .	59
5.3	Non-pointing photons . . . . .	61
5.3.1	Identification . . . . .	61
5.3.2	Clustertime measurement with the ECal . . . . .	63
5.3.3	Projected photon path . . . . .	65
5.4	Jet reconstruction and missing transverse energy . . . . .	67
5.4.1	Jet reconstruction . . . . .	67
5.4.2	Missing transverse energy measurement . . . . .	68
<b>6</b>	<b>Discovery potential for GMSB models with photon final states</b>	<b>71</b>
6.1	Benchmark points and datasets . . . . .	71
6.1.1	GMSB scenarios . . . . .	71
6.1.2	Datasets and Monte Carlo simulations . . . . .	75
6.2	Discovery potential in the prompt photon scenario . . . . .	77
6.2.1	Signal trigger strategy . . . . .	77
6.2.2	Properties of the reconstructed signal events . . . . .	80
6.2.3	Signal selection . . . . .	81
6.2.4	GMSB parameter scan . . . . .	85
6.3	Discovery potential in the non-pointing photon scenario . . . . .	87
6.3.1	Signal trigger strategy . . . . .	87
6.3.2	Signal selection . . . . .	88
<b>7</b>	<b>Measurements from GMSB events</b>	<b>91</b>
7.1	Measurements of kinematic edges and particle masses . . . . .	91
7.1.1	Event selection . . . . .	92
7.1.2	Measurement of endpoints involving leptons and photons . . . . .	92
7.1.3	Measurement of endpoints involving leptons and jets . . . . .	96
7.2	Neutralino lifetime determination . . . . .	100
7.2.1	Datasets . . . . .	100
7.2.2	Method using the photon clustertime . . . . .	100
7.2.3	Dependence of the clustertime method on GMSB parameters . . . . .	105
7.2.4	Method using the photon direction . . . . .	107
7.2.5	Method using kinematic constraints in events with additional leptons . . . . .	110
<b>8</b>	<b>Determination of underlying GMSB parameters</b>	<b>115</b>
8.1	The fitting package Fittino . . . . .	115
8.2	Fitting a GMSB model to observables . . . . .	116
8.2.1	Expectations and fitting performance . . . . .	116
8.2.2	Determination of GMSB parameters from realistic measurements . . . . .	118
8.2.3	Alternative data interpretations . . . . .	121
<b>9</b>	<b>Summary, conclusions and outlook</b>	<b>125</b>
9.1	Summary and conclusions . . . . .	125
9.2	Outlook . . . . .	126
<b>A</b>	<b>Additional tables</b>	<b>129</b>





# Chapter 1

## Introduction

The Standard Model of elementary particle physics is very successful in describing the fundamental constituents of matter and their interactions. Nevertheless, there are theoretical as well as experimental difficulties that point towards an extension of the Standard Model to a more general theory. Supersymmetry has been proven outstandingly interesting for the solution of many problems of the Standard Model and is among the most favoured and most studied extensions.

Since supersymmetric theories predict a partner particle for every Standard Model particle and since none of these particles have been observed so far, supersymmetry has to be broken on the electroweak scale. This breaking usually takes place at a high energy scale, such as the Planck scale, in some kind of hidden sector and has to be mediated to the electroweak scale via some mechanism. Several models have been proposed, among them gravity, gauge and anomaly mediation. The resulting collider phenomenology is largely determined by these mechanisms, in particular by the nature of the lightest supersymmetric particle (LSP), which is stable if R-parity is assumed to be conserved, as well as the next-to-lightest supersymmetric particle (NLSP).

It is one of the main physics goals of the ATLAS experiment at the CERN Large Hadron Collider to search for signatures of supersymmetric processes, since the LHC will be able to copiously produce supersymmetric particles with masses up to several TeV, if they exist. Once found, it is important to investigate the properties of the produced particles, such as masses, couplings and lifetimes. Mainly, this has been done in the framework of minimal supergravity (mSUGRA), where the LSP is usually the lightest neutralino leading to final states characterised by multiple high energetic jets and large missing transverse energy.

However, supersymmetric models exist which predict final states not covered by the generic mSUGRA search strategies and for which these strategies might not be optimal. New strategies have to be developed. One example of such models, as studied in this thesis, is the Gauge Mediated Supersymmetry Breaking (GMSB) model, in which the LSP is the gravitino and the NLSP is the lightest neutralino. This results in final states containing high energetic photons, which might be produced in the interaction vertex (*prompt photons*) or somewhere in the inner detector (*non-pointing photons*), if the lifetime of the NLSP is finite. In the latter case a measurement of the lifetime of the neutralino allows one to gain additional information about the underlying supersymmetric model. Additionally, the final state photons can be used to determine some of the involved supersymmetric particle masses using kinematic endpoints.

In this thesis the discovery potential of the ATLAS experiment for prompt and non-pointing photon signatures is investigated. A full detector simulation is used for single benchmark studies as well as a fast simulation for a parameter scan. In addition, the possibility to measure some of the supersymmetric particle masses with a few  $\text{fb}^{-1}$  of data is studied using kinematic endpoints in invariant mass distributions, in which several combinations of photons, leptons and jets are used. In comparison to studies in mSUGRA it turns out that additional information can be gained due to the decaying lightest neutralino.

Furthermore, three methods are presented for the measurement of the neutralino lifetime using (i) the arrival time of the photon cluster in the electromagnetic calorimeter, (ii) the directional information of the photon cluster measured by the calorimeter and (iii) additional kinematic constraints in events with additional leptons, which partially incorporate the mass measurements. The measurement of the neutralino lifetime is particularly interesting (as well as challenging), since the initial state in  $pp$ -collisions is unknown and no assumptions on the neutralino boost and decay vertex can be made. Instead only information provided by the calorimeter can be used, since all particles involved in the decay process are neutral and no tracks or secondary vertices can be measured.

Once some observables or particle properties have been measured, a model can be fitted to the data. In this thesis the endpoint and lifetime measurements will be used in the fit to determine at least some of the underlying parameters or combinations of them. In the case of long-lived neutralinos this offers the possibility to measure the underlying supersymmetry breaking scale.

The work is organized as follows. After a description of the Standard Model and the idea of supersymmetry and its gauge mediated breaking in chapter 2, the LHC and the ATLAS detector are described in chapter 3. The event generation and detector simulation techniques as well as the particle reconstruction and identification methods are presented in chapter 4 and chapter 5, respectively, followed by the discussion of the discovery potential of ATLAS for GMSB models in chapter 6. Afterwards, the measurement methods for the determination of supersymmetric particle masses and the neutralino lifetime are discussed in chapter 7 and the final GMSB fit is presented in chapter 8. A summary and conclusions are given in chapter 9.

## Chapter 2

# The Standard Model and supersymmetric extensions

The current knowledge about the fundamental constituents of matter and their interactions (except gravity) is summarized in the Standard Model of elementary particle physics [1, 2, 3]. This model is very successful in describing most of the experimental physical data available and has been tested to very high precision. Nevertheless, there are theoretical and experimental difficulties, such as the existance of dark matter and neutrino masses, which point to an extension of the model to a more general theory in which the standard model can be embedded. Such an extension could base on the idea of supersymmetry, which has the potential of solving all known theoretical problems.

This chapter gives a brief introduction to the Standard Model and describes the main ingredients, as well as the main problems. The theoretical basis of supersymmetry is discussed and the minimal supersymmetric extension of the Standard Model is introduced. As a result of the problem of broken supersymmetry, the possibility of mediating supersymmetry breaking via gauge interactions to the electroweak scale is presented.

### 2.1 The Standard Model

#### 2.1.1 Main building blocks

The Standard Model of particle physics describes all known elementary particles and their interactions, except gravity. It is based on a relativistic quantum field theory, which is usually formulated within the Lagrangian formalism using the Lagrangian density  $\mathcal{L}$ . The model contains the following main ingredients:

- Matter is described by fermion fields.
- The interactions are mediated via vector bosons.
- Masses and particle mixings are introduced via the Higgs mechanism.

#### Fermions

Fermions are particles that carry half-integer spin. In the Standard Model all fermions have spin  $\frac{1}{2}$  and they can be divided into two groups: the quarks and leptons. Leptons, which can be subdivided into electrically charged leptons and uncharged neutrinos, only participate in electroweak interactions, while the quarks additionally interact strongly. All fermions appear in three families: each family consists of

Leptons		Quarks		
	mass [MeV]	charge [e]	mass [MeV]	charge [e]
$\nu_e$	$< 5 \cdot 10^{-6}$	0	up	1.5-3
electron	0.511	-1	down	3-7
$\nu_\mu$	$< 0.27$	0	charm	1270
muon	105.7	-1	strange	104
$\nu_\tau$	$< 31$	0	top	171200
tauon	1777	-1	bottom	4200

Table 2.1: Mass and electric charge of the fundamental fermions. The quark masses are given in the  $\overline{\text{MS}}$ -scheme [4], except of the top-mass, which can be measured directly.

a lepton and the corresponding neutrino, as well as an up- and a down-type quark. The masses of the particles range from a few eV or less of the electron-neutrino up to more than 170 GeV of the top-quark. They cannot be calculated within the Standard Model and have to be determined from experiments. Since fermions are spinorial objects, they appear in a left-handed and a right-handed version, except neutrinos, which in the Standard Model are assumed to exist as left-handed particles only. The current knowledge of the fermion masses and electrical charges is summarized in Tab. 2.1.

## Interactions

The interactions between the particles can be derived mathematically from the principle of local gauge invariance. The underlying symmetry group is

$$SU(3)_C \otimes SU(2)_L \otimes U(1)_Y. \quad (2.1)$$

This group describes two different parts of the Standard Model interactions:

- $SU(3)_C$  describes the strong interactions by coupling the quarks (with color charge  $C$ ) to the massless  $SU(3)_C$ -octett gluons in the framework of quantum chromodynamics (QCD).
- $SU(2)_L \otimes U(1)_Y$  is the symmetry group of electroweak interactions. The corresponding gauge bosons mix to form the massless photon and the massive  $W^\pm$  and  $Z^0$ . They couple via the weak isospin  $T_3$  and the weak hypercharge  $Y$  to all fermions.

The electric charge of a particle is then given by the relation

$$Q = T_3 + \frac{Y}{2}. \quad (2.2)$$

From the electroweak symmetry a gauge boson  $SU(2)_L$  triplet and a  $U(1)$  singlet arise. These are denoted  $W_\mu^{1,2,3}$  and  $B_\mu$ , respectively, and are massless fields. After electroweak symmetry breaking the mass eigenstates, which represent the physically observable fields, are rotations of the weak eigenstates:

$$\begin{pmatrix} W_\mu^+ \\ W_\mu^- \end{pmatrix} = \frac{1}{\sqrt{2}} \begin{pmatrix} 1 & -1 \\ 1 & 1 \end{pmatrix} \begin{pmatrix} W_\mu^1 \\ W_\mu^2 \end{pmatrix} \quad (2.3)$$

$$\begin{pmatrix} Z_\mu^0 \\ A_\mu \end{pmatrix} = \begin{pmatrix} \cos \theta_W & -\sin \theta_W \\ \sin \theta_W & \cos \theta_W \end{pmatrix} \begin{pmatrix} W_\mu^3 \\ B_\mu \end{pmatrix}, \quad (2.4)$$

where the angle  $\theta_W$  parametrizes the mixing of the fields and its value  $\sin^2 \theta_W \approx 0.231$  is obtained from experiments.  $A_\mu$  represents the massless photon field known from quantum electrodynamics, while the

	$T_3$	$Y$	$Q$
$\begin{pmatrix} v_e \\ e \end{pmatrix}_L \quad \begin{pmatrix} v_\mu \\ \mu \end{pmatrix}_L \quad \begin{pmatrix} v_\tau \\ \tau \end{pmatrix}_L$	$\begin{pmatrix} +1/2 \\ -1/2 \end{pmatrix}$	$\begin{pmatrix} -1 \\ -1 \end{pmatrix}$	$\begin{pmatrix} -1 \\ 0 \end{pmatrix}$
$\begin{pmatrix} u \\ d' \end{pmatrix}_L \quad \begin{pmatrix} c \\ s' \end{pmatrix}_L \quad \begin{pmatrix} t \\ b' \end{pmatrix}_L$	$\begin{pmatrix} +1/2 \\ -1/2 \end{pmatrix}$	$\begin{pmatrix} +1/3 \\ +1/3 \end{pmatrix}$	$\begin{pmatrix} +2/3 \\ -1/3 \end{pmatrix}$
$e_R \quad \mu_R \quad \tau_R$	0	-2	-1
$v_{e,R} \quad v_{\mu,R} \quad v_{\tau,R}$	0	0	0
$u_R \quad c_R \quad t_R$	0	+4/3	+2/3
$d'_R \quad s'_R \quad b'_R$	0	-2/3	-1/3

Table 2.2:  $SU(2)_L$  doublets and singlets and electroweak quantum numbers with resulting electromagnetic charge.

other fields couple to the Higgs field and acquire mass terms. The  $SU(2)_L \otimes U(1)_Y$  theory includes two coupling constants, which parametrize the strength of the interactions and are denoted  $g$  and  $g'$ . They are connected to the electric charge via the mixing angle by

$$e = g \sin \theta_W = g' \sin \theta_W. \quad (2.5)$$

The fermions that couple to the gauge bosons are grouped into multiplets of the Standard Model gauge group. The left-handed fermions of each family are weak-isospin doublets, while the right-handed ones are singlets and thus do not couple to the  $W^\pm$  bosons. Table 2.2 summarizes the electroweak fermion multiplets and the corresponding quantum numbers.

In addition to the weak gauge boson mixing the mass eigenstates of the quarks are not identical to their weak eigenstates. This can be modelled by introducing two complex  $3 \times 3$  matrices  $Y^{u,d}$ , which arise in the Yukawa couplings of the quarks:

$$\mathcal{L}_Y = -Y_{ij}^d \bar{Q}_{L,i} \phi d_{R,j} - Y_{ij}^u \bar{Q}_{L,i} \epsilon \phi^* u_{R,j} + \text{h.c.}, \quad (2.6)$$

where  $\phi$  is the Higgs field,  $i, j$  are generation labels and  $\epsilon$  is the anti-symmetric  $2 \times 2$  tensor.  $Q_L$  are left-handed quark doublets and  $d_R$  and  $u_R$  are the right-handed down- and up-type quark singlets, respectively. The quark mass eigenstates can be obtained by diagonalising  $Y^{u,d}$  by four unitary matrices  $V_{L,R}^{u,d}$ . The generation mixing leads to flavor conserving and flavor changing charged current ( $W^\pm$ ) interactions with couplings given by the Cabibbo-Kobayashi-Maskawa (CKM) matrix

$$V_{CKM} \equiv V_L^u V_L^{d\dagger} = \begin{pmatrix} V_{ud} & V_{us} & V_{ub} \\ V_{cd} & V_{cs} & V_{cb} \\ V_{td} & V_{ts} & V_{tb} \end{pmatrix}. \quad (2.7)$$

On the other hand, flavor changing neutral currents are suppressed. This matrix can be parametrized by three angles and a complex phase, which is the only source of CP violation in the Standard Model [5]. Generation mixing is in principle also possible in the lepton sector and recent results from neutrino experiments show that neutrino mixing in fact occurs [6]. Although in the standard formulation of the Standard Model neutrinos are massless, this shows that they are in fact massive and the investigation of this phenomenon is an active research field.

### The Higgs mechanism

An important difficulty in the Standard Model is that simple mass terms for the weak gauge bosons and the fermions break local gauge invariance. For the weak gauge bosons the necessity for a mass

term already follows from considerations about the range of the forces that has to be small enough to fit with the experimental observations. Furthermore, the masses of the gauge bosons, as well as of the fermions, have been measured in experiments, showing that mass terms are needed. The solution to this problem is to generate masses in a gauge invariant dynamical way by the interaction of the particles with a scalar field. This is known as the *Higgs mechanism*, which is based on the idea of spontaneous  $SU(2)_L$  symmetry breaking:

$$SU(3)_C \otimes SU(2)_L \otimes U(1)_Y \rightarrow SU(3)_C \otimes U(1)_{\text{em}}. \quad (2.8)$$

The Higgs field is a complex scalar isospin doublet

$$\phi = \frac{1}{\sqrt{2}} \begin{pmatrix} \phi_1 + i\phi_2 \\ \phi_3 + i\phi_4 \end{pmatrix} = \begin{pmatrix} \phi^+ \\ \phi^0 \end{pmatrix} \quad (2.9)$$

with four degrees of freedom. The (Klein-Gordon) Lagrangian density reads as

$$\mathcal{L} = \frac{1}{2} (\partial_\mu \phi) (\partial^\mu \phi) - V(\phi) \quad (2.10)$$

with the  $SU(2)_L$  symmetric potential

$$V(\phi) = \mu^2 \phi^\dagger \phi + \lambda (\phi^\dagger \phi)^2. \quad (2.11)$$

The real parameter  $\lambda$  has to be positive to ensure that  $V \rightarrow \infty$  when  $\phi \rightarrow \pm\infty$ . As can be seen from Eq. (2.11), the minimum of the potential is no longer at  $\phi = 0$ , if  $\mu^2$  is chosen to be negative. Instead, the minimum lies at

$$|\phi_0| = \sqrt{\frac{-\mu^2}{\lambda}} = v. \quad (2.12)$$

With this parameter setting the potential  $V$  itself is still  $SU(2)_L$  symmetric, while every possible ground state breaks the  $SU(2)_L$  symmetry. This is known as *spontaneous symmetry breaking*. Now one chooses a specific ground state with  $\phi_1 = \phi_2 = \phi_4 = 0$  and expands the field around the minimum:

$$\phi = \frac{1}{\sqrt{2}} \begin{pmatrix} \xi_1(x) + i\xi_2(x) \\ v + h(x) + i\xi_3(x) \end{pmatrix}, \quad (2.13)$$

with  $h(x)$  and  $\xi_{1,2,3}(x)$  being real scalar fields. In the resulting Lagrangian density a mass term for  $h$  appears with  $m_h = \sqrt{2}\mu$ , while the other fields remain massless due to the vanishing derivatives in the tangential directions of the potential. The corresponding field quanta are called *Goldstone bosons*. If one requires local gauge invariance, the  $\xi_{1,2,3}(x)$  fields couple to the gauge bosons and create mass terms. The kinetic terms of the  $\xi_{1,2,3}(x)$  fields vanish in the *unitarity gauge* showing that they do not appear as independent physical particles. The ground state is chosen such that the photon remains massless and the masses are given by:

$$m_W = \frac{1}{2} g v \quad (2.14)$$

$$m_Z = \frac{1}{2} v \sqrt{g^2 + g'^2} \quad (2.15)$$

$$m_\gamma = 0. \quad (2.16)$$

Due to the gauge boson mixing, the masses of the  $W$  and  $Z$  are not independent and are given by

$$m_W = m_Z \cos \theta_W. \quad (2.17)$$

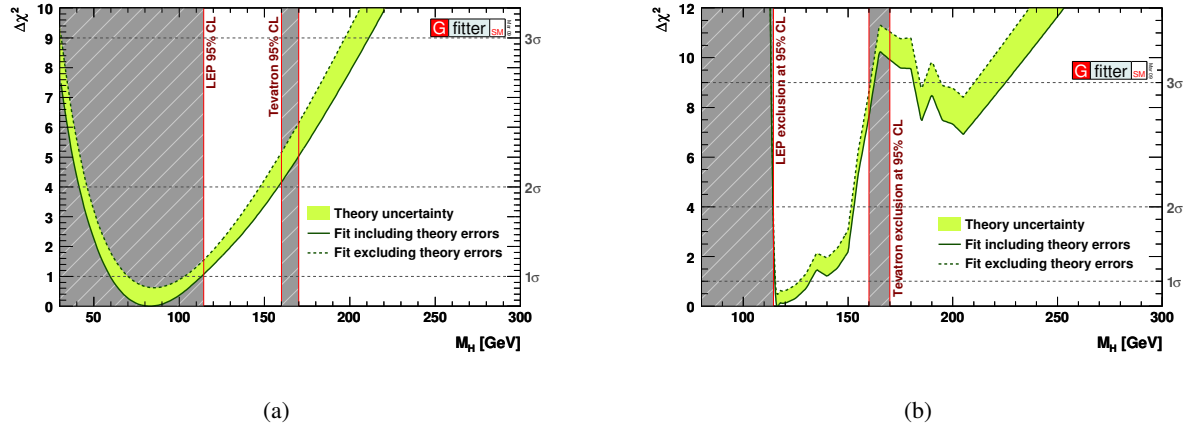


Figure 2.1:  $\Delta\chi^2$  as a function of  $m_H$  for (a) the *standard* and for (b) the *complete* fit of the electroweak observables. The solid (dashed) line gives the results when including (ignoring) theoretical errors. The minimum  $\chi^2$  of the fit including theoretical errors is used for both curves to obtain the offset-corrected  $\Delta\chi^2$  [10].

From this and from Eq. (2.5) follows that all effects of  $W$  and  $Z$  exchange processes can be described by the three parameters  $e$ ,  $\theta_W$  and  $m_Z$ . Since  $m_W$ ,  $m_Z$  and  $\sin \theta_W$  have already been measured in experiments, the vacuum expectation value  $v$  can be calculated to be

$$v \approx 246 \text{ GeV}. \quad (2.18)$$

The Higgs mechanism also allows for mass terms for all fermions. These are given by Yukawa coupling terms in the Lagrangian, while the coupling constants  $\lambda_f$  are free parameters of the model:

$$m_f = \lambda_f \frac{v}{\sqrt{2}}. \quad (2.19)$$

Important to note is that there is no fundamental reason why all fermions should couple to the same Higgs field. For instance, in supersymmetric theories one needs at least two Higgs doublets to assign a mass to every fermion.

The Higgs particle itself has not been discovered yet and its mass is a free parameter of the model. Direct searches from the LEP experiments [7] have set a lower limit of  $m_H = 114.4$  GeV on the Higgs mass, while the direct searches from the TeVatron [8] exclude the region  $m_H = [160, 170]$  GeV at 95% CL. Since the radiative correction of the self energy of the weak gauge bosons depends only logarithmically on the Higgs mass, no precise measurement of  $m_H$  could be done.<sup>1)</sup> Nevertheless, its most probable value can be determined in a global fit of the electroweak observables [10, 11]. Figure 2.1(a) shows the  $\Delta\chi^2 = \chi^2 - \chi_{\min}^2$  as a function of the Higgs mass of the *standard* fit, defined as the fit to the electroweak precision observables, excluding the direct Higgs searches. The resulting estimate of the Higgs mass is then  $m_H = 83^{+30}_{-23}$  GeV, while the  $2\sigma$  and  $3\sigma$  intervals are [42, 158] GeV and [28, 211] GeV, respectively. When the direct search results are included in the fit (*complete* fit), the best estimate of the Higgs mass is  $m_H = 116.3^{+15.6}_{-1.3}$  GeV, while the  $2\sigma$  interval is reduced to [114, 145] GeV. The corresponding  $\Delta\chi^2$  distribution is shown in Fig. 2.1(b).

<sup>1)</sup>This is in contrast to the top mass, which has been predicted from the LEP experiments [9], since the radiative correction of the self energy of the weak gauge bosons depends quadratically on the top mass.

## Renormalization

Another important issue for a successful and consistent model for particle physics arises from a calculational point of view. Calculations in quantum field theories are often performed by Taylor expanding the Lagrangian into a power series of the coupling constants. Every term can be represented by Feynman diagrams. Diagrams that contain particle loops tend to be divergent and hence the scattering amplitude is also divergent. To make sense of the results of the computations one has to cope with these infinities and a procedure has been developed to do so [12, 13], which is called *renormalization*. Every divergent diagram can be corrected by a counterterm, if a theory is renormalizable. This is the case for the Standard Model, but *e.g.* the naive quantization of general relativity fails to be renormalizable.

## Quantum Chromodynamics

The quantum field theory of the strong interactions is called *Quantum Chromodynamics* [14] (QCD). It is based on the gauge group  $SU(3)_C$  and describes the interactions between gluons and quarks. As in the case of the electroweak theory, the gluons are the gauge bosons and enter the theory after localization of the gauge group. They are massless and are not affected by the breaking of  $SU(2)_L$ . The charge of QCD is called *color* and due to the non-abelian character of  $SU(3)_C$  not only the quarks, but also the gluons are colored. The gluons carry a color and an anti-color each and of the nine possible combinations only the  $SU(3)_C$  octet is realized in nature. Leptons are color singlets and therefore do not participate in the strong interaction.

The value of the strong coupling constant  $\alpha_S$  depends on the momentum transfer  $Q^2$ , as do the coupling constants of  $SU(2)_L \otimes U(1)_Y$ . Due to the non-abelian gauge group  $\alpha_S$  is large at low values of  $Q^2$  and approaches zero for very large  $Q^2$ . This leads to the phenomenon of *asymptotic freedom* [15, 16] and the confinement of colored objects. Quarks are confined to hadronic bound states and can appear as baryons or mesons consisting of three quarks or a quark and an anti-quark, respectively.

The proton is the most important baryon and in the most simple picture it is made of two up-quarks and one down- quark (valence quarks) such that the electric charge is 1. A better description is that the proton is made of partons, namely quarks and gluons. It turns out experimentally, that in addition to the valence quarks sea quarks and gluons are present. The sea quarks arise from gluons splitting up into a quark-antiquark pair. All quarks and gluons together carry the total momentum of the proton. The momentum fraction of each parton can be investigated experimentally by deep inelastic scattering (DIS) of electrons and protons. This has been done with the experiments built at the HERA electron-proton accelerator, which have precisely measured the so-called *Parton Density Functions* (PDFs). Two main variables are used to describe the PDFs: the parton momentum  $x$  as the fraction of the total proton momentum and the momentum transfer  $Q^2$  from the electron to the interacting parton. As an example, Fig. 2.2 shows the combined results from the ZEUS and H1 experiments for the valence quarks ( $xu_v$  and  $xd_v$ ), the gluons ( $xg$ ) and sea quarks ( $xS$ ) at a momentum transfer  $Q^2 = 10 \text{ GeV}^2$ .

The detailed knowledge of the proton structure is essential for the analysis of LHC data. Especially the search strategies for physics beyond the Standard Model are optimized using simulated Monte Carlo events, where a precise prediction of the proton interactions is necessary. At the LHC processes will be investigated, which differ in their cross sections over more than 10 orders of magnitude, as shown in Fig. 2.3. For comparison, the total production cross section of a typical supersymmetric scenario studied with ATLAS is of the order of  $10^{-2} \text{ nb}$  [18]. It should be noted that due to the partonic structure of the proton the effective center of mass energy at the LHC is much below 14 TeV and lies around 2 TeV, depending on the scattering process and the involved partons.

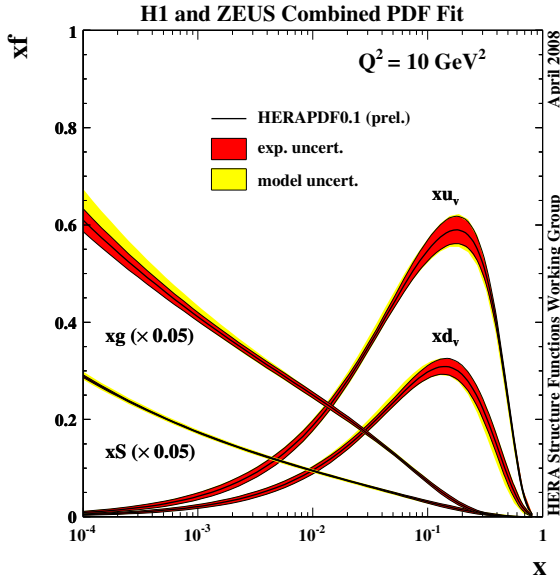


Figure 2.2: Parton density functions of the valence quarks  $u_v$ ,  $d_v$ , the gluons  $g$  and sea quarks  $S$  as obtained from the combined results of the ZEUS and H1 collaborations [17].

### 2.1.2 Problems of the Standard Model

Although the Standard Model describes the fundamental particles and their interactions with great success, there are some unsolved problems that point towards an extension of the model. Some of them are intrinsic problems, some arise from cosmological measurements and some have a pure theoretical nature:

- **General:** There is no explanation for the observed multiplet structure and mass hierarchy.
- **Unification:** The quark-to-lepton charge relation is puzzling and there is no unification of the coupling constants at a high scale.
- **Astrophysical:** There is an unexplained matter-antimatter-asymmetry in the universe and the matter is mainly made of unknown dark matter.
- **Intrinsic:** The stability of the Higgs mass cannot be understood in a natural way.
- **Theoretical:** Gravity is not included in the Standard Model.

The first item expresses part of the fact that the Standard Model includes many ad-hoc assumptions and free parameters that cannot be justified or calculated within the model itself. This leads to the hope that there is a more fundamental underlying theory that overcomes this problem. Attempts have been made by defining Grand Unified Theories (GUTs) [20], which have a simpler gauge group (such as SU(5) or SO(10)) and thus have fewer coupling constants and a simpler multiplet structure. Within such models also the quark-to-lepton charge relation can be calculated, but other problems, such as the instability of the proton, require new ideas. Another problem related to GUTs is the unification of the coupling constants, which cannot be achieved within the Standard Model. This can be solved by the formulation of supersymmetric theories [21, 22, 23], where the running couplings converge in one point at the GUT scale, as depicted in Fig. 2.4. Also the proton is stable enough in supersymmetric GUTs.

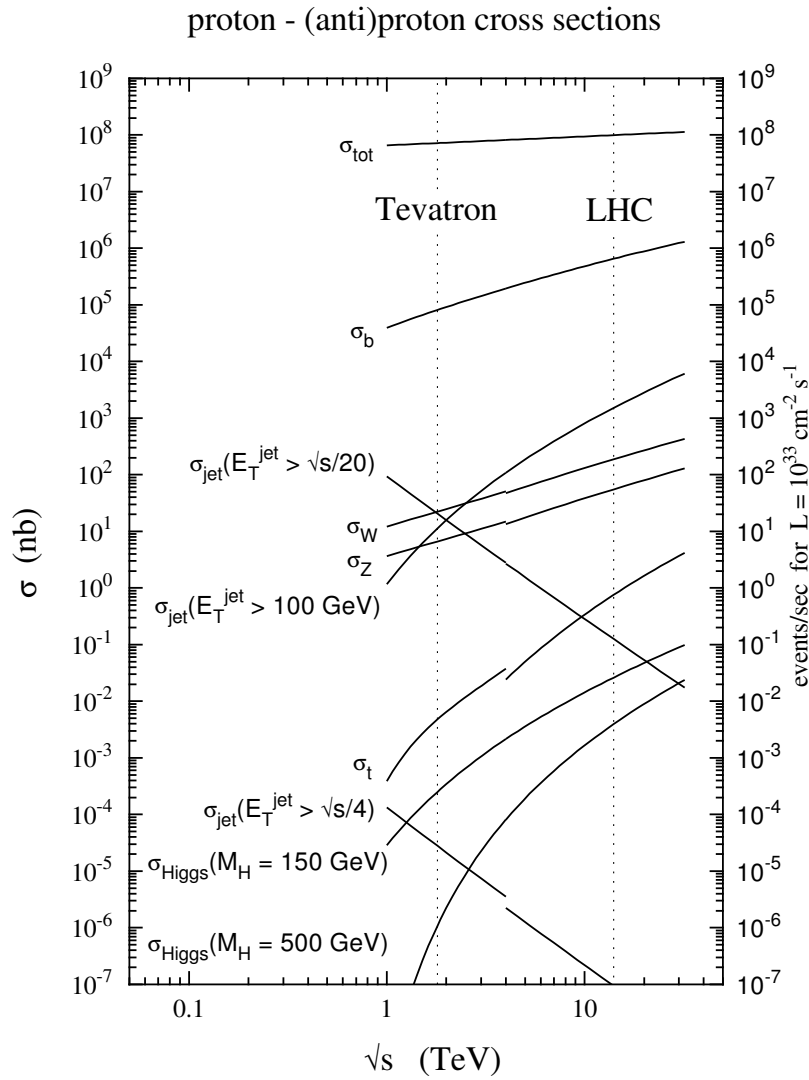


Figure 2.3: Cross sections for hard proton - (anti)proton scattering as a function of the center of mass energy. The total production cross section for a typical supersymmetric model at the LHC is about  $10^{-2}$  nb [19].

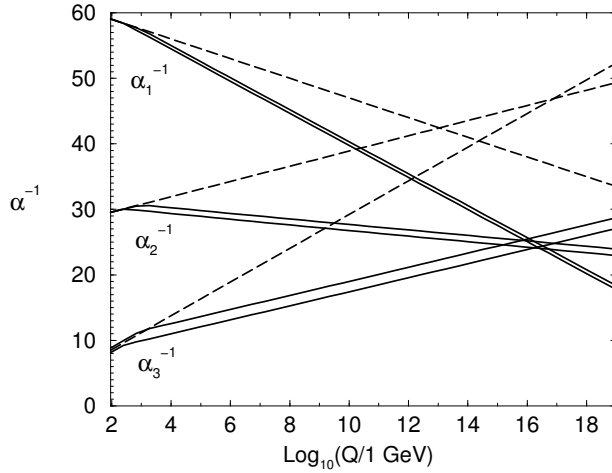


Figure 2.4: Running of the coupling constants ( $\alpha_1 \sim$  electromagnetic,  $\alpha_2 \sim$  weak,  $\alpha_3 \sim$  strong) in the Standard Model (dashed lines) and in the minimal supersymmetric extension of the Standard Model (solid lines) as a function of the energy scale [23].

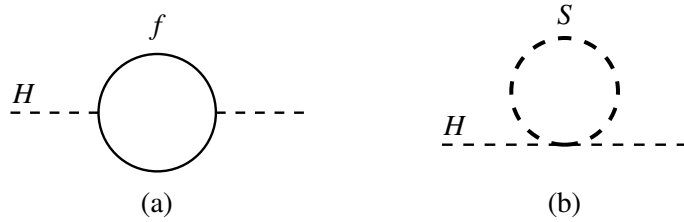


Figure 2.5: Loop corrections to  $m_H^2$  from (a) a fermion  $f$  with mass  $m_f$  and (b) of a heavy complex scalar with mass  $m_S$  [23].

The third item touches the problem of CP violation. The complex phase of the CKM matrix is the only source of CP violation in the Standard Model, but it is not sufficient to explain the cosmologically observed matter-antimatter-asymmetry in the universe [24, 25, 26]. Supersymmetric extensions of the Standard Model contain the possibility to have up to 43 additional complex phases [27]. Another important cosmological observation is the fact that the matter described by the Standard Model accounts for only 4% of the content of the universe. Around 76% is made of dark energy, which is responsible for the accelerated expansion of the universe, while around 20% is made of dark matter [28]. If dark matter is made of particles that can be described by particle physics, then these particles must only interact via the weak interactions and/or gravitational interactions. The only candidate in the Standard Model is the neutrino, which is excluded to be the only source of the observed gravitational effects of dark matter due to its very small mass. Again, supersymmetric theories provide good possibilities to solve this problem. Depending on the model they have a variety of candidate particles that could account for the observed amount of dark matter, such as the lightest neutralinos or the gravitinos.

The fourth item has to do with the Higgs mechanism, that has been invented to solve the problem of symmetry breaking in the Standard Model, but causes new problems itself [29, 30, 31, 32]. The Higgs mass squared  $m_H^2$  receives enormous quantum corrections from loop effects of every particle coupling to the Higgs. Figure 2.5 shows a corrections to  $m_H^2$  from a fermion  $f$  with mass  $m_f$ . If the coupling reads as  $-\lambda_f H \bar{f} f$ , then the contribution to the Higgs mass is

$$\Delta m_H^2 = -\frac{|\lambda_f|^2}{16\pi^2} [2\Lambda_{UV}^2 - 6m_f \ln(\Lambda_{UV}/m_f) + \dots], \quad (2.20)$$

where  $\Lambda_{\text{UV}}$  is an ultraviolet momentum cutoff. If this cutoff is chosen to be at the Planck scale, then  $\Delta m_H^2$  is about 30 orders of magnitudes larger than the true value of around  $(100 \text{ GeV})^2$ . This results in a finetuning of the cutoff in every order of perturbation theory and the possible interpretation of the cutoff as a natural scale for new physics. This is known as the *hierarchy problem*. As an example for a solution to this problem, Fig. 2.5 shows the contribution of a heavy complex scalar with mass  $m_S$  and a coupling  $-\lambda_S |H|^2 |S|^2$ . The contribution of  $s$  scalars to the Higgs mass is then

$$\Delta m_H^2 = \frac{\lambda_S}{16\pi^2} [\Lambda_{\text{UV}}^2 - sm_S^2 \ln(\Lambda_{\text{UV}}/m_S) + \dots], \quad (2.21)$$

which can cancel a fermion contribution due to the minus sign. Supersymmetric theories provide a variety of heavy charged scalar particles to cancel the fermion contributions from the Standard Model, in particular in the MSSM there is one partner scalar particle to each Standard Model particle cancelling its contribution to the Higgs mass.

Finally, the Standard Model cannot be the final description of nature, since it does not incorporate gravitational interactions. The gravitational force is weak enough to be neglected in elementary particle interactions at the electroweak scale, but at energies up to the Planck scale gravity becomes as strong as the Standard Model forces. The extension of the Standard Model to a theory of gravity poses large theoretical difficulties (renormalizability), but again supersymmetry is a popular candidate for an elegant solution. If supersymmetry is treated as a local gauge symmetry, as is done with  $SU(3)_C \otimes SU(2)_L \otimes U(1)_Y$  in the Standard Model, it becomes automatically a theory of gravity, since a supersymmetric transformation also includes a space-time transformation. This is utilized in supergravity theories. The question is then, if it is possible to formulate a perturbatively finite theory of gravity and the hope is that additional symmetries (such as supersymmetry) impose enough constraints to cancel all divergencies. It turns out, that not only supersymmetric string theories are finite, but also in four dimensional supersymmetric quantum field theories it might be possible to cancel all divergencies in every order of perturbation theory [33].

## 2.2 Supersymmetry

As discussed in section 2.1.2, supersymmetric theories provide elegant solutions to a variety of problems of the Standard Model. In the following, the basic principles and physical consequences of supersymmetry will be discussed briefly. The minimal supersymmetric extension of the Standard Model (MSSM) will be introduced and its particle content and other properties will be summarized. Since supersymmetry has to be broken at the electroweak scale, some of the breaking mechanisms will be introduced and the special case of gauge mediated supersymmetry breaking (GMSB) will be discussed in some detail.

### 2.2.1 Introduction and theoretical basis

Every relativistic quantum field theory is invariant under the Poincaré group  $\mathcal{P}$  and most often also under an internal symmetry group  $\mathcal{G}$ , *i.e.* under  $\mathcal{P} \otimes \mathcal{G}$ . The generators of the corresponding Lie-algebra are  $P^\mu$ ,  $M^{\mu\nu}$  and  $T_a$ , such that  $[P^\mu, T_a] = [M^{\mu\nu}, T_a] = 0$ . An interesting question is, if a group exists that contains  $\mathcal{P}$  and  $\mathcal{G}$  as subgroups, *i.e.* if a group exists with  $[M^{\mu\nu}, T_a] \neq 0$ . Due to the no-go theorem of COLEMAN and MANDULA [34] such a group cannot be generated by Lorentz-tensors. A possible way out is a symmetry with spinorial charges rather than tensorial charges. The corresponding algebra is called a *Lie-superalgebra* and the corresponding theorem for supersymmetric theories is the HAAG-LOPUSZANSKI-SOHNIES theorem [35].

Due to the Spin-Statistic-Theorem [36] the proposed set of spinorial charges<sup>2)</sup>  $Q_\alpha$ , with  $\alpha = 1, \dots, 4$  is closed through anti-commutators.  $Q_\alpha$  can be expressed in terms of a Weyl spinor  $Q_A$ , with  $A = 1, 2$ :  $Q_\alpha = (Q_A, \bar{Q}^{\dot{A}})$  with  $\bar{Q}^{\dot{A}} = (Q_A)^*$ . Together with the generators of the Poincaré group they form the following algebra [22]:

$$[M^{\mu\nu}, Q_\alpha] = \frac{1}{2}(\Sigma^{\mu\nu})^\beta_\alpha Q_\beta \quad (2.22)$$

$$[Q_\alpha, P^\mu] = 0 \quad (2.23)$$

$$\{Q_\alpha, \bar{Q}_\beta\} = 2(\gamma^\mu)_{\alpha\beta} P_\mu, \quad (2.24)$$

where  $\gamma^\mu$  is given by  $\{\gamma^\mu, \gamma^\nu\} = 2g^{\mu\nu}$  and  $\Sigma^{\mu\nu} = \frac{i}{2}[\gamma^\mu, \gamma^\nu]$ .<sup>3)</sup> From these relations two very fundamental consequences arise:

- The particles in a supermultiplet have the same mass, but differ in their spin by half a unit.
- There is the same number of fermionic and bosonic degrees of freedom in every irreducible representation of supersymmetry.

Hence, in supersymmetric theories every boson has a fermionic partner particle with the same mass and vice versa. In particular, the supermultiplets are chosen such that every Standard Model particle with spin 0,  $\frac{1}{2}$ , 1, 2 has a partner with spin  $\frac{1}{2}$ , 0,  $\frac{1}{2}$ ,  $\frac{3}{2}$ , respectively. The corresponding multiplets are often called *chiral*, *vector* and *gravity* supermultiplet:

	chiral	chiral	vector	gravity
SM particle spin	0	$\frac{1}{2}$	1	2
SUSY particle spin	$\frac{1}{2}$	0	$\frac{1}{2}$	$\frac{3}{2}$

For the construction of supersymmetric models so-called *superfields* are used, which are reducible representations of the supersymmetry algebra and contain a variety of *component fields*. Supersymmetric conditions are imposed to project out the respective irreducible representations. The corresponding superfields are then called *chiral* or *vector* superfields, which are used to describe the matter or gauge content of the theory, respectively. The supersymmetric version of a Lagrangian is easily derived by simply applying the same rules as for the original model.

There is an additional continuous symmetry called *R-symmetry*  $U(1)_R$  under which the minimal supersymmetric extension of the Standard Model is invariant [37]. Since this symmetry acts chirally on the *gluinos*, the partner particles of the gluons, and would constrain them to be massless even after spontaneous supersymmetry breaking, it has to be broken.<sup>4)</sup> In most of the supersymmetric models a discrete  $Z_2$  remnant of the continuous symmetry remains, called *R-parity* [38, 39], which is given by

$$R_P = (-1)^{3(B-L)+2S} \quad (2.25)$$

and is closely connected to the baryon number  $B$ , lepton number  $L$  and the spin  $S$ . It is a multiplicative quantum number, which is +1 for all Standard Model particles and -1 for all supersymmetric partner particles. If R-parity is assumed to be conserved in a supersymmetric model no baryon or lepton number violation occurs. Two of the most important consequences of R-parity conservation are:

<sup>2)</sup>Only the case of a single generator ( $N = 1$ ) will be discussed here. Theories with extended supersymmetry ( $N > 1$ ) have an extended algebra, an extended particle content per multiplet and are usually not considered in simulation studies in ATLAS.

<sup>3)</sup>From Eq. (2.24) it can be seen that a supersymmetry transformation includes space-time transformations. If supersymmetry is treated as a local gauge symmetry, the transformations include local space-time transformations, which means that the theory is a theory of gravity.

<sup>4)</sup>Massless gluinos would lead to relatively light *R-hadrons* made of quarks, antiquarks and gluinos, which have not been observed.

- At colliders supersymmetric particles can only be produced in pairs.
- The lightest supersymmetric particle (LSP) is stable.

The first item ensures that a supersymmetric particle always decays into another supersymmetric particle and that there are always two decay chains of (unstable) supersymmetric particles in each supersymmetric event at colliders. The second item has cosmological consequences, since the LSP could serve as a candidate for the yet unknown dark matter, if there are large remnants of them in the universe. This also means in turn that the LSP cannot carry an electromagnetic or color charge and that it only interacts weakly, since otherwise they would have been observed in astrophysical experiments. Another consequence is that the LSP only interacts weakly with a particle detector and thus cannot be observed directly, but leads to the signature of missing energy.

If R-parity is violated additional  $B$  and  $L$  violating terms appear in the Lagrangian, which has a variety of phenomenological consequences. One interesting example is the most general Lagrangian, where all  $B$  and  $L$  violating terms are allowed. In such a model the proton is unstable and decays rapidly. This can be avoided by setting at least one of the coupling constants to zero [38]. The breaking of R-parity can be done by introducing appropriate terms in the Lagrangian or by using a mechanism of spontaneous R-parity breaking [40, 41]. Also in ATLAS R-parity violating models are studied, but throughout this thesis R-parity conservation will be assumed.

## 2.2.2 The MSSM

### Model and particle content

The minimal supersymmetric extension of the Standard Model (MSSM) is the simplest and most general supersymmetric model based on the Standard Model Lagrangian [42]. This means that the field content is one of vector supermultiplets associated with the gauge symmetry  $SU(3)_C \otimes SU(2)_L \otimes U(1)_Y$  coupling to chiral supermultiplets containing the matter particles of the Standard Model. The partner particles of the gauge bosons are called *gauginos*, while the partners of the Standard Model fermions are called *squarks* and *sleptons*. In particular, the gauginos are the *winos*, *zinos* and *photinos*. Table 2.3 shows the particle content and the corresponding quantum numbers of the MSSM for one generation. The  $D$ - and  $F$ -fields denote auxiliary fields.<sup>5)</sup>

Besides the 19 parameters of the Standard Model the most general MSSM contains 105 additional parameters, among them 43 CP violating phases and 21 masses. The number of parameters can be constrained by requiring underlying physics such as Grand Unification, family symmetries etc. As an example, the minimal supergravity model contains only five additional parameters, while the minimal GMSB model includes six parameters besides those of the Standard Model.

At the LHC the cross section for gluino and squark production is much larger than for electroweak gaugino production, if the corresponding particle masses lie in the reach of the LHC. Figure 2.6 shows the tree-level Feynman diagrams for the production of squarks and gluinos via gluon-gluon and quark-gluon fusion, while Fig. 2.7 shows the production via quark-antiquark annihilation and quark-quark scattering.

### The Higgs sector

As in the Standard Model the gauge symmetry of the MSSM is broken spontaneously by a Higgs mechanism. In the Standard Model a single Higgs doublet is used in order to give mass to all fermions.

---

<sup>5)</sup>The auxiliary fields are needed to close the supersymmetry algebra off-shell, since the numbers of fermionic and bosonic degrees of freedom have to be equal. They can be used for spontaneous supersymmetry breaking.

$SU(2)_L$	$U(1)_Y$	particle content (weak eigenstates)
triplet	1	$W_\mu^a, \lambda^a, D^a$
singlet	0	$B_\mu, \lambda, D$
doublet	-1	$\begin{pmatrix} v_L \\ e_L \end{pmatrix}, \begin{pmatrix} \tilde{v}_L \\ \tilde{e}_L \end{pmatrix}, \begin{pmatrix} F(v_L) \\ F(e_L) \end{pmatrix}$
singlet	2	$e_R, \tilde{e}_R, F(e_R)$
doublet	$\frac{1}{3}$	$\begin{pmatrix} u_L \\ d_L \end{pmatrix}, \begin{pmatrix} \tilde{u}_L \\ \tilde{d}_L \end{pmatrix}, \begin{pmatrix} F(u_L) \\ F(d_L) \end{pmatrix}$
singlet	$-\frac{4}{3}$	$u_R, \tilde{u}_R, F(u_R)$
singlet	$\frac{2}{3}$	$d_R, \tilde{d}_R, F(d_R)$
doublet	-1	$\begin{pmatrix} H_1^0 \\ H_1^- \end{pmatrix}, \begin{pmatrix} \tilde{H}_1^0 \\ \tilde{H}_1^- \end{pmatrix}, \begin{pmatrix} F(H_1^0) \\ F(H_1^-) \end{pmatrix}$
doublet	1	$\begin{pmatrix} H_2^+ \\ H_2^0 \end{pmatrix}, \begin{pmatrix} \tilde{H}_2^+ \\ \tilde{H}_2^0 \end{pmatrix}, \begin{pmatrix} F(H_2^+) \\ F(H_2^0) \end{pmatrix}$
$SU(3)$	$SU(2)_L \times U(1)_Y$	particle content (weak eigenstates)
octet	singlet	$g_\mu^\alpha, \tilde{g}^\alpha, D^\alpha$

Table 2.3: Particle content and quantum numbers of the MSSM particles for one generation. The latin indizes are flavor indizes, while the greek ones denote color-indizes [22, 42].

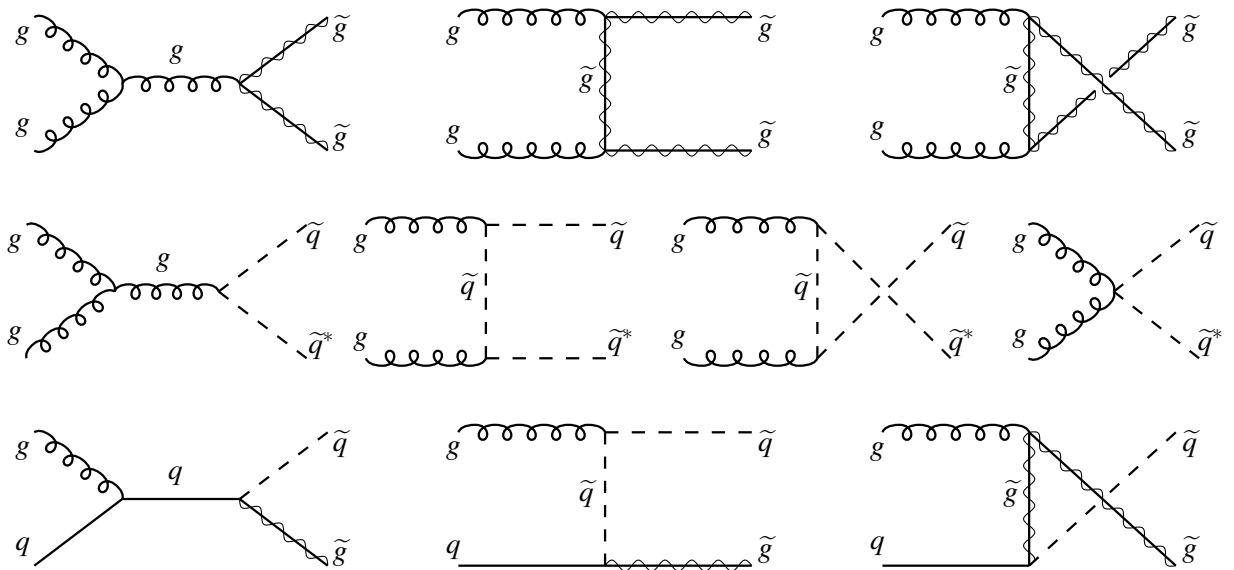


Figure 2.6: Diagrams for squark and gluino production at the LHC from gluon-gluon and gluon-quark fusion.

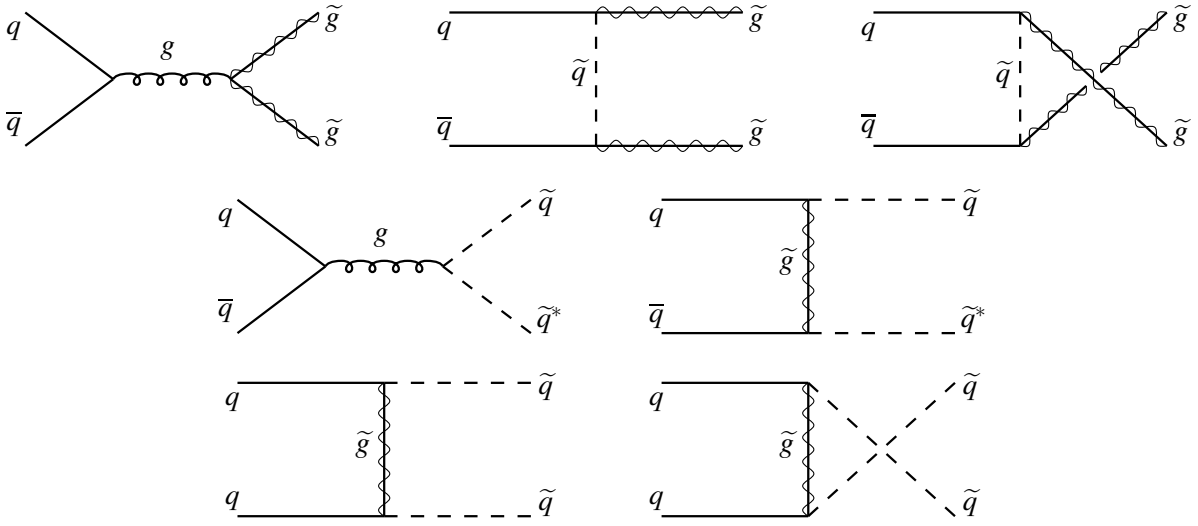


Figure 2.7: Diagrams for squark and gluino production at the LHC from strong quark-antiquark annihilation and quark-quark scattering.

Therefore, isospin invariant combinations of the Higgs field with the left-handed fermion doublets are constructed:

$$\begin{aligned} \phi^\dagger \begin{pmatrix} \psi_{1L} \\ \psi_{2L} \end{pmatrix} &= \phi_1^\dagger \psi_{1L} + \phi_2^\dagger \psi_{2L}, \\ \phi^T \epsilon \begin{pmatrix} \psi_{1L} \\ \psi_{2L} \end{pmatrix} &= \phi_1 \psi_{2L} - \phi_2 \psi_{1L}, \end{aligned} \quad (2.26)$$

where  $\begin{pmatrix} \psi_{1L} \\ \psi_{2L} \end{pmatrix}$  and  $\phi = \begin{pmatrix} \phi_1 \\ \phi_2 \end{pmatrix}$  are a left-handed fermion doublet and the Higgs doublet, respectively, and  $\epsilon = \begin{pmatrix} 0 & 1 \\ -1 & 0 \end{pmatrix}$ . The coupling to the right-handed fermions then allows transitions like

$$\psi_{1L} \longrightarrow \psi_R + \phi_2. \quad (2.27)$$

If one examines the weak hypercharges of the quark doublets and singlets in Tab. 2.3, it is clear that both couplings in Eq. (2.26) (hypercharge  $Y = \frac{1}{2}$  and  $Y = -\frac{1}{2}$ ) are needed in order to conserve the weak hypercharge in processes like (2.27) and to assign a mass to the up-type as well as the down-type quarks.

In the MSSM this imposes a problem, since either only left- or right-chiral superfields can be used in the construction of the Lagrangian and since the hermitian conjugate of a left-chiral superfield is right-chiral and vice versa, the coupling to a hermitian conjugated Higgs superfield is forbidden. This leads to the usage of two Higgs superfields, one for the up-type quarks and one for the down-type quarks, and five physical Higgs bosons. With the two Higgs superfields a quadratic term using the Higgs fields only can be formed and added to the superpotential. From this term the additional Higgs mass parameter  $\mu$  is introduced, which plays an important role in the gaugino mixing. The corresponding vacuum expectation values of the Higgs fields are denoted  $v_1$  and  $v_2$  and their ratio  $\tan \beta = \frac{v_1}{v_2}$  is an important parameter of supersymmetric models.

## 2.3 Supersymmetry breaking

As discussed above, the supersymmetric particles have the same masses as their Standard Model partners, also after spontaneous  $SU(2)_L$  symmetry breaking via the Higgs mechanism. However, since none of the

supersymmetric particles have been observed so far, supersymmetry has to be broken. In this section the introduction of soft-breaking terms and the resulting gaugino mixing is discussed, as well as the general theoretical description of supersymmetry breaking and the example of gauge mediation.

### 2.3.1 Soft-breaking and gaugino mixing

For the generation of additional masses for the supersymmetric particles additional mass terms have to be introduced in the Lagrangian, which then is no longer supersymmetric. In the general MSSM one parametrizes the underlying breaking mechanism by so-called *soft-breaking* terms [22, 42]:

$$\begin{aligned} \mathcal{L}_{\text{soft}} = & -\frac{1}{2}M_1\lambda\lambda - \frac{1}{2}M_2\lambda^a\lambda^a - \frac{1}{2}M_3\tilde{g}^\alpha\tilde{g}^\alpha + h.c. \\ & - \tilde{m}_1^2\mathbf{H}_1^*\mathbf{H}_1 - \tilde{m}_2^2\mathbf{H}_2^*\mathbf{H}_2 - (\tilde{m}_{12}^2\mathbf{H}_1\mathbf{H}_2 + h.c.) - \sum_{\tilde{f}_i} \tilde{m}_{\tilde{f}_i}^2\tilde{f}_i^*\tilde{f}_i \\ & - \frac{\sqrt{2}m_u}{v_2}A_u\mathbf{H}_2\tilde{q}_L\tilde{u}_R + \frac{\sqrt{2}m_d}{v_1}A_d\mathbf{H}_1\tilde{q}_L\tilde{d}_R + h.c. \\ & + \frac{\sqrt{2}m_e}{v_1}A_e\mathbf{H}_1\tilde{l}_L\tilde{e}_R + h.c., \end{aligned} \quad (2.28)$$

where  $\mathbf{H}_1 \equiv (H_1^0, H_1^-)$  and  $\mathbf{H}_2 \equiv (H_2^+, H_2^0)$ .  $A_u$ ,  $A_d$  and  $A_e$  are trilinear scalar coupling constants, while the other parameters are explicit mass terms for the gauginos, Higgs particles and sfermions. In the following the gaugino mass terms will be discussed in some detail, since they play a crucial role in the phenomenology of supersymmetry. First, the mixing of the charged gauginos with the charged Higgsinos will be discussed, followed by a discussion of the neutral gaugino-higgsino mixing.

In the soft-breaking term (2.28) only the  $SU(2)_L$  triplet superfield contains two charged gauginos (in analogy to the Standard Model  $W$  bosons)

$$\lambda^\pm = \frac{1}{\sqrt{2}}(\lambda^1 \mp i\lambda^2), \quad (2.29)$$

i.e. only the term with  $M_2$  enters the charged gaugino mixing:

$$\mathcal{L}_{\text{soft}} = -\frac{1}{2}M_2\lambda^+\lambda^- - \frac{1}{2}M_2\lambda^-\lambda^+. \quad (2.30)$$

Additionally, a Higgsino-gaugino mixing term and the Higgs mass term

$$\mathcal{L}_{\tilde{H}\tilde{V}} = -\sqrt{2}m_W \cos\beta \tilde{H}_1^-\lambda^+ - \sqrt{2}m_W \sin\beta \tilde{H}_2^+\lambda^-, \quad (2.31)$$

$$\mathcal{L}_{\tilde{H}_{\text{mass}}} = -\mu \tilde{H}_1^-\tilde{H}_2^+ \quad (2.32)$$

enter, where  $m_W$  is the  $W$  boson mass. From these equations one can construct a mass term

$$\mathcal{L}_{\text{CM}} = -\left(\frac{\lambda^+}{\tilde{H}_2^+}\right)^\dagger X_{\alpha\beta} \left(\frac{\lambda^-}{\tilde{H}_1^-}\right) \quad (2.33)$$

that contains the mass matrix

$$X_{\alpha\beta} = \begin{pmatrix} M_2 & \sqrt{2}m_W \cos\beta \\ \sqrt{2}m_W \sin\beta & \mu \end{pmatrix}. \quad (2.34)$$

$X_{\alpha\beta}$  can be diagonalized by two complex unitary  $2 \times 2$ -matrices  $U_{mn}$  and  $V_{mn}$ :

$$U_{m\alpha}^* X_{\alpha\beta} V_{\beta n}^{-1} = m_{\tilde{\chi}_i^\pm} \delta_{mn}, \quad (2.35)$$

where the eigenvalues are given by the particle masses

$$m_{\tilde{\chi}_{1,2}^\pm}^2 = \frac{1}{2} (|\mu|^2 + M_2^2 + 2m_W^2 \mp \Delta_C). \quad (2.36)$$

The quantity

$$\Delta_C = \sqrt{(M_2^2 - |\mu|^2)^2 + 4m_W^2 \cos^2 2\beta + 4m_W^2 (M_2^2 + |\mu|^2) + 8m_W^2 M_2 |\mu| \sin 2\beta \cos \phi_\mu}, \quad (2.37)$$

where  $\phi_\mu$  denotes the complex phase of the Higgsino mass parameter  $\mu$ , determines the mass difference of the two physical mass eigenstates

$$\tilde{\chi}_i^+ = \begin{pmatrix} \bar{\lambda}_{iR}^- \\ \lambda_{iL}^+ \end{pmatrix} \quad \text{and} \quad \tilde{\chi}_i^- = \begin{pmatrix} \bar{\lambda}_{iL}^+ \\ \lambda_{iR}^- \end{pmatrix}, \quad i = 1, 2, \quad (2.38)$$

that are constructed from the four Weyl-spinors and

$$\begin{pmatrix} \lambda_{1R}^- \\ \lambda_{2R}^- \end{pmatrix} = V \begin{pmatrix} \lambda^- \\ \tilde{H}_1^- \end{pmatrix}, \quad (2.39)$$

$$\begin{pmatrix} \lambda_{1L}^+ \\ \lambda_{2L}^+ \end{pmatrix} = U \begin{pmatrix} \lambda^+ \\ \tilde{H}_2^+ \end{pmatrix}. \quad (2.40)$$

$\tilde{\chi}_i^+$  and  $\tilde{\chi}_i^-$  are called *charginos*.

A similar procedure can be performed for the neutral gauginos and Higgsinos. In principle the same terms contribute as in the case of the charginos, but they look different. From Eq. (2.28) the  $SU(2)_L$  singlet and triplet superfields enter, while the neutral gaugino of the latter is denoted  $\lambda^0$ . The terms are

$$\mathcal{L}_{\text{soft}} = -\frac{1}{2} M_1 \lambda \lambda - \frac{1}{2} M_2 \lambda^0 \lambda^0, \quad (2.41)$$

$$\mathcal{L}_{\tilde{H}\tilde{V}} = -m_Z \cos \beta \cos \theta_W \tilde{H}_1^0 \lambda^0 + m_Z \cos \beta \tilde{H}_1^0 \sin \theta_W \lambda, \quad (2.42)$$

$$+ m_Z \sin \beta \cos \theta_W \tilde{H}_2^0 \lambda^0 - m_Z \sin \beta \sin \theta_W \tilde{H}_2^0 \lambda, \quad (2.43)$$

$$\mathcal{L}_{\tilde{H}_{\text{mass}}} = \mu \tilde{H}_1^0 \tilde{H}_2^0, \quad (2.44)$$

where  $\theta_W$  is the Standard Model mixing angle and  $m_Z$  is the  $Z$  boson mass. Again, a mass term

$$\mathcal{L}_{NM} = -\frac{1}{2} \begin{pmatrix} \lambda \\ \lambda^0 \\ \tilde{H}_1^0 \\ \tilde{H}_2^0 \end{pmatrix}^\dagger Y_{\alpha\beta} \begin{pmatrix} \lambda \\ \lambda^0 \\ \tilde{H}_1^0 \\ \tilde{H}_2^0 \end{pmatrix} \quad (2.45)$$

can be constructed with the symmetric mixing matrix

$$Y_{\alpha\beta} = \begin{pmatrix} M_1 & 0 & -m_Z \sin \theta_W \cos \beta & m_Z \sin \theta_W \sin \beta \\ * & M_2 & m_Z \cos \theta_W \cos \beta & -m_Z \cos \theta_W \sin \beta \\ * & * & 0 & -\mu \\ * & * & * & 0 \end{pmatrix}. \quad (2.46)$$

$Y_{\alpha\beta}$  can be diagonalized by a complex unitary  $4 \times 4$  - matrix  $N_{ij}$ :

$$N_{i\alpha}^* Y_{\alpha\beta} N_{\beta k}^\dagger = m_{\tilde{\chi}_i^0} \delta_{ik}, \quad (2.47)$$

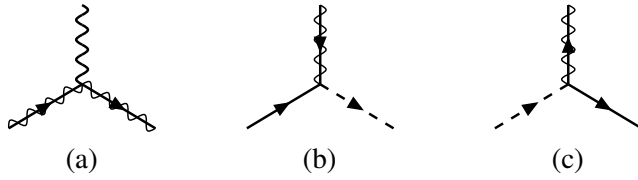


Figure 2.8: Couplings of gauginos (solid plus wavy) to (a) gauge bosons (wavy) and (b,c) sfermions (dashed) and fermions (solid).

where the eigenvalues represent the masses of the mass eigenstates

$$\tilde{\chi}_i^0 = \begin{pmatrix} \bar{\lambda}_i \\ \lambda_i \end{pmatrix}, \quad i = 1, \dots, 4, \quad (2.48)$$

where

$$\begin{pmatrix} \lambda_1 \\ \lambda_2 \\ \lambda_3 \\ \lambda_4 \end{pmatrix} = N \begin{pmatrix} \lambda \\ \lambda^0 \\ \tilde{H}_1^0 \\ \tilde{H}_2^0 \end{pmatrix}. \quad (2.49)$$

$\tilde{\chi}_i^0$  are called *neutralinos*. Together with the charginos they are also called gauginos, as the unmixed states. This terminology will be used from now on. The couplings of the gauginos to other particles are determined by the couplings of their individual components, i.e the wino, zino, photino or Higgsino fraction. The general couplings to sfermions, fermions and gauge bosons are depicted in Fig. 2.8.

### 2.3.2 General theoretical description

Supersymmetry breaking is achieved, if the physical vacuum state  $|0\rangle$  is not invariant under supersymmetry transformations. This is the same requirement as in the Standard Model and electroweak symmetry breaking. Equivalently,  $|0\rangle$  should not be annihilated by all supersymmetry generators:

$$\begin{aligned} Q_A |0\rangle &\neq 0 \quad \text{or} \\ \bar{Q}^A |0\rangle &\neq 0. \end{aligned} \quad (2.50)$$

From Eq. (2.24) follows that when supersymmetry is unbroken in the vacuum state this state has zero energy and in the spontaneously broken case it has positive energy. Therefore, whenever a supersymmetric vacuum state exists as a local minimum of the effective potential, it is also the global minimum. If the physical vacuum shall not be supersymmetric, it is therefore necessary for the effective potential  $V^{(6)}$  to possess no supersymmetric minimum. Figure 2.9 shows generic forms of the potential for broken and unbroken supersymmetry. Supersymmetry breaking arises from a field in the model having a non-zero vacuum expectation value. One can either use one of the  $F$ - or  $D$ -auxiliary fields of chiral or vector superfields, respectively, but only the so-called *F-term supersymmetry breaking* will be discussed here due to the connection to gauge mediation models. Hence, the criterion for supersymmetry breaking is

$$\langle 0 | F_i | 0 \rangle \neq 0 \quad (2.51)$$

for one of the auxiliary fields  $F_i$ .

<sup>6)</sup>The effective potential is given by  $V = F_i^\dagger F_i$  for Lagrangians for chiral superfields, where  $F_i$  are the auxiliary component fields of the superfield.

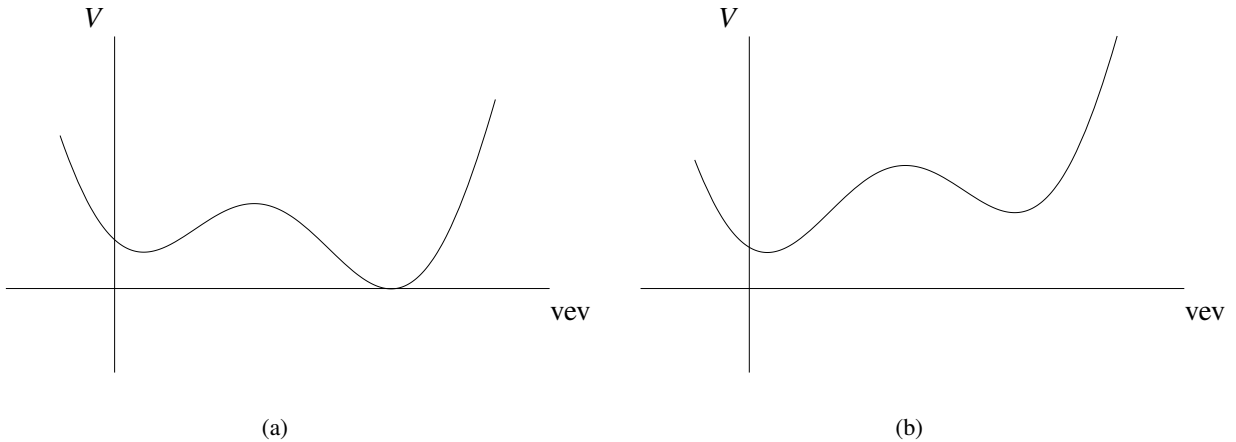


Figure 2.9: Generic forms of the effective potential  $V$  as a function of some vacuum expectation value for (a) unbroken supersymmetry and (b) broken supersymmetry.

The simplest model of F-term breaking is the O'RAIFEARTAIGH model [43], which has three chiral superfields  $\Phi_1$ ,  $\Phi_2$  and  $\Phi_3$  with the superpotential

$$W = \lambda \Phi_1 (\Phi_3^2 - M^2) + \mu \Phi_2 \Phi_3, \quad (2.52)$$

where  $\lambda > 0$ ,  $M \neq 0$  and  $\mu \neq 0$  are parameters of the model. The absolute minimum of this potential is at

$$F_1^\dagger = \lambda M^2, \quad F_2^\dagger = F_3^\dagger = 0 \quad (2.53)$$

and

$$V = \lambda^2 M^4 > 0. \quad (2.54)$$

The supersymmetry breaking scale can be defined as the expectation value of the F-term responsible for supersymmetry breaking.

In analogy to the Standard Model, where massless Goldstone bosons appear after spontaneous breaking of the global gauge symmetry, a massless Goldstone fermion with spin  $\frac{1}{2}$  is expected in broken global supersymmetry, since the supersymmetry generators are fermionic. The spinor  $\psi_i$  of the superfield  $\Phi_i$  to which  $F_i$  belongs will be the Goldstone fermion.

The Goldstone fermion might be a problem for globally supersymmetric models, but the models studied in the literature are mostly locally supersymmetric. When supersymmetry is localized in analogy to the localization of the Standard Model gauge group by the Noether procedure, then a gauge field for supersymmetry appears in the theory. Due to the fermionic character of supersymmetry and due to the preservation of the Lorentz structure, the gauge field is described by a RARITA-SCHWINGER vector-spinor  $\Psi_\mu$  with spin  $\frac{3}{2}$  [44], also called *gravitino*. Its free field equation simply reads

$$\epsilon^{\lambda\mu\nu\rho} \gamma_5 \gamma_\mu \partial_\nu \Psi_\rho = 0 \quad (2.55)$$

with  $\epsilon^{0123} = 1$  and its partner field in the supermultiplet is a spin 2 field, called *graviton*. After the breaking of local supersymmetry the Goldstone fermion is absorbed by the gravitino, becoming its longitudinal component and giving mass to the gravitino [45, 46]:

$$m_{3/2} \sim \frac{\langle F \rangle}{M_P}, \quad (2.56)$$

where  $\langle F \rangle$  is a vacuum expectation value and  $M_P$  is the Planck scale. Hence, the gravitino mass can vary over many orders of magnitude, depending on the scale of supersymmetry breaking. In particular, its mass can be almost zero in models of gauge mediated supersymmetry breaking.

A problem in constructing theories with spontaneous supersymmetry breaking is that there is no candidate gauge singlet in the MSSM whose F-term could develop a vacuum expectation value [23]. Additionally, it is very difficult to mediate supersymmetry breaking to the MSSM fields by including renormalizable interactions at tree level only, even if the model has been extended by additional superfields. Therefore, one expects that the MSSM mass terms (2.28) arise radiatively and that supersymmetry breaking occurs in a *hidden* sector, which does not or only weakly couple directly to the MSSM sector.

There are two main mechanisms of mediating supersymmetry breaking to the MSSM scale. The first one assumes that the mediation is due to gravitational interactions and the MSSM mass terms are given by

$$m_{\text{MSSM}} \sim \frac{\langle F \rangle}{M_P}. \quad (2.57)$$

For masses of a few 100 GeV one therefore expects a supersymmetry breaking scale of about

$$\sqrt{F} \sim 10^{11} \text{ GeV}. \quad (2.58)$$

This mechanism is called *minimal supergravity* (mSUGRA) [47, 48, 49, 50, 51] and the gravitino mass is of the order of a few 100 GeV. The second possibility assumes that the mediation is due to the ordinary electroweak and QCD gauge interactions. The MSSM masses are given by

$$m_{\text{MSSM}} \sim \frac{\langle F \rangle}{M_{\text{mess}}}, \quad (2.59)$$

where  $M_{\text{mess}}$  is the mass scale of an intermediate sector of *messenger* particles. The expected supersymmetry breaking scale can then be as low as

$$\sqrt{F} \sim 10^4 \text{ GeV} \quad (2.60)$$

to assign the right mass to the MSSM particles. These models are called *gauge mediated supersymmetry breaking* models [52, 53, 54, 55] or *GMSB* models and will be discussed in some detail in the next section.

### 2.3.3 Gauge mediated supersymmetry breaking

#### General model

In GMSB models a messenger sector of chiral supermultiplets is introduced, which couples to the sector of supersymmetry breaking and transforms under the Standard Model gauge group. These messenger particles then couple indirectly to the MSSM particles through ordinary gauge and gaugino interactions. As in the case of supergravity models there is also gravitational interaction between the supersymmetry breaking sector and the MSSM, but this effect is relatively unimportant compared to the gauge interaction effects. GMSB can then be understood in terms of loop effects in a renormalizable framework in contrast to gravity mediation. In the simplest model the messenger fields can be chosen to be chiral supermultiplets  $q, \bar{q}, l$  and  $\bar{l}$  transforming under the Standard Model gauge group in the same way as the MSSM quark and lepton supermultiplets (see Tab. 2.3). The particle content of these supermultiplets has to acquire large masses, since it has not been discovered so far. Therefore, they couple to a gauge-singlet chiral supermultiplet  $S$  through the superpotential

$$W_{\text{mess}} = y_1 S l \bar{l} + y_2 S q \bar{q}, \quad (2.61)$$

Figure 2.10: 1-loop contributions from messenger scalars (dashed) and messenger fermions (solid) to the MSSM gaugino masses.

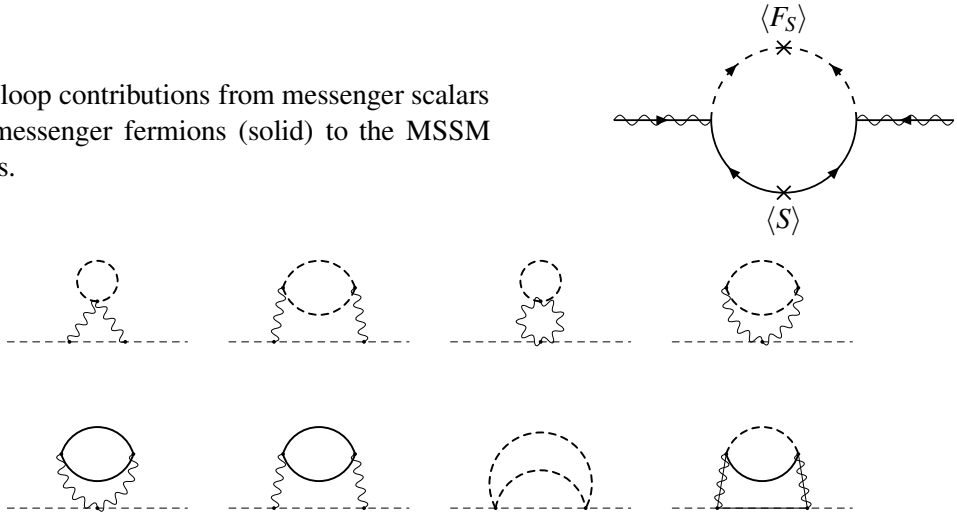


Figure 2.11: 2-loop contributions from messenger scalars (dashed), messenger fermions (solid), Standard Model gauge bosons (wavy) and MSSM gauginos (solid plus wavy) to the MSSM scalar masses in GMSB models [23].

where  $y_1$  and  $y_2$  are coupling constants. Supersymmetry breaking can be accomplished by *e.g.* using  $S$  in an O'RAIFEARTAIGH model and the scalar component of  $S$  and its  $F$ -term auxiliary field acquire vacuum expectation values  $\langle S \rangle$  and  $\langle F \rangle$ , respectively. This leads to mass terms and a mass splitting of each messenger supermultiplet:

$$l, \bar{l} : \quad m_{\text{fermions}}^2 = |y_1 \langle S \rangle|^2, \quad m_{\text{scalars}}^2 = |y_1 \langle S \rangle|^2 \pm |y_1 \langle F_S \rangle|, \quad (2.62)$$

$$q, \bar{q} : \quad m_{\text{fermions}}^2 = |y_2 \langle S \rangle|^2, \quad m_{\text{scalars}}^2 = |y_2 \langle S \rangle|^2 \pm |y_2 \langle F_S \rangle|, \quad (2.63)$$

where the breaking order parameter  $F_S$  felt by the messengers may not coincide with the underlying breaking parameter  $F$ . A dimensionless parameter  $C_{\text{grav}} \geq 1$  is introduced, relating  $F$  and  $F_S$  by

$$F = C_{\text{grav}} \cdot F_S. \quad (2.64)$$

Hence, the supersymmetry breaking in the messenger sector is due the  $F$ -term vacuum expectation value and is communicated to the MSSM sector via radiative corrections. The overall messenger mass scale is denoted  $M_{\text{mess}} \sim y_{1,2} \langle S \rangle$ . The MSSM gauginos obtain their masses from 1-loop corrections, shown in Fig. 2.10, while the MSSM scalars obtain masses at the 2-loop level, shown in Fig. 2.11.

Messengers transforming under the ordinary Standard Model gauge group might impose problems for the gauge coupling unification, if their masses are far below the GUT scale. This can be avoided by requiring that the messengers consist of  $N_5$  multiplets transforming under a  $SU(5)$  group containing the Standard Model group.<sup>7)</sup> This is called the *minimal GMSB* (mGMSB) model.<sup>8)</sup>  $N_5$  may not be too large, in order to avoid that the running gauge couplings diverge before unifying at the GUT scale. For instance, one needs  $N_5 \leq 4$  for messenger masses of order  $10^6$  GeV. The masses of the gauginos and

<sup>7)</sup>This restriction is not necessary and more general models have been identified, which are not particularly more unnatural than the minimal model [56].

<sup>8)</sup>The mGMSB model achieves gauge coupling unification at 1-loop level. However, at 2-loop level the unification fails and the model has to be extended to a model with larger  $SU(5)$  representations [57].

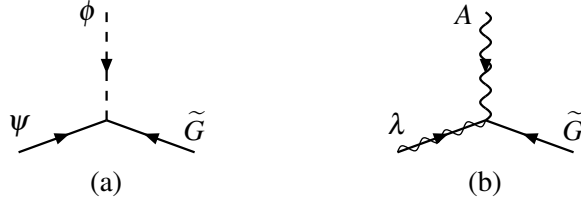


Figure 2.12: Goldstino  $\tilde{G}$  coupling to superpartner pairs (a)  $(\phi, \psi)$  and (b)  $(\lambda, A)$ .

MSSM scalars can be computed to be

$$M_a = \frac{\alpha_a}{4\pi} \Lambda N_5, \quad (2.65)$$

$$m_{\phi_i}^2 = 2\Lambda^2 N_5 \sum_{a=1}^3 C_a(i) \left( \frac{\alpha_a}{4\pi} \right)^2, \quad (2.66)$$

where  $C_a(i)$  are numerical constants of order  $\sim 1$  and

$$\Lambda = \frac{F_S}{M_{\text{mess}}} \quad (2.67)$$

is called the *effective visible sector breaking parameter*. With this parameter  $F$  can be written as

$$F = C_{\text{grav}} \cdot \Lambda \cdot M_{\text{mess}}. \quad (2.68)$$

GMSB models predict that the gravitino  $\tilde{G}$  is the LSP and that all MSSM sparticles will decay to final states including it. One might think that these decays are very slow due to the gravitational coupling of the gravitino, but since its longitudinal component is the Goldstino, also non-gravitational couplings are present. Only the Goldstino component plays a role in collider phenomenology and the denotations *Goldstino* and *gravitino* can be used interchangeably. In GMSB models each Standard Model particle is coupled to its supersymmetric partner particle through the Goldstino with a strength inversely proportional to  $F$ , as depicted in Fig. 2.12. In particular, a sparticle  $\tilde{X}$  can decay to its Standard Model partner  $X$  and a Goldstino with a decay rate of

$$\Gamma(\tilde{X} \rightarrow X \tilde{G}) = \frac{\kappa m_{\tilde{X}}^5}{16\pi F^2} \left( 1 - \frac{m_X^2}{m_{\tilde{X}}^2} \right)^4, \quad (2.69)$$

where  $\kappa$  is a mixing parameter. For slepton decays  $\kappa = 1$ , while for a pure  $U(1)_Y$  bino decay to a photon and a Goldstino  $\kappa = \cos^2 \theta_W$ , where  $\theta_W$  is the electroweak mixing angle. The decay rate (2.69) corresponds to a decay length of

$$c\tau(\tilde{X} \rightarrow X \tilde{G}) = \left( \frac{100 \mu\text{m}}{\kappa} \right) \left( \frac{100 \text{GeV}}{m_{\tilde{X}}} \right)^5 \left( \frac{\sqrt{F}}{100 \text{TeV}} \right)^4 \left( 1 - \frac{m_X^2}{m_{\tilde{X}}^2} \right)^{-4}. \quad (2.70)$$

In summary, the minimal GMSB model is described by the following 6 parameters:

- $\Lambda$  is the effective visible sector supersymmetry breaking parameter given by Eq. (2.67). The MSSM superpartner masses scale linearly with  $\Lambda$ , which is of the order  $\sim 100 \text{TeV}/\sqrt{N_5}$ .
- $N_5$  is the number of  $SU(5)$  messenger multiplets. The gaugino masses scale linearly with  $N_5$ , while the scalar masses scale like  $\sqrt{N_5}$ . For low values a neutralino  $\tilde{\chi}_1^0$  is the NLSP, while for larger values a right-handed slepton  $\tilde{l}$  is the NLSP.

- $M_{\text{mess}}$  is the overall mass scale of the messenger sector. All sparticle masses depend only logarithmically on  $M_{\text{mess}}$ , while the lifetime of the NLSP depends quadratically on  $M_{\text{mess}}$ .  $M_{\text{mess}} > \Lambda$  is required to avoid color and charge breaking in the messenger sector.
- $\tan\beta$  is the ratio of the vacuum expectation values of the Higgs fields and lies in the region  $1.5 < \tan\beta < 60$ . The lower limit leads to a light CP-even Higgs scalar below the LEP exclusion limit, while large values of  $\tan\beta$  leads to  $\tilde{\tau}$  slepton that is significantly lighter than the other sleptons.
- $\text{sign}(\mu)$  is the sign of the Higgs mass parameter  $\mu$  appearing in the gaugino mixing matrices.
- $C_{\text{grav}}$  is the scale factor of the Goldstino coupling. It can be used to control the NLSP lifetime, which scales like  $C_{\text{grav}}^2$ .

### General phenomenology

The phenomenology of GMSB is largely determined by the nature of the NLSP leading to different types of final state particles, such as leptons or photons. Since the scalars have a different dependence on the model parameters as the gauginos, the nature of the NLSP also depends on the parameters. Especially the value of  $N_5$  has a big influence, as discussed above, but also  $\tan\beta$ , which determines the mixing in the  $\tilde{\tau}$  sector and thus the mass of the lighter  $\tilde{\tau}$ .

Figure 2.13(a) shows the mass difference  $m_{\tilde{\tau}} - m_{\tilde{l}}$  in the  $\Lambda - \tan\beta$  plane for  $\text{sign}(\mu) = 1$ ,  $C_{\text{grav}} = 1$ ,  $M_{\text{mess}} = 250$  TeV and  $N_5 = 3$ . For low values of  $\tan\beta$  the selectrons, smuons and staus are degenerate and the region is called *co-NLSP region*. For increasing values of  $\tan\beta$  the difference between the masses of the two staus becomes larger and the lighter stau is the NLSP. The lightest neutralino is heavier than the sleptons and does (most often) not decay directly to the gravitino. In this part of the parameter space one expects leptons from the  $\tilde{l} \rightarrow l\tilde{G}$  decay in the final state, while the gravitino escapes detection due to the weak interaction with the detector material. This can lead to a large amount of missing transverse energy. If the lifetime of the NLSP is large, such that the decay occurs outside the detector, one expects heavily ionising heavy charged particles in the detector leading to very interesting signatures (see [18] for ATLAS studies and [58] for searches at the TeVatron experiments).

Figure 2.13(b) shows the mass difference  $m_{\tilde{\tau}} - m_{\tilde{\chi}_1^0}$  in the  $\Lambda - \tan\beta$  plane for  $\text{sign}(\mu) = 1$ ,  $C_{\text{grav}} = 1$ ,  $M_{\text{mess}} = 500$  TeV and  $N_5 = 1$ . The lightest neutralino is now the NLSP for small values of  $\tan\beta$  due to the low value of  $N_5$ . For larger values of  $\tan\beta$  the stau mass splitting is again large enough to render the lightest stau the NLSP. In this region of the parameter space one expects photons from the  $\tilde{\chi}_1^0 \rightarrow \gamma\tilde{G}$  decay in the final state, since the lightest neutralino is almost a pure bino in the minimal GMSB model and thus the branching ratio to photons dominates. Again, one expects a large amount of missing transverse energy due to the escaping gravitino. If the lifetime of the neutralino is large, such that it decays outside the detector, it might become difficult to distinguish this signature from those arising in mSUGRA models where the neutralino is the LSP and also escapes detection. In this thesis the focus lies on GMSB models with a neutralino NLSP decaying to a photon and a gravitino.

### 2.3.4 Experimental results

Searches for signatures arising from GMSB, especially with photons in the final state, have been performed at a variety of experiments [59], including the LEP experiments ALEPH [60], L3 [61], DELPHI [62] and OPAL [63] and the TeVatron experiments D0 [64, 65, 66] and CDF [67, 68]. Also combined TeVatron analysis have been presented [69, 70, 71], but no evidence for a GMSB signal has been found so far. The current best limit is derived from the TeVatron experiments due to the large center-of-mass energy in  $p\bar{p}$  collisions.

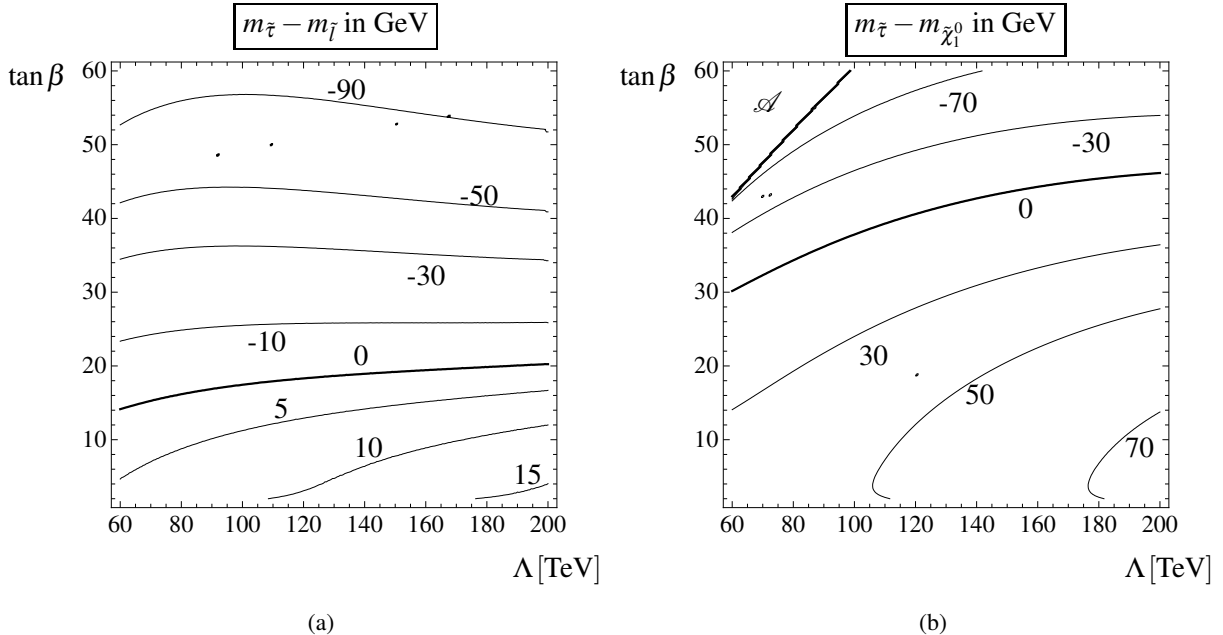


Figure 2.13: Mass differences (a)  $m_{\tilde{\tau}} - m_{\tilde{l}}$  and (b)  $m_{\tilde{\tau}} - m_{\tilde{\chi}_1^0}$  in GeV in the  $\Lambda - \tan\beta$  plane for  $\text{sign}(\mu) = 1$ ,  $C_{\text{grav}} = 1$  and (a)  $M_{\text{mess}} = 250$  TeV,  $N_5 = 3$  and (b)  $M_{\text{mess}} = 500$  TeV,  $N_5 = 1$ . Region  $\mathcal{A}$  is theoretically excluded, due to the existence of tachyonic states. Below the  $m_{\tilde{\tau}} - m_{\tilde{\chi}_1^0} = 0$  line a neutralino is the NLSP decaying to a photon and a gravitino.

As an example, the CDF collaboration has searched for neutralino decays to photons and gravitinos in the two photons plus missing transverse energy  $E_T^{\text{miss}}$  channel [71]. The requirements have been two isolated photons  $\gamma_{1,2}$  with transverse energy  $E_T > 13$  GeV each,  $\Delta\phi(\gamma_1, \gamma_2) < \pi - 0.15$ ,  $H_T > 200$  GeV<sup>9)</sup> and  $E_T^{\text{miss}}$  significance<sup>10)</sup> of larger than three. These requirements have been optimized in order to obtain the largest possible significance for the GMSB signal and additional requirements have been imposed to reduce non-collision background. After all selections a single event remained being consistent with the expected background of  $0.62 \pm 0.29$  events. Figure 2.14 shows the derived exclusion limits as a function of the neutralino mass and lifetime. For a vanishing neutralino lifetime the mass below 138 GeV is excluded at 95% C.L.. Based on these results and experiences search strategies have been developed for the LHC experiments analysing several benchmark points and trying to identify reasonable search strategies.

GMSB models have also been investigated in the cosmological context of the WMAP data and the constraining of warm dark matter candidates [72, 73, 74, 75]. Usually dark matter candidates are classified according to their velocity dispersion which defines a free-streaming length. For cold dark matter this is by definition so small that it is irrelevant for cosmological structure formation. In the case of hot dark matter the free-streaming length is so large that it smoothes out fluctuations in the total matter density even on galaxy cluster scales. Strong constraints on the mass of hot dark matter candidates can be derived. Warm dark matter is in the region between these two alternatives and it is found that gravitinos arising in GMSB models might lie within this region and that GMSB models with gravitino LSPs cannot be excluded cosmologically in general, since the limits on the GMSB parameters depend strongly on the

<sup>9)</sup>  $H_T$  is the scalar sum  $p_T$  of all identified objects in the event.

<sup>10)</sup> The significance is calculated by performing pseudo-experiments for each event and it is defined as  $-\log(\mathcal{P})$ , where  $\mathcal{P}$  is the probability for the  $E_T^{\text{miss}}$  drawn from the expected mis-measured  $E_T^{\text{miss}}$  distribution to be equal to or larger than the observed  $E_T^{\text{miss}}$ .

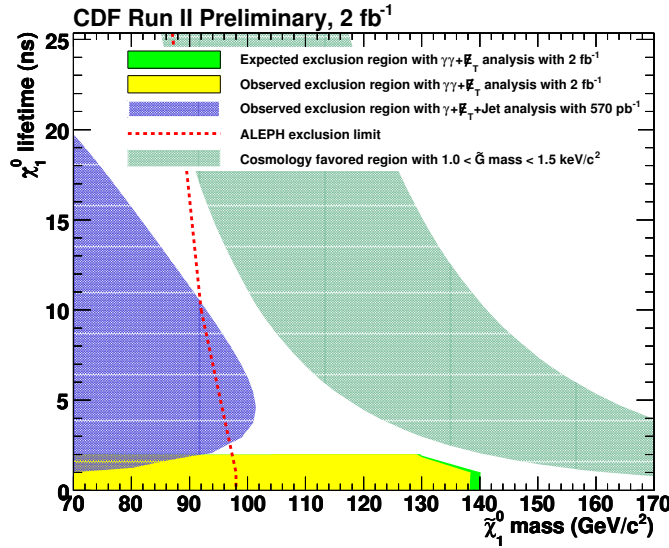


Figure 2.14: Exclusion limits for GMSB signatures with photons in the final state derived from the CDF searches as a function of the neutralino mass and lifetime [71].

cosmological assumptions, such as the details of inflation or leptogenesis [76, 77, 78].

# Chapter 3

## The LHC and the ATLAS detector

The Large Hadron Collider (LHC) [79] is a proton-proton collider with a center of mass energy of 14 TeV. For the investigation of the products of the collisions, four large experiments have been built. ATLAS (A Toroidal LHC ApparatuS) is one of two general purpose detectors, built to detect final state particles produced with the LHC. CMS (Compact Muon Solenoid) is the other general purpose detector and the remaining two experiments are ALICE (A Large Ion Collider Experiment), a dedicated detector for heavy ion collisions, and LHCb (Large Hadron Collider beauty), which investigates the decay products of B-hadrons. In this chapter the LHC will be described briefly and the several subcomponents of the ATLAS detector will be presented.

### 3.1 The Large Hadron Collider

The LHC is a ring accelerator of 27 km circumference, which has been built by the European Organization for Nuclear Reseach (CERN), based near Geneva. It is located in the former LEP tunnel between 70 m and 140 m underground. Proton-proton collisions, as well as heavy ion collisions will be provided, but only the proton-proton collisions are relevant in this thesis. The main operation mode starts in the end of 2009 with a center of mass energy of 10 TeV, which will be increased later. The layout and the position of the experiments are shown in Fig. 3.1.

The nominal center of mass energy is  $\sqrt{s} = 14 \text{ TeV}$  with 7 TeV energy per beam. The protons are pre-accelerated by different systems, including the Proton Synchrotron (PS) and the Super Proton Synchrotron (SPS). The injection into the LHC is done by the SPS at a beam energy of 450 GeV and the protons need approximately 20 minutes to reach the design energy in the LHC. The energy is provided by superconductive radio frequency cavities, while the protons are kept on track by magnetic fields. These are provided by 1232 superconductive dipole magnets with a length of 15 m each, which are configured such that both proton beams in both directions are deflected correctly. With a radius of  $r_{LHC} = 4298 \text{ m}$  a magnetic field of  $B = 8.33 \text{ T}$  is needed. Additional magnets are used for focussing and correcting the beams. In total 9300 superconductive magnets operate at a temperature of 1.7 K.

The interaction rate  $\dot{N}$  is proportional to the cross section  $\sigma$  of a specific process and the proportionality factor is called the instantaneous luminosity  $\mathcal{L}$ . It can be expressed by the colliders beam configuration:

$$\mathcal{L} = f \frac{k n_1 n_2}{4\pi \sigma_x \sigma_y} R_\phi, \quad (3.1)$$

where  $n_1$  and  $n_2$  are the numbers of particles in each of the  $k$  bunches in each beam,  $\sigma_x$  and  $\sigma_y$  give the extensions of the bunches perpendicular to the beam direction,  $f$  is the revolution frequency and  $R_\phi$  is a luminosity reduction factor due to the non-vanishing LHC beam crossing angle. In each bunch there

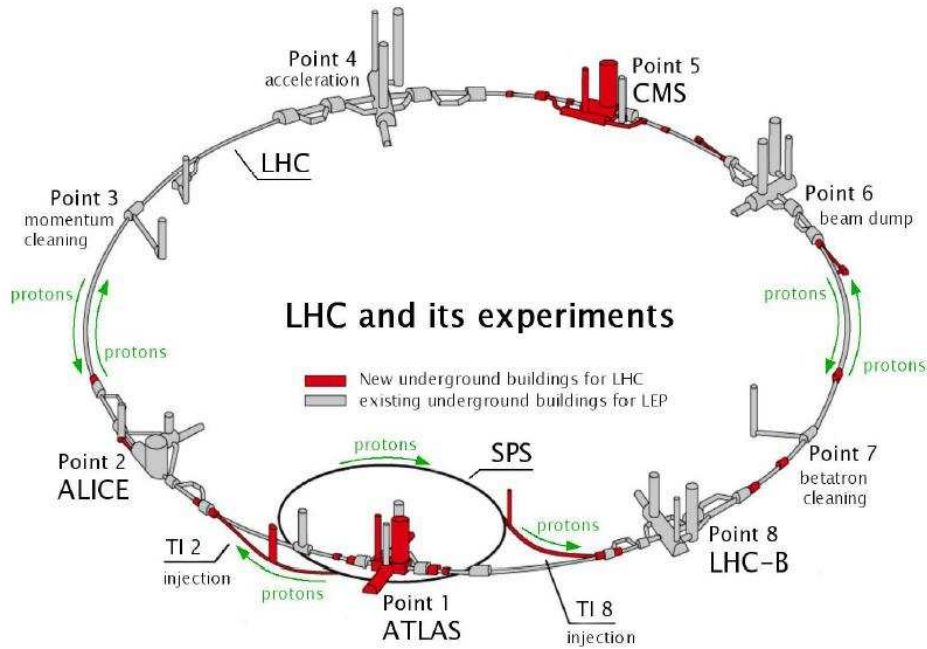


Figure 3.1: Layout of the LHC and the position of the experiments.

are about  $1.15 \cdot 10^{11}$  protons and in the whole collider 2808 bunches are circulating. The revolution frequency is fixed to  $f = 11.25$  kHz and the bunch crossing rate is 40 MHz leading to a bunch spacing of 25 ns. The total number of events is given by

$$N = L \cdot \sigma, \quad (3.2)$$

where  $L$  is the integrated luminosity

$$L = \int dt \mathcal{L}. \quad (3.3)$$

For the running of the LHC several different luminosity phases are planned. The first phase will be at around  $\mathcal{L} = 10^{31} \text{ cm}^{-2}\text{s}^{-1}$  and will be used for commissioning of the collider and for first physics results. Then the luminosity will be increased to  $\mathcal{L} = 10^{33} \text{ cm}^{-2}\text{s}^{-1}$  and later to  $\mathcal{L} = 10^{34} \text{ cm}^{-2}\text{s}^{-1}$ , which is the design luminosity. This design phase is intended to last several years and an integrated luminosity of some  $100 \text{ fb}^{-1}$  of data will be collected. For the far future additional luminosity upgrades are planned and are discussed under the name SLHC (Super-LHC).

The total inelastic proton-proton cross section is around 99 mb [19] at a center of mass energy of 14 TeV. Therefore, around 23 proton-proton interactions are expected per bunch crossing at a luminosity of  $\mathcal{L} = 10^{34} \text{ cm}^{-2}\text{s}^{-1}$ , while one of these interactions is a hard scattering process. However, the overlap of these pile-up events imposes a great challenge for the data analysis in order to assign all final state particles to the correct interaction. The detector components also have to deal with the high radiation level and especially the components of the ATLAS detector have been built in this respect.

## 3.2 The ATLAS detector

ATLAS is one of the four LHC experiments and one of two multipurpose detectors, which have been built to cover a broad range of physics topics expected at the LHC. It is designed to measure electrons, muons,

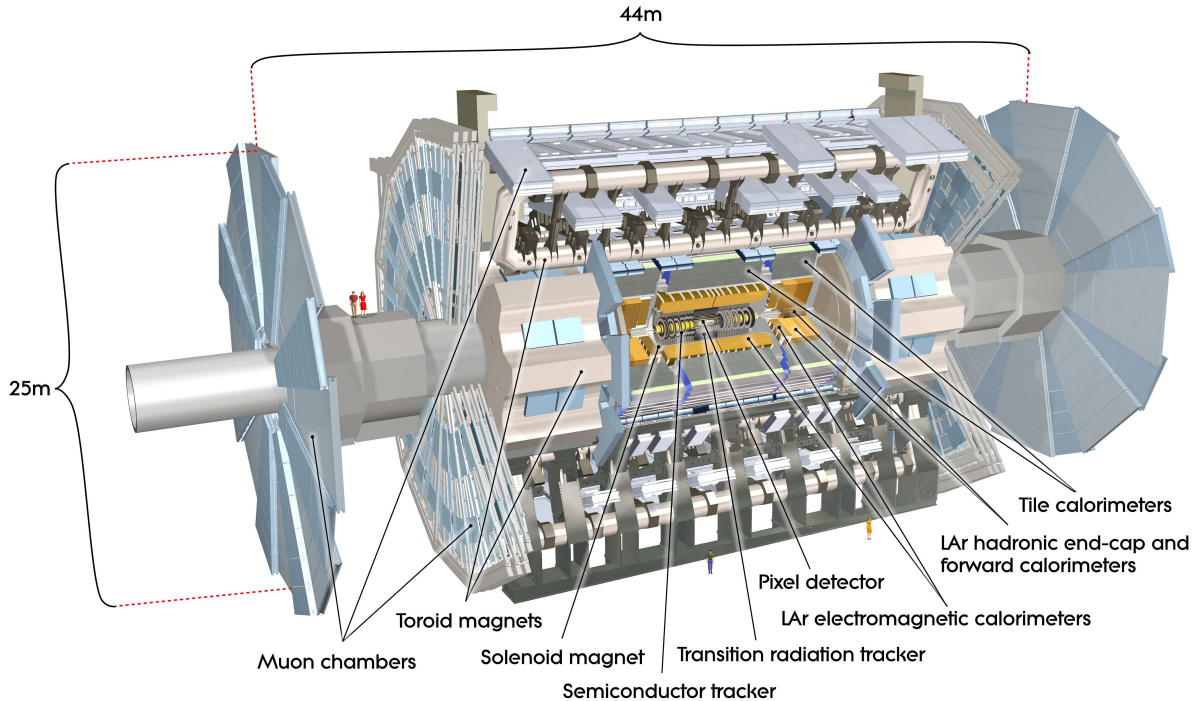


Figure 3.2: Schematic view of the ATLAS detector [80].

photons and hadronic particles with high precision and high acceptance. Therefore it has an onion-like structure and is built around the beam pipe, as shown in Fig. 3.2. ATLAS is forward backward symmetric and can be divided into three parts, the barrel and two endcaps. The innermost part of the detector is the tracking system, where the momenta of charged particles are measured with high precision. It consists of the pixel detector, the silicon microstrip tracker (SCT) and the transition radiation tracker (TRT) and is surrounded by a superconductive solenoid with a magnetic field of 2 T. The electromagnetic and hadronic calorimeters are built behind the tracking system to measure the energy of electromagnetically and strongly interacting particles. The outermost system is the muon spectrometer with the barrel and endcap toroid magnets providing a field of 0.5 T and 1 T, respectively. In total ATLAS is 44 m long and 25 m high and weights around 7000 tonnes. Table 3.1 lists some of the important performance goals for the ATLAS detector.

### 3.2.1 The coordinate system

The nominal interaction point is in the center of the ATLAS coordinate system and is located in the center of the detector. The  $x$ -axis is pointing towards the center of the accelerator, while the  $y$ -axis is pointing upwards. To define a right-handed coordinate system the  $z$ -axis is chosen to point counter-clockwise along the beam direction. The polar angle  $\theta$  is measured with respect to the positive  $z$ -axis such that the pseudo-rapidity can be defined as

$$\eta = -\ln \tan \left( \frac{\theta}{2} \right). \quad (3.4)$$

This reflects the problem of the unknown initial boost along the  $z$ -axis at hadron colliders as  $\Delta\eta$  is invariant under Lorentz boosts. For massless particles  $\eta$  is the same as the rapidity. The coverage of

Detector component	Required resolution	$\eta$ coverage	
		Measurement	Trigger
Tracking	$\sigma_{p_T}/p_T = 0.05\% p_T \oplus 1\%$	$\pm 2.5$	
EM calorimetry	$\sigma_E/E = 10\%/\sqrt{E} \oplus 0.7\%$	$\pm 3.2$	$\pm 2.5$
Had. calorimetry barrel and endcap forward	$\sigma_E/E = 50\%/\sqrt{E} \oplus 3\%$	$\pm 3.2$	$\pm 3.2$
	$\sigma_E/E = 100\%/\sqrt{E} \oplus 10\%$	$3.1 <  \eta  < 4.9$	$3.1 <  \eta  < 4.9$
Muon Spectrometer	$\sigma_{p_T}/p_T = 10\%$ at $p_T = 1 \text{ TeV}$	$\pm 2.7$	$\pm 2.4$

Table 3.1: Performance goals of the ATLAS detector. The muon-spectrometer performance is independent of the inner tracking system for high energetic muons [80].

each detector component in  $\eta$  is listed in Tab. 3.1. The  $x$ -axis and  $y$ -axis define the azimuthal angle  $\phi$  by  $\tan \phi = \frac{y}{x}$ , which varies between  $-\pi$  and  $\pi$ . The distance of two particles can be defined in terms of  $\eta$  and  $\phi$  as

$$\Delta R = \sqrt{(\Delta\eta)^2 + (\Delta\phi)^2}. \quad (3.5)$$

The transverse momentum  $p_T = \sqrt{p_x^2 + p_y^2}$  of a particle and the missing transverse energy are also measured in the  $x$ - $y$ -plane and are Lorentz-invariant along the  $z$ -axis.

### 3.2.2 The magnet system

The ATLAS magnet system provides the magnetic fields needed to measure the particle momenta in the tracking system. It consists of four superconductive parts, one solenoid and three toroids (one barrel and two endcaps) and is 22 m in diameter and 26 m long. Figure 3.3 shows a drawing of the geometry of the magnet windings and the tile calorimeter steel. In total the magnets store an energy of 1.6 GJ.

The solenoid provides an axial field of 2 T, which bends the particle tracks in the inner tracking system. It is designed such that it minimizes the amount of material in front of the electromagnetic calorimeter to ensure a good energy resolution. In total it contributes around 0.66 radiation lengths. The inner and outer radius of the solenoid are 2.46 m and 2.56 m and its axial length is 5.8 m.

The barrel (endcap) toroids deliver a toroidal field of 0.5 T (1 T) to measure the momenta of the muons traversing the muon spectrometer. Each of the toroids consists of eight coils assembled radially and symmetrically around the beam axis. The endcaps are rotated by  $22.5^\circ$  with respect to the barrel system to provide overlap and optimize the bending power at the interface of the systems.

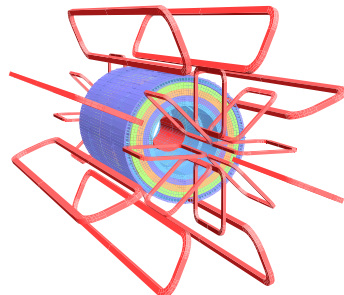


Figure 3.3: Layout of the ATLAS magnet system. The eight barrel and endcap toroid coils and their relative position to the tile calorimeter steel are shown. The solenoid windings lie inside the calorimeter [80].

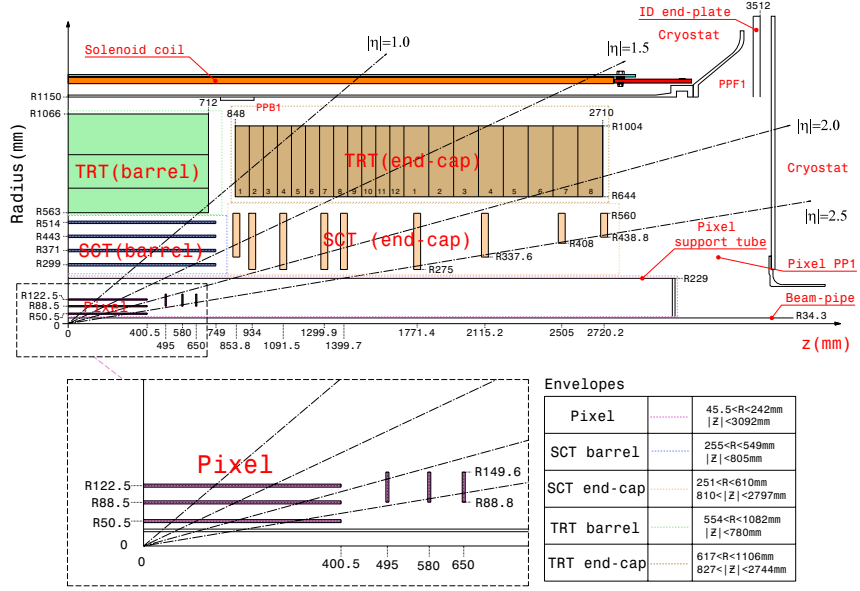


Figure 3.4: Schematic view of a quarter of the ATLAS inner detector. Each of the major elements is shown with the active dimensions [80].

### 3.2.3 Inner detector

The purpose of the inner detector is to measure the momentum of charged particles as precisely as possible. Additionally, secondary vertices can be measured to determine the lifetime of charged particles, reconstruct photon conversions or allow b-tagging. The momentum and the sign of the charge are determined by measuring the bending of the track in the  $r\phi$ -plane by the Lorentz force in the magnetic field. Since the solenoidal field is parallel to the  $z$ -axis, only the transverse momentum can be measured. The hits needed for fitting the tracks are provided by all three subcomponents of the inner detector. To optimize the accuracy of the momentum measurement one has to choose a high magnetic field, a long lever arm on the track, a maximal single hit position resolution and one has to use as many hits as possible.

For the analysis of photon final states in GMSB models the tracker plays an important role. Although photons do not have a track, they have to be distinguished from electrons and the most important criterion is the electron track. A high efficiency reduces the number of electrons misidentified as photons. Additionally, photon conversions can be reconstructed with inner detector information. On the other hand, the selection of signal events requires a good understanding of jets and missing transverse energy. The jet energy measurement can be enhanced by a good understanding of the charged fraction of a jet, which in turn leads to a better estimate of the missing transverse energy.

Fig. 3.4 shows a schematic view of a quarter of the inner detector with all relevant subsystems. The outer radius is 115 cm, given by the dimension of the cryostat, which contains the electromagnetic calorimeter. The total length is 7 m, again given by the position of the endcap calorimeter. The acceptance in pseudo-rapidity is  $|\eta| < 2.5$ . In the following the three subsystems are described.

#### The pixel detector

The pixel detector is the innermost part of the inner detector. It is designed to provide exact measurements of the primary vertex, as well as the starting point of any charged track. This is necessary for an exact reconstruction of all tracks. With this ability the pixel detector can distinguish secondary vertices from the primary vertex, which is needed for the identification of heavy quark decays, such as bottom quarks.

Also in some supersymmetric scenarios long-lived heavy charged particles might decay inside the pixel detector allowing their lifetime to be measured. The suppression of pile-up events is another important issue, since these events do not originate from the hard scattering process and often have a different vertex.

The pixel detector provides three precision measurements of hits over the full acceptance region, as can be seen in Fig. 3.4. The barrel part consists of three cylindrical layers, while three discs on each side are used for the endcaps. The system consists of approximately 1500 identical barrel modules and 1000 disc modules, while the modules themselves have more than 60 000 pixel elements of size  $50 \times 400 \mu\text{m}^2$ . This structure allows for a spatial resolution of  $10 \mu\text{m}$  in the  $R - \phi$ -plane and  $115 \mu\text{m}$  in  $z$ -direction. Each layer has a thickness of around 1% of a radiation length. The total number of readout channels amounts to 80.4 million, which is around 90% of the total number of readout channels of the ATLAS detector.

The lifetime of the pixel detector is limited by radiation damage and needs to be replaced after a few years of data-taking, depending on the luminosity.

### **The semiconductor tracker**

Since the number of hits is limited to three in the pixel detector, the semiconductor tracker (SCT) extends the inner detector system in the intermediate radial range with a barrel part and two endcaps. It provides additional four high precision measurements per track and contains  $63 \text{ m}^2$  of silicon detectors. Each of these silicon detectors has a surface of  $6.36 \times 6.40 \text{ cm}^2$  with 768 readout strips each with  $80 \mu\text{m}$  pitch. In the barrel two detectors are wire-bonded together to form 12.8 cm long strips of which two are glued together back-to-back at a 40 mrad stereo-angle to form a module. The forward modules, 7 and 12 cm long, are similar in construction, but use tapered strips. In total the SCT consists of 4088 modules with 6.2 million readout channels, while the spatial resolution is  $17 \mu\text{m}$  in  $R\phi$ -direction and  $580 \mu\text{m}$  in  $z$ -direction. Tracks can be distinguished, if they are separated by more than  $200 \mu\text{m}$ . The full length of the SCT is almost 6 m, while the outer radius is at 50 cm.

### **The transition radiation tracker**

To further extend the radius of the tracking detector, the transition radiation tracker (TRT) is added to the structure outside the SCT. It is a drift chamber with about 370 000 straw tubes containing 70% Xenon, 27% CO<sub>2</sub> and 3% Oxygen. Each straw tube has a diameter of 4 mm.

The barrel part consists of 50 000 straws, which have a length of 144 cm and cover the radial range from 56 to 107 cm. For the ease of construction and maintainance it is built of three rings of 32 individual modules with 329 to 793 axial straws each. The straws are equipped with  $31 \mu\text{m}$  diameter tungsten wires plated with 0.5–0.7  $\mu\text{m}$  gold as anodes and aluminium cased coats as cathodes. The readout is at each end of the tubes. The endcaps contain 320 000 radial straws, which are organized in 20 wheels each, as depicted in Fig. 3.4. The first 12 wheels near the interaction point contain 8 successive straw layers spaced 8 mm apart. The last 8 wheels also contain 8 straw layers, but with a spacing of 15 mm. Each layers contains 768 straws of 37 cm length, while the readout is at the outer radius. The TRT contains 420 000 electronic channels in total, which also provide a drift-time measurement to determine the distance of the track from the readout wire. This results in a spatial resolution of  $130 \mu\text{m}$  in  $R\phi$ -direction.

An additional feature of the TRT is its electron identification capability due to the transition radiation fibres that are interleaved between the straws. Low energy transition radiation photons are absorbed in the Xenon gas and give larger signal amplitudes than minimum-ionising charged particles. Low and high thresholds are used to distinguish between transition radiation signals and normal track signals for each straw providing discrimination power between electrons and charged pions. Also for the identification

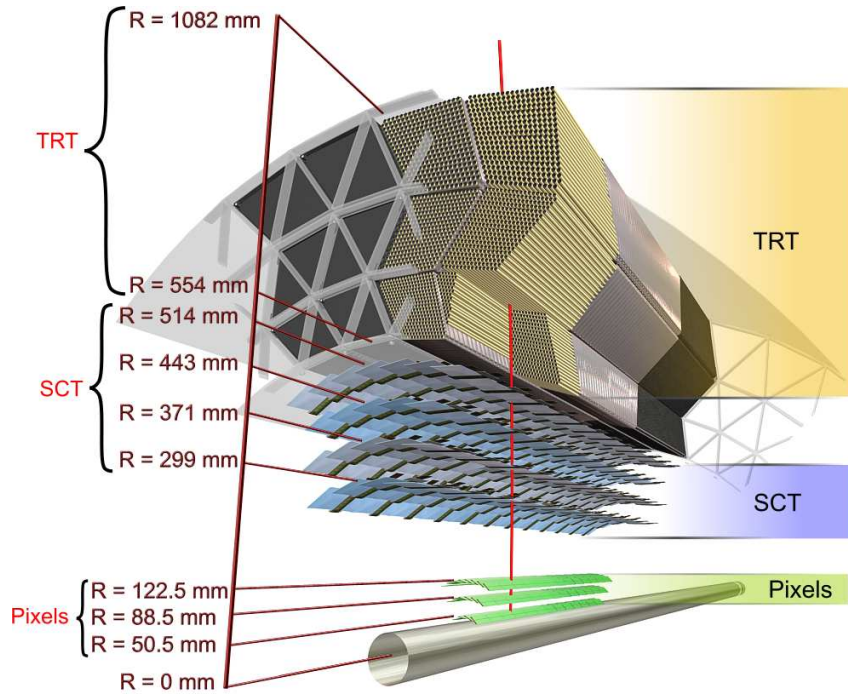


Figure 3.5: Schematic view of the inner detector showing a particle ( $\eta = 0.3$ ) traversing the three pixel layers, the four SCT layers and about 36 straw tubes in the TRT [80].

of heavy stable charged particles, which appear also in GMSB models, the TRT can be used. From time-over-threshold measurements the particle  $\beta$  can be determined, which can be used to select the signal and measure the particle mass.

Figure 3.5 shows a particle ( $\eta = 0.3$ ) traversing the complete inner detector. After having passed the beam pipe, it traverses the three pixel layers, the four cylindrical double layers of the SCT and approximately 36 axial straw tubes in the TRT. The overall performance of the tracking system has been studied in [18] for the reconstruction of muons, electrons and pions. The muon momentum resolution for  $1/p_T$  has been found to be  $0.34 \text{ TeV}^{-1}$  in the barrel and the resolution of the transverse impact parameter is  $10 \mu\text{m}$ . The muon and electron charge can be measured for particles with  $p_T$  up to 1 TeV with misidentification rates of a few percent. In the barrel muons can be identified with an efficiency of almost 100%, while the electron and pion identification suffers from material effects and are reconstructed with efficiencies between 70% and 95%. The rate of pions misidentified as electrons is of the order of a few percent for an electron efficiency of 90% at  $p_T = 25 \text{ GeV}$ . Primary and secondary vertices can be identified with high efficiency ( $\sim 99\%$ ) in the presence of low-luminosity pile-up. The performance of the conversion reconstruction is discussed in Sect. 5.2.

### 3.2.4 Calorimetry

Calorimeters are used to measure the energy of the final state particles. While the inner detector contains as little material as possible to not disturb the path of the traversing particle, the principle of a calorimeter is to fully absorb the particle by using material of several radiation lengths. The particle interacts with the absorber material and produces secondary particles, which in turn interact with the material. The result is a shower of particles, whose energy can be measured. The ATLAS calorimeter is a sampling calorimeter consisting of layers of active, as well as passive absorbers. The latter causes the shower development,

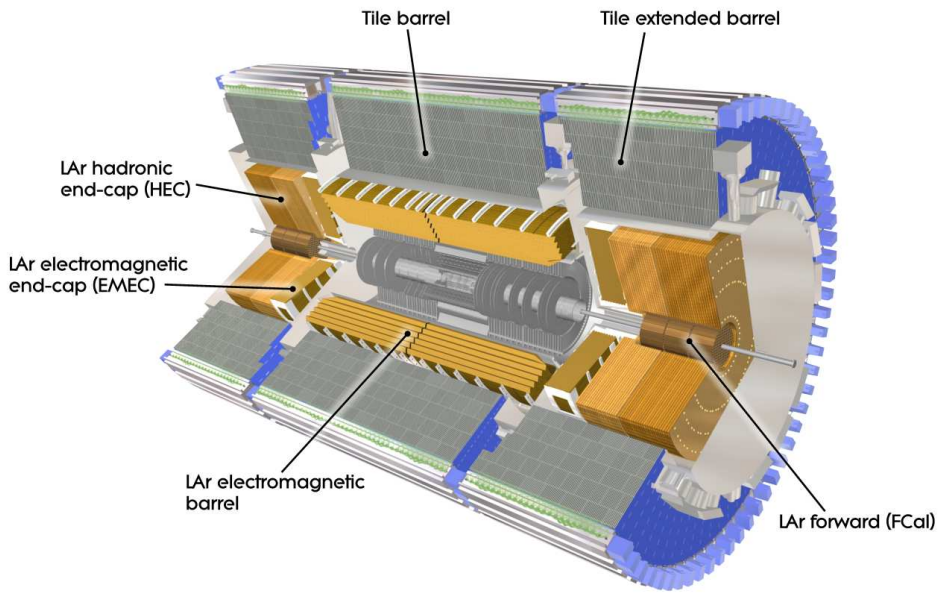


Figure 3.6: Drawing of the ATLAS calorimeter system [80].

while the former is mainly meant for the measurement of the deposited energy. Also neutral particles can be measured in the calorimeter, as long as they are electromagnetically or hadronically interacting. Only weakly interacting particles escape the calorimeter completely and cannot be measured with the detector at all. If the calorimeter is designed granularly, a position measurement of the deposited energy is possible and a geometrical matching with the tracking system can be performed. Also the shape of the shower can be determined and used for particle discrimination. In particular, the separation of pions and photons has to be done with the calorimeter.

ATLAS contains four systems for calorimetry: the electromagnetic calorimeter, the hadronic tile calorimeter, the hadronic endcap calorimeter and the forward calorimeter. Figure 3.6 shows a drawing of the complete system. One can see the barrel and endcap parts of the electromagnetic and hadronic calorimeters, as well as the extension of the hadronic tile barrel and the forward calorimeter. For the study of supersymmetric events all subsystems are crucial: the electromagnetic part for the identification and measurement of photons and leptons and the hadronic part for jets and missing transverse energy. For the precise determination of the latter the complete system must cover as much of the  $\eta$ - and  $\phi$ -directions as possible to measure the complete transverse energy of the event. All subsystems will be described in the following.

### The electromagnetic calorimeter

The ATLAS electromagnetic calorimeter (ECal) is a lead-liquid-Argon (LAr) detector with accordion geometry. The main task is the measurement and identification of electrons and photons over a broad energy range. It is therefore particularly important for the study of GMSB events in this thesis. The lead layers serve as absorbers and the liquid argon is the active material for detection. The ECal is divided into a barrel part ( $|\eta| < 1.475$ ) and two endcaps ( $1.375 < |\eta| < 3.2$ ). The central solenoid position is in front of the ECal demanding an optimization of the material in order to achieve the desired performance. The calorimeter has to be thick enough in terms of radiation lengths in order to limit the punch-through into other systems. The ECal therefore has a total thickness of more than 22 radiation lengths in the barrel

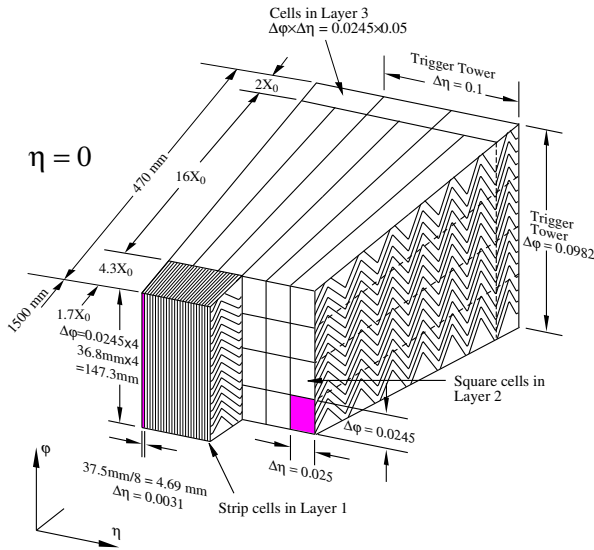


Figure 3.7: Sketch of a module of the electromagnetic barrel calorimeter. The different compartments with the accordion shape and the corresponding granularities in  $\phi$ - and  $\eta$ -directions are shown [80].

and more than 24 radiation lengths in the endcaps. In the region  $|\eta| < 1.8$  a LAr-presampler is installed to correct for the energy losses of electrons and photons in the inner detector as well as the cryostats and the solenoid.

The barrel part consists of two identical half-barrels of 3.2 m length, separated by a small gap of 4 mm at  $z = 0$ . Also the endcaps are divided into two parts: an outer wheel covering the region  $1.375 < |\eta| < 2.5$  and an inner wheel covering the region  $2.5 < |\eta| < 3.2$ . The accordion shaped geometry with the kapton electrodes provides a complete  $\phi$  uniformity without azimuthal cracks, as shown in Fig. 3.7. One can also see the segmentation into three samplings for the region  $|\eta| < 2.5$  used for precision measurements. The endcap inner wheel is segmented into two samplings in depth and has a coarser granularity than for the rest of the acceptance, which is sufficient to measure jet energies and missing transverse energy precisely enough.

The first sampling of the precision region is equipped with very fine strips allowing for a precise determination of the  $\eta$  position of a particle and therefore the distinction from *e.g.* two photons coming from a neutral pion decay. This is important to separate single photons or electrons from jets and for the reconstruction of  $\tau$  leptons. The second sampling is the longest one and absorbs most of the energy with cubic cells of size  $\Delta\eta \times \Delta\phi = 0.025 \times 0.025$ . The resolution in  $\phi$  direction is better than in the first sampling and allows for the determination of the  $\phi$  position of a particle. The  $\eta$  direction of a photon is determined from the  $\eta$  position of the cluster in the first and second layer. The determination of the  $\phi$  direction is hardly possible due to the insufficient  $\phi$  resolution in the first sampling. The third sampling is used to estimate the leakage into the hadronic calorimeter. The values for the rapidity coverage, the granularity and the longitudinal segmentation of the ATLAS ECal subsystems are listed in Tab. 3.2.

As an example, the energy of an electron in each layer,  $E_0$  for the presampler and  $E_1$ ,  $E_2$  and  $E_3$  for the different samplings, is the sum of the energies in each selected cell in the cluster. The cluster is constructed first in the second sampling, where cells within a square window of  $3 \times 3$  cells around the cell with the highest energy are clustered together. The total energy is given by

$$E = \text{offset} + w_0 \times E_0 + w_{01} \times \sqrt{E_0 E_1} + \lambda (E_1 + E_2 + E_3) + w_3 \times E_3, \quad (3.6)$$

where  $w_{0,01,3}$  and  $\lambda$  are different correction factors depending on the electron energy and  $\eta$ . The energy

	Barrel		Endcap	
Number of layers and $\eta$ coverage				
Presampler	1	$ \eta  < 1.52$	1	$1.5 <  \eta  < 1.8$
Calorimeter	3	$ \eta  < 1.35$	2	$1.375 <  \eta  < 1.5$
	2	$1.35 <  \eta  < 1.475$	3	$1.5 <  \eta  < 2.5$
Granularity $\Delta\eta \times \Delta\phi$ versus $ \eta $				
Presampler	$0.025 \times 0.1$	$ \eta  < 1.52$	$0.025 \times 0.1$	$1.5 <  \eta  < 1.8$
Calorimeter 1st layer	$0.025/8 \times 0.1$	$ \eta  < 1.40$	$0.050 \times 0.1$	$1.375 <  \eta  < 1.425$
	$0.025 \times 0.025$		$1.40 <  \eta  < 1.475$	$0.025 \times 0.1$
				$1.425 <  \eta  < 1.5$
				$0.025/8 \times 0.1$
				$1.5 <  \eta  < 1.8$
				$0.025/6 \times 0.1$
				$1.8 <  \eta  < 2.0$
Calorimeter 2nd layer	$0.025 \times 0.1$		$0.050 \times 0.025$	$2.0 <  \eta  < 2.4$
	$0.075 \times 0.025$		$0.025 \times 0.025$	$2.4 <  \eta  < 2.5$
Calorimeter 3rd layer	$0.050 \times 0.025$		$0.1 \times 0.1$	$2.5 <  \eta  < 3.2$
	$0.050 \times 0.025$		$0.050 \times 0.025$	$1.5 <  \eta  < 2.5$
Number of readout channels				
Presampler	7808		1536 (both sides)	
Calorimeter	101760		62208 (both sides)	

Table 3.2: Main parameters of the ATLAS electromagnetic calorimeter and its subsystems [80].

resolution has been studied in test beam measurements and simulation and can be parametrized as [81]

$$\frac{\sigma(E)}{E} = \frac{a}{\sqrt{E(\text{GeV})}} \oplus b, \quad (3.7)$$

where  $a = 10\% \cdot \sqrt{\text{GeV}}$  is a stochastic term and  $b = 0.17\%$  is a constant term. In the energy range from 15 GeV to 180 GeV the energy response is linear within  $\pm 0.1\%$ .

### The tile calorimeter

The main task of the ATLAS hadronic calorimeter (HCal) is the measurement of jet energies and the reconstruction of missing transverse energy together with the ECal. This is particularly important for studies of supersymmetric events, since multiple jets and missing transverse energy from weakly interacting neutralinos or gravitinos is expected in many models.

The barrel part of the HCal uses steel as absorber material and scintillating tiles for detection. Figure 3.8 shows the construction principle and arrangement of the steel plates and tiles. It is placed directly outside the ECal envelope and covers the region  $|\eta| < 1.7$ . The barrel part covers  $|\eta| < 1.0$  and has a length of 5.8 m, while the two extended barrels cover  $0.8 < |\eta| < 1.7$  and have a length of 2.6 m, as can be seen in Fig. 3.6. Radially, it reaches from an inner radius of 2.28 m to an outer radius of 4.25 m and is divided into three layers. Azimuthally, each barrel consists of 64 modules of size  $\Delta\phi \approx 0.1$ ; the layout and principle are depicted in Fig. 3.9. The granularity of the calorimeter is  $\Delta\eta \times \Delta\phi = 0.1 \times 0.1$  ( $0.2 \times 0.1$  in the last layer). The rapidity coverage and granularity of the tile calorimeter are summarized in Table 3.3.

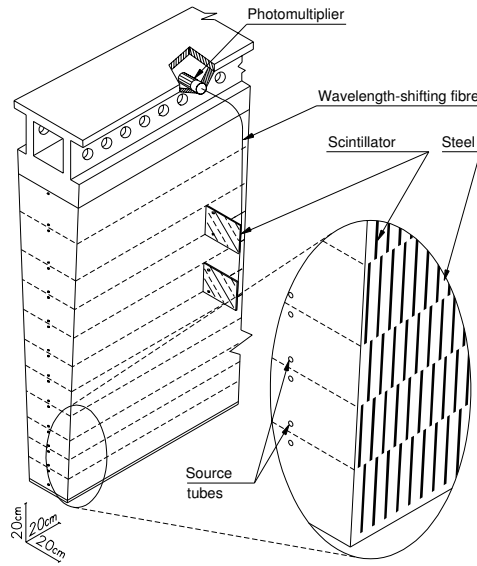


Figure 3.8: Schematic view of the tile calorimeter. The tiles, fibres and photomultipliers are shown [80].

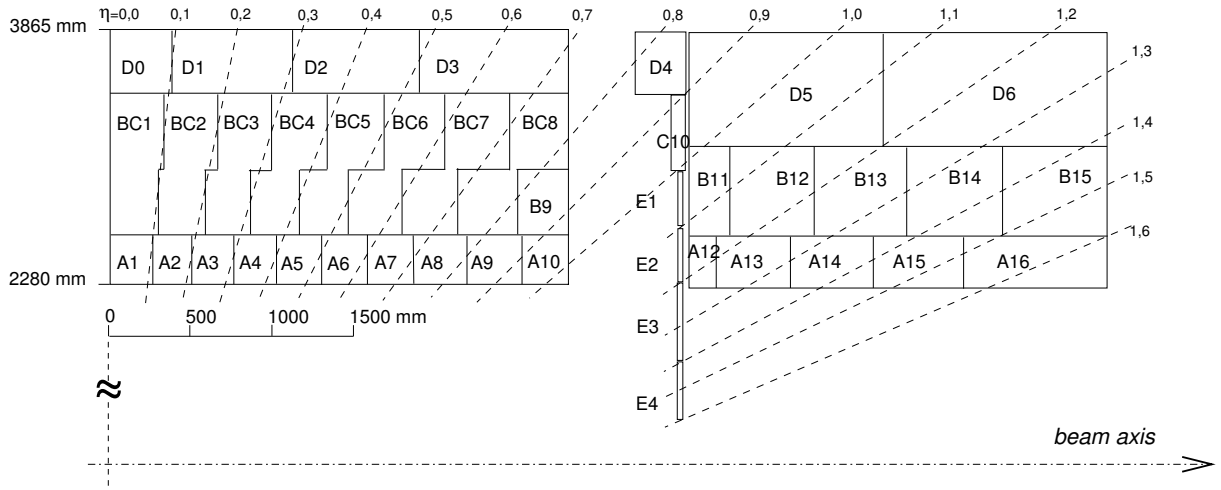


Figure 3.9: Segmentation in depth and  $\eta$  of the tile calorimeter in the central (left) and extended (right) barrels [80].

	Barrel	Extended barrel
$ \eta $ coverage	$ \eta  < 1.0$	$0.8 <  \eta  < 1.7$
Number of layers	3	3
Granularity $\Delta\eta \times \Delta\phi$	$0.1 \times 0.1$	$0.1 \times 0.1$
Last layer	$0.2 \times 0.1$	$0.2 \times 0.1$
Readout channels	5760	4092 (both sides)

Table 3.3: Main parameters of the ATLAS tile calorimeter [80].

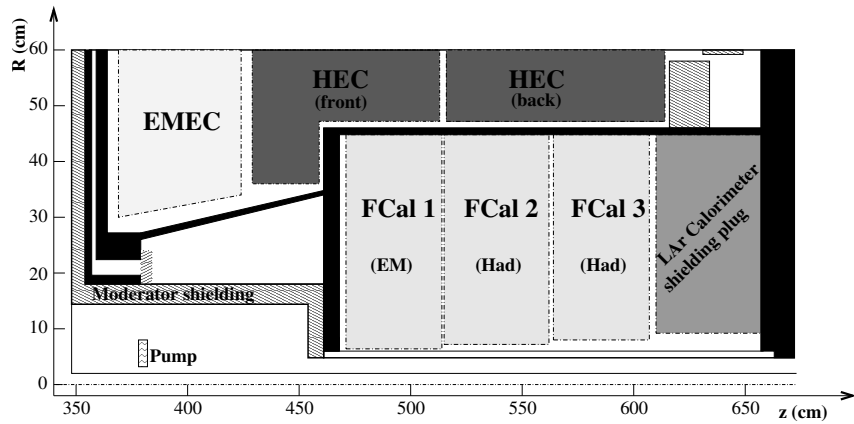


Figure 3.10: Schematic view of the three FCal modules and their position relative to the EMEC and HEC. The black regions are parts of the cryostat [80].

Systematic studies of the energy resolution have been performed with beams of isolated pions [80]. The fractional energy resolution  $\sigma(E)/E$  has been modelled with Eq. (3.7) and the best fit yields  $a = (56.4 \pm 0.4)\%$  and  $b = (5.5 \pm 0.1)\%$ .

### LAr hadronic endcap and forward calorimeter

For the measurement of jets (and missing transverse energy) in the region  $1.5 < |\eta| < 3.2$  two hadronic endcap calorimeters (HEC) have been built. Due to the higher radiation exposure the intrinsically radiation hard LAr technology has been chosen. Parallelly arranged copper plates are used as absorber material. The HEC consists of two wheels in each endcap: a front and a rear wheel with an outer radius of 2030 mm, each containing two longitudinal sections. The system has a total length of 1818 mm and the size of the individual readout cells is  $\Delta\eta \times \Delta\phi = 0.1 \times 0.1$  for  $|\eta| < 2.5$  and  $\Delta\eta \times \Delta\phi = 0.2 \times 0.2$  for larger values of  $\eta$ .

For the region  $3.1 < |\eta| < 4.9$  the forward calorimeter (FCal) has been built at a distance of 4.7 m from the interaction point. The active material is again liquid argon, while two different absorber materials have been chosen. The first of the three modules features copper for electromagnetic measurements, while tungsten is used for hadronic measurements in the other two layers. Each module has a length of 45 cm, as shown in Fig. 3.10. One can clearly see the relative position of the electromagnetic endcap (EMEC), the HEC and the FCal.

### 3.2.5 The muon spectrometer

Muons are very important for the search for new physics. In many models heavy particles decay into high energetic muons yielding important information on particle masses and couplings. The muon spectrometer of the ATLAS detector enables a very good identification and reconstruction of these muons. Additionally, heavy stable charged particles are predicted by some supersymmetric models, which leave a track in the inner detector, but cannot be stopped by the calorimeters. Some of the properties of these particles, such as mass and velocity, can also be measured with a muon detector [18].

The muon system is the outermost part of ATLAS. Since muons are minimal ionising particles, they traverse the inner detector and the calorimeters relatively undisturbed and a track can be measured in the muon system. The magnetic field for the bending of the tracks is generated by the toroid magnet system. In the region  $|\eta| < 1.4$  the bending is provided by the barrel part of the magnet system, while

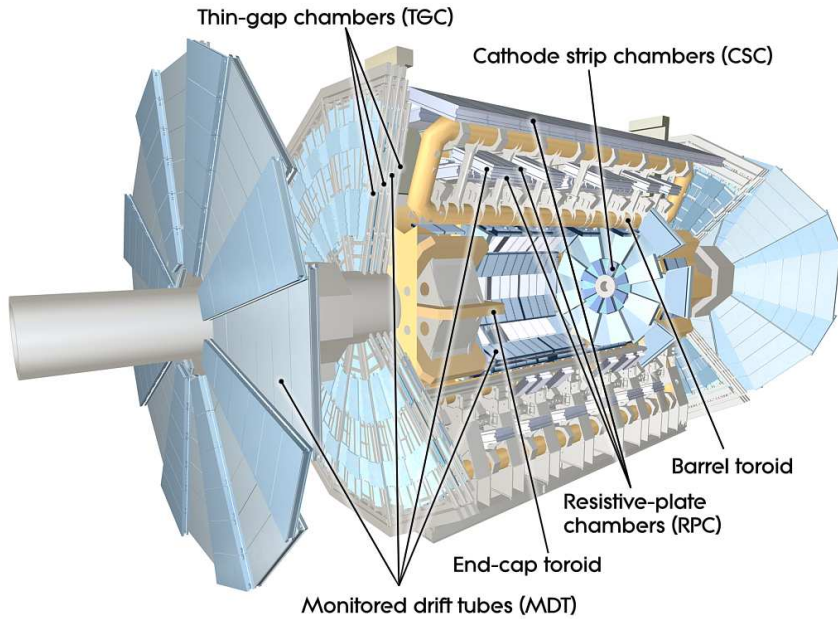


Figure 3.11: Cut-away view of the ATLAS muon system and its individual components: MDTs, CSCs, TGCs and RPCs [80].

in the region  $1.6 < |\eta| < 2.7$  the endcap toroids provide the magnetic field. In the transition region both systems are used. The fields are mostly orthogonal to the muon trajectories.

Four different gaseous detector technologies are used (Fig. 3.11): monitored drift tubes (MDT), cathode strip chambers (CSC), thin-gap chambers (TGC) and resistive plate chambers (RPC). Over most of the  $\eta$  range, the MDTs are used to provide precision measurements of the track coordinates. These chambers consist of three to eight layers of drift tubes (Fig. 3.12,  $R_{\min}$  is used to measure the coordinate) that measure the drift time of an electron produced by the ionizing muon. The maximal drift time from the wall to the wire is 700 ns. The tubes are made of aluminium and possess a diameter of 30 mm, while the gas in the tubes consists of 93% Ar and 7% CO<sub>2</sub>. This mixture is responsible for the long drift time, but has been chosen due to good aging properties. An average resolution of 80  $\mu\text{m}$  is achieved per tube, or around 35  $\mu\text{m}$  per chamber. There are 1088 MDT chambers in ATLAS with 18 main types. A considerable number of chambers with special shapes have been built in order to minimize acceptance losses.

In the forward region  $2.0 < |\eta| < 2.7$  CSCs are used in the innermost tracking layer. They are multiwire proportional chambers with cathode planes segmented into strips in orthogonal directions. The measurement principle is different from the MDTs, since induced-charge distributions are determined to measure the track coordinates. A resolution of 40  $\mu\text{m}$  is achieved with each chamber in the bending plane and 5 mm in the transverse plane. The CSCs have a higher rate capability and a better time resolution than the MDTs due to the gas mixture of 30% Ar, 50% CO<sub>2</sub> and 20% CF<sub>4</sub>.

An important performance goal of the muon system is the measurement of a 1 TeV track with a resolution of 10%. To achieve this goal the position of the MDTs wires and the CSC strips have to be known with a precision of better than 30  $\mu\text{m}$ . Therefore, a high precision optical alignment system monitors the positions and internal deformations of the system.

Another very important task of the muon system is to trigger efficiently on muon tracks and identify the corresponding bunch-crossing. For this purpose additional fast trigger chambers have to be built

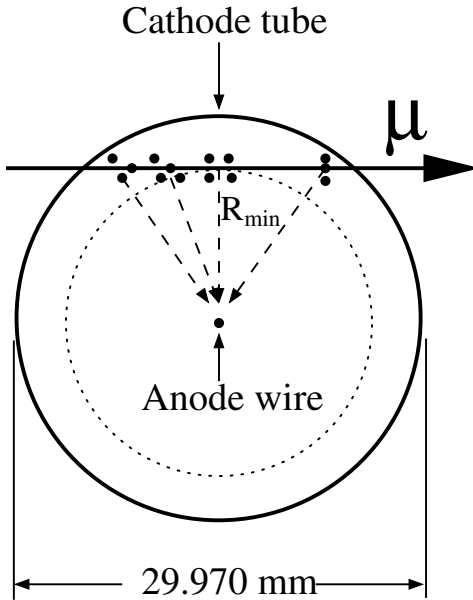


Figure 3.12: Cross section of an MDT tube [80].

		Chamber resolution (RMS) in			Measurements/tracks		Number of	
Type	Function	$z/R$	$\phi$	time	barrel	endcap	chambers	channels
MDT	tracking	$35 \mu\text{m} (z)$	-	-	20	20	1088 (1150)	339k (354k)
CSC	tracking	$40 \mu\text{m} (R)$	5 mm	7 ns	-	4	32	30.7k
RPC	trigger	10 mm ( $z$ )	10 mm	1.5 ns	6	-	544 (606)	359k (373k)
TGC	trigger	2-6 mm ( $R$ )	3-7 mm	4 ns	-	9	3588	318k

Table 3.4: Main parameters of the ATLAS muon system [80].

to complement the precision tracking chambers. RPCs have been chosen in the barrel region  $|\eta| < 1.05$ , which have a time resolution of 1.5 ns. In the endcap region  $1.05 < |\eta| < 2.4$  TGCs have been chosen with a time resolution of 4 ns. The RPCs are gaseous detectors, which do not use a wire but two resistive plates as parallel electrodes with a distance of 2 mm. Electron avalanches are produced along the ionizing track towards the anode due to the electric field of 4.9 kV/mm. The TGCs are multiwire proportional chambers, which function similar to the CSCs. To achieve a better time resolution, they have a smaller anode to cathode distance and a different gas mixture. In addition to the time measurement, the TGCs also determine the azimuthal coordinate of a muon track to complement the measurement of the MDTs. The inner layer of the MDTs is complemented by two layers of TGCs, while the middle layer is complemented by seven TGC layers. Table 3.4 summarizes the main parameters of the ATLAS muon system.

### 3.2.6 Trigger and data acquisition

The high interaction rate in  $pp$  collisions at the LHC is a great challenge for all experiments. As described in chapter 3.1 around 23 hard interactions per bunch crossing at a bunch crossing rate of 40 MHz lead to an approximate interaction rate of 1 GHz at high luminosity. This is opposed to the maximum rate of about 100 Hz that can be written to permanent storage. This results in the need of a rejection factor

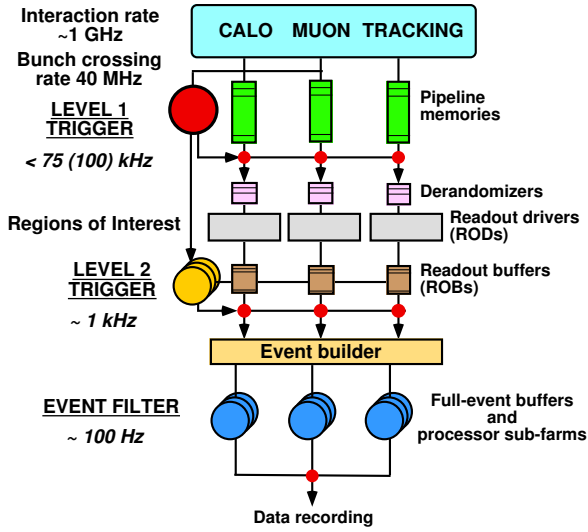


Figure 3.13: Organization of the ATLAS trigger and data acquisition system [82].

of  $10^7$ . The rate of interesting events for the search for new physics will be much lower than that. As an example, for some of the studied supersymmetric models in ATLAS around 10 events per hour are expected. Most of the rejected events are minimum-bias processes, which will also be studied, but do not have priority to be stored. Therefore not only a high rejection is required, but also a high detection efficiency for rare and interesting events is needed. The ATLAS trigger system is designed to provide such a high rejection, while accommodating different and also changing requirements for many different physics analyses, including standard model physics and new physics searches.

The event selection is performed by three different levels, as shown in Fig. 3.13. At each level the rate is reduced by a few orders of magnitude, allowing for an increased decision complexity, which requires more time, at each level. The first step is done by the Level-1 Trigger (L1), that is based on very fast custom-made hardware and reduces the rate to 75 kHz. Every decision has to be made in less than  $2.5 \mu\text{s}$ . The Level-2 Trigger (L2) is run on a large computer farm and is solely based on software. It reduces the rate further down to about 1 kHz, while having around 40 ms for each decision. The final step is done by the Event Filter (EF) reducing the rate to approximately 100 Hz, while each decision can take up to a few seconds.

### Level-1 Trigger

The task of L1 is to search for high energetic muons, electrons, photons, hadronically decaying  $\tau$ -leptons and jets. Also events with large missing transverse energy and total transverse energy are selected. For the search for muons it uses dedicated fast muon trigger chambers, the RPCs and TGCs as discussed in section 3.2.5. Electrons and photons are selected by calorimeter information. Since L1 has to provide very fast decisions, a reduced granularity is used.

All the information from each detector channel has to be retained, while the L1 decision is formed. This is done in pipeline memories, which are contained in electronics placed physically close to the detector. About  $1 \mu\text{s}$  of the total decision time of  $2.5 \mu\text{s}$  is needed for pure cable propagation delays. Also the bunch crossing identification is an important task for L1, which is challenging due to the short bunch crossing interval of 25 ns. The size of the muon system alone implies that the time-of-flight of particles is larger than the bunch crossing interval. Also the width of the calorimeter signals extends over

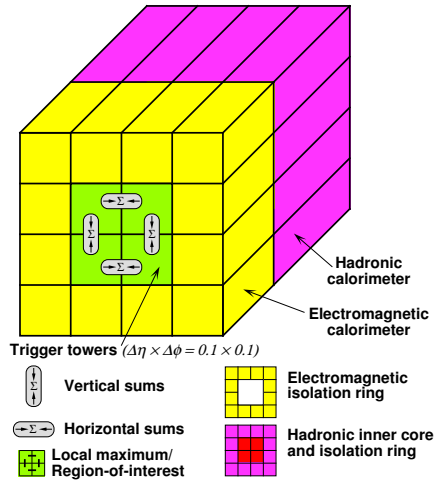


Figure 3.14: Sketch of the electron and photon trigger algorithm [80].

many bunch crossings.

Since also minimum-bias events or other processes with a very high cross section will be investigated, it is necessary to have the possibility to prescale trigger items on L1. This allows the optimal use of the bandwidth and a flexible physics program. The prescales of each item can in principle be changed during run time to account for the decreasing luminosity in a certain run or for other changing conditions.

For the study of GMSB events the calorimeter trigger is of special interest. Both the standard supersymmetry selection based on missing transverse energy and multiple jet triggers, as well as a special treatment of GMSB events with photons in the final state use the calorimeter trigger items. The L1 calorimeter trigger (L1Calo) is based on trigger towers of size  $0.1 \times 0.1$  in  $\eta \times \phi$  (in the central region and larger at higher  $|\eta|$ ). The result is sent to the CTP 1.5  $\mu$ s after the event occurs. L1Calo consists of three subsystems: for the digitization of the calorimeter signal and the bunch crossing identification the pre-processor is used. A look-up table is used for the production of the transverse energy values of each object. Then the Cluster Processor (CP) identifies electrons, photons and  $\tau$ -lepton candidates with transverse energy above the given threshold, while the Jet/Energy-sum Processor (JEP) identifies jets and calculates global sums of (missing) transverse energy from  $0.2 \times 0.2$  trigger elements in  $\eta \times \phi$ .

The algorithm triggering on electrons and photons is shown in Fig. 3.14.  $2 \times 2$  clusters of trigger towers are identified of which at least one of the four possible sums of two towers,  $1 \times 2$  or  $2 \times 1$  exceeds a given threshold. The 12 towers surrounding the core, as well as the  $2 \times 2$  hadronic tower sum are used for the isolation threshold, which is an absolute value rather than a ratio of isolation energy to cluster energy. The algorithms are run over all possible  $4 \times 4$  windows and slide in steps of 0.1 in both  $\eta$  and  $\phi$ . If an electron or photon candidate is found, the location of the  $2 \times 2$  cluster is also the location of the region-of-interest (ROI) seeding the L2 decision.

The overall L1 trigger decision is made by the central trigger processor (CTP). It combines the information from the muon system with the information from the calorimeters, as shown in Fig. 3.15. The decision is based on the multiplicity of trigger objects, such as calorimeter clusters, and the corresponding energy thresholds. The information about the location of the trigger object is retained and sent as a ROI to seed the L2 decision. The trigger menu consists of up to 256 trigger items, while each item is some combination of requirements on the input data. These trigger items can be programmed with 4 to 16 transverse energy thresholds per object type. After the L1 selection the data from the detector front-end is transferred over 1574 readout links (ROLs) and received into the 1574 readout buffers (ROBs) contained in the readout system units (ROSs), where it is temporarily stored for later usage.

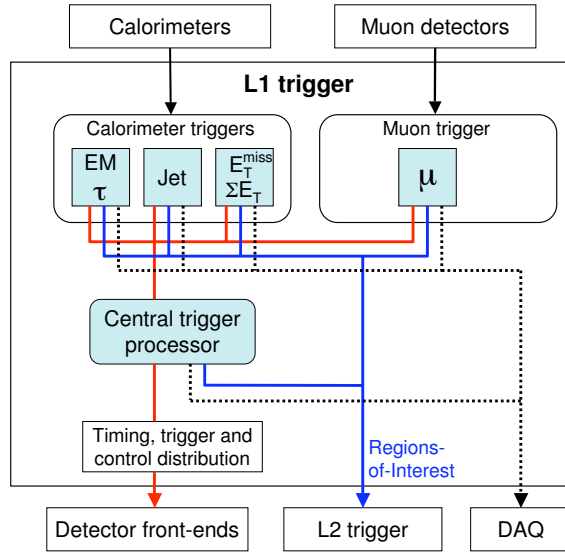


Figure 3.15: Diagram of the ATLAS L1 trigger system. The trigger decision is made by the central trigger processor, which receives input from the muon trigger chambers and the calorimeters. The ROI information is transferred to L2 [80].

### The High-Level Trigger

After the L1 decision the ROI data is passed to the High-Level trigger (HLT) system, which consists of L2 and the EF and applies trigger decisions in a series of steps, each refining existing information by acquiring additional data from more and more detector subsystems. First the L2 trigger receives coordinate, energy and signature type information to reduce the amount of data that has to be read out from the detector subsystems. This is seeded by the ROIs and accounts for about 2% of the total data of an event. Every detector subsystem including the tracker is used. The ROI information is provided over eight dedicated ROLs to the ROI builder, which is the first subsystem of L2 and where the information from each L1 subsystem (calorimeter, muon system and CTP) is assembled to an integrated data structure. Then it is forwarded to the next L2 step, the L2 supervisors, which assign each event to one of the L2 processing units and receive their results from analysing the ROI data requested from the corresponding event. These results are forwarded to the data flow manager (DFM), which manages the event building process. All data from the ROBs are taken. The outcome is a single event data structure, which is given to the third level of the trigger system, the EF. In total the L2 processing farm provides an event rejection factor of about 30.

At the EF level the complete detector information from all subsystems not constrained to ROIs is available to make a last decision, if the event is permanently stored on tape. Additionally, the EF classifies each event according to a predefined set of event streams and adds this information to the event structure. Selected events are sent to the output nodes (SFOs) of the data acquisition system, while all event data from rejected events is removed from the system. Again the EF is a processing farm where on each processing node a configurable list of tasks receives and processes events. Unlike L2, the decisions are based on standard ATLAS event reconstruction and analysis applications. The results are objects that are close to the ones in the offline analysis: electron, photon, muon or jet candidates.

In the case of GMSB events with photons in the final state one could use a dedicated photon signature to build a trigger chain. As an example, on L1 one could look for one or more isolated clusters in the

electromagnetic calorimeter and refine the selection with the HLT to have good photon candidates with a certain transverse energy threshold in the end. It is also possible to logically combine different trigger chains. Especially multijet triggers could be combined with triggers based on the selection of missing transverse energy, which is used for general supersymmetry searches.

## Chapter 4

# Monte Carlo generation and detector simulation

The results of a huge experiment like the ATLAS detector cannot be interpreted without a detailed understanding of every single subcomponent. Therefore, the simulation of the detector response to various physics processes is necessary in order to optimize the whole setup and estimate the performance for physics studies. Particle identification strategies can be developed in advance and the efficiencies of analysis algorithms can be tested. Also the preparation of searches for new physics needs a detailed detector simulation in order to estimate the discovery potential and to find methods for measuring particle properties. When real collision data are available simulated data are needed in order to apply corrections to the real data and to find deviations from the Standard Model. Figure 4.1 shows a schematic representation of the ATLAS event simulation procedure.

First of all, the event under study has to be generated by a Monte Carlo event generator program [84, 85], which delivers four-vectors of the final state particles. Afterwards the detector simulation [86] is run that delivers the hits in the detector, which have to be digitized and reconstructed. The digitized data are equivalent to real data. The reconstructed events are used as input for the final data analysis in the form of AOD (Analysis Object Data) files.

The complete generation, simulation and reconstruction of an event can take up to 15 min in the current ATLAS software [87]. A large fraction of this time is needed for the simulation of the shower development in the calorimeter. For large scale productions of event samples the ATLAS computing grid resources are used and the production is centrally organized. If large amounts of data are needed that cannot be produced centrally, a fast detector simulation (ATLFAST [88]) can be used that takes the generated events as input and performs the simulation and reconstruction in a single, simplified step. In this chapter all relevant computing steps are briefly discussed.

### 4.1 Generation of simulated events

Events have to be generated by a Monte Carlo generator to study the physics of a given process in detail. Since calculations in quantum mechanics only give the probability of an outcome of the experiment, the event generator uses (pseudo)random numbers event by event to produce a result. A couple of programs exist which are used by ATLAS, depending on the type of process under study. The different programs differ in the way they implement the several substeps of event generation:

- **Hard scattering:** The primary parton-parton interaction is determined from the matrix elements calculated using perturbative QCD (and electroweak theory). The PDFs have to be taken into

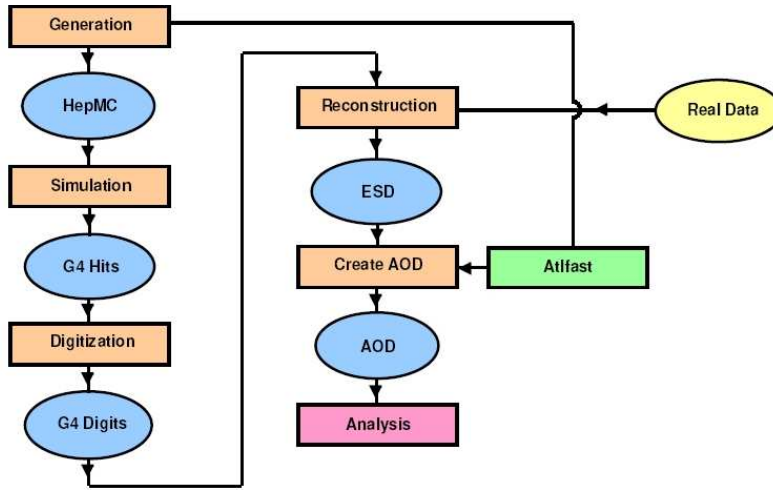


Figure 4.1: Schematic overview of the ATLAS simulation chain. The single steps are shown (rectangles) together with the corresponding data formats (ellipses) [83].

account in that step. Tree level as well as higher order matrix elements are used by different generators.

- **Initial and final state radiation:** Radiative corrections from QCD and electroweak theory are applied by adding gluon and photon emission from initial or final state particles. This step can be absorbed in the first step by using the corresponding amplitudes and calculating the Feynman diagrams order by order. It is possible to go to quite high orders of up to eight partons in the final state, if one solely uses tree-level diagrams. This approach is very time consuming, but gives a quite accurate estimate of the final state particle multiplicities which is important *e.g.* for multijet events. Soft and collinear partons can better be described by the *parton shower* approach [85], which approximates the full matrix elements in a phenomenological way by allowing the initial or final state partons to split up into pairs of other partons. Initial (final) state radiation can be modelled by so-called *space-like* (*time-like*) parton showers.
- **Hadronization:** All partons in the final state have to be combined to colorless hadrons. This cannot be described from first principals within any calculational technique and several models have been used for this step. In the *string fragmentation* process [89] two partons that are produced in the primary interaction are connected via a one-dimensional string. As the partons move apart the potential energy stored in the string increases and the string can break by the production of two new partons that form color-singlets with the initial partons. Depending on the invariant mass of the string pieces further string breaks may occur. This process continues until only on-shell hadrons remain. Finally the hadrons may decay evolving into hadronic showers and leading to a realistic final state. If long-lived particles are generated that decay somewhere in the detector, the event generator has to be connected to a detector simulation, since interactions with the detector material may happen before the particle decays.
- **Multiple interactions:** Since the proton consists of multiple partons, there is some probability that more than one parton is involved in a hard scattering process. This is called *multiple interactions* and may not be confused with *pile-up events* where several hadrons in the same bunch crossing collide and which is not modelled by the event generator [84]. The parts of the proton that do not

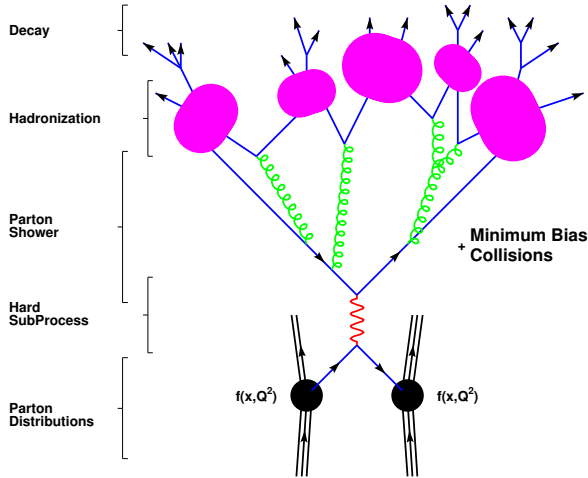


Figure 4.2: Schematic overview of the computational steps of a Monte Carlo event generator [96].

directly participate in the hard interaction also carry part of the total beam energy and are color connected to the rest of the interaction.

Figure 4.2 schematically shows the development of a hard proton-proton interaction with all involved substeps. Several multipurpose generators exist like PYTHIA [90], HERWIG [91], ALPGEN [92] and MC@NLO [93] and a variety of specialised generators that can be used as plugins for the former ones. To allow the interoperability of different generators, spectrum calculators [94] and detector simulations several standards have been developed, *e.g.* the SUSY Les Houches Accord [95] allowing for the standardized transfer of mass spectra, couplings and branching ratios to other programs.

## Pythia

PYTHIA [90] is one of the most commonly used event generators. It provides code for all relevant subprocesses of the event generation, as shown in Fig. 4.2 including parton showering and hadronization. It provides almost all  $2 \rightarrow 1$  and  $2 \rightarrow 2$  and some  $2 \rightarrow 3$  Standard Model and some beyond Standard Model leading order processes. It can be used as showering and hadronization program by other event generator codes that have not implemented these algorithms themselves. The Les Houches Accord PDFs as described in [97] can be used and linked in easily. The hadronization is implemented via the *Lund string fragmentation framework* [89]. PYTHIA is written in FORTRAN until version 6 and is currently rewritten in C++ [98]. It is used for the generation of a broad spectrum of Standard Model processes in ATLAS.

## Herwig

HERWIG [91] is a general purpose leading order event generator for the simulation of lepton-lepton, lepton-hadron and hadron-hadron collisions. It provides a large range of hard scattering processes including initial and final state radiation using angular-ordered parton showers, hadronization via the *cluster hadronization model* [85] and underlying event simulation. The cluster hadronization is based on the color pre-confinement property of the angular-ordered parton showers. After the parton shower phase all partons can be uniquely formed into color singlet clusters. Due to the color pre-confinement the distribution of the cluster mass spectrum is strongly peaked at low masses. The high mass clusters are split into

low mass clusters using a string-like mechanism which is followed by the decay of the low mass clusters to the final state hadrons. The program includes a Les Houches Accord interface for other programs to allow users the implementation of additional processes, as well as the use of external PDFs. A special interface to ISAJET [99] exists to allow the transfer of supersymmetric mass spectra and branching ratios. Additionally, a large range of MSSM processes with and without R-parity violation is included in HERWIG [100] and used in ATLAS. HERWIG is written in FORTRAN, but a completely new event generator written in C++ based on the experience gathered with the FORTRAN code is under development called HERWIG++ [101].

### Alpgen

ALPGEN [92] is an event generator designed for the generation of Standard Model processes in hadronic collisions with emphasis on final states with large jet multiplicities. It uses the exact leading order calculations for partonic matrix elements in order to provide accurate predictions for final state particle multiplicities. No contributions from loop diagrams are used. The parton shower approach is used in addition to simulate the emission of soft/collinear gluons. Therefore, interfaces to HERWIG and PYTHIA are provided using the Les Houches format. The code is written in FORTRAN77 and is used in ATLAS for the generation of Standard Model background processes for studies of supersymmetric models.

### MC@NLO

The MC@NLO generator [93] includes the full next-to-leading order (NLO) QCD matrix elements in the calculations of hard subprocesses and is therefore able to provide sensible descriptions of multiple soft and collinear emissions. It is written in FORTRAN and makes use of HERWIG for the showering and hadronization steps. Since soft emissions are described by the NLO matrix elements, double counting of radiated partons due to the showering step has to be avoided by a dedicated mechanism. Therefore MC@NLO produces events with negative weight, typically 15% of all events.

### Supersymmetric events in ATLAS

In ATLAS the program ISASUGRA, which is part of the ISAJET package, is used to calculate the supersymmetric mass spectrum, all branching fractions and particle widths in leading order. This is used as input for HERWIG/JIMMY [102] for the sparticle cascade decays, parton showers, hadronization and the simulation of the underlying event.

## 4.2 Detector Simulation

Although generated events can be used for approximate studies of the properties of *e.g.* supersymmetric models, a detailed detector simulation is needed in order to estimate the detector response on all generated objects. Only with a detector simulation it is possible to estimate efficiencies and to optimize the identification criteria for final state particles.

### 4.2.1 Full GEANT4 simulation

The **G**Eometry **A**Nd **T**racking (GEANT4) program [103, 104] is a toolkit for the simulation of the passage of particles through matter. In ATLAS it is used for several tasks. First of all a detector which has not been built yet can be designed and optimized using a detector simulation toolkit. It also serves as

a tool for understanding a concrete detector concept and its interaction with elementary particles. Additionally, the reconstruction tools can be tested as well as associated systems like the trigger and data acquisition. In the end, all precise analysis studies are based on GEANT4 in ATLAS as long as no real data are available. Once this is the case, many analysis results depend on an accurate detector simulation, since not all effects and efficiencies can be estimated from the data itself.

For a precise simulation the exact geometry of all subsystems described in Sec. 3.2 has to be known. All physical effects of the interaction of the particle with several materials are included as well as the interaction with the magnetic fields. The trajectories of particles passing through the detector are recorded by GEANT4 by simulating the energy loss due to material interactions. The positions of the interactions are stored and called *hits*. In the *digitization* step the simulated signals are converted to a format which looks like the output of the real readout channels of the various subsystems. Inefficiencies and estimates of internal noise due to deficient hardware have to be taken into account.

Electron-positron pairs and other particles that are produced in the interactions are generated by GEANT4 and also bremsstrahlung is taken into account. Especially the case of photon conversions is interesting for this thesis, since GMSB models with photons in the final state are studied. If long-lived particles have been generated by the event generator, it is important to simulate their passage through the detector before they decay. That means not all final state particles can be created by the generator, but GEANT4 has to take over this task. Therefore, an interface to the generator is used in order to transfer the relevant information to the detector simulation, such as the lifetime of the decaying particle and the masses and couplings of the final state particles. In this thesis long-lived neutralinos decaying to photons and gravitinos are studied, which are generated by GEANT4.

The output digits of the simulation serve as input for the reconstruction algorithms that try to identify candidates of various particle types. This step is necessary for Monte Carlo generated events as well as for real data. The reconstruction and final identification of objects relevant for this thesis are discussed in the next chapter. Finally, a graphical representation of the simulated events is available to visualize the detector response.

### 4.2.2 Fast simulation approach

For analyses that need very large amounts of data, such as multidimensional supersymmetric parameter scans, the application of a full detector simulation is not feasible due to the enormous amount of CPU time needed. Therefore, the fast simulation package ATLFAST has been developed, which has been extensively used in the context of the ATLAS Physics Performance Technical Design Reports [105, 106]. Since a fast simulation can never be as accurate as a full GEANT4 simulation, a careful validation of the performance has to be done and eventually the results have to be tuned in order to match the full simulation results [107]. It should be noted that critical issues like the treatment of converted photons or the estimation of detector efficiencies need to be studied with the full simulation, since they are not implemented in ATLFAST.

#### Principals of the fast simulation ATLFAST

To keep the CPU time per event at a reasonable level, no detailed simulation of the interaction of particles with any of the detector components is performed. Instead, the detector response is parametrized to take the interactions into account implicitly. The reconstructed particles are created directly from the generated particles by tracking the particle through the perfect magnetic field and geometrically matching the built calorimeter clusters to the true particle. No interaction of the particle with the tracker or the muon system is simulated and thus no energy loss or bremsstrahlung is included. This has to be taken into account in the energy resolution functions. The primary vertex is assumed to be at the center of the detector and the impact point of any stable particle in the calorimeter surface is calculated.

The calorimeter is a single entity without a separation between electromagnetic and hadronic part. Particle energies are deposited in a calorimeter cell map, while the response of the calorimeter is assumed to be one and uniform over the full detector region. The cell map has a granularity of  $\Delta\eta \times \Delta\phi = 0.1 \times 0.1$  for  $|\eta| < 3.2$  and  $\Delta\eta \times \Delta\phi = 0.2 \times 0.2$  for  $3.2 < |\eta| < 5.0$ . The entire energy of the particle is deposited in the hit cell, *i.e.* no lateral nor longitudinal shower development is simulated and a shower fine structure cannot be taken into account. The clusters are reconstructed with a simple seeded cone algorithm, while otherwise no reconstruction based on the simulated detector information is implemented. The Monte Carlo information on generator level is used for this purpose.

The reconstruction procedure for the objects relevant in this thesis is the following:

- **Clusters** are reconstructed from the calorimeter cell map via a cone algorithm with a cone size of  $\Delta R = \sqrt{\Delta\eta^2 + \Delta\phi^2} = 0.4$  and a seed cell energy above 1.5 GeV. A particular cell can only be associated to a single cluster that has to pass an energy threshold of 5 GeV. The clusters are classified as electrons, photons, taus or jets, as detailed in the following.<sup>1)</sup>
- **Electrons** are searched by matching a cluster with a true electron with a matching radius of  $\Delta R = 0.15$ . An isolation criterion can be defined to search for isolated electrons by requiring that the difference of the energy in a cone of  $\Delta R = 0.2$  around the electron direction and the smeared energy needs to be below 10 GeV. The reconstructed electron energy is obtained by smearing the true energy with a resolution function based on test beam studies [81]. Slight modifications to Eq. (3.7) have to be applied, since energy losses due to bremsstrahlung in the inner detector are not simulated in the fast simulation and have to be taken into account in the calculation of the energy resolution. Identified electrons are recorded with the  $\eta$  and  $\phi$  coordinates of the electron on generator level and the associated cluster is removed from the list of clusters.
- **Photons** are treated in the same way as electrons concerning isolation. Again Eq. (3.7) is used as the photon energy resolution function. In contrast to the electron energy calculation it has to be considered that no energy loss in the inner detector due to bremsstrahlung is present. Converted and unconverted photons are not distinguished. Since the  $\eta$  direction of a photon cannot be reconstructed from a track as in the case of electrons, the following smearing of the  $\eta$  direction is applied:

$$\begin{aligned}\sigma(\theta) &= \frac{65 \text{ mrad}}{\sqrt{E}} && \text{for } |\eta| < 0.8 \\ \sigma(\theta) &= \frac{50 \text{ mrad}}{\sqrt{E}} && \text{for } 0.8 \leq |\eta| < 1.4 \\ \sigma(\theta) &= \frac{40 \text{ mrad}}{\sqrt{E}} && \text{for } 1.4 \leq |\eta|\end{aligned}\tag{4.1}$$

- **Muons** are reconstructed by applying a  $p_T$ ,  $\eta$  and  $\phi$  dependent resolution function to the generated muon momentum. They are further classified as isolated or non-isolated by applying the same energy isolation criterion as for electrons. If the muon lies inside a  $\Delta R = 0.4$  cone of a jet, it is added to the jet and the jet momentum is changed accordingly.
- **Jets** are constructed from all clusters with  $E_T > 10 \text{ GeV}$  that have not been assigned to a true electron or photon. The jet energy is taken to be the cluster energy including muons and is also smeared with the resolution function (3.7). The direction of the jet is the direction of the cluster.

---

<sup>1)</sup>Since  $\tau$  leptons are not used in this study, they will not be discussed here.

- **Missing transverse momentum** is calculated from all reconstructed objects and the remaining clusters that are not associated to any object. Additionally, all cells that have not been associated to clusters are also included. Their energies are smeared with the jet resolution function.

In the reconstruction process no detector efficiency corrections are applied, except for  $\tau$  leptons and in b-tagging procedures. The appropriate correction factors have to be taken into account in the analysis and can be taken from the GEANT4-based simulation.

### 4.3 Event data model

After the trigger selection the amount of data produced by ATLAS is still so large that it is impossible to distribute it completely to the worldwide community. It is therefore necessary to reduce the stored amount of data in such a way that only the analysis specific information remain. In ATLAS a chain of data formats is used that incorporates smaller and smaller datasets [108].

- **RAW** data are events coming from the *byte stream* of the EF. At this stage the data are not stored in an object oriented representation. It reflects the format in which the data are delivered from the detector and the size of a single event is about 1.6 MB.
- **ESD** (Event Summary Data) are the result of the reconstruction process and have an already reduced dataset size compared to RAW data. The data content is sufficient for most of the physics analysis, such that access to RAW data is not necessary. The reconstructed objects are stored in an object oriented way in POOL ROOT data format [109]. The size of an event is currently about 1 MB, but aiming for a size of 500 kB.
- **AOD** (Analysis Object Data) are derived from the ESD and contain physics objects suitable for analysis. The event size is further reduced to about 100 kB compared to the ESD. The AOD is intended to be general enough for most types of analyses.
- **DPD** (Derived Physics Data) are more specialized compared to the AOD and are classified according to three stages. The *primary* DPD are subdivided into *performance* DPD and *physics* DPD and are already made for specific purposes. The data structure is the same as for the AOD, but can contain additional ESD information. Also the *secondary* DPD are written in the POOL format and are again more specific than the primary DPD. The *tertiary* DPD are finally organized in simple ROOT [110] trees and are intended to be the most specialized data format for a given analysis. An analysis framework like *EventView* [111] can be used for the production, which includes a very modular set of analysis tools. In this thesis such flat *n-tuples* are used.



# Chapter 5

# Object reconstruction and identification

The discovery potential of ATLAS for signatures with photons in the final state arising from GMSB models relies heavily on the photon identification performance as well as on the identification of jets and the calculation of missing transverse energy. These are the most important physics objects needed in the analysis and the discussion of the ATLAS identification performance will be restricted to them.

In the following the identification of photons will be described in some detail, starting with the trigger selection of photons followed by the offline reconstruction and identification procedure. A few remarks on electron identification will be made to compare with the photon criteria. Photon conversions will briefly be discussed, since a good conversion recovery also contributes to the discovery potential. Non-pointing photons occur in GMSB models for non-vanishing  $C_{\text{grav}}$ , which impose some problems for the identification. The solution adopted in this thesis will be discussed briefly. Finally, the reconstruction of jets as well as the calculation of missing transverse energy will be described.

## 5.1 Photon identification

### 5.1.1 Trigger strategy

The L1 calorimeter (L1Calo) trigger algorithm has briefly been described in Sec. 3.2.6. Figure 3.14 shows how the trigger towers of size  $\Delta\eta \times \Delta\phi \approx 0.1 \times 0.1$  are used to construct electromagnetic clusters with a sliding  $4 \times 4$  window. This window searches for local maxima inside the  $2 \times 2$  core, while the 12 towers surrounding the core are used for the isolation criterion. For each tower the energy of all cells of the full depth of the ECal are summed. At least one of the four possible sums of two towers,  $1 \times 2$  or  $2 \times 1$ , must exceed a given threshold in order that the cluster is selected by the L1 trigger. Isolation provides a good handle to reduce the jet background rate, which is typically needed at low transverse energy thresholds.

The L2 selection is based on the L1 ROIs. The  $\eta$  and  $\phi$  position as well as energy and object type information are passed to L2 and based on this information the L2 cluster building algorithm scans the cells in the second layer of the ECal and searches for the cell with the largest transverse energy. A cluster of size  $\Delta\eta \times \Delta\phi = 0.075 \times 0.175$  is built around this seed cell, where the larger cluster size in  $\phi$  is due to the effect of the magnetic field resulting in photon conversions and electron bremsstrahlung. The L2 photon selection cuts on the following four quantities in order to separate photon candidates from jets [18]:

- Transverse energy of the electromagnetic cluster ( $E_T^{\text{EM}}$ ): The jet cross section decreases with energy and thus a cut on this variable provides the best rejection power against jet background.

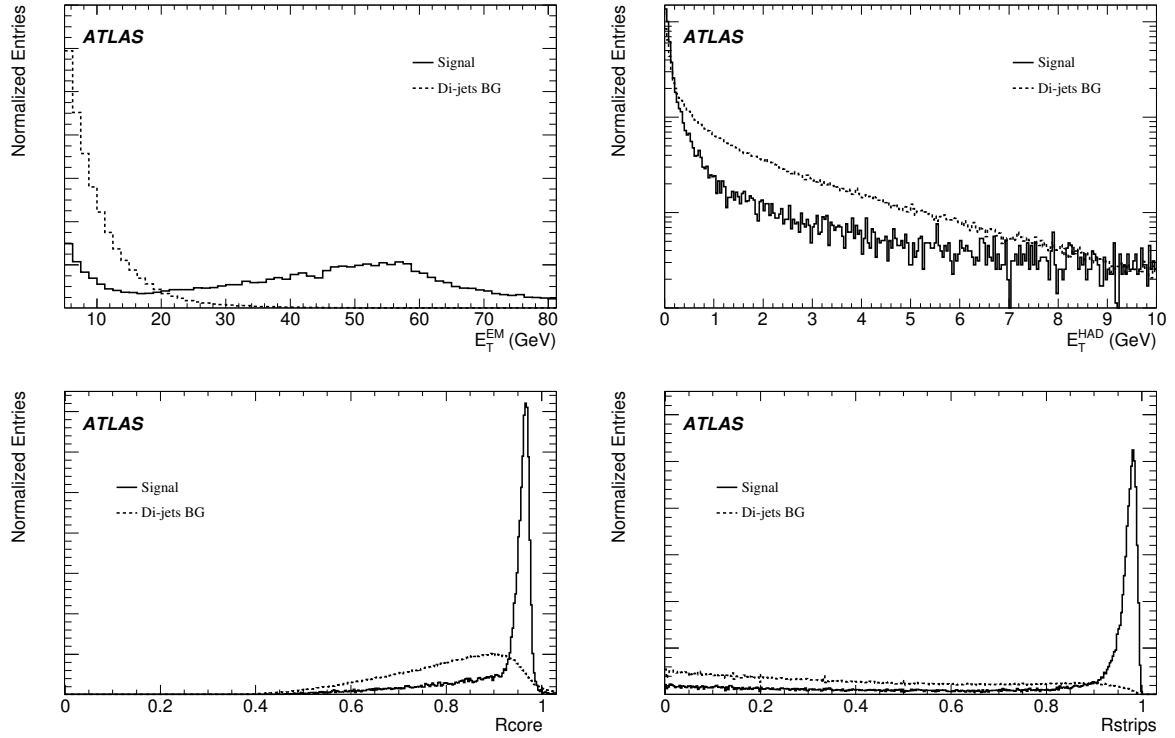


Figure 5.1: Distributions of the L2 photon selection variables as described in the text for a  $H \rightarrow \gamma\gamma$  signal and dijet background. Both distributions are normalized to unity [18].

- Transverse energy in the first layer of the HCal ( $E_T^{\text{HAD}}$ ): Photons deposit typically less than 1% of their energy in the HCal.
- Shower shape in  $\eta$  direction in the second sampling of the ECal (Rcore): Showers from photons are typically smaller in the plane transverse to their direction than showers from jets. The cut variable is the ratio of the energy deposited in  $3 \times 7$  cells and in  $7 \times 7$  cells. For photons this ratio is typically larger than 80%.
- Search for a second maximum in the first sampling of the ECal (Rstrips): A  $\pi^0$  decays to two photons leaving very small hadronic activity and can be separated from single photons with the fine granularity in  $\eta$  in the first sampling of the ECal. In a  $\Delta\eta \times \Delta\phi = 0.125 \times 0.2$  window the ratio of the difference between the energy deposited in the bin with highest energy  $E_{1st}$  and the energy deposited in the bin with second highest energy  $E_{2nd}$  divided by the sum of both energies is calculated. For isolated photons this ratio tends to be one, while for the background it tends to be zero.

Figure 5.1 shows the distributions of the four variables for a  $H \rightarrow \gamma\gamma$  sample (dashed line) with  $m_H = 120 \text{ GeV}^1)$  and for jet background from a dijet sample (solid).

The EF selection is based on the offline reconstruction algorithms with the difference that the EF reconstruction runs once over every L2 seed and thus only uses part of the whole detector information. Compared to L2 additional shower shape variables are used as well as leakage into the HCal and the

<sup>1)</sup>The photon selection criteria on trigger level and for the offline selection have been optimized used a sample of  $H \rightarrow \gamma\gamma$  decays.

Cluster type	$N_\eta^{\text{window}} \times N_\phi^{\text{window}}$	$E_T^{\text{thresh}}$ [GeV]	$N_\eta^{\text{pos}} \times N_\phi^{\text{pos}}$	$\Delta\eta_{\text{dupl}}, \Delta\phi_{\text{dupl}}$
Size	$5 \times 5$	3	$3 \times 3$	$2 \times 2$

Table 5.1: Window size and parameters for the seed finding algorithm as described in the text.

transverse energy of the cluster. Together with an improved calibration this leads to a further reduction of the trigger rate.

### 5.1.2 Cluster reconstruction

Before an object can be ultimately identified as a photon with complicated shower shape variables the cells in the ECal have to be clustered together such that these variables can be calculated and the total amount of deposited energy can be measured. Two clustering algorithms are used in ATLAS, which are called *sliding-window* and *topological* algorithm [112]. Only the former one is used in this thesis, but it should be noted that the latter one also promises to have advantages for the identification of non-pointing photons.<sup>2)</sup>

As soon as an event has passed the L1 requirements, the analog signal from the ECal is sampled and digitized and the energy deposited in each cell is computed using an optimal filtering algorithm [113]. The cell energies are corrected for effects coming from the calorimeter defects.<sup>3)</sup> The sliding-window algorithm used for photon identification is subdivided into three steps: the *tower building*, the *seed finding* and the *cluster formation*.

For the tower building process the ECal is divided into a grid of  $N_\eta \times N_\phi = 200 \times 256$  elements with the size  $\Delta\eta \times \Delta\phi = 0.025 \times 0.025$ . Inside each element the energy of all cells is summed up over all longitudinal layers defining the *tower energy*. After the towers have been built, a window of fixed size  $N_\eta^{\text{window}} \times N_\phi^{\text{window}}$  in units of the tower size in  $\eta \times \phi$  is moved across each element of the tower grid. A precluster serving as a seed for the cluster formation is formed, if the transverse energy of the sum of all towers inside a window exceeds a given threshold  $E_T^{\text{thresh}}$  and is a local maximum. The preclusters position is calculated using a window of size  $N_\eta^{\text{pos}} \times N_\phi^{\text{pos}}$  as the energy-weighted barycenter of all cells. It might be that duplicated preclusters with positions within  $\Delta\eta_{\text{dupl}} \times \Delta\phi_{\text{dupl}}$  appear and only the one with the larger transverse energy is kept. Table 5.1 summarizes the window sizes and thresholds used for the seed finding.

The final electromagnetic cluster is built by using all cells within a window of size  $N_\eta^{\text{cluster}} \times N_\phi^{\text{cluster}}$  centered around the seed position that depends on the layer. First the middle layer is processed, where the seed position  $\eta_{\text{precl}}, \phi_{\text{precl}}$  is taken from the precluster barycenter. The position  $\eta_{\text{middle}}, \phi_{\text{middle}}$  of the barycenter of the cells in the middle layer is determined, which is used as the seed for the strip layer. Finally, the preshower and back layers are computed, using the strip layer barycenter and the middle layer barycenter, respectively. The sizes of the windows used for different particle types are summarized in Tab. 5.2. The sizes for electrons and photons are chosen differently, since the showers from electrons are wider in the barrel due to bremsstrahlung and the interaction with the magnetic field. All cells collected with these algorithms are merged to a cluster, that serves for the identification procedure of photons (and electrons).

<sup>2)</sup>The topological clustering is based on grouping cells in clusters based on their neighbor relations and on the significance of their energy contents. The resulting clusters can have a different number of cells in contrast to the fixed size clusters provided by the sliding-window algorithm.

<sup>3)</sup>Such corrections are not applied in the detector simulation used in this thesis. Instead the energy of each cell is scaled by some random factor in order to simulate the miscalibrations.

Particle type	Barrel	Endcap
Electron	$3 \times 7$	$5 \times 5$
Converted Photon	$3 \times 7$	$5 \times 5$
Unconverted Photon	$3 \times 5$	$5 \times 5$

Table 5.2: Size  $N_\eta^{\text{cluster}} \times N_\phi^{\text{cluster}}$  of the ECal cluster windows for different particle types in the barrel and endcap.

### 5.1.3 Identification

Once the clusters have been defined selection criteria can be used to ultimately identify photons and reject background from jets and  $\pi^0$ 's decaying into two photons. In this thesis the standard ATLAS cut-based identification method [18] is used and will be described in the following.

As described for the case of the L2 selection not only information about the energy of a cluster is used, but variables describing the shape of the electromagnetic shower are needed in order to distinguish real photons from fake photons. The standard ATLAS photon identification is based on the variables from three sections of the calorimeter: the HCal and the first and second sampling layers of the ECal. For each variable there are up to 20  $p_T$  and  $\eta$  dependent cut values:

- **Hadronic cuts:**

- Hadronic leakage (HadEM) defined as the ratio of the transverse energy deposited in the first layer of the HCal in a window  $\Delta\eta \times \Delta\phi = 0.024 \times 0.024$  and the energy deposited in the ECal.

- **Second sampling cuts:** Most of the energy of electromagnetic showers is deposited in the second sampling of the ECal.

- $R_\phi$ : Ratio of the uncalibrated energy (sum of cells) of the second sampling in a window of size  $3 \times 3$  to the energy in a  $3 \times 7$  rectangle.
- $R_\eta$ : Ratio of the uncalibrated energy (sum of cells) of the second sampling in a window of size  $3 \times 7$  to the energy in a  $7 \times 7$  rectangle. The magnetic field increases the width of the converted photon contributions in the  $\phi$  direction and thus  $R_\phi$  is less discriminating than  $R_\eta$ .
- The lateral shower width in  $\eta$  direction calculated in a window of  $3 \times 5$  cells, using the energy weighted sum over all cells  $w_2 = \sqrt{\frac{\sum(E_C \times \eta_C^2)}{\sum E_C} - \left( \frac{\sum(E_C \times \eta_C^2)}{\sum E_C} \right)^2}$ , where  $E_C$  is the energy deposited in each cell and  $\eta_C$  is the  $\eta$  position of each cell.

- **First sampling cuts:** Jets containing high energy hadrons result in broad showers that can be rejected with cuts on the second sampling and HCal variables. Jets containing neutral hadrons have to be rejected with variables from the first sampling due to the very fine granularity in  $\eta$ . The rejection power is due to the resolution of substructures inside jets. The fraction  $f$  of the total energy deposited in the first layer is required to be at least 0.5%.

- The decay  $\pi^0 \rightarrow \gamma\gamma$  leads to two energy maxima in the shower and thus a second maximum is searched in a window  $\Delta\eta \times \Delta\phi = 0.125 \times 0.2$  around the cell with the highest transverse energy:
  - \* Difference  $\Delta E_S = E_{\text{max}2} - E_{\text{min}}$  of the energy associated with the second maximum ( $E_{\text{max}2}$ ) and the energy reconstructed in the strip with the minimal value ( $E_{\text{min}}$ ) between the first and second maximum.

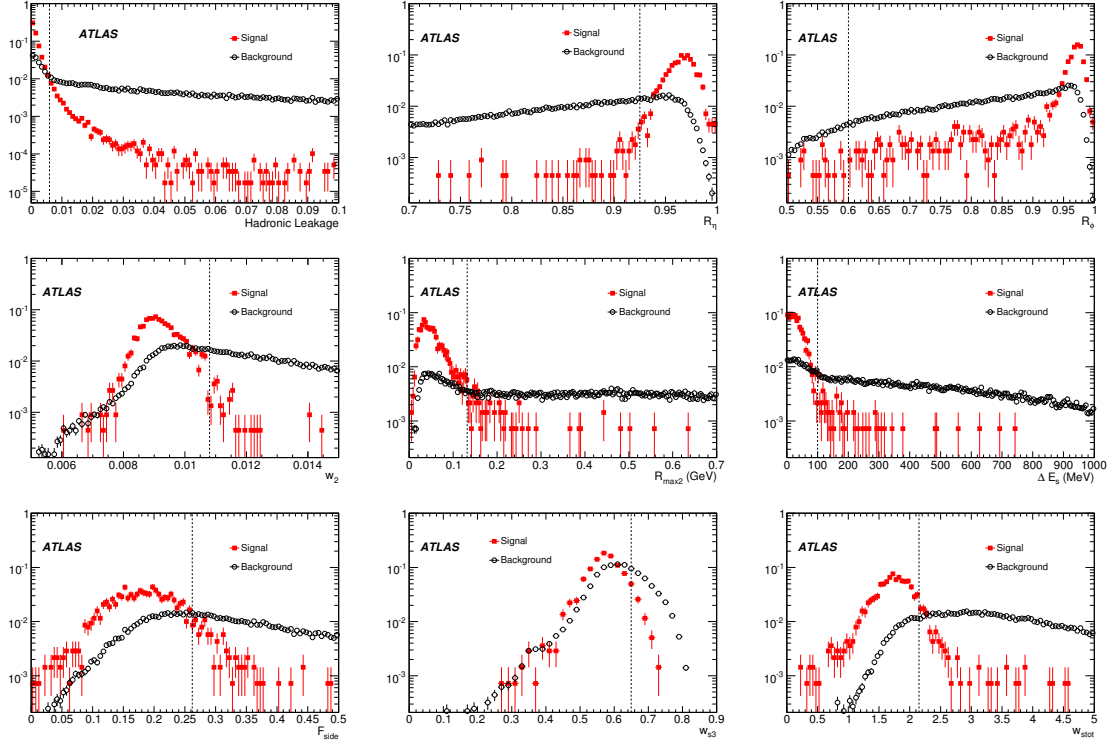


Figure 5.2: Distributions of the offline photon selection variables for true and fake photons with  $|\eta| < 0.7$  and  $20 < E_T < 30 \text{ GeV}$  and normalized to unity [18].

\*  $R_{\max 2} = E_{\max 2}/(1 + 9(5) \times 10^{-3} E_T)$ , with  $E_T$  the transverse energy of the cluster in the ECal and the constant value 9(5) refers to low(high) luminosity.

- Fraction  $F_{\text{side}} = [E(\pm 3) - E(\pm 1)]/E(\pm 1)$  of energy deposited outside the shower core in  $\eta$  of three central strips.  $E(\pm n)$  is the energy deposited in  $n$  strips around the strip with the highest energy.
- Shower width  $w_{s3} = \sqrt{\sum E_i \times (i - i_{\max})^2 / \sum E_i}$  using the three strips  $i$  around the one  $i_{\max}$  with the maximal energy.
- Total width  $w_{\text{stot}}$  over the strips that cover 2.5 cells of the second layer.

The distributions of each variable for true photons (coming from a Higgs decaying into two photons) and fake photons (coming from a dijet sample) are shown in Fig. 5.2 for  $|\eta| < 0.7$  and  $20 < E_T < 30 \text{ GeV}$  including the cut values. The same cuts are applied for converted and unconverted photons, however, this might be improved in the future, since converted photons appear as a pair of electrons in the ECal which looks different to a single photon.

With the cuts on the shower shape variables the background from fake photons is already greatly reduced. In addition, an isolation criterion is imposed by requiring that the energy deposited in a region of  $\Delta R < 0.45$  around the photon cluster does not exceed 10 GeV. The efficiency of the calorimeter cuts defined as the ratio of the number of identified photons and generated photons as a function of  $\eta$  and  $p_T$  is shown in Fig. 5.3 for  $H \rightarrow \gamma\gamma$  photons with  $p_T > 25 \text{ GeV}$  and  $0 < |\eta| < 1.37$  or  $1.52 < |\eta| < 2.47$ . The restrictions in the  $\eta$  region are made to account for the *crack* region of the calorimeter, where the barrel and endcap overlap and the identification of photons is insecure. Three different samples of  $H \rightarrow \gamma\gamma$  decays have been used using an ideal detector geometry with and without pile-up and a misaligned detector

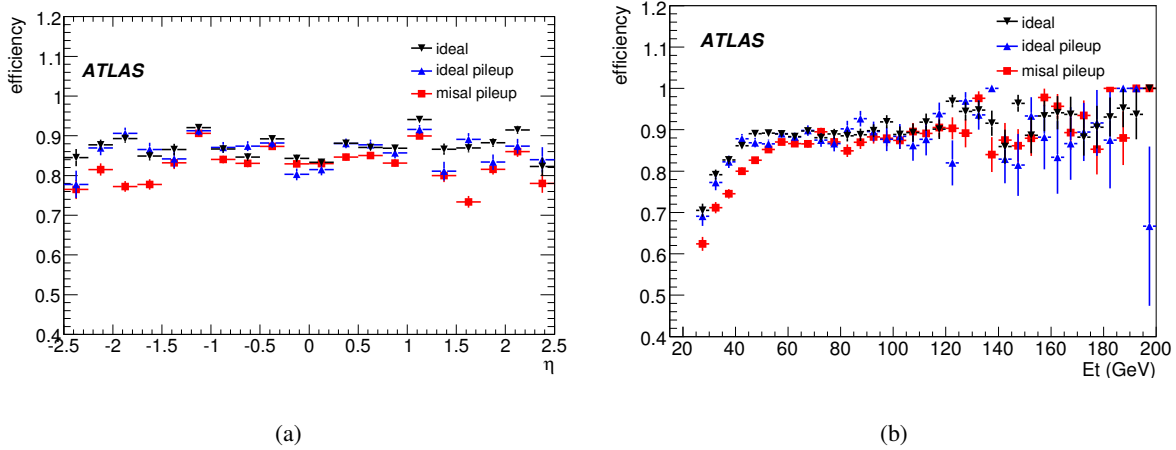


Figure 5.3: Efficiency of the photon identification criteria as a function of (a)  $\eta$  and (b)  $p_T$  for three different samples of  $H \rightarrow \gamma\gamma$  decays using an ideal detector geometry with and without pile-up and a misaligned detector geometry with pile-up [18].

geometry with pile-up. The overall photon identification efficiency is  $87.6 \pm 0.2\%$  using the nominal geometry without pile-up events and decreases to  $83.6 \pm 0.2\%$  with a distorted geometry including pile-up. The fake rate defined as the ratio of all misidentified jets in the dijet sample and the total number of jets reconstructed in a normalization sample as a function of  $\eta$  is shown in Fig. 5.4 with and without isolation requirement.

### 5.1.4 Electron/photon discrimination and electron identification

At this stage most of the electrons are also identified as photons, since they interact similarly in the calorimeter. Their showers can just be slightly wider in  $\phi$  direction due to their interaction with the magnetic field. In this thesis the discrimination between electrons and photons is done via a dedicated electron identification procedure. After an electromagnetic cluster has been identified as an electron, it is removed from the collection of electron/photon candidates and can thus no longer be identified as a photon.

Three successive sets of electron identification criteria are used in ATLAS: *loose*, *medium* and *tight*. The loose electron is identified only via the hadronic leakage and the shower variables in the second compartment of the ECal. This definition obviously allows for an excellent identification efficiency, but with very low background rejection. The medium electron is selected analogously to the photon with cuts on hadronic leakage and the shower shape variables from the second and first layer of the ECal and additional quality criteria for a track. These are a minimum number of hits in the pixel detector (at least one), a minimum number of hits in the pixel and SCT detectors (at least 9) and a minimal transverse impact parameter ( $< 1$  mm). The track quality criteria are refined in the definition of the tight electron. Additional to the medium electron criteria, isolation is required, as well as a minimal number of hits in the vertexing layer and a good matching between the track and the cluster. TRT variables are also used, such as the number of hits in the TRT and the ratio of the number of high-threshold hits to the total number of hits. Most of the criteria depend on  $\eta$  and  $p_T$  and provide a very good electron identification efficiency with good background rejection power. Medium electrons will be used in this thesis for the measurement of supersymmetric particle masses and the neutralino lifetime.

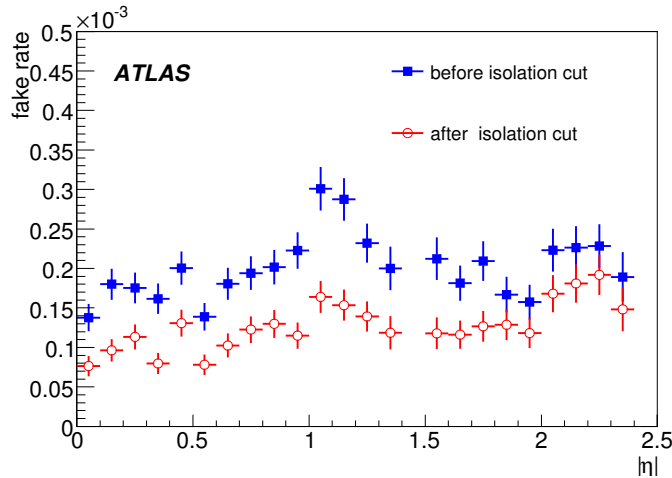


Figure 5.4: Photon fake rate as a function of  $\eta$  with and without isolation criterion [18].

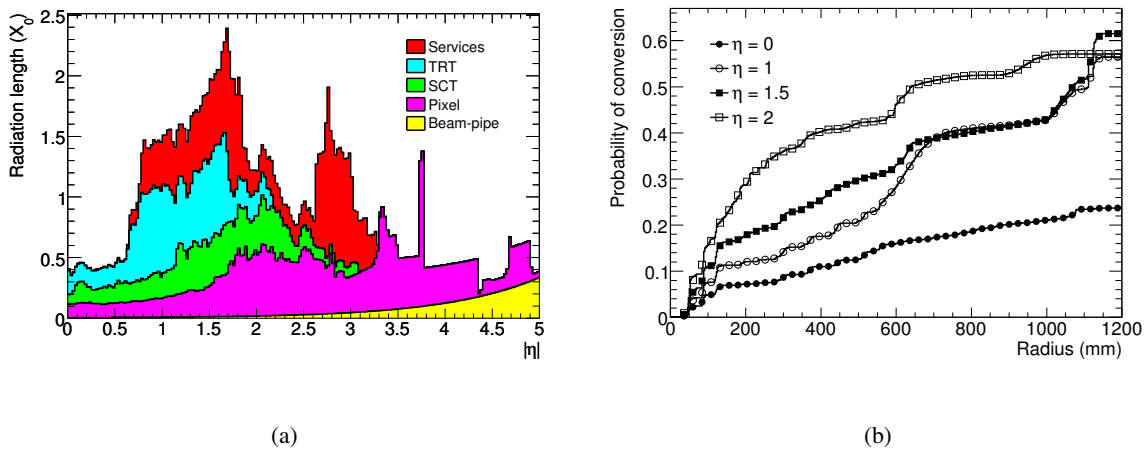


Figure 5.5: (a) Material budget in the inner detector and (b) resulting photon conversion probability [18].

## 5.2 Photon conversions

Since photons can convert into an electron-positron pair at any point in the tracker in the presence of material, it is important to develop efficient algorithms to reconstruct such conversions in order not to misidentify them as electrons or jets. The probability of a conversion is proportional to the amount and density of the material in the trajectory of a photon, which is measured in terms of radiation lengths. The total amount of material in the inner detector as a function of  $\eta$  is shown in Fig. 5.5(a). The resulting dependence of the conversion probability on  $\eta$  and the distance from the interaction vertex is shown in Fig. 5.5(b). It can clearly be observed that the overall conversion probability in the inner detector is around 50% and that a recovery strategy has to be developed.

The ability to reconstruct a photon conversion depends on the type of tracking algorithm that is used and thus on the coordinates in the tracker where the conversion occurs. Photons that convert within 300 mm of the beam axis can be reconstructed with the efficient standard silicon-seeded tracking algorithm (*inside-out tracking*). Photons that convert at a larger distance of the beam axis do not leave enough hits in the silicon tracker such that additional tracking algorithms have to be used that are seeded from

TRT hits and may or may not incorporate hits from the silicon tracker (*outside-in* and *standalone TRT tracking*).

- **Inside-out tracking:** Seeds are formed using three combinations of space-points in the pixel detector and SCT by imposing some constraints such as the curvature to limit the number of candidates. Afterwards a geometrical tool is used to identify detector elements that are searched for additional hits. A fitting procedure is used every time after adding a hit to the track and outliers are efficiently eliminated. Around 10% of all seeds lead to a fully reconstructed track. The tracks are subject to quality criteria and are ranked accordingly for comparison. After a silicon track has been accepted it is extrapolated into the TRT and combined with TRT hits. If the extended track has a higher quality than the original silicon track, the extension is kept, otherwise only the silicon track is stored. Since the inside-out tracking algorithm requires at least 7 silicon hits it is inefficient for late photon conversions.
- **Outside-in tracking:** The TRT is divided into 24 slices in  $\eta$  direction and a histogramming technique is used to scan for straight line patterns that are fitted to extract the track parameters. A minimal number of hits in the straw tubes is required. The reconstructed TRT segments are extrapolated into the silicon tracker where space-points are searched seeded by the track parameters. At least 2 hits in the SCT are required which are selected using quality criteria such as the curvature. Once a silicon extension is found, it can serve as seed for searching new TRT extensions as in the case of the inside-out tracking. In order to reduce the time needed for the procedure all TRT and silicon hits are excluded that are already part of an inside-out track. The main improvement of the track reconstruction efficiency due to outside-in tracking is in the region of 300 mm to 450 mm in radial distance.
- **Standalone TRT tracking:** All TRT segments that are not assigned a silicon extension are finally transformed into tracks by resolving remaining ambiguities. No track refitting is done. The total track reconstruction efficiency is improved in the region from 450 mm in radial distance to the calorimeter surface significantly by the TRT tracks.

The total track reconstruction efficiency as a function of the conversion radius is shown in Fig. 5.6. All three track collections are finally merged into a single track collection that serves as input for the following building of track pairs and secondary vertex fitting procedure after overlap is removed [18].

Track pairs are built by selecting a positively and a negatively charged track and imposing selection criteria on the tracks and on the pair selection in order to reduce the number of electron tracks and otherwise wrongly selected pairs. Cuts are imposed on the perigee, the longitudinal track impact parameter and on the minimum transverse momentum. Cutting on the ratio of high-threshold TRT hits over the total number of TRT hits selects tracks from electrons. Additionally, the polar angles of the two tracks should be small as well as the distance between the first hits of the tracks.

After having selected track pairs the conversion vertex has to be fitted, which is quite different compared to the fitting of ordinary tracks that are assumed to come from the primary interaction vertex. The massless nature of the photon can be used as additional constraint and a specific algorithm has been developed. A new track perigee is calculated using an initially estimated secondary vertex candidate and a new vertex is fitted with a fast Kalman filtering method using the full three dimensional information of the refitted conversion tracks. Again, quality criteria are imposed in order to select good vertex candidates.

Finally, the conversion tracks have to be matched to an electromagnetic cluster that has been reconstructed with the standard reconstruction method discussed above. Once a track (not necessarily a conversion track) is matched to a cluster, it is labeled as electron-like and is re-examined in order to determine whether or not it originates from a photon conversion. Two algorithms are used for this purpose:

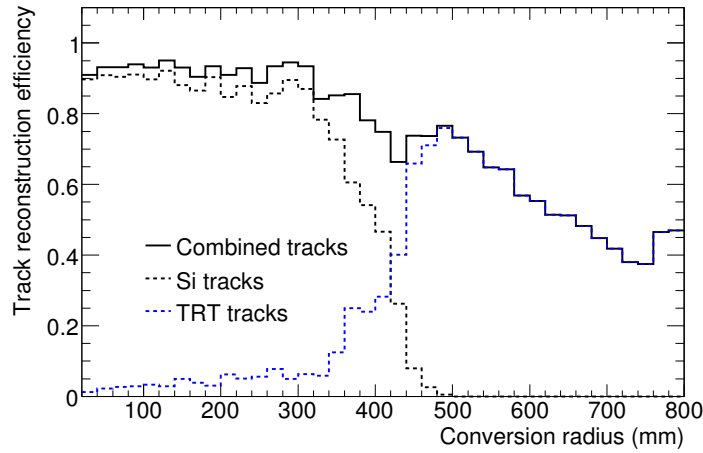


Figure 5.6: Total track reconstruction efficiency for converted photons with  $p_T = 20$  GeV. The individual contributions from inside-out plus outside-in tracking (“Si tracks”) and standalone TRT tracking are also shown [18].

the *angle-based matching* and the *track-based matching*. For the latter the conversion track collection is searched for candidates that match exactly with the best-match tracks associated with the electron-like clusters. If that is the case, further quality checks are performed in order to avoid declaring an electron which emits converting bremsstrahlung as a converted photon. In the angle-based matching the  $\eta$  and  $\phi$  coordinates of the center of the cluster are compared with the  $\eta$  and  $\phi$  coordinates of the candidate conversion vertices. If a candidate matches a cluster within a window of  $\Delta\eta = 0.048$  and  $\Delta\phi = 0.048$ , it is declared as a conversion with the corresponding flag.

In some cases not both of the tracks of a photon conversion can be reconstructed successfully. For instance, the photon can decay so late in the tracker, that the tracks cannot be distinguished from each other or the photon decays asymmetrically such that only one track has high enough momentum ( $> 500$  MeV) to be reconstructed. These *single track conversions* can be reconstructed by re-examining the remaining tracks from the conversion track collection that could not be assigned to a conversion. The effect of including these conversions into the overall conversion reconstruction efficiency is significant. Figure 5.7 shows the efficiency as a function of the conversion radius. As expected, the efficiency of the vertex reconstruction drops for radii larger than 300 mm, while the single track conversions occur mainly in the region of the TRT. Identified converted photons will be included in the set of photons used in this thesis.

## 5.3 Non-pointing photons

### 5.3.1 Identification

The standard photon identification as discussed above has been optimized for the selection of photons coming from the primary interaction vertex (*prompt photons*) and leads to inefficiencies for the selection of non-pointing photons that occur somewhere in the inner detector. Figure 5.8 shows a sketch of a delayed neutralino decay to a gravitino and a non-pointing photon. The shower axis does not point back to the interaction vertex and therefore the shower of a non-pointing photon seems to be broader than that of a prompt photon and thus it might not survive the cuts on the shower shape variables.

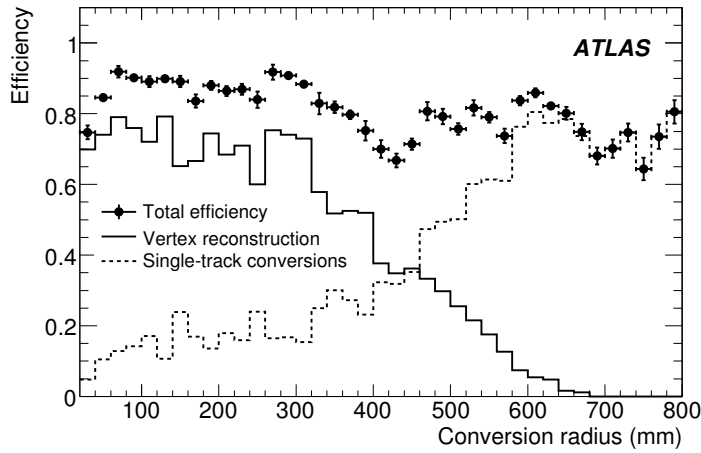


Figure 5.7: The total efficiency of the photon conversion reconstruction algorithms is shown as data points for photons with  $p_T = 20\text{ GeV}$ . The individual contributions from vertex reconstruction (solid) and single-track conversion reconstruction (dotted) are also shown [18].

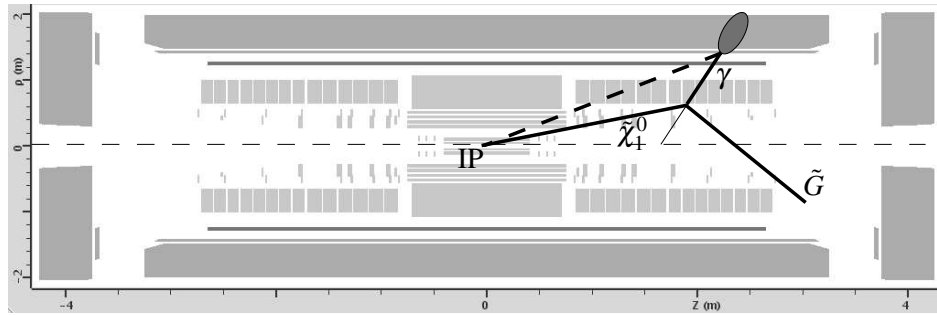


Figure 5.8: Schematic view of a non-pointing photon coming from a delayed neutralino decay using the ATLAS event display ATLANTIS [114].

Figure 5.9 shows the selection efficiencies of the various shower shape variables defined as the number of photons with  $|\eta| < 2.5$  and  $p_T > 20\text{ GeV}$  that pass the cut on the given variable divided by the number of reconstructed photons as a function of the  $z$ -component of the neutralino decay length. A significant dependence on five of the identification variables can be observed, namely  $R_\eta$ ,  $w_2$ ,  $F_{\text{side}}$ ,  $w_{s3}$  and  $w_{\text{stot}}$ . The relative effect of loosening the cuts on these variables on the background has been investigated using a jet sample [18]. Table 5.3 shows the fraction of jets reconstructed as photons and passing all photon criteria. The hadronic, second sampling and first sampling cuts have been applied sequentially. The slightly increased jet fake rate is taken as acceptable for the studies in this thesis since the photon identification efficiency for a GMSB sample with a non-zero neutralino decay length is increased, as discussed in Sect. 6.3. The cuts on these five shower shape variables will therefore be skipped in this thesis whenever non-pointing photons are used and only the *unbiased* selection will be used.

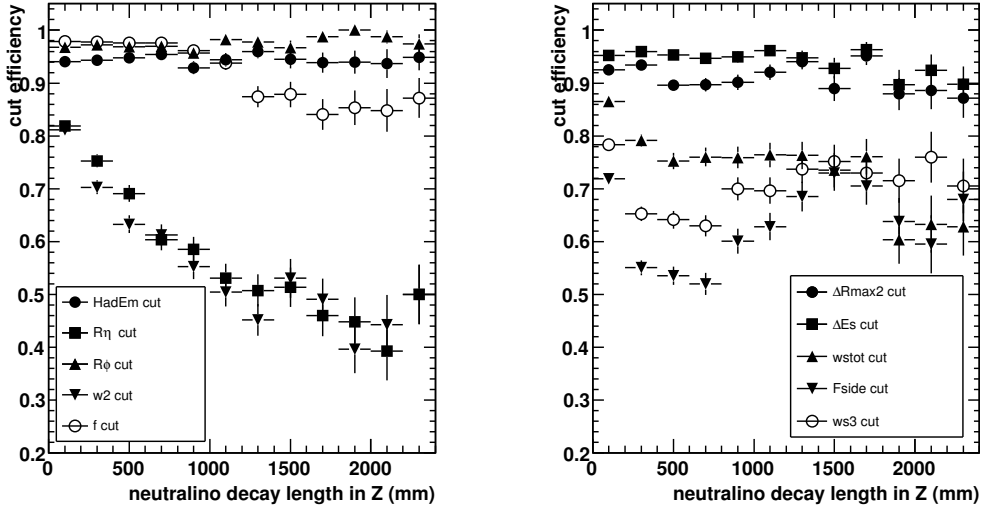


Figure 5.9: Efficiencies of the various photon identification cuts as a function of the neutralino decay length in  $z$ -direction [18].

Selection	hadronic	2nd sampling	1st sampling
default	$3.4\% \pm 0.1\%$	$0.57\% \pm 0.06\%$	$0.19\% \pm 0.03\%$
unbiased	$3.4\% \pm 0.1\%$	$2.7\% \pm 0.1\%$	$0.70\% \pm 0.07\%$

Table 5.3: Fraction of jets reconstructed as photons and passing the given photon criteria. The cuts have been applied sequentially [18].

### 5.3.2 Clustertime measurement with the ECal

In GMSB events with long-lived neutralino NLSPs it is expected that the resulting non-pointing photon arrives later in the calorimeter than the photons from prompt neutralino decays. This is due to two effects: First, the sum of the paths of the neutralino and the photon is longer than the path of a prompt photon coming from the primary interaction vertex as is depicted in Fig. 5.8, since the angle between the neutralino direction and the photon direction is non-zero. Hence, a longer time period is needed before the photon arrives at the surface of the calorimeter. Second, the neutralino is a heavy particle and hence travels with a velocity  $\beta \cdot c$  through the detector that is significantly lower than the speed of light  $c$ . The neutralino  $\beta$  spectrum for neutralinos with a mass of  $m_{\tilde{\chi}_1^0} = 118$  GeV is shown in Fig. 5.10(a). The relative importance of both effects is shown in Fig. 5.10(b) for a typical GMSB scenario with  $m_{\tilde{\chi}_1^0} = 118.85$  GeV and  $\tau_{\tilde{\chi}_1^0} = 11.2$  ns, where the additional time needed due to the longer path is denoted  $\Delta t_{\text{path}}$  and the additional time needed due to the neutralino velocity is denoted  $\Delta t_\beta$ . The time differences are given by

$$\Delta t_{\text{path}} = \frac{|\text{non-pointing photon path}| - |\text{prompt photon path}|}{c} \quad (5.1)$$

$$\Delta t_\beta = \frac{\text{neutralino path} \cdot (1 - \beta)}{\beta \cdot c}. \quad (5.2)$$

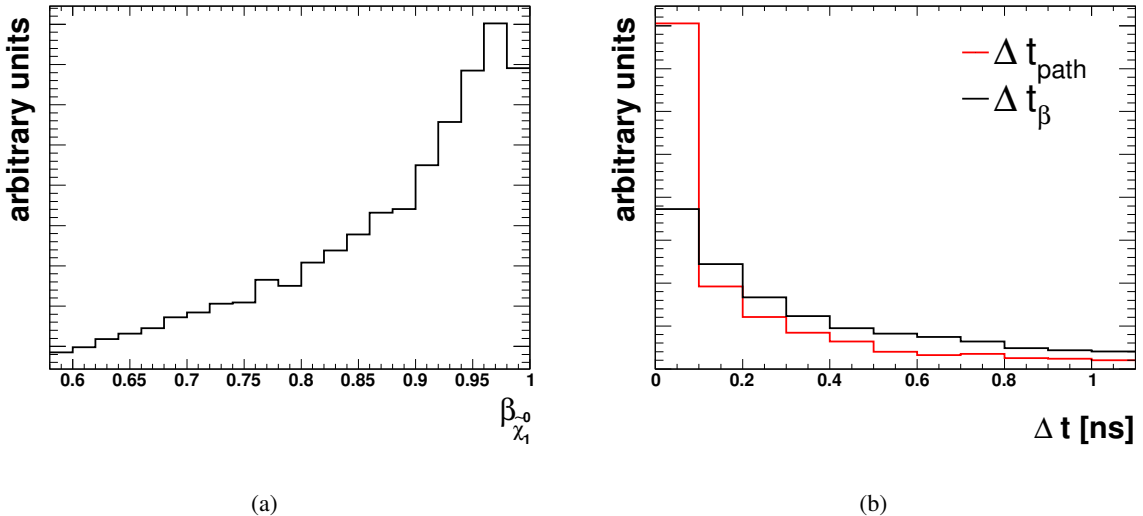


Figure 5.10: (a)  $\beta$  spectrum of a neutralino with mass  $m_{\tilde{\chi}_1^0} = 118.85$  GeV. (b)  $\Delta t_{\text{path}}$  and  $\Delta t_\beta$  distributions for a neutralino with mass  $m_{\tilde{\chi}_1^0} = 118.85$  GeV and lifetime  $\tau_{\tilde{\chi}_1^0} = 11.2$  ns.

It can be observed that the effect of the finite neutralino mass dominates the effect of the decay angle between the neutralino and the photon. This is due to the fact that the photon as well as the gravitino are (almost) massless and thus are strongly boosted in the direction of the neutralino and hence have a small decay angle.

The arrival time of the electromagnetic cluster in the ECal (referred to as *clustertime* in the following) can be measured with ATLAS [115]. It is defined as the measured time of the cell in the second layer with the largest energy with respect to the bunch crossing time, where the time of flight of a particle travelling with  $c$  and coming from the interaction vertex is subtracted. The triangular shaped ionization signal of a cell as a function of time is shown in Fig. 5.11(a), where the pulse is obtained from a large number of physics pulses averaged after normalization to their amplitudes and with the time derived from scintillator signals. The first 125 ns are used for the reconstruction of the amplitude  $A$  and the time  $\tau$ . The signal is digitized every 25 ns such that  $n = 5$  samples are used. The optimal filtering method is used for the reconstruction [113]:

$$A = \sum_{i=1}^n a_i s_i, \quad \tau = \frac{1}{A} \sum_{i=1}^n b_i s_i, \quad (5.3)$$

where  $s_i$  is the amplitude of the sample  $i$  and  $a_i$  and  $b_i$  are the optimal filtering coefficients, which are determined by minimizing the variance of  $A$  and  $A\tau$  under specific constraints. The computation requires the knowledge of the noise autocorrelation matrix and the signal waveform and its derivative. The physics waveform can be numerically computed from a calibration waveform obtained in special delay runs. The resulting precision of the physics waveform is about 1-2% over the first 125 ns used for time reconstruction, as shown in Fig. 5.11(a).<sup>4)</sup>

If the calorimeter signal shape is distorted, a bias can be introduced in the clustertime reconstruction. Therefore, the detailed study of cross talk between the single calorimeter cells for each module is important and a complete map has been extracted from test beam runs and the different sources have been identified [116]:

<sup>4)</sup>The dispersion on the LHC beam crossing time is 186 ps, while the dispersion from the longitudinal beam position induces a time dispersion of about 170 ps, if not corrected [115].

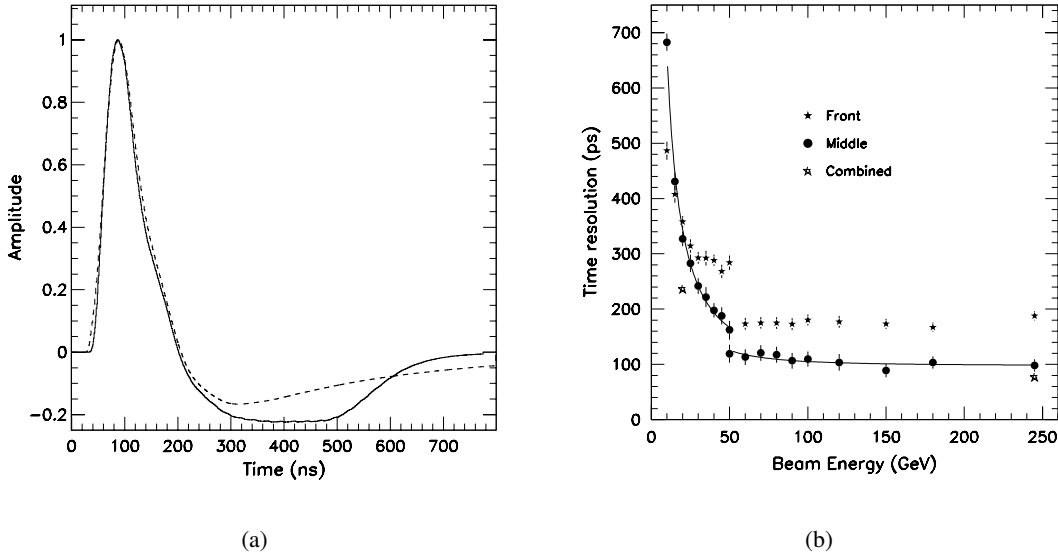


Figure 5.11: (a) Ionization signal collected on ECal cell electrodes. A calibration pulse (dashed line) and a measured pulse from an electron test beam (solid line) are shown. The first 125 ns are used for the energy and time measurement [115]. (b) Time resolution of the middle and front layer of the ECal as a function of the test beam energy in the medium (high) gain of the electronics above (below) 50 GeV beam energy [115].

- **Front layer:** The amplitude of the cross talk in first neighboring cells is about 10% of the signal amplitude due to a capacitive coupling on the electrodes in  $\eta$  direction.
- **Middle layer:** In  $\phi$  direction an inductive and uniform contribution of about -2% comes from the summing board. In  $\eta$  direction a capacitive contribution from the electrodes contributes about 0.8% of the signal amplitude.

The resolution  $\sigma_\tau$  of the clustertime measurement depends on the accurate correction of the noise and cross-talk effects and is parameterized as

$$\sigma_\tau = \frac{a}{E} \oplus c. \quad (5.4)$$

After all corrections a constant term  $c$  of about 100 ps is the ultimate goal, while at the beginning of data taking a constant term of about 1 ns seems to be realistic. The term including  $a$  depends on the energy of the particle and its impact on the overall resolution is shown in Fig. 5.11(b). The time resolution has been measured in test beam runs and it can be observed that for beam energies above 50 GeV the resolution is flat and about 100 ps. The discontinuity at 50 GeV is due to the fact that for beam energies larger (smaller) than 50 GeV the middle layer cell is always reconstructed in the medium (high) gain regime of the electronics.

### 5.3.3 Projected photon path

As can be observed in Fig. 5.8, the delayed neutralino decay leads to a photon path that does not point back to the interaction vertex. This is due to the non-vanishing angle between the direction of the neutralino momentum and the direction of the photon momentum. For illustration, the angle  $\Delta\theta(\tilde{\chi}_1^0, \gamma)$  in  $\theta$  direction obtained from the generator information is shown in Fig. 5.12 for a neutralino with mass  $m_{\tilde{\chi}_1^0} = 118.85$  GeV and lifetime  $\tau_{\tilde{\chi}_1^0} = 11.2$  ns. The width of the distribution is  $\sim 0.62$  corresponding

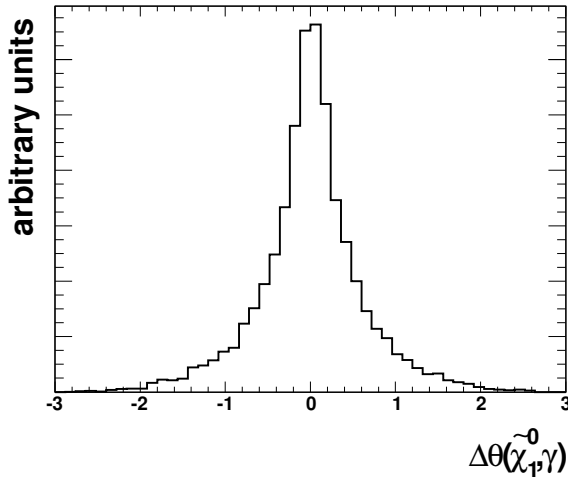


Figure 5.12:  $\Delta\theta(\tilde{\chi}_1^0, \gamma)$  for a neutralino with mass  $m_{\tilde{\chi}_1^0} = 118.85$  GeV and lifetime  $\tau_{\tilde{\chi}_1^0} = 11.2$  ns leading to a non-vanishing  $|z_{\text{cluster}}|$ .

to an angle of  $\sim 36^\circ$  leading to a displaced intersection point of the  $z$ -axis with the projected photon path with respect to the primary interaction vertex. This intersection point (referred to as  $z$ -*vertex* in the following) can be calculated. Since photons leave no tracks in the inner detector, the calorimeter system has to be used to reconstruct the photon path. This is possible due to the excellent resolution in  $\eta$  direction of the first and second compartment of the ECal. The  $\phi$  direction cannot be measured, but for the calculation of the z-vertex this is not necessary.

The  $\eta$  position of the photon cluster in the first and second ECal layer is needed, denoted by  $\eta_1$  and  $\eta_2$ , respectively. Furthermore, the radial distances  $R_1$  and  $R_2$  of the cluster in the first and second layer, respectively, have to be known. The z-vertex  $z_{\text{cluster}}$  is given by a simple geometrical equation:

$$z_{\text{cluster}} = \frac{R_1 \cdot R_2}{R_2 - R_1} \cdot (\sinh \eta_1 - \sinh \eta_2). \quad (5.5)$$

The  $\eta_p$  direction of the photon is defined by the angle

$$\theta = \text{atan2}(R_2 - R_1, z_2 - z_1), \quad (5.6)$$

with  $z_1 = R_1 \cdot \sinh \eta_1$  and  $z_2 = R_2 \cdot \sinh \eta_2$ , between the  $z$ -axis and the projected photon path. However, if a photon is selected for analysis and a geometrical  $\eta$  cut is imposed due to the detector acceptance region, the usual  $\eta$  variable has to be used defined by the interaction vertex. The uncertainty on the z-vertex position is given by two  $\eta$  and photon energy  $E$  dependent functions, one for the barrel and one for the endcap section:

$$\Delta z_{\text{cluster}}^{\text{barrel}} = 13 \cdot \cosh \eta \cdot \sqrt{500 \cdot \frac{\cosh \eta}{E}} \quad (5.7)$$

$$\Delta z_{\text{cluster}}^{\text{endcap}} = 70 \cdot \sqrt{25 \cdot \frac{\cosh \eta}{E}}. \quad (5.8)$$

The resolution of the z-vertex lies typically in the region of 5-10%. The variable will later be used for the measurement of the neutralino lifetime.

## 5.4 Jet reconstruction and missing transverse energy

### 5.4.1 Jet reconstruction

Produced partons hadronize which leads to a jet of particles that has to be identified and the corresponding transverse energy has to be measured correctly. Depending on the particle types contained in the jet, different fractions of the transverse energy are deposited in the ECal and the HCal. If a jet mainly consists of heavy hadrons it will deposit most of the energy in the HCal. If it consists of neutral pions that decay to photons, most of the energy is deposited in the ECal and the jet has to be differentiated from electrons and photons. Therefore, the multiplicity of jets strongly depends on the identification performance of electrons, photons and other objects.

The jet trigger algorithm on L1 searches for local maxima in the energy sums of  $2 \times 2$  trigger towers, as described briefly in Sect. 3.2.6. Afterwards the energy sums of the deposited energies are calculated using a window of size  $\Delta\eta \times \Delta\phi = 0.8 \times 0.8$  and are compared with 8 different energy thresholds. The multiplicities of the individual thresholds are derived in this step and are sent to the CTP. On L2 and EF level similar algorithms as for the offline reconstruction of jets are used based on the scanning of the calorimeter with a cone of fixed size in  $\eta$  and  $\phi$  direction, as described in the following.

In ATLAS two main jet algorithms are used [18]: the *cone* algorithm as well as the  $k_T$  algorithm.<sup>5)</sup> Only jets reconstructed with the cone algorithm will be used throughout this thesis.<sup>6)</sup> There are some principal guidelines for the efficient and high quality jet reconstruction:

- **Infrared safety:** The presence or absence of soft particles between two particles belonging to the same jet should not affect the combination of these particles to a jet.
- **Collinear safety:** The splitting of a high energetic particle into two collinear particles with lower energy should not affect the jet finding.
- **Technology independence:** The reconstructed jet should not depend on the signal source, *i.e.* all detector inefficiencies have to be corrected, such as the detector resolution or environment.
- **Event independence:** The jet should be reconstructed independently of multiple interactions or pile-up events.

For the seeded cone algorithm two parameters are needed: the transverse energy threshold of 1 GeV and the cone size  $\Delta R = \sqrt{\Delta\eta^2 + \Delta\phi^2}$  with  $\Delta R = 0.4$  for narrow jets and  $\Delta R = 0.7$  for wider jets. The input for this algorithm are reconstructed calorimeter signals, such as reconstructed calorimeter towers or topological clusters, as described above. First, all input is ordered in decreasing order in transverse momentum and it is checked, if the object with highest  $p_T$  is above the seed threshold. All objects within the given cone are combined with the seed followed by a new calculation of the direction from all four-momenta inside the cone. A new cone is centered around the new direction in order to recollect objects inside this new cone and recalculate the direction. This process continues until the direction does not change anymore. The same procedure is run on the next seed candidate until no more seeds are available. Finally, the jets are calibrated using a method originally developed for the H1 experiment [119]: all calorimeter cells are resummed using weighting functions that depend on the cell signal density and on the location in the calorimeter.

<sup>5)</sup>The development of more sophisticated jet finding algorithms is an ongoing process.

<sup>6)</sup>In contrast to the cone algorithm the  $k_T$  algorithm is more complex and takes into account the structure of the jet rather than just scanning the calorimeter with a cone of fixed size. Details can be found in [117, 118]. However, the cone algorithm is considered to be simpler and more robust and therefore the  $k_T$  algorithm will not be described in detail.

The jet energy resolution is fitted with a function considering three independently contributing terms [18]:

$$\frac{\sigma}{E} = \frac{a}{\sqrt{E(\text{GeV})}} \oplus b \oplus \frac{c}{E}, \quad (5.9)$$

where the term including  $a$  is a sampling term due to statistical fluctuations in the energy deposits,  $b$  is a constant term reflecting the effect of the calorimeter non-compensation<sup>7)</sup> and the term including  $c$  is a noise term describing the noise contribution to the energy measurement. For central jets the stochastic term is about  $a \approx 60\%$ , while the other terms are  $b \approx 3\%$  and  $c \approx 5\%$  [18].<sup>8)</sup>

Due to the highly granular calorimeters in ATLAS the jet direction can be determined precisely together with the primary vertex from the inner detector. Almost all jets with transverse energies above 100 GeV can be matched to the true jet within a cone of  $\Delta R < 0.2$ . However, at lower energies the precision of the jet axis reconstruction degrades and a non-negligible fraction of reconstructed jets lies outside the matching cone. The jet reconstruction efficiency is almost 100% for jets with a transverse momentum larger than 30 GeV [18].

With the given jet reconstruction algorithms also electrons, photons and other particles are identified as jets. This is taken into account in the analysis by an overlap removal step.

#### 5.4.2 Missing transverse energy measurement

The accurate reconstruction of missing transverse energy  $E_T^{\text{miss}}$  is a very complex task in ATLAS due to the dependence of the calculation on multiple objects ranging from the individual cell calibration in the calorimeters to the accurate reconstruction of muon tracks in the muon system over the full  $\eta$  range of the detector. The most relevant issues for a good  $E_T^{\text{miss}}$  reconstruction are [18]:

- The suppression of electronics noise.
- After noise suppression, all calorimeter cells have to be used.
- Accurate calorimeter (inter-) calibration, in particular in the barrel and endcap region.
- The full  $|\eta| < 5$  range of the calorimeter has to be used.

Two different approaches are utilized in ATLAS: the *cell-based* and the *object-based* reconstruction. Only the cell-based approach will be discussed here, since it is commonly used for supersymmetry analyses.

The cell-based algorithm uses the energy deposits in each of the calorimeter cells that have been calibrated with global weights depending on their energy density. Only the cells that remain after a noise suppression procedure are used. Additional corrections are applied for the muon energy and the energy lost in the cryostats. This algorithm is stable also for early data taking, since it does not rely on the accurate reconstruction of physics objects in contrast to the object-based algorithm.

Due to the large number of read-out channels in the calorimeters ( $\approx 200K$ ) the amount of electronics noise can contribute as much as 13 GeV [18] to the width of the  $E_T^{\text{miss}}$  resolution. The standard method for suppressing the noise is based on only using calorimeter cells with energies larger than  $2 \times \sigma_{\text{noise}}$ , where  $\sigma_{\text{noise}}$  is the width of the noise distribution which has to be known. If the cells are used with the usual electromagnetic calibration, the calculated amount of  $E_T^{\text{miss}}$  has a shift of 30% with respect to the truth information. This shows that a dedicated algorithm for the cell calibration has to be developed in

<sup>7)</sup>The ATLAS calorimeter is a *non-compensating* calorimeter, *i.e.* the response to hadrons is lower than to electrons and photons.

<sup>8)</sup>Equation (5.9) has been found to be best suited for the determination of the jet energy resolution [18], while Eq. (3.7) has been used to parametrize the energy resolution of the calorimeters using isolated pion beams [80].

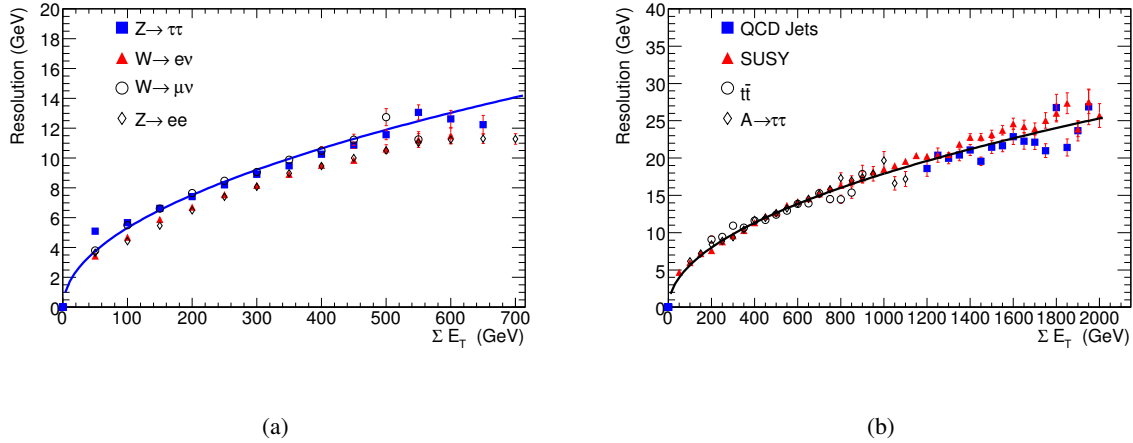


Figure 5.13: Resolution of  $E_T^{\text{miss}}$  after calibration as a function of the total transverse energy measured in the calorimeters for different physics processes. The curves correspond to the fit to (a)  $Z \rightarrow \tau\tau$  and (b)  $A \rightarrow \tau\tau$  [80].

order to reduce the systematic shift and optimize the resolution. A cell classification scheme is used for this purpose by defining the energy deposit in a cell as hadronic or electromagnetic, since hadronic showers tend to have lower energy densities compared to electromagnetic ones.

Since muons do not deposit their energy in the calorimeters, their tracks have to be used separately in the calculation of  $E_T^{\text{miss}}$ . The muon momentum as measured in the muon system is taken and the energy loss in the calorimeters is already taken into account in the calorimeter cell term. Muons that are lost outside the acceptance region of the muon system of  $|\eta| < 2.7$  are not taken into account, but the muon term in general only marginally influences the overall  $E_T^{\text{miss}}$  reconstruction performance [18], since the muon system provides a very good muon reconstruction efficiency. However, lost muons can be a source of large fake  $E_T^{\text{miss}}$ .

The third important source of  $E_T^{\text{miss}}$  in ATLAS is the cryostat system. The thickness of the system between the ECal barrel and the tile barrel calorimeter is about half an interaction length. Therefore, jets can lose a significant amount of their energy leading to additional fake  $E_T^{\text{miss}}$ . This energy loss can be recovered by using the correlation of the energy measurements in the last layer of the ECal and the first layer of the HCal. The same is done for the endcap sections. The correction is applied to all reconstructed jets in the event, which in turn leads to a better estimate of  $E_T^{\text{miss}}$ . The cryostat correction contributes at a level of  $\sim 5\%$  per jet with a transverse momentum above 500 GeV and is therefore non-negligible for high momentum jets.

The expected performance of the  $E_T^{\text{miss}}$  reconstruction is estimated by comparing the measured value with the true value as a function of the total transverse energy. Figure 5.13 shows the  $E_T^{\text{miss}}$  resolution defined as the width of the  $E_{x,y}^{\text{miss}} - E_{x,y}^{\text{miss,true}}$  distribution in a certain  $E_T$  bin. The distribution is fitted with a function  $\sigma = a \cdot \sqrt{\sum E_T}$ , where the fit parameter  $a$  varies between 0.53 and 0.57 for different physics processes [18].

In supersymmetry studies it can be important to suppress fake  $E_T^{\text{miss}}$  to reduce the Standard Model background. One possibility is to look for correlations between the direction of the reconstructed  $E_T^{\text{miss}}$  and the direction of jets, which can hint at fake  $E_T^{\text{miss}}$  from badly measured jets. In general, the resolution of the  $E_T^{\text{miss}}$  direction for events with genuine  $E_T^{\text{miss}}$  depends on the relative fraction of fake  $E_T^{\text{miss}}$  and on the event topology. As an example, Fig. 5.14 shows the resolution of the  $E_T^{\text{miss}}$  measurement in  $\phi$  direction as a function of the true  $E_T^{\text{miss}}$  for different physics processes. It can be observed that the measurement is more accurate for  $W \rightarrow e\nu$  events, which contain moderate hadronic activity compared

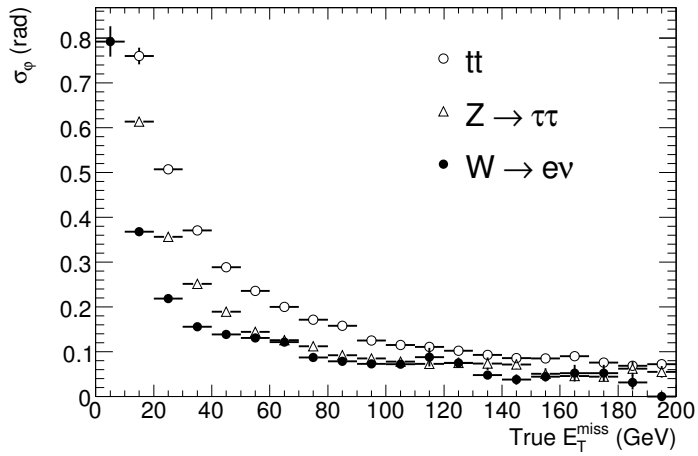


Figure 5.14: Performance of the  $\phi$ -direction measurement of  $E_T^{\text{miss}}$  for different physics processes [80].

to  $t\bar{t}$  events. For values below 40 GeV the accuracy degrades rapidly, while for large values of true  $E_T^{\text{miss}}$  the accuracy can reach 100 mrad and below [18].

# Chapter 6

## Discovery potential for GMSB models with photon final states

In GMSB models with  $N_5 = 1$  and low  $\tan\beta$  the lightest neutralino  $\tilde{\chi}_1^0$  is the NLSP and decays to a gravitino  $\tilde{G}$  and a photon, since the neutralino is mainly a photino in the minimal GMSB model. Therefore the standard mSUGRA-like decay cascade of squarks and gluinos is extended by the decay

$$\tilde{\chi}_1^0 \rightarrow \gamma \tilde{G}. \quad (6.1)$$

Depending on the branching ratio of the squarks and gluinos decaying to various types of supersymmetric particles, the decay chain may also contain multiple jets. Events with high energetic photons are expected, if the NLSP lifetime is not too long, such that most of the NLSPs decay outside the detector. The corresponding event signatures and the discovery potential of the ATLAS detector for these models are discussed in this chapter, including the optimization of the signal selection, the role of the trigger signatures and the expected background from Standard Model processes. The scenarios in the GMSB parameter space chosen for detailed reconstruction and trigger studies are described in Sect. 6.1. The case of prompt photons ( $C_{\text{grav}} = 1$ ) is investigated in Sect. 6.2, while the case of non-pointing photons ( $C_{\text{grav}} > 1$ ) and therefore larger NLSP lifetimes is studied in Sect. 6.3. The discovery potential in a wider range of the parameter space is presented in Sect. 6.2.4, where a fast simulation approach has been used and a comparison of full and fast simulation results is presented.

### 6.1 Benchmark points and datasets

#### 6.1.1 GMSB scenarios

In this chapter, the following GMSB scenarios are studied:

- **For the detailed study of properties of GMSB models with prompt photon final states** and their signatures in the ATLAS detector, the specific GMSB scenario called *GMSB1* has been chosen. The parameters of this benchmark point are  $\Lambda = 90 \text{ TeV}$ ,  $N_5 = 1$ ,  $M_{\text{mess}} = 500 \text{ TeV}$ ,  $\tan\beta = 5$ ,  $\text{sign}(\mu) = +$  and  $C_{\text{grav}} = 1$ .

In the GMSB1 scenario the total cross section for the production of supersymmetric particles in  $pp$ -collisions at 14 TeV is about 7.8 pb calculated in NLO. The resulting mass spectrum is shown in Fig. 6.1. Apart from the quasi-massless gravitino ( $m_{\tilde{G}} = 1.08 \cdot 10^{-8} \text{ GeV}$ , not shown), it features squarks with masses around 1 TeV and gluinos that are significantly lighter than the squarks, while the sleptons and gauginos have lower masses around (100 – 500) GeV. The NLSP is the lightest neutralino  $\tilde{\chi}_1^0$  with  $m_{\tilde{\chi}_1^0} = 118.85 \text{ GeV}$ . Due to its dominant photino component it decays

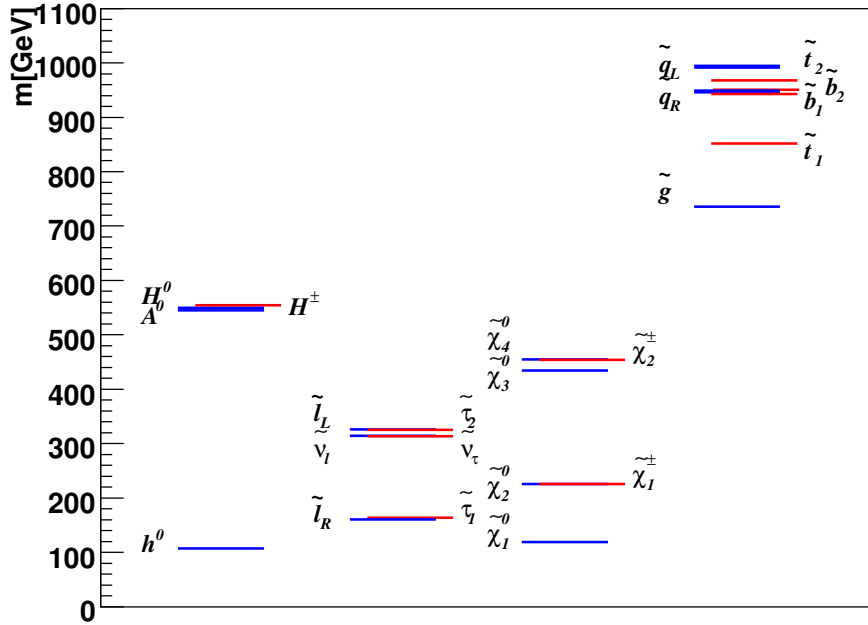


Figure 6.1: Supersymmetric mass spectrum of the GMSB1 scenario. The quasi-massless gravitino is not shown.

Particle	Mass [GeV]	Particle	Mass [GeV]	Process	BR [%]
$\tilde{\chi}_1^0$	118.85	$\tilde{G}$	$1.08 \cdot 10^{-8}$	$\tilde{q}_{L(R)} \rightarrow \tilde{g}q$	53 (> 80)
$\tilde{\chi}_2^0$	225.47	$\tilde{g}$	735.58	$\tilde{q}_{L(R)} \rightarrow \tilde{\chi}_2^0 q$	14 (< 1)
$\tilde{\chi}_3^0$	434.30	$\tilde{u}_R, \tilde{c}_R$	944.50	$\tilde{g} \rightarrow \tilde{\chi}_1^\pm q$	50
$\tilde{\chi}_4^0$	455.23	$\tilde{d}_R, \tilde{s}_R$	941.02	$\tilde{g} \rightarrow \tilde{\chi}_2^0 q\bar{q}$	27
$\tilde{\chi}_1^\pm$	225.32	$\tilde{u}_L, \tilde{c}_L$	987.30	$\tilde{\chi}_1^\pm \rightarrow \tilde{\chi}_1^0 W^\pm$	90
$\tilde{\chi}_2^\pm$	453.82	$\tilde{d}_L, \tilde{s}_L$	990.33	$\tilde{\chi}_1^0 \rightarrow \gamma \tilde{G}$	97
$\tilde{e}_R, \tilde{\mu}_R$	160.54	$\tilde{b}_1$	938.16	$\tilde{\chi}_1^0 \rightarrow Z^0 \tilde{G}$	1
$\tilde{e}_L, \tilde{\mu}_L$	326.34	$\tilde{t}_1$	843.08		
$\tilde{\tau}_1$	164.01	$\tilde{b}_2$	946.53		
$\tilde{\tau}_2$	325.07	$\tilde{t}_2$	966.61		
$\tilde{\nu}$	314.76	$h^0$	107.11		

Table 6.1: Mass spectrum and important branching ratios of the GMSB1 benchmark scenario.

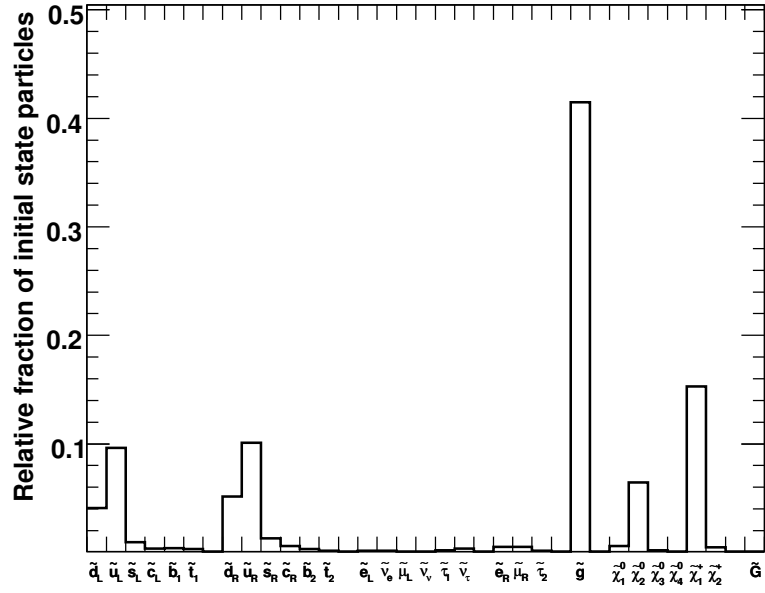


Figure 6.2: Relative fraction of the numbers of the initial supersymmetric particles in  $pp$ -collisions at 14 TeV for the GMSB1 benchmark point.

to a gravitino and a photon with a branching ratio of 97%. The masses of all supersymmetric particles and the branching ratios of some important decays in the GMSB1 scenario are summarized in Tab. 6.1. Figure 6.2 shows the relative fraction of the numbers of the initial supersymmetric particles for all types of particles. In total, squarks (gluinos) are produced in 36% (43%) of the GMSB1 events at 14 TeV. The remaining events mainly consist of gaugino pair production, while the initial production of sleptons is strongly suppressed.

The initial pair of squarks and gluinos can decay via two main decay classes, as shown in Figs. 6.3(a) and 6.3(b). Since (i) the branching ratio of left- (right-) handed squarks decaying to a gluino  $\tilde{g}$  is 53% ( $> 80\%$ ), (ii) the gluino decays predominantly (50%) to a  $\tilde{\chi}_1^\pm$  and (iii) the  $\tilde{\chi}_1^\pm$  in turn decays with a branching ratio of 90% into a  $\tilde{\chi}_1^0$  and a  $W^\pm$  boson, the decay chain in Fig. 6.3(a) dominates. In contrary, the decay chain of Fig. 6.3(b) has a smaller total branching ratio, since left- (right-) handed squarks and gluinos decay to a  $\tilde{\chi}_2^0$  only with a branching ratio of 14% ( $< 1\%$ ) and 27%, respectively. However, the latter case leads to the interesting signature of opposite-sign-same-flavor (OSSF) lepton pairs in the final state, which is used for the measurement of kinematic endpoints in Sect. 7.1 and in one of the methods to determine the  $\tilde{\chi}_1^0$  lifetime (see Sect. 7.2.5). Figure 6.4 shows the number of particles being the mother particle of the NLSP in a certain event.<sup>1)</sup> If the mother particle is a right-handed slepton, an OSSF lepton pair is present in the event<sup>2)</sup>. The two decay classes shown in Figs. 6.3(a) and 6.3(b) cover a combined branching ratio of almost 100% of

<sup>1)</sup>The next-to-next-to-lightest supersymmetric particle in the mass hierarchy shown in Fig. 6.1 is the  $\tilde{l}_R$ . However, e.g. the  $\tilde{\chi}_1^\pm$  can also be the mother particle of the lightest neutralino, as shown in Fig. 6.3(a).

<sup>2)</sup>A right-handed slepton always decays to a  $\tilde{\chi}_1^0$  and a lepton and its mother particle is always a (heavier) neutralino decaying to the slepton and a lepton. Since GMSB models are flavor-conserving, both leptons have the same flavor. The mother particle of a right-handed slepton cannot be a chargino, since the wino component of the chargino only couples to left-handed particles and the chargino does not couple to sleptons via its higgsino component.

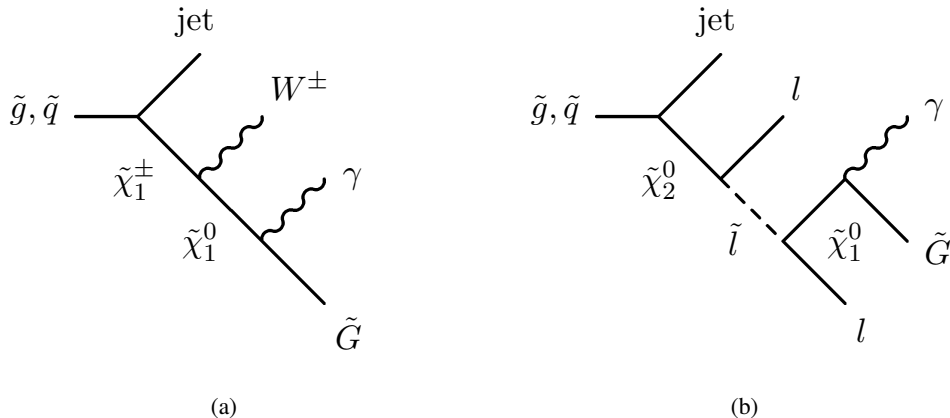


Figure 6.3: Main decay channels of squarks and gluinos in GMSB1-like scenarios: (a) decay via  $\tilde{\chi}_1^\pm$ ; (b) decay via  $\tilde{\chi}_2^0$ .

the initial squark and gluino production. In summary, hard jets from the initial squark and gluino decays, hard prompt photons from the  $\tilde{\chi}_1^0$  decay,  $E_T^{\text{miss}}$  from the escaping gravitinos and depending on the decay chain additional leptons are expected.

- **For the study of the discovery potential in the  $\Lambda - \tan\beta$ -plane** a scan is performed, while the other parameters are fixed to the GMSB1 values. Hence, the properties of the various model points under study are similar to the GMSB1 benchmark scenario with different cross sections and slightly shifted mass hierarchies. In some regions of the scanned parameter space the  $\tilde{\tau}_1$  becomes the NLSP leading to  $\tau$ -leptons in the final state. An analysis based on photons in the final state is not sensitive to this signature and dedicated search strategies have to be developed [120].
- **For detailed studies of the discovery potential for GMSB models featuring non-pointing photons** in the final state, a benchmark point called *GMSB3* has been chosen. The parameters of this scenario are similar to the parameters of the GMSB1 scenario, except for  $C_{\text{grav}} = 55$ . This leads to a finite  $\tilde{\chi}_1^0$  lifetime of  $\tau_{\tilde{\chi}_1^0} = 11.2$  ns, which corresponds to a decay length of  $c\tau_{\tilde{\chi}_1^0} = 3.2$  m, and a gravitino mass of  $m_{\tilde{G}} = 5.95 \cdot 10^{-7}$  GeV. Again, this mass is much too small to have any influence on the phenomenology. Due to the finite  $\tilde{\chi}_1^0$  lifetime, a certain number of  $\tilde{\chi}_1^0$  escape the detector before they decay leading to a final state with a reduced number of photons compared to the prompt photon case. All other features of the GMSB3 scenario, like cross sections and branching ratios, are identical to those of the GMSB1 scenario and the above discussion of the phenomenology of GMSB1 is also valid for GMSB3.

Table 6.2 summarizes the parameters of the benchmark scenarios used in this chapter. In Fig. 6.5(a) an optical event display of a typical GMSB event with prompt photons and jets in the final state in the ATLAS detector is shown in the  $x - y$ -profile. The inner detector is shown in black, while the ECal and HCal systems are displayed in green and red, respectively. The segmentation of the calorimeters is also indicated. The muon system is shown in blue. The tracks coming from the primary interaction vertex belong to jets and have a transverse momentum larger than 10 GeV. Jets are indicated as brown bars outside the muon system. The corresponding clusters are also shown in the calorimeter system as gray bars and their lengths correspond to the deposited amounts of energy, which is larger than 10 GeV. Photons are indicated with yellow bars outside the muon system and it can be observed that no tracks belong to the photon clusters. The direction of the missing transverse energy is indicated with a dashed red line. Note, that the event display is shown in a strong fish eye perspective and that therefore the size relations between the individual detector components are not realistic. Figure 6.5(b) shows the same

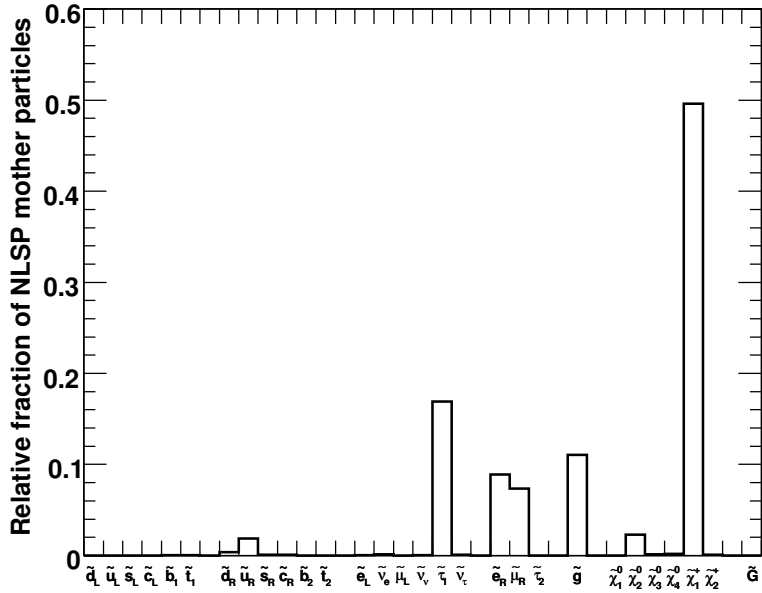


Figure 6.4: Relative fraction of the numbers of particles being the mother particle of the NLSP in the GMSB1 benchmark scenario.

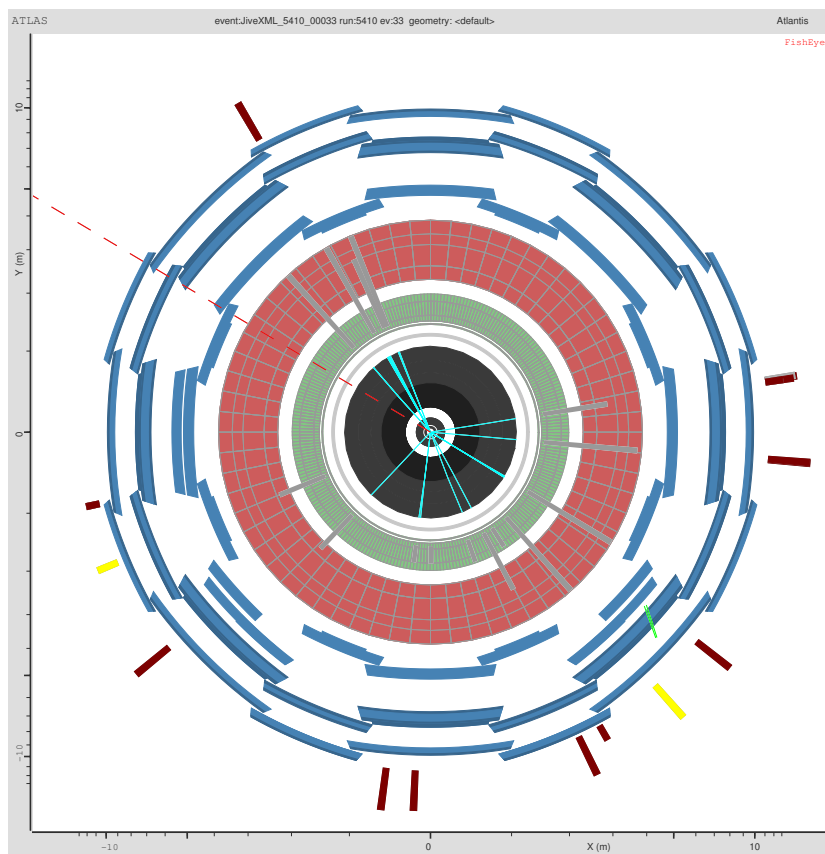
Name	$\sigma_{\text{NLO(LO)}} [\text{pb}]$	$\Lambda [\text{TeV}]$	$M_{\text{mess}} [\text{TeV}]$	$N_5$	$\tan \beta$	$\text{sign}(\mu)$	$C_{\text{grav}}$	$c\tau_{\tilde{\chi}_1^0} [\text{mm}]$
GMSB1	7.8 (5.1)	90	500	1	5	+	1.0	1.1
GMSB3	7.8 (5.1)	90	500	1	5	+	55.0	$3.2 \cdot 10^3$

Table 6.2: Summary of the benchmark scenarios used in this chapter. GMSB1 is a prompt photon scenario, while dataset GMSB3 features non-pointing photons.

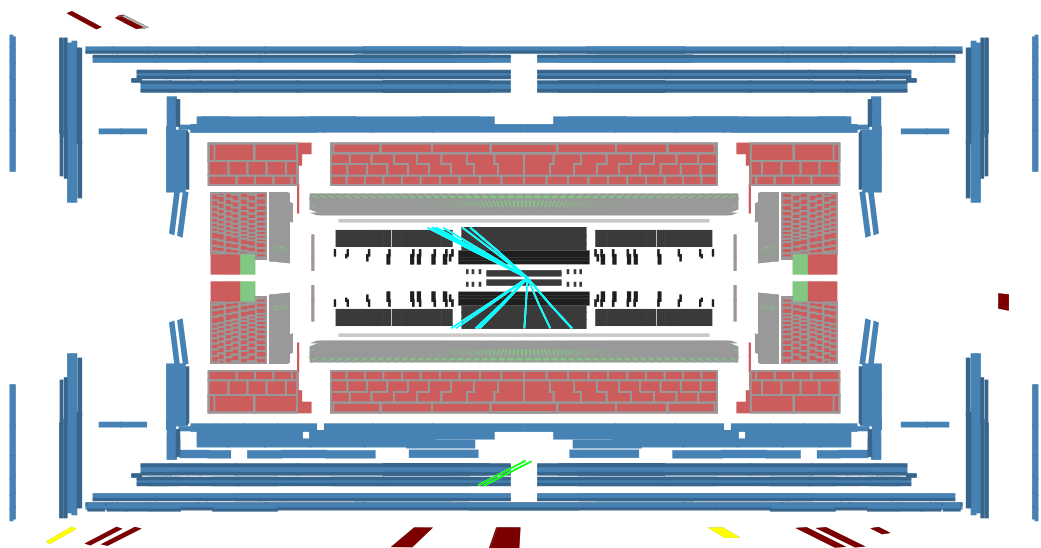
event and the same detector components in the  $y - z$ -profile. Most of the activity of the event is found in the barrel part of the detector, while only one jet is emitted in the forward direction.

### 6.1.2 Datasets and Monte Carlo simulations

In this thesis various datasets simulating the response of the ATLAS detector for the supersymmetric signal and all relevant Standard Model background processes, as listed in Tab. A.1, are used. Since the GMSB signal under study has a complex final state including high multiplicities of several particle types, such as jets, photons and leptons, as well as high missing transverse energy, a wide range of Standard Model processes can potentially be misidentified as a GMSB event and thus have to be investigated. Therefore, the samples used range from pure jet production to  $t\bar{t}$  production and gauge boson production with additional jets and photons. In addition, direct photon production and di-boson production are investigated. As indicated in the table, the events have been generated with ALPGEN, HERWIG or PYTHIA. The corresponding datasets have been produced within the standard central ATLAS production



(a)



(b)

Figure 6.5: Schematic view of a typical GMSB event with prompt photons in the (a)  $x - y$ -profile and (b)  $y - z$ -profile of the ATLAS detector.

procedure and are widely used in the ATLAS SUSY working group [18].<sup>3)</sup>

As described in Sect. 4.1, the supersymmetric mass spectrum is calculated using ISASUGRA, while HERWIG/JIMMY is used for the sparticle cascade decays, parton showers, hadronization and the simulation of the underlying event. For the generation of events with a non-zero lifetime of the  $\tilde{\chi}_1^0$ , as in the GMSB3 scenario, the lifetime threshold above which the particles are not decayed, was set to  $3.3 \times 10^{-11}$  s in HERWIG similar to the default ATLAS configuration<sup>4)</sup>. In the detector simulation the ATLAS interface for GEANT4 was used to define the properties of the long-lived particles, such as the decay length of the lightest neutralino  $\tilde{\chi}_1^0$ .

## 6.2 Discovery potential in the prompt photon scenario

The discovery potential of ATLAS for GMSB models with prompt photons in the di-photon channel is investigated in this section. Characteristic features, such as multiple jets, high missing transverse energy and high energetic photons will be used to separate the signal events from the Standard Model background. The first step is to investigate the possible trigger strategies to select the signal events on trigger level. This mainly aims at a high signal efficiency, rather than at a high background rejection power. Once a data stream coming from the trigger system is recorded, the second step is to optimize the selection criteria in order to separate the signal events from the Standard Model background with high signal efficiency and high background rejection power simultaneously. For this purpose, a signal significance is maximized. Using the selection criteria defined in the study of the fully simulated GMSB1 benchmark scenario, a fast simulation scan can be performed to estimate the overall discovery potential of ATLAS for GMSB1-like scenarios.

### 6.2.1 Signal trigger strategy

The generic features of supersymmetric events, such as multiple high energetic jets and large missing transverse energy can be used to trigger GMSB events. Additionally, the final state photons coming from the  $\tilde{\chi}_1^0$  decay provide a good possibility for the online selection.

As discussed in Sect. 3.1, the LHC will be run in different luminosity phases. The first phase will start at around  $\mathcal{L} = 10^{31} \text{ cm}^{-2} \text{ s}^{-1}$  and later the luminosity will be increased stepwise to  $\mathcal{L} = 10^{33} \text{ cm}^{-2} \text{ s}^{-1}$  and  $\mathcal{L} = 10^{34} \text{ cm}^{-2} \text{ s}^{-1}$ . Depending on the luminosity the event rate will be different and therefore also selections based on different trigger menus are foreseen:<sup>5)</sup>

- The menu for initial data taking will be solely based on the L1 selection, since the rates are low enough to allow for a transparent mode of the HLT. The entire trigger menu is subdivided into several groups of trigger items that are interesting for different physics analyses or performance analyses. For the study of GMSB events only the triggers for electromagnetic clusters, as described in Sect. 5.1.1, and for jets and missing transverse energy are relevant. The several trigger items can in principle also be combined in an analysis and thus a variety of possibilities for a GMSB trigger is available. Figure 6.6 shows the trigger efficiencies of various L1 trigger items for the GMSB1 scenario. Here and in the following, the trigger efficiency is defined as the ratio of the number of events without any preselection cuts passing a certain trigger requirement divided by the total number of simulated events. The nomenclature of the trigger items is such that the first

<sup>3)</sup>Cuts on generator level have been applied during the production of the background samples. This allows for a faster simulation of the most relevant background processes, since events with *e.g.* very low  $E_T^{\text{miss}}$  are rejected in any case. For details see Tab. A.2.

<sup>4)</sup>This value is set in order not to decay  $K^0$  and  $\Lambda$  particles at the generator level, such that they can interact with the detector material before they decay. Therefore, removing or changing the cut is not allowed.

<sup>5)</sup>These menus can currently change on a day-by-day basis and therefore no actual trigger menus can be presented here.

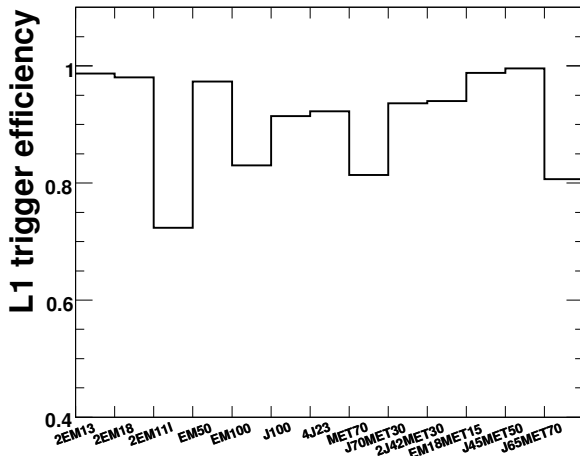


Figure 6.6: L1 efficiency of various possible trigger items, as described in the text, for the selection of the GMSB1 signal in the low luminosity running phase of the LHC.

Trigger item	Efficiency [%]	Trigger item	Efficiency [%]
2EM13	$98.71 \pm 0.11$	MET70	$81.39 \pm 0.39$
EM100	$83.00 \pm 0.38$	J70+MET30	$93.64 \pm 0.25$
EM18+MET15	$98.79 \pm 0.12$	2J42+MET30	$93.98 \pm 0.24$
J100	$91.43 \pm 0.28$	4J23	$92.27 \pm 0.27$

Table 6.3: Trigger efficiencies and statistical uncertainties for some interesting trigger items for the GMSB1 scenario for the low luminosity running phase of the LHC.

number gives the multiplicity of the trigger object, the second part of the name gives the type of the trigger object, *e.g.* “EM” for “electromagnetic”, “J” for “jet” and “MET” for “ $E_T^{\text{miss}}$ ”, and the second number gives the energy threshold. An additional “I” at the end of the name indicates the application of an isolation criterion. The combined trigger items, such as “J70MET30”, are combined with a logical AND. It can be observed that there is a variety of possibilities to trigger events of the GMSB1 scenario in the low luminosity running phase of the LHC. Table 6.3 summarizes the total efficiencies of some of the interesting trigger items for GMSB1 with the corresponding statistical uncertainties, that come from the limited statistics used in the simulation.

- The menu for the stable running phase with a luminosity of  $\mathcal{L} = 10^{33} \text{ cm}^{-2} \text{ s}^{-1}$  will include the decisions of all three available trigger levels in the selection. Only the trigger items without a prescale factor<sup>6)</sup> are interesting for the study of GMSB events, since a maximal signal selection efficiency is required to collect as much data as possible. Again, a variety of possibilities to trigger GMSB events exists based on electromagnetic, jet or  $E_T^{\text{miss}}$  trigger items. The L1, L2 and EF efficiencies of four interesting possibilities are listed in Tab. 6.4, where the L2 and EF efficiencies also include the efficiencies of the previous levels. These are a single photon trigger (photons are denoted with a “g” in the name of the trigger item) for high energetic photons with  $p_T > 55 \text{ GeV}$ ,

<sup>6)</sup>Trigger items can be *prescaled*, which means that not every selected event will be recorded due to the limited output rate of the trigger system. If *e.g.* minimum bias events are studied, not every single event can be written to permanent storage due to the large cross section. Instead only every  $n$ th event will be recorded, where  $n$  is the configurable prescale factor.

Trigger item	L1	L1+L2	L1+L2+EF
g55	$97.18 \pm 0.60$	$84.47 \pm 1.32$	$80.47 \pm 1.44$
2g17i	$71.13 \pm 1.65$	$55.07 \pm 1.81$	$47.91 \pm 1.81$
j65+xE70	$80.66 \pm 0.40$	$80.63 \pm 0.40$	$69.53 \pm 0.46$
3j65	$83.63 \pm 0.37$	$83.55 \pm 0.37$	$83.37 \pm 0.37$

Table 6.4: Trigger efficiencies and statistical uncertainties for some interesting trigger items for the GMSB1 scenario for the  $\mathcal{L} = 10^{33} \text{ cm}^{-2} \text{ s}^{-1}$  running phase of the LHC.

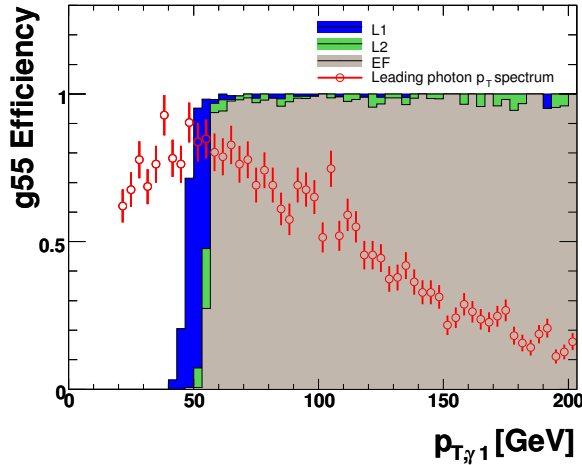


Figure 6.7: L1 (blue), L2 (green) and EF (gray) efficiencies of the g55 trigger for the GMSB1 scenario as a function of the reconstructed  $p_T$  of the leading photon. The  $p_T$  distribution of the leading photon with  $p_T > 20 \text{ GeV}$  and  $| \eta | \leq 1.37$ ,  $1.52 < | \eta | < 2.5$  is also shown.

an isolated di-photon trigger with a threshold of  $p_T > 17 \text{ GeV}$  that could also be combined with the single photon trigger, a combined jet (“j”) plus missing transverse energy (“xE”) trigger and a multijet trigger with a threshold of  $p_T > 65 \text{ GeV}$ , which will become especially interesting in the analysis of the non-pointing photon scenario in Sect. 6.3. It can be observed that for both of the planned running phases the photon triggers as well as the  $E_T^{\text{miss}}$  and jet triggers provide possibilities to trigger efficiently on GMSB1 events. The efficiencies of the g55 photon trigger after the L1, L2 and the EF selections as a function of the reconstructed  $p_T$  of the leading photon are shown in Fig. 6.7 for the GMSB1 scenario. As expected, after a steep turn on around  $60 \text{ GeV}$  a plateau is reached. The integrated EF efficiency after the threshold of  $60 \text{ GeV}$  is  $\sim 98\%$ . Additionally, the distribution of the reconstructed transverse momentum of the photons is illustrated. Since the selection criteria, as described in Sect. 5.1.1, are refined from level to level, the efficiency drops slightly, but remains very high in the region above  $60 \text{ GeV}$ . The trigger menu for the stable running phase is used for the signal selection as discussed in the following.

- A trigger menu for the  $\mathcal{L} = 10^{34} \text{ cm}^{-2} \text{ s}^{-1}$  running phase does not yet exist and will be constructed based on the trigger operating experiences of the other phases.

In summary the use of photon triggers is possible for initial running conditions as well as at higher luminosity. The efficiencies are as high as for the triggers based on jets and  $E_T^{\text{miss}}$  and can therefore provide good redundancy.

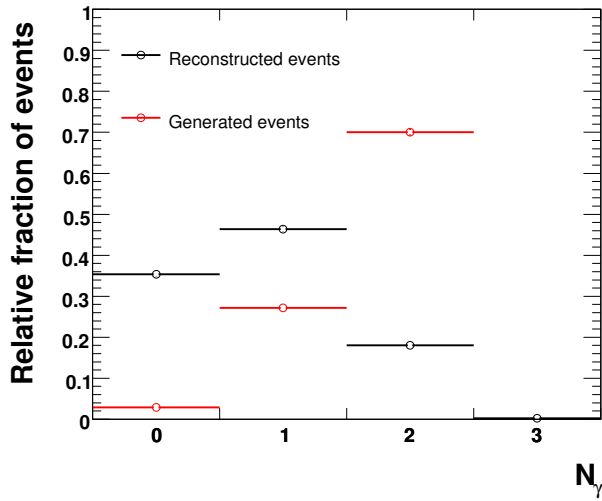


Figure 6.8: Distributions of the relative fraction of events with a given number of photons with  $p_T > 20 \text{ GeV}$  and  $|\eta| \leq 1.37$ ,  $1.52 < |\eta| < 2.5$  in the final state for the GMSB1 scenario for events on generator level (red) and for the reconstructed events (black).

### 6.2.2 Properties of the reconstructed signal events

In the GMSB1 scenario 46.5% (18.5%) of the signal events have one (two) reconstructed photons with  $p_T > 20 \text{ GeV}$  in the fiducial acceptance region  $|\eta| < 2.5$  used for photon identification. Photons that are found in the region where the barrel and the endcap calorimeters overlap, *i.e.*  $1.37 < |\eta| \leq 1.52$ , are excluded. Figure 6.8 shows the distribution of the relative fraction of events with a given number of final state photons with  $p_T > 20 \text{ GeV}$  and  $|\eta| \leq 1.37$ ,  $1.52 < |\eta| < 2.5$  on generator level as well as after the simulation and identification process without any preselection cuts.<sup>7)</sup> It can be observed that there are events that contain more than two identified high energetic photons. These can be bremsstrahlung or more likely misidentified electrons, where the track has not been reconstructed, or pions that decay to two photons and where the substructure of the shower could not be used for the rejection (see Sect. 5.1.3). The fraction of fake photons in the set of all reconstructed photons can be estimated by matching all reconstructed photons to a generated photon, pion or electron within a cone of  $\Delta R < 0.1$ . About 94% of the reconstructed photons come from photons from neutralino decays, while about 5% come from pion decays and a little fraction of less than 1% comes from misidentified electrons.

The jets initiated by the squark and gluino decays as shown in Figs. 6.3(a) and 6.3(b) are very high energetic due to the large mass difference of about 700 GeV (500 GeV) between the squarks (gluinos) and the gauginos (see Fig. 6.1). As discussed above, multiple jets can be present in the event depending on the decay chain. The distribution of the relative fraction of events with a given number of reconstructed jets with  $p_T > 10 \text{ GeV}$  and  $|\eta| \leq 1.37$ ,  $1.52 < |\eta| < 2.5$  for  $1 \text{ fb}^{-1}$  is shown in Fig. 6.9(a). The average jet multiplicity is high, since in addition to the squark and gluino decays also  $W^\pm$  decays and initial state radiation can produce jets. About 90% of the events have at least four jets in the final state in the fiducial acceptance region. This feature is used to reject Standard Model background events with low jet multiplicity.

The distribution of the transverse momentum of the leading jet is shown in Fig. 6.9(b). It can be observed that two different contributions are present. Due to the large mass difference to the daughter

<sup>7)</sup>The number of available signal MC events is 10 000 corresponding to an integrated luminosity of  $1282.05 \text{ pb}^{-1}$ .

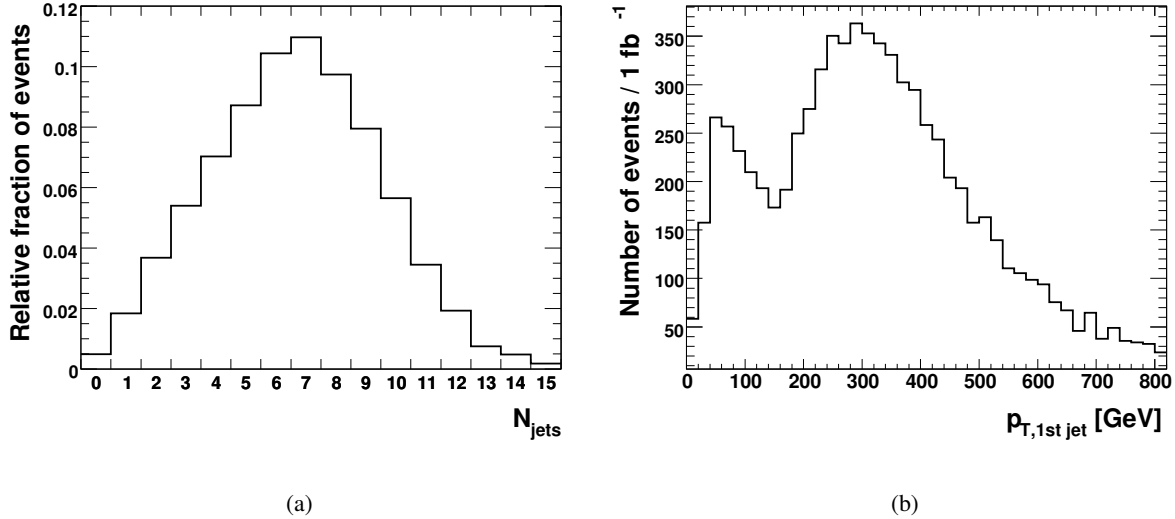


Figure 6.9: Distribution of (a) the relative fraction of events with a given number of reconstructed jets and (b) the transverse momentum of the leading jet for the GMSB1 scenario with  $p_T > 10 \text{ GeV}$  and  $|\eta| \leq 1.37$ ,  $1.52 < |\eta| < 2.5$  for  $1 \text{ fb}^{-1}$ .

particles, very high energetic jets originate from a squark or gluino decay. The jets in the lower transverse momentum region arise from gaugino pair production events, where charginos decay to  $W^\pm$  bosons that lead to final state jets.

In the GMSB1 scenario the decay chains of the two initial supersymmetric particles always lead to two gravitinos in the final state that escape detection. Depending on the transverse momentum and the relative orientation between the two gravitinos this leads to a significant amount of missing transverse energy  $E_T^{\text{miss}}$ . Additional neutrinos in the decay chain originating either from sneutrino decays or Standard Model  $W^\pm$  decays as well as fake  $E_T^{\text{miss}}$  as discussed in Sect. 5.4.2 also contribute to the total amount of  $E_T^{\text{miss}}$ . The distribution of the transverse momentum of the leading gravitino as taken from the generator information for the GMSB1 scenario is shown in Fig. 6.10(a) leading to the distribution of the reconstructed  $E_T^{\text{miss}}$  as shown in Fig. 6.10(b).  $E_T^{\text{miss}}$  is a very important variable for the rejection of all kinds of Standard Model background in many analyses of supersymmetric models at the LHC [18] and is also used in this analysis of the GMSB1 scenario to strongly suppress the multijet QCD background.

### 6.2.3 Signal selection

As shown in Sect. 6.2.1, events of the GMSB1 scenario can be selected online efficiently by using photon triggers. The combination of the single photon trigger “g55” and the di-photon trigger “2g17i” from the trigger menu of the stable running phase reaches a combined efficiency of about 85%. Figure 6.11(a) shows the distribution of  $E_T^{\text{miss}}$  for the signal and the Standard Model background after the application of the trigger requirement for  $1 \text{ fb}^{-1}$ . It can clearly be observed that for low values of  $E_T^{\text{miss}}$  the QCD multijet background dominates.<sup>8)</sup> For large values of  $E_T^{\text{miss}}$  the GMSB signal distribution decreases much slower than the Standard Model background distributions. In order to further separate the signal from the Standard Model background the following preselection cuts have been applied:

1. Missing transverse energy  $E_T^{\text{miss}} > 60 \text{ GeV}$ .

<sup>8)</sup>It should be noted that the distribution for the  $W^\pm$  background is unrealistic for  $E_T^{\text{miss}} < 50 \text{ GeV}$  due to the generator precut (see Tab. A.2).

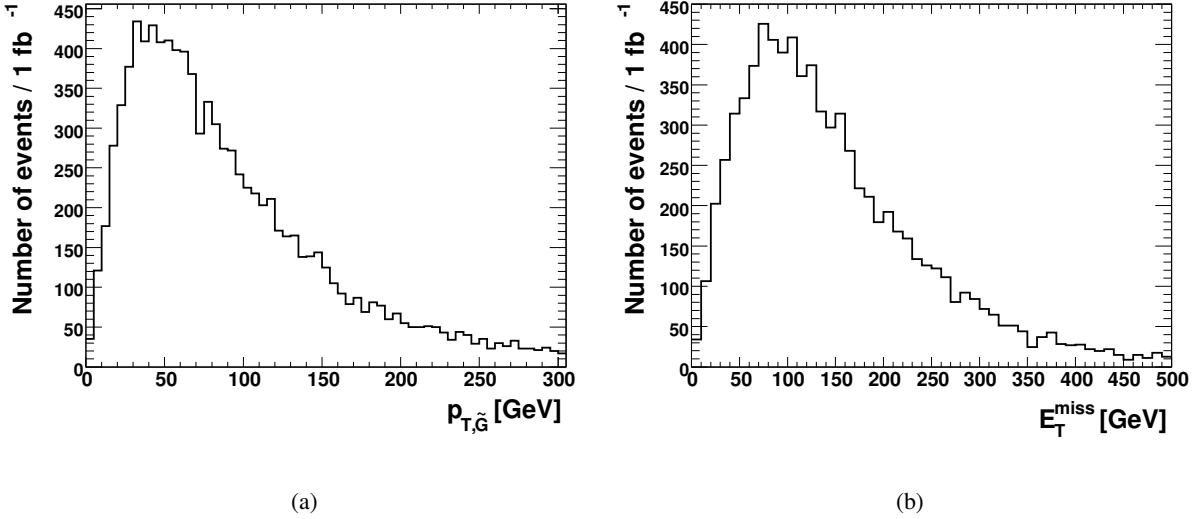


Figure 6.10: Distribution of (a) the transverse momentum of the leading gravitino (taken from the generator information) and (b) the reconstructed missing transverse energy for the GMSB1 scenario for  $1 \text{ fb}^{-1}$ .

2. At least four jets are found with transverse momentum  $p_T > 50 \text{ GeV}$  ( $p_T > 100 \text{ GeV}$  for the leading jet).

Figure 6.11(b) shows the distributions of the number of jets with  $p_T > 10 \text{ GeV}$  and  $| \eta | \leq 1.37, 1.52 < | \eta | < 2.5$  after the application of the cut on  $E_T^{\text{miss}}$  for the GMSB1 signal and the Standard Model background for  $1 \text{ fb}^{-1}$ . It can be observed that the cut on the number of jets is very efficient in reducing all sources of background. Additionally, a cut on the momentum of the jets is imposed, since large jet momenta are expected due to the large mass differences between the squarks and gauginos, see Fig. 6.9(b).

After these precuts 4809 background events remain, while 3813 signal events are selected for  $1 \text{ fb}^{-1}$ . However, due to the large jet cross section at the LHC, QCD multiple jet events, as well as other background processes, remain that have large values of  $E_T^{\text{miss}}$  due to poorly measured jets. Therefore, a third cut is applied in the preselection:

3. The angle  $|\Delta\phi|$  between  $E_T^{\text{miss}}$  and the first, second and third jet must be larger than 0.2 in order to reduce the background from poorly measured jets.

Fig. 6.12(a) shows the  $\Delta\phi(E_T^{\text{miss}}, 1\text{st jet})$  distribution after the first and second cut for the GMSB1 signal and the remaining Standard Model background events for  $1 \text{ fb}^{-1}$ . It can be observed that this cut further rejects QCD multijet background. After all preselection cuts 3216 signal events and 2894 background events remain for  $1 \text{ fb}^{-1}$ . However, as shown in Fig. 6.12(b) a cut on the number of reconstructed photons with  $p_T > 20 \text{ GeV}$  and  $| \eta | \leq 1.37, 1.52 < | \eta | < 2.5$  provides an efficient way to efficiently suppress the background.

Table 6.5 shows the numbers of selected signal and background events for different cut values on  $E_T^{\text{miss}}$  and the number of photons including the preselection cuts and the trigger requirement (g55 OR 2g17i). To define a final set of cuts a signal significance has been defined as

$$\sigma_{\text{GMSB1}} = \# \text{Signal events} / \sqrt{\# \text{BG events}}. \quad (6.2)$$

The set of cuts is optimal, when the significance reaches its maximum. Additionally, the statistical and systematic uncertainties are given. The former are given by the statistics of the Monte Carlo samples

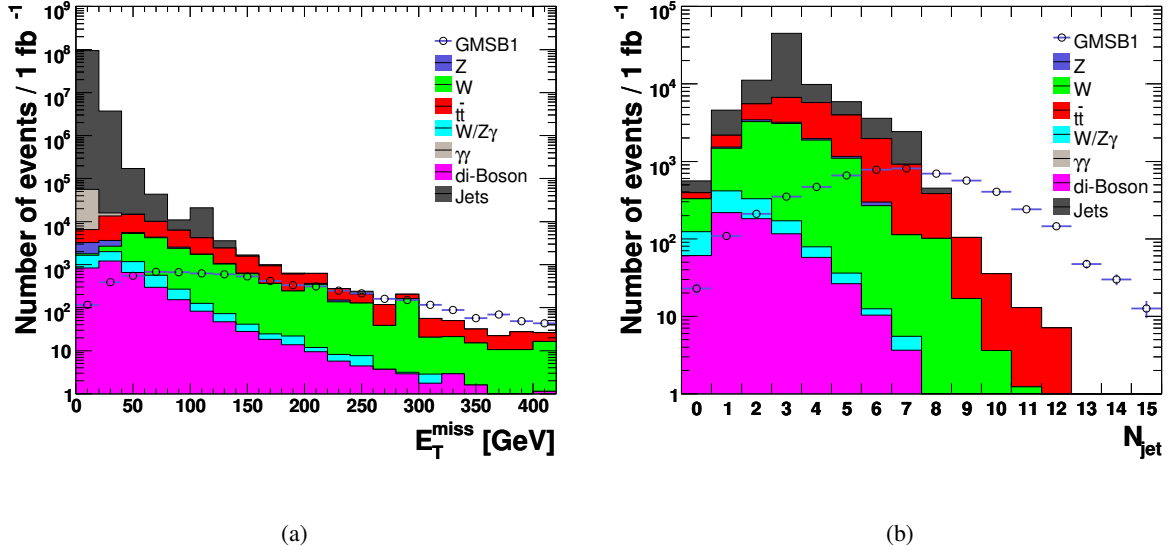


Figure 6.11: Distribution of (a) the reconstructed  $E_T^{\text{miss}}$  after the photon trigger selection and (b) of the number of jets with  $p_T > 10 \text{ GeV}$  and  $|\eta| \leq 1.37$ ,  $1.52 < |\eta| < 2.5$  after the cut on  $E_T^{\text{miss}}$  for the GMSB1 signal (open symbols) and the Standard Model background (histograms) for  $1 \text{ fb}^{-1}$ .

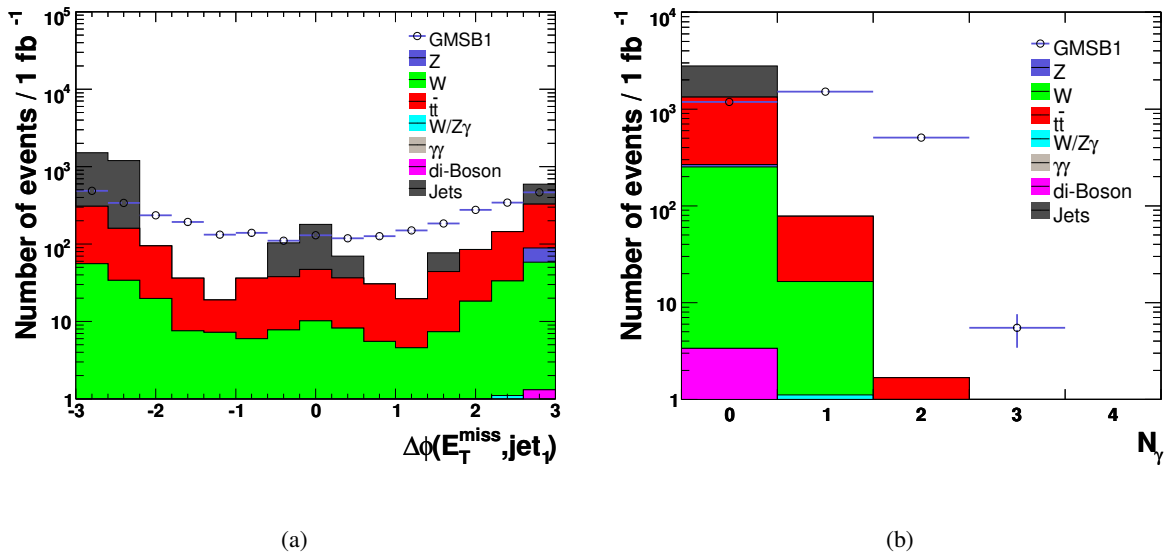


Figure 6.12: Distribution of (a) the angle  $\Delta\phi$  between  $E_T^{\text{miss}}$  and the leading jet after the first and second preselection cut and (b) of the number of reconstructed final state photons with  $p_T > 20 \text{ GeV}$  and  $|\eta| \leq 1.37$ ,  $1.52 < |\eta| < 2.5$  after all preselection cuts for the GMSB1 signal (open symbols) and the Standard Model background (histograms) for  $1 \text{ fb}^{-1}$ .

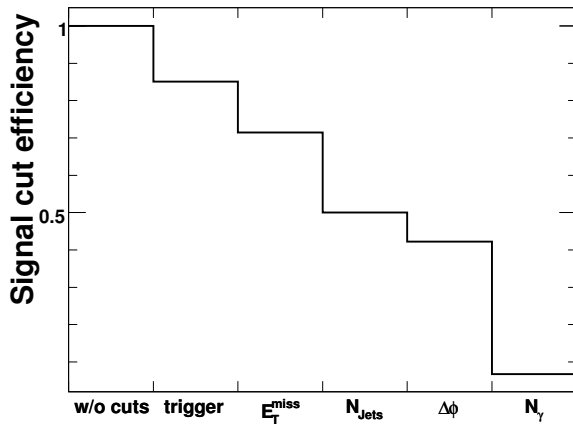


Figure 6.13: Efficiency of the GMSB1 signal selection as a function of the cuts that have been applied sequentially.

$E_T^{\text{miss}} >$	$N_\gamma \geq$	Signal±stat.±syst.	$\Sigma \text{BG} \pm \text{stat.} \pm \text{syst.}$	$\sigma_{\text{GMSB1}}$	QCD	$t\bar{t}$	$W^\pm$	$Z^0$
60 GeV	0	$3216 \pm 50 \pm^{195}_{226}$	$2893 \pm 980 \pm^{711}_{420}$	60	1468	1142	265	15
60 GeV	1	$2030 \pm 40 \pm^{132}_{176}$	$80 \pm 11 \pm^{63}_{24}$	227	0	64	17	0
60 GeV	2	$511 \pm 20 \pm^{33}_{58}$	$2 \pm 2 \pm^0_0$	361	0	2	0	0
70 GeV	0	$3047 \pm 49 \pm^{221}_{223}$	$2456 \pm 977 \pm^{581}_{334}$	61	1269	947	223	15
70 GeV	1	$1922 \pm 39 \pm^{150}_{164}$	$65 \pm 10 \pm^{30}_{26}$	238	0	50	15	0
70 GeV	2	$477 \pm 19 \pm^{44}_{44}$	$2 \pm 2 \pm^0_2$	337	0	2	0	0

Table 6.5: Number of selected signal and background events for  $1 \text{ fb}^{-1}$  after the preselection for different cuts on  $E_T^{\text{miss}}$  and the number of photons. The statistical and systematic uncertainties are given as well as the signal significance  $\sigma_{\text{GMSB1}}$ . The numbers of selected QCD multijet,  $t\bar{t}$ ,  $W^\pm$  and  $Z^0$  events are also listed.

used in the study<sup>9)</sup>, while the latter are obtained by varying the jet energy scale and the electromagnetic energy scale. The systematic uncertainties on the energy scales are assumed to be 5% and 0.5%, respectively [18]. The systematic uncertainty is completely dominated by the jet energy scale, since it strongly affects the measured value of  $E_T^{\text{miss}}$  due to the numerous jets in the events. The effect of the electromagnetic energy scale uncertainty on the number of selected events is negligible.

It turns out that an optimal event selection for the GMSB1 scenario is given by the above defined preselection cuts plus an additional requirement on the minimal number of final state photons:

4.  $N_\gamma \geq 2$ ,

where the signal significance is largest,  $\sigma_{\text{GMSB1}} = 361$ . After requiring at least two photons in the final state the signal (511 events) is almost background free (two remaining  $t\bar{t}$  events) and cutting harder on  $E_T^{\text{miss}}$  just reduces the number of selected signal events. In event selections optimized for mSUGRA scenarios (and other supersymmetric scenarios without photons in the final state) the cut on  $E_T^{\text{miss}}$  is typically harder and additional selection criteria such as a minimal number of leptons or OSSF lepton

<sup>9)</sup>Due to the large event weights of the QCD jet samples, the statistical uncertainty on the number of selected background events is large, when the fraction of QCD jet events is large.

pairs have to be chosen [18]. Due to the presence of decay chains shown in Fig. 6.3(b), OSSF lepton pairs can also be present in the GMSB1 scenario, but this decay chain is only exclusively selected for the measurements of endpoints in invariant mass spectra as discussed in the next chapter. Figure 6.13 shows the efficiency for selecting the GMSB1 signal events as a function of the final selection cuts. It can be observed that the preselection cuts are quite efficient in selecting the signal events, while the cut on the number of photons reduces the signal significantly. However, the signal significance is largest for this cut, since the number of remaining background events drops to almost zero. In summary, it can be concluded that with a simple event selection based on a few variables the GMSB1 signal can be discovered with high significance with  $1 \text{ fb}^{-1}$  of data.

#### 6.2.4 GMSB parameter scan

The selection criteria discussed in the last section have been optimized for a single benchmark point in the GMSB parameter space. For the investigation of the discovery potential of this selection over a wider range of the parameter space, it is necessary to make use of a fast detector simulation to obtain adequate statistics for the signal. As described in Sect. 4.2.2 the fast simulation package ATLFast has been developed, which performs no detailed simulation of particle interactions with the detector material, but instead parametrizes the response.

Before the fast simulation can be used for a parameter scan, it has to be ensured that the results of the fast simulation are reliable. This can be done by comparing the distributions of the variables used for the analysis with the results obtained from the full GEANT4 detector simulation. In case of significant deviations, the fast simulation result has to be corrected. Figure 6.14 shows the distributions of  $E_T^{\text{miss}}$ , the number of reconstructed photons with  $p_T > 20 \text{ GeV}$  and  $|\eta| \leq 1.37$ ,  $1.52 < |\eta| < 2.5$  and the transverse momenta of the first and second leading photon for the GMSB1 scenario. The red histogram shows the result from the full detector simulation, while the black data points show the result from the fast simulation. It can be observed that the distributions of  $E_T^{\text{miss}}$  agree reasonably well to be used in a parameter scan. On the other hand large discrepancies between the distributions of the number of photons and the transverse photon momenta can be observed, since in the fast simulation no reconstruction efficiencies are applied and no particle misidentifications are present. This is corrected by the application of correction factors. In the present analysis this has been done by calculating correction factors in 13 bins of the photon  $p_T$  that are used to randomly reject photons event by event according to the probability given by the correction factor.<sup>10)</sup> The resulting corrected  $p_T$  distributions for the first and second leading photon are shown as green data points in Figs. 6.14(c) and 6.14(d), respectively. The corrected distribution of the number of final state photons is shown in Fig. 6.14(b). After these corrections and the application of the preselection cuts and the requirement of at least two photons in the final state the number of selected events from the fast simulation is 568 agreeing with the full simulation result (511) within the uncertainties, see Tab. 6.5.<sup>11)</sup> After correction the fast simulation is assumed to be reliable to perform the parameter scan.

As shown in Fig. 2.13(b), the type of the NLSP, *i.e.* the discovery potential in the two photon channel, depends on the value of  $\tan\beta$ . Therefore,  $\tan\beta$  has been chosen as one scan parameter. The other parameter that is interesting to investigate is  $\Lambda$ , since the masses of the supersymmetric particles scale linearly with  $\Lambda$ . Hence, the total supersymmetric cross section decreases with  $\Lambda$  and it is expected that this is also true for the discovery potential for these scenarios. On the other hand, no strong dependence of the discovery potential on  $M_{\text{mess}}$  is expected, since the particle masses scale only logarithmically in

<sup>10)</sup>The correction factors are obtained by calculating the relative photon identification efficiency of the GEANT4 simulation and the fast simulation as a function of the transverse photon momentum.

<sup>11)</sup>Since the fast simulation does not include a trigger simulation, the photon trigger decision has been emulated by randomly rejecting events using the trigger efficiencies from Tab. 6.4.

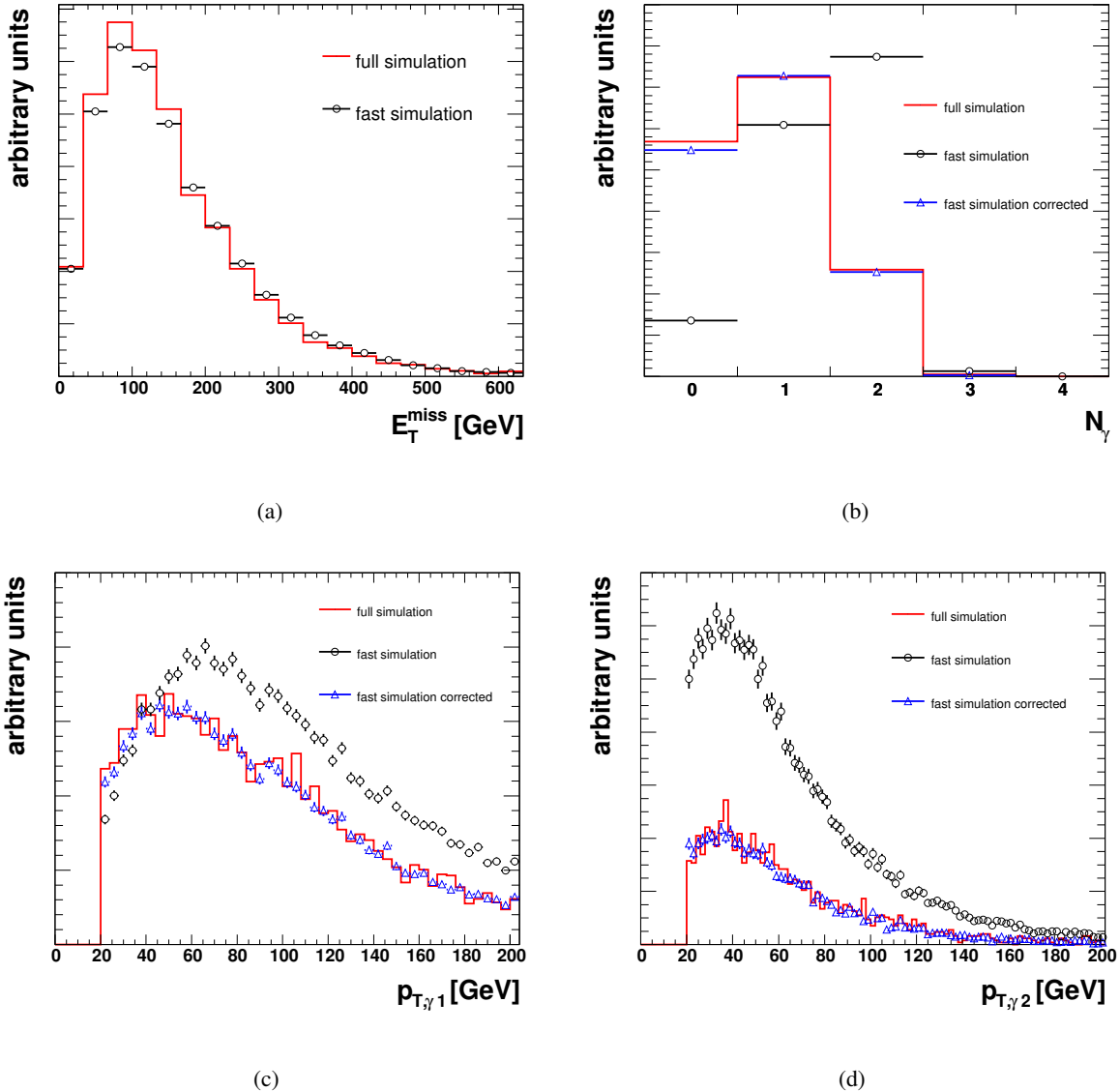


Figure 6.14: Distributions of (a)  $E_T^{\text{miss}}$ , (b) the number of reconstructed photons with  $p_T > 20 \text{ GeV}$  and  $|\eta| \leq 1.37$ ,  $1.52 < |\eta| < 2.5$  and the transverse momenta of the (c) first and (d) second leading photon for the GMSB1 scenario.

$M_{\text{mess}}$ ,  $N_5 = 1$  and  $C_{\text{grav}} = 1$  are also fixed to obtain a scenario with photons in the final state ( $N_5 = 1$ ) that come from the interaction vertex ( $C_{\text{grav}} = 1$ ).<sup>12)</sup>

For the scan  $\Lambda$  has been varied from  $60 \text{ TeV}$  to  $200 \text{ TeV}$  in steps of  $10 \text{ TeV}$ , while  $\tan \beta$  has been varied from  $2$  to  $50$  in steps of  $2$ . The other model parameters are fixed to  $N_5 = 1$ ,  $M_{\text{mess}} = 500 \text{ TeV}$ ,  $\text{sign}(\mu) = +$  and  $C_{\text{grav}} = 1$ , as for the GMSB1 scenario. The scanned region concurs with the region used in Fig. 2.13(b) in which the  $\tilde{\chi}_1^0$  is most often the NLSP. In each point of the parameter space  $12\,500$  events have been generated and passed through the fast simulation. The event selection as described in the last section has been applied to each signal sample. Figure 6.15 shows the contour lines with ten signal events for different integrated luminosities.<sup>13)</sup> It can be seen that for large values of  $\tan \beta$

<sup>12)</sup>The simulation of non-pointing photons is not possible with ATLFast.

<sup>13)</sup>The criterion of 10 signal events for a discovery has been chosen arbitrarily, but corresponds to  $\sigma_{\text{GMSB1}} \approx 7$  given the definition of a significance as discussed in Sect. 6.2.3 under the assumption of two remaining background events. For integrated

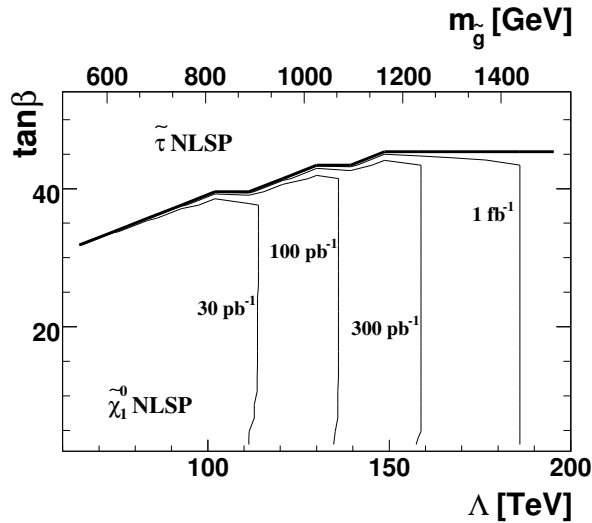


Figure 6.15: Discovery potential in the  $\Lambda$  –  $\tan\beta$  plane for  $N_5 = 1$ ,  $M_{\text{mess}} = 500 \text{ TeV}$ ,  $\text{sign}(\mu) = +$  and  $C_{\text{grav}} = 1$ . The contour lines with ten signal events are shown for different integrated luminosities.

no discovery can be made with the selection based on hard photons, since the  $\tilde{\tau}_1$  is the NLSP and no photons are expected in the final state<sup>14)</sup>. However, in the region where the  $\tilde{\chi}_1^0$  is the NLSP, already with  $300 \text{ pb}^{-1}$  the region up to  $\Lambda \approx 160 \text{ TeV}$  can be covered corresponding to squark masses of  $m_{\tilde{q}} \approx 1.7 \text{ TeV}$  and gluino masses of  $m_{\tilde{g}} \approx 1.3 \text{ TeV}$ . In general, the discovery potential for GMSB with prompt photons is large in the scanned regions of the parameter space. This result gives confidence that an early discovery of GMSB1-like scenarios is possible with the ATLAS detector.

### 6.3 Discovery potential in the non-pointing photon scenario

The discovery potential of ATLAS for GMSB models with non-pointing photons is investigated in this section. In general, the same features, such as large  $E_T^{\text{miss}}$  and multiple jets, as in the event selection for the GMSB1 scenario, can be used for the background rejection. Additionally, the non-vanishing lifetime of the neutralino can be exploited.

The first step is to define a trigger strategy to select the events on trigger level. The second step is the optimization of criteria to efficiently select the signal events and reject the Standard Model background in the offline data analysis. The GMSB3 scenario as discussed in Sect. 6.1.1 is used as the benchmark scenario.

#### 6.3.1 Signal trigger strategy

Since the only difference between the GMSB1 and the GMSB3 scenario is the neutralino lifetime, the same features as discussed in Sect. 6.2 can in principle be used for triggering on GMSB3 events. Especially the trigger items shown in Tab. 6.4 are interesting for this purpose. Table 6.6 shows the efficiencies of these trigger items for the GMSB3 scenario for the  $\mathcal{L} = 10^{33} \text{ cm}^{-2} \text{ s}^{-1}$  running phase of the LHC and it can be observed that the triggers based on  $E_T^{\text{miss}}$  and jets are as efficient as in the prompt photon

<sup>14)</sup>The discovery potential for final states including  $\tau$  leptons in the GMSB model is discussed in [120].

Trigger item	L1	L1+L2	L1+L2+EF
g55	$90.19 \pm 1.08$	$46.04 \pm 1.81$	$36.88 \pm 1.75$
2g17i	$34.13 \pm 1.72$	$17.77 \pm 1.39$	$12.87 \pm 1.22$
j65+xE70	$80.38 \pm 0.56$	$80.24 \pm 0.56$	$71.18 \pm 0.64$
3j65	$79.80 \pm 0.57$	$79.66 \pm 0.57$	$79.62 \pm 0.57$

Table 6.6: Trigger efficiencies and statistical uncertainties for some interesting trigger items for the GMSB3 scenario for the  $\mathcal{L} = 10^{33} \text{ cm}^{-2} \text{ s}^{-1}$  running phase of the LHC.

case.<sup>15)</sup> On the other hand, a large deviation can be observed for the triggers based on photon selections (g55 and 2g17i). The efficiency loss for the g55 trigger on L1 arises from the number of photons which are produced within the fiducial region of the detector. The larger the NLSP lifetime is, the larger is the number of NLSPs that will decay outside the inner detector and the resulting photons cannot be measured. This effect is even more pronounced for the 2g17i trigger, which is optimized for the production of two photons within the inner detector volume. On L2 and EF level cuts are imposed on the shape of the electromagnetic shower, as discussed in Sect. 5.1.1. Since photons that appear at a certain distance from the primary interaction vertex have a wider shower shape than prompt photons, an additional loss in efficiency is present (see Fig. 5.9 and the corresponding discussion).

Since one cannot assume that the online selection of photons will change before a positive signal for non-pointing photons appears, the signal will be selected using a trigger based on the requirement of multiple hard jets (“3j65”) in this analysis. The transverse energy threshold for the jets is chosen such that on the one hand the trigger rate remains low enough to have no prescale factor and on the other hand the selection efficiency is as high as possible. A threshold of 65 GeV is used in the following to select the GMSB3 signal on trigger level.

### 6.3.2 Signal selection

For the final selection of the events in the GMSB3 scenario again the same features as in the GMSB1 scenario can be used. Again, large  $E_T^{\text{miss}}$  and multiple high energetic jets are expected in the final state. On the other hand, Fig. 6.16 shows that the distribution of the relative fraction of events with a given number of final state photons with  $p_T > 20 \text{ GeV}$  and  $|\eta| \leq 1.37$ ,  $1.52 < |\eta| < 2.5$  is different due to the reduced identification efficiency for non-pointing photons. The red data points show the distribution taken from the generator information, while the blue and black data points show the distribution for the standard and unbiased (see Sect. 5.3) photon identification, respectively. It can be observed that the total number of reconstructed photons is reduced compared to the GMSB1 scenario (see Fig. 6.8) and it is expected that the requirement of at least two photons in the final state is inefficient in this case. The following preselection cuts are imposed:

1. The missing transverse energy  $E_T^{\text{miss}}$  must be larger than 60 GeV.
2. At least three jets with  $p_T > 65 \text{ GeV}$  and  $|\eta| < 2.5$  (due to the jet trigger requirement) and a fourth jet with  $p_T > 10 \text{ GeV}$  must be found.
3. The angle  $|\Delta\phi|$  between  $E_T^{\text{miss}}$  and the first, second and third jet must be larger than 0.2.
4. At least one photon using the unbiased selection must be present with  $p_T > 20 \text{ GeV}$  and  $|\eta| \leq 1.37$ ,  $1.52 < |\eta| < 2.5$ . Since the photon identification efficiency is lower than in the prompt photon case

<sup>15)</sup>The slight drop of the efficiency of the 3j65 trigger is due to the non-vanishing  $\tilde{\chi}_1^0$  lifetime. Some fraction of the neutralinos decay outside the inner detector volume and no photons can be measured. Since photons can also be recognized by the jet triggers, this leads to a decreased efficiency.

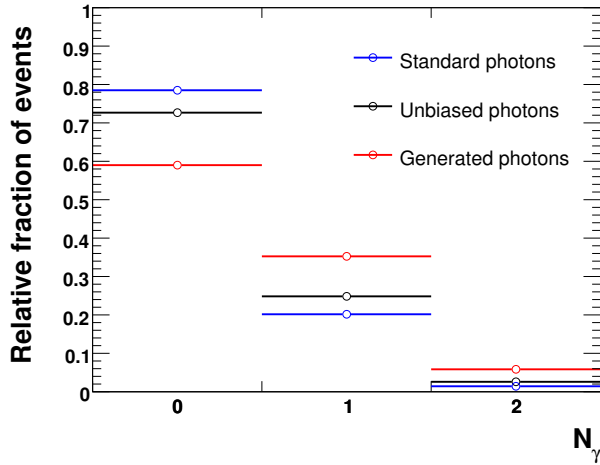


Figure 6.16: Distributions of the relative fraction of events with a given number of photons with  $p_T > 20 \text{ GeV}$  and  $|\eta| \leq 1.37$ ,  $1.52 < |\eta| < 2.5$  in the final state for the GMSB3 scenario for the generator events (red) and for the reconstructed events for the standard (blue) and unbiased (black) photon identification.

and some fraction of the neutralinos decay outside the detector, the required multiplicity compared to Sect. 6.2.3 is reduced.

As in the case of the GMSB1 scenario the first and second cut greatly reduce the Standard Model background, while the third cut serves as a good handle to reject QCD multijet background that leads to fake  $E_T^{\text{miss}}$ . The cut on the number of photons further reduces the Standard Model background and after this preselection 1441 events of the GMSB3 signal sample and 606 background events remain for  $1 \text{ fb}^{-1}$ . The Standard Model background is mainly dominated by  $t\bar{t}$  and  $W^\pm \rightarrow e^\pm \nu$  events, where real  $E_T^{\text{miss}}$  is present due to the neutrinos in the final state and electrons are misidentified as photons.

The special kinematics of non-pointing photons offers additional opportunities to discriminate the signal photons from the background using the measurement of the clustertime  $\tau_{\text{cluster}}$ , as discussed in Sect. 5.3.2. The distribution of the reconstructed clustertime of the leading photon with  $p_T > 20 \text{ GeV}$  and  $|\eta| \leq 1.37$ ,  $1.52 < |\eta| < 2.5$  for the GMSB3 signal is shown in Fig. 6.17(a) without any event selection cuts for  $1 \text{ fb}^{-1}$ . It can be seen that a delayed clustertime is indeed expected for the GMSB3 signal. The clustertime distribution for the signal and the Standard Model background after the preselection cuts is shown in Fig. 6.17(b) for  $1 \text{ fb}^{-1}$ . The background distribution has a Gaussian shape around  $\tau_{\text{cluster}} = 0$ , as expected. The total resolution is around 200 ps agreeing with the expectation of a value larger than 100 ps including an energy dependent term, as discussed in Sect 5.3.2. This result is exploited for the separation of the signal from the background by the following cut, which is applied in the final event selection:

5. At least one identified photon must be found with a measured clustertime larger than 0.6 ns.

Fig. 6.18(a) shows the signal significance  $\sigma_{\text{GMSB3}}$  as a function of the clustertime threshold used in the final cut.<sup>16)</sup> As can be observed, the maximum is reached for  $\tau_{\text{cluster}} > 0.6 \text{ ns}$ . Figure 6.18(b) shows the efficiency for selecting the GMSB3 signal events as a function of the final selection cuts. It can be

<sup>16)</sup>It is assumed that for  $\tau_{\text{cluster}} > 0.6 \text{ ns}$  at least two background events remain, since any calculation of a significance is doubtful for zero background events.

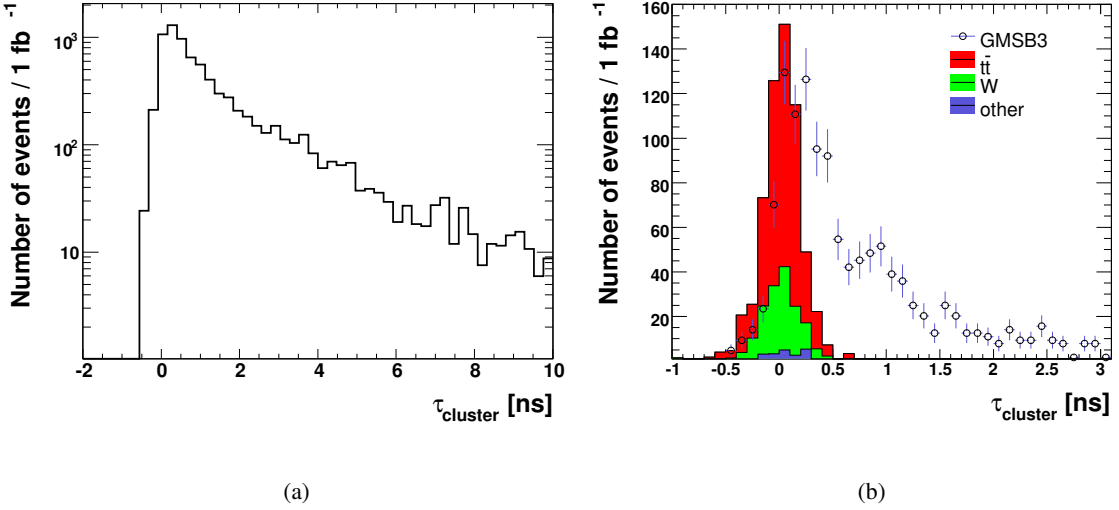


Figure 6.17: Distribution of the clustertime of the leading photon (a) for the GMSB3 scenario without any selection cuts for photons with  $p_T > 20 \text{ GeV}$  and  $|\eta| \leq 1.37$ ,  $1.52 < |\eta| < 2.5$  and (b) for the GMSB3 scenario (open symbols) and the Standard Model background (histograms) after the preselection for  $1 \text{ fb}^{-1}$ .

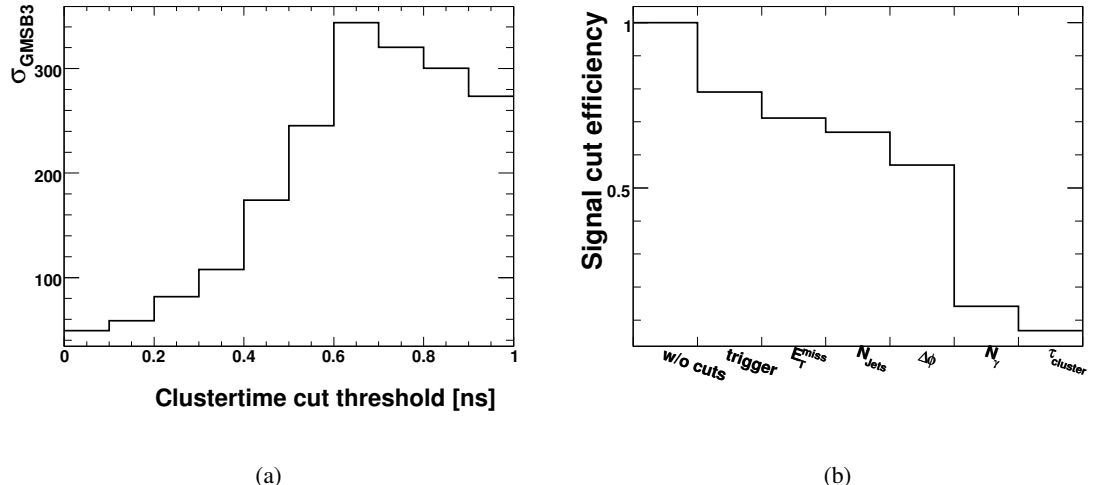


Figure 6.18: (a) Dependence of the signal significance  $\sigma_{\text{GMSB3}}$  on the clustertime threshold used in the final cut for  $1 \text{ fb}^{-1}$ . (b) Efficiency of the GMSB3 signal selection as a function of the cuts.

observed that the preselection cuts without the requirement of at least one photon in the final state are efficient in selecting the signal events (as is the case for the GMSB1 scenario), while the cuts on the number of photons and the measured clustertime reduce the signal significantly. However, the signal significance is largest for these cuts, since the number of remaining background events again drops to almost zero. With the final selection cuts the GMSB3 signal is almost free from background contributions for  $1 \text{ fb}^{-1}$  and a discovery can be made with high significance: 504 signal events and only two background events remain.<sup>17)</sup>

<sup>17)</sup>If the GMSB3 signal events are selected using the final selection cuts of Sect. 6.2.3 including the photon trigger requirement, only 16 events remain. Hence, the specialized non-pointing photon selection is much more efficient in the case of a GMSB3 scenario.

# Chapter 7

## Measurements from GMSB events

It has been shown in the last chapter that supersymmetry based on a GMSB model with photons in the final state can be discovered by ATLAS with a small data set, if the masses of some of the colored supersymmetric particles are of the order of 1 TeV. Once a signature consistent with supersymmetry has been established, measurements of the properties of the supersymmetric particles can help to constrain the underlying model realised in nature:

- Kinematic edges in invariant mass spectra can be used to constrain the masses of the particles involved in the decay. This has been studied in detail for mSUGRA-like scenarios [18], as well as for GMSB models with  $\tilde{\tau}$  NLSPs [120]. In the GMSB models studied here, the additional photons in the final state can be used to built additional invariant mass combinations [121].
- If the GMSB model has non-pointing photons in the final state, the NLSP lifetime can be measured and the underlying model can be further constrained.

In the following sections measurement techniques for supersymmetric particle masses using kinematic edges in invariant mass spectra, as well as methods to determine the neutralino lifetime are presented and tested in a certain benchmark scenario.

In principle, the kinematic edges are identical for prompt and non-pointing photon scenarios as they only depend on the masses of the particles involved in the decay and are independent of the neutralino lifetime. Since a scenario with a non-vanishing neutralino lifetime represents the more general case and the influence of the lifetime measurement in a global GMSB fit is investigated in Chap. 8, a non-pointing photon scenario (*GMSB2* with  $C_{\text{grav}} = 30$  and  $\tau_{\tilde{\chi}_1^0} = 3.34 \text{ ns}$ ) for the mass measurements is used in the following.<sup>1)</sup>

### 7.1 Measurements of kinematic edges and particle masses

In supersymmetric models with R-parity conservation the particle decay chain cannot be reconstructed completely, since two LSPs leave the detector undetected. For this reason, kinematic endpoints in invariant mass distributions rather than mass peaks are measured and from the combination of several such measurements the particle masses can be reconstructed. Extensive studies in this field have been done in the past to analyse the potential of the ATLAS detector for mSUGRA-like scenarios with leptons and

<sup>1)</sup>The GMSB2 scenario has the same parameters as the GMSB1 and GMSB3 scenarios, but with  $C_{\text{grav}} = 30$ . This results in a lifetime of  $\tau_{\tilde{\chi}_1^0} = 3.34 \text{ ns}$ . The GMSB2 scenario has been chosen, since it turns out that its NLSP lifetime is in a well measureable region. The uncertainties on the lifetime measurement in GMSB3 are much larger than in the GMSB2 case. A sample of 60 000 GMSB2 events has been generated and passed through a full GEANT4 detector simulation for this study corresponding to approximately  $7.5 \text{ fb}^{-1}$ .

jets in the final state [18]. However, for the GMSB2 scenario discussed here, the additional photons in the final state provide extra information to be exploited [121].

In this study the decay channel shown in Fig. 6.3(b) is investigated:

$$\tilde{q} \rightarrow \tilde{\chi}_2^0 q \rightarrow \tilde{l}_R^\pm l^\mp q \rightarrow \tilde{\chi}_1^0 l^+ l^- q \rightarrow \tilde{G} \gamma l^+ l^- q, \quad l = e, \mu. \quad (7.1)$$

The final state therefore contains at least two OSSF leptons, where only electrons and muons are considered as leptons.<sup>2)</sup> Additionally, the final state photons as well as the jets arising from the squark and gluino decays are used.

### 7.1.1 Event selection

The additional requirement of leptons in the final state leads to slight modifications of the selection cuts of the other final state objects compared to the discovery analysis for non-pointing photons discussed in Sect. 6.3. Here, events are selected, which contain two photons with  $p_T > 20$  GeV and  $|\eta| < 2.5$  (using the unbiased identification criteria, as discussed in Sect. 5.3) and exactly two electrons (see Sect. 5.1.4) or two muons<sup>3)</sup> with  $|\eta| < 2.5$  and  $p_{T,e} > 10$  GeV and  $p_{T,\mu} > 5$  GeV, respectively<sup>4)</sup>. Although a non-pointing photon scenario is chosen, two photons in the final state are required to be able to resolve ambiguities in the assignment of the photons to the decay chain that contains the lepton pair. Additionally, three jets with  $p_T > 65$  GeV and values of the missing transverse energy larger than 50 GeV are required. Again the multiple jets trigger requirement (“3j65”) has been imposed. With these cuts, 772 signal GMSB2 events remain for  $7.5 \text{ fb}^{-1}$  of data while the SM background is negligible.<sup>5)</sup> For smaller values of integrated luminosities the statistics of the selected signal was found to be too small for a reliable measurement of the kinematic edges.

### 7.1.2 Measurement of endpoints involving leptons and photons

The  $\tilde{\chi}_2^0$  decay shown in Fig. 6.3(b) is particularly suited to measure the masses of the  $\tilde{\chi}_2^0$ , the  $\tilde{l}_R$  and the  $\tilde{\chi}_1^0$ .<sup>6)</sup> These can be reconstructed from the four invariant mass spectra [121] that can be measured using only the leptons and photons of the final state:

- 1) If at least one of the sleptons is lighter than the  $\tilde{\chi}_2^0$  (as in the GMSB2 scenario), the two-body decay channel  $\tilde{\chi}_2^0 \rightarrow \tilde{l}_R^\pm l^\mp \rightarrow \tilde{\chi}_1^0 l^+ l^-$  dominates and the spectrum of the invariant mass of the two leptons features a sharp endpoint at

$$M_{ll}^{\max} = \sqrt{\frac{(m_{\tilde{\chi}_2^0}^2 - m_{\tilde{l}_R}^2) \cdot (m_{\tilde{l}_R}^2 - m_{\tilde{\chi}_1^0}^2)}{m_{\tilde{l}_R}^2}} = 106.4 \text{ GeV}, \quad (7.2)$$

where the numerical value corresponds to the expected result in the GMSB2 scenario using the values of the particle masses as calculated with ISAJET. In the reconstruction of the di-lepton

<sup>2)</sup>For a discussion of invariant mass distributions involving  $\tau$  leptons in the final state, see *e.g.* [18, 120].

<sup>3)</sup>For the details of the muon reconstruction, see *e.g.* [18].

<sup>4)</sup>The region  $1.37 < |\eta| \leq 1.52$ , where the barrel calorimeters and the endcap calorimeters overlap, are excluded for the photons, leptons and jets throughout this chapter.

<sup>5)</sup>The signal selection efficiency is decreased compared to Sect. 6.3 due to the small branching ratio for the decay (7.1) involving OSSF lepton pairs.

<sup>6)</sup>It should be noted that this is only possible under the assumption of a massless gravitino. The invariant mass distributions may eventually be interpreted in a different way, *e.g.* including a left-handed instead of a right-handed slepton. All possible interpretations have to be investigated in global fits of the different models to the data and the resulting  $\chi^2$ -distributions have to be compared in order to decide which model describes the data best. This is investigated in Chap. 8

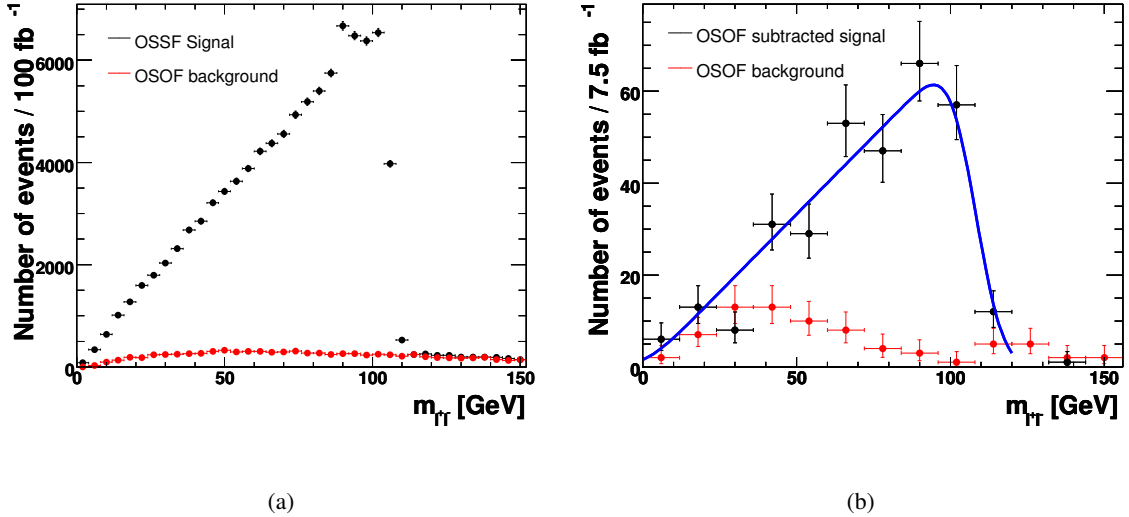


Figure 7.1: (a) Di-lepton invariant mass distribution in the GMSB1 scenario for  $100 \text{ fb}^{-1}$  of data simulated with a fast simulation. (b) Flavor-subtracted di-lepton invariant mass distribution in the GMSB2 scenario for  $7.5 \text{ fb}^{-1}$ . The flavor background from the signal is also shown in both cases.

invariant mass spectrum possibly remaining background from two independent leptonic decays in Standard Model processes, as well as in the supersymmetric process itself, can be removed by using the flavor-subtracted combination

$$N(e^+e^-)/\beta + \beta N(\mu^+\mu^-) - N(e^\pm\mu^\mp), \quad (7.3)$$

where  $N$  is the number of events in a certain bin. Since GMSB models are flavor- (and charge-) conserving, the leptons from the decay (7.1) are 100% correlated in flavor, whereas the leptons from the background processes can have the same or opposite flavor (OSOF) with the same probability. The efficiency correction factor  $\beta = 0.86$  is equal to the ratio of the electron and muon reconstruction efficiencies [18]. As an illustration of the expected shape of the distribution, Fig. 7.1(a) shows the di-lepton invariant mass (black data points) of a GMSB1 scenario for  $100 \text{ fb}^{-1}$  of data simulated with a fast simulation together with the distribution of the flavor background (red data points). As expected, it can be observed that the flavor background distribution cancels the signal distribution exactly for values larger than the expected endpoint that is given by a sharp edge. Since the branching ratio for the decay  $\tilde{\chi}_2^0 \rightarrow \tilde{\chi}_1^0 Z^0$  is non-vanishing ( $\sim 3\%$ ) the decaying  $Z^0$  contributes a small peak at  $m_Z$  clearly visible in the figure. The flavor-subtracted di-lepton distribution for the GMSB2 scenario passing a GEANT4-based detector simulation for  $7.5 \text{ fb}^{-1}$  is shown in Fig. 7.1(b). The peak from the  $Z^0$  decay is no longer visible due to the smaller dataset and the endpoint is smeared out. This distribution has been fitted with a triangle convoluted with a Gaussian resolution function and the resulting fit function is also shown in the figure.

- 2) The sequential two-body decays of the  $\tilde{\chi}_2^0$ , the  $\tilde{l}_R$  and the  $\tilde{\chi}_1^0$  in the decay (7.1) lead to an endpoint with a linear vanishing in the invariant  $l^+l^-\gamma$  mass spectrum at

$$M_{ll\gamma}^{\max} = \sqrt{m_{\tilde{\chi}_2^0}^2 - m_{\tilde{\chi}_1^0}^2} = 191.6 \text{ GeV}. \quad (7.4)$$

Due to the presence of two photons in the final state two different  $l^+l^-\gamma$  combinations can be constructed. Since at least one of the combinations must have an invariant mass less than the

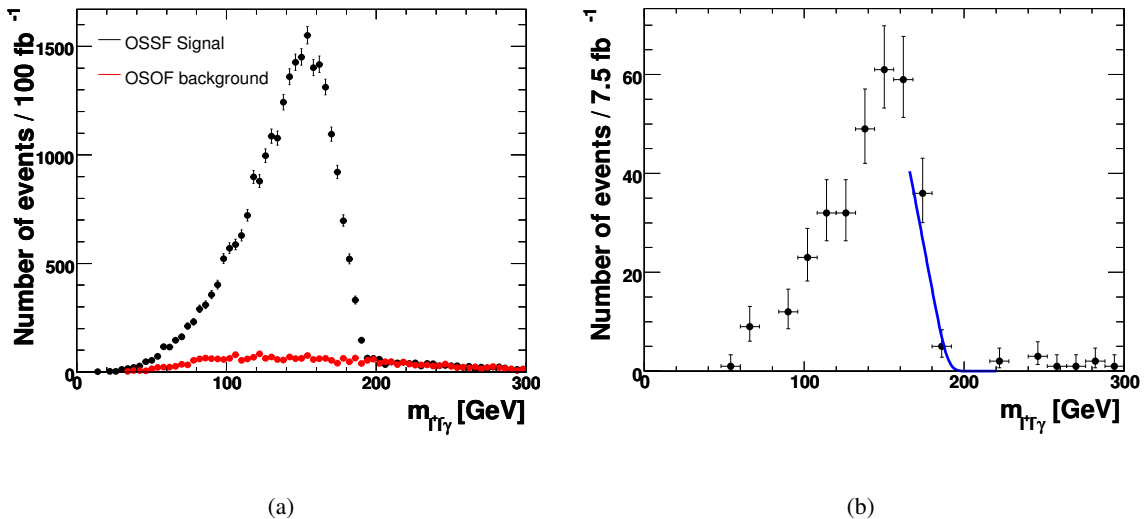


Figure 7.2: (a)  $l^+l^-\gamma$  invariant mass distribution in the GMSB1 scenario for  $100\text{ fb}^{-1}$  of data simulated with a fast simulation. The flavor background from the signal is also shown. (b) Flavor subtracted  $l^+l^-\gamma$  invariant mass distribution in the GMSB2 scenario for  $7.5\text{ fb}^{-1}$ .

value given in Eq. (7.4), the distribution of the smaller invariant mass vanishes at this point. Figure 7.2(a) shows the expected shape of the distribution (black data points) for the GMSB1 scenario for  $100\text{ fb}^{-1}$  of data simulated with a fast simulation. The flavor background (red data points) is also shown and again the two distributions cancel each other for invariant mass values larger than the expected endpoint. Figure 7.2(b) shows the flavor-subtracted distribution of the  $l^+l^-\gamma$  invariant mass for the GMSB2 scenario for  $7.5\text{ fb}^{-1}$  of GEANT4-based simulated MC data. Again, the endpoint is smeared out due to the smaller statistics of the MC sample. The linear vanishing can be fitted with a linear function convoluted with a Gaussian to obtain a measurement for the endpoint. The fit result is also shown in the figure.

- 3) + 4) Finally, the  $l^\pm\gamma$  invariant mass distribution can be exploited. Due to the two leptons in the final state this distribution has two contributions: a distribution with a sharp endpoint is expected for the combination of the photon with the second (so-called *near*) lepton (*i.e.* the lepton which arises from the  $\tilde{l}_R$  decay) and a distribution with a linear vanishing is expected for the combination of the photon with the first (*far*) lepton (*i.e.* the lepton that arises from the  $\tilde{\chi}_2^0$  decay). The corresponding endpoints are expected at:

$$M_{l\gamma}^{\text{near,max}} = \sqrt{m_{\tilde{l}_R}^2 - m_{\tilde{\chi}_1^0}^2} = 107.9 \text{ GeV}, \quad (7.5)$$

$$M_{l\gamma}^{\text{far,max}} = \sqrt{m_{\tilde{\chi}_2^0}^2 - m_{\tilde{l}_R}^2} = 158.3 \text{ GeV}. \quad (7.6)$$

The ambiguity arising from the presence of the additional photon from the other supersymmetric decay chain can be resolved by choosing the photon for which the invariant mass of the two  $l^+l^-\gamma$  combinations is smaller than the endpoint measured in Eq. (7.4). This requirement ensures that this  $l^\pm\gamma$  combination is a result of the  $\tilde{\chi}_2^0$  decay. If none or both of the combinations lead to an invariant mass smaller than the endpoint, the event is rejected. This reduces the statistics in the analysis<sup>7)</sup>, but is the only possibility to resolve the ambiguities and to obtain a precise measurement of the  $l^\pm\gamma$  invariant mass endpoint. Figure 7.3(a) shows the invariant mass distribution (black data

<sup>7)</sup>Around 45% of the events that have at least one combination smaller than the endpoint, have both combinations smaller.

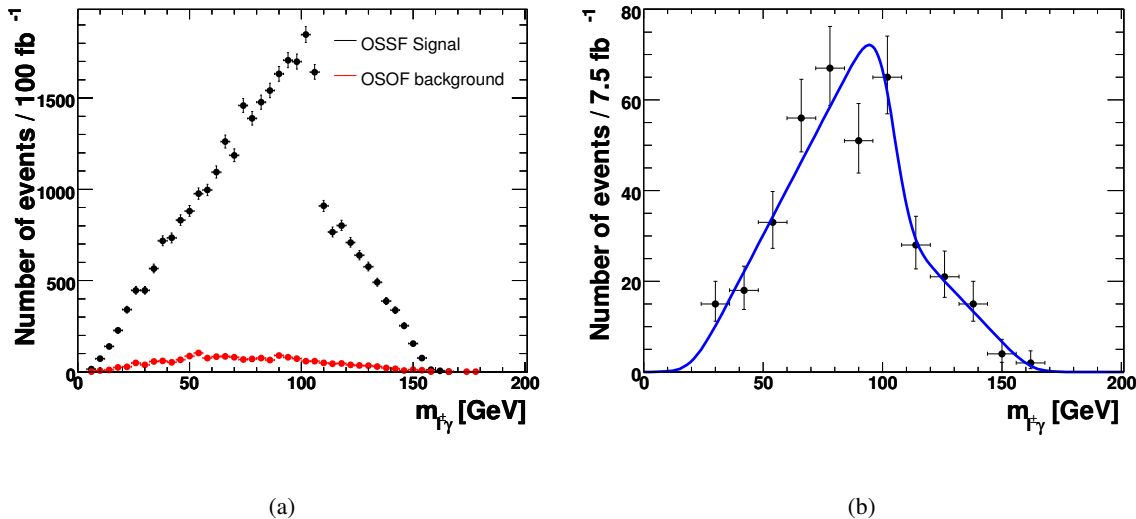


Figure 7.3: (a)  $l^\pm\gamma$  invariant mass distribution in the GMSB1 scenario for  $100 \text{ fb}^{-1}$  of data simulated with a fast simulation. The flavor background from the signal is also shown. (b) Flavor subtracted  $l^\pm\gamma$  invariant mass distribution in the GMSB2 scenario for  $7.5 \text{ fb}^{-1}$ .

points) for the GMSB1 scenario for  $100 \text{ fb}^{-1}$  of data simulated with a fast simulation. The sharp edge and the linear vanishing are clearly visible. For this distribution no background remains for values larger than the expected endpoint. The flavor-subtracted  $l^\pm\gamma$  invariant mass distribution is shown in Fig. 7.3(b) for the GMSB2 scenario for  $7.5 \text{ fb}^{-1}$  of GEANT4-based simulated MC data. As for the other invariant mass combinations the sharp endpoint as well as the linear vanishing are smeared out and can be fitted by a connection of linear functions convoluted with a Gaussian. The fit result is also shown in the figure.

The functions used to fit the invariant mass distributions are parameterized such that the endpoints are free fit parameters and their statistical uncertainties can be read off directly from the fit results. The systematic uncertainties from binning effects, starting values of the fit and choice of the fit ranges dominate the systematic uncertainties from variations of the electromagnetic energy scale. Both have been added in quadrature to obtain the total uncertainty on the measured endpoints. The values obtained in the fits and the uncertainties are listed in Tab. 7.1 together with their expected values for the GMSB2 scenario. It can be observed that the expected endpoint values can be reproduced within their uncertainties.

These fit results are used as input for a global GMSB fit in Chap. 8. Additionally, the four measured endpoints can be used to calculate directly the masses  $m_{\tilde{\chi}_1^0}$ ,  $m_{\tilde{\chi}_2^0}$  and  $m_{\tilde{l}_R}$  of the three supersymmetric particles involved in the investigated decay chain. The Eqs. 7.2, 7.4 and 7.6 can be exploited in a numerical  $\chi^2$  minimization to extract the particle masses from the combination of endpoints. The  $\chi^2$  is defined as

$$\chi^2 = \sum_{k=1}^4 \frac{(m_k^{\max} - t_k^{\max}(m_{\tilde{\chi}_1^0}, m_{\tilde{\chi}_2^0}, m_{\tilde{l}_R}))^2}{\sigma_k^2}, \quad (7.7)$$

where  $m_k^{\max}$  and  $\sigma_k$  denote the fit value and its uncertainty, respectively. The theoretical expressions for the endpoints are denoted  $t_k^{\max}$ . The fit is stable for large variations ( $\sim \pm 50\%$ ) of the starting values of the fit. The results of this calculation together with the true values for the GMSB2 scenario are also listed in Tab. 7.1. Again, the values obtained from this analysis agree with the expected values within their uncertainties. In summary, it can be concluded that for this analysis of the GMSB2 scenario the masses of the supersymmetric particles can be determined within a precision of a few percent with  $7.5 \text{ fb}^{-1}$ .

Observable	expected value [GeV]	fitted value [GeV]
$M_{l^+l^-}^{\max}$	106.4	$108.0 \pm 4.3$
$M_{l^+l^-\gamma}^{\max}$	191.6	$189.6 \pm 3.8$
$M_{l^\pm\gamma}^{\text{near,max}}$	107.9	$104.4 \pm 3.7$
$M_{l^\pm\gamma}^{\text{far,max}}$	158.3	$161.9 \pm 3.9$
$m_{\tilde{\chi}_1^0}$	118.8	$114.0 \pm 9.5$
$m_{\tilde{\chi}_2^0}$	225.5	$222.5 \pm 6.3$
$m_{\tilde{l}_R}$	160.5	$154.1 \pm 8.0$

Table 7.1: Expected and fitted values of the kinematic endpoints and supersymmetric particle masses in the GMSB2 scenario for  $7.5 \text{ fb}^{-1}$ .

### 7.1.3 Measurement of endpoints involving leptons and jets

In the last section only the decay of the  $\tilde{\chi}_2^0$  with the resulting final state particles has been investigated. Similar to the studies of the mSUGRA models [18] the jets of the final state arising from the initial squark or gluino decay can also be used to constrain the squark and gluino mass scale by combining them with the final state leptons from the  $\tilde{\chi}_2^0$  and  $\tilde{l}_R$  decays:

$$\tilde{q} \rightarrow \tilde{\chi}_2^0 q \rightarrow \tilde{l}_R^\pm l^\mp q \rightarrow \tilde{\chi}_1^0 l^+ l^- q. \quad (7.8)$$

The following three endpoints of invariant mass distributions involving jets and leptons can be reconstructed:

- As in the case of the final state photon of the previous section, the jet can be combined with the two leptons to form the  $l^+l^-q$  invariant mass. The endpoint of this distribution is given by [122]

$$M_{llq}^{\max} = \max \left[ \frac{\left( m_{\tilde{q}/\tilde{g}}^2 - m_{\tilde{\chi}_2^0}^2 \right) \cdot \left( m_{\tilde{\chi}_2^0}^2 - m_{\tilde{\chi}_1^0}^2 \right)}{m_{\tilde{\chi}_2^0}^2}, \frac{\left( m_{\tilde{q}/\tilde{g}}^2 - m_{\tilde{l}_R}^2 \right) \cdot \left( m_{\tilde{l}_R}^2 - m_{\tilde{\chi}_1^0}^2 \right)}{m_{\tilde{l}_R}^2}, \right. \\ \left. \frac{\left( m_{\tilde{q}/\tilde{g}}^2 m_{\tilde{l}_R}^2 - m_{\tilde{\chi}_2^0}^2 m_{\tilde{\chi}_1^0}^2 \right) \cdot \left( m_{\tilde{\chi}_2^0}^2 - m_{\tilde{l}_R}^2 \right)}{m_{\tilde{\chi}_2^0}^2 m_{\tilde{l}_R}^2} \right]^{\frac{1}{2}}, \quad (7.9)$$

where  $m_{\tilde{q}/\tilde{g}}$  is the mass of the decaying squark or gluino, respectively. However, the type of the initial colored particle cannot be determined from the reconstructed jet and the distribution is a combination of the distributions of all squark and gluino decays.<sup>8)</sup> In the GMSB2 scenario studied here, the different squark types have similar masses *e.g.*  $m_{\tilde{u}_L} = 987.3 \text{ GeV}$ ,  $m_{\tilde{u}_R} = 944.5 \text{ GeV}$ ,  $m_{\tilde{d}_L} = 990.3 \text{ GeV}$  and  $m_{\tilde{d}_R} = 941.0 \text{ GeV}$ , while the gluino mass is given by  $m_{\tilde{g}} = 735.6 \text{ GeV}$ . In principal, the different squark flavor contributions can be separated by combining reasonable fitting functions for each of the contributions that contain the corresponding endpoint as a free parameter. However, due to the smallness of the differences of the squark masses, the limited statistics and the experimental resolution, such a decomposition in terms of the squark flavor is not possible in the present analysis.

In the calculation of the invariant mass of Eq. (7.10) it is assumed that the colored particle arising from the initial squark/gluino decay produces one of the two jets with the highest transverse

<sup>8)</sup>The possibility of b-tagging or top quark reconstruction is not considered here.

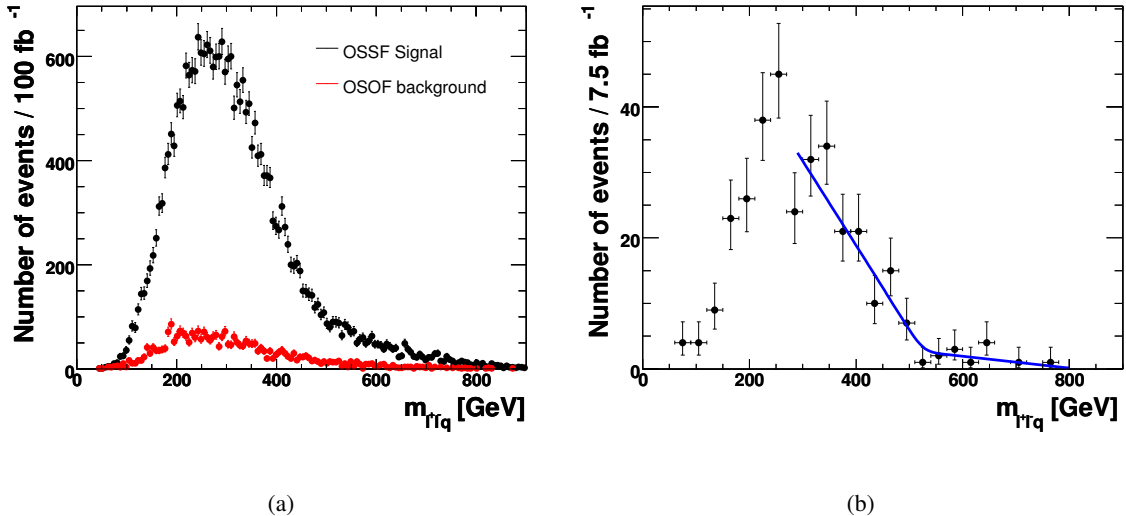


Figure 7.4: (a)  $m_{l^+l^-q}$  invariant mass distribution in the GMSB1 scenario for  $100 \text{ fb}^{-1}$  of data simulated with a fast simulation. The flavor background from the signal is also shown. (b) Flavor subtracted  $m_{l^+l^-q}$  invariant mass distribution in the GMSB2 scenario for  $7.5 \text{ fb}^{-1}$ .

momentum in the event due to the large mass difference between the squarks/gluino and the second lightest neutralino. Since a maximum value is expected for the distribution, the jet giving the lower invariant mass is used.<sup>9)</sup> Figure 7.4(a) shows the expected invariant mass distribution (black data points) for the GMSB1 scenario for  $100 \text{ fb}^{-1}$  of data simulated with a fast detector simulation together with the flavor background (red data points). The distribution features a long tail with an endpoint around 800 GeV from all the squark decays and a separate endpoint for the contribution of the gluino decays and possibly wrongly assigned  $l^+l^-q$  combinations which is clearly visible for smaller masses. In the following analysis it is assumed that the second contribution is mainly due to decaying gluinos to interpret the endpoint in terms of a gluino mass. Figure 7.4(b) shows the flavor-subtracted  $l^+l^-q$  invariant mass distribution for the GMSB2 scenario for  $7.5 \text{ fb}^{-1}$ . To determine the endpoints of the two contributions the shape of the tails is parameterized with two linear functions convoluted with a Gaussian resolution function [18]. The result of the fit is also shown in the figure. The endpoint of the squark contribution is determined to be  $(810 \pm 60) \text{ GeV}$ , while the endpoint of the gluino contribution given by the first part of the linear functions is determined to be  $(530 \pm 50) \text{ GeV}$ . As can be seen from the distributions these values (and also the following in this section) are quite uncertain with the given statistics and will not be used in the global fits of Chap. 8. The value for the squark measurement is in good agreement with the endpoint  $M_{llq}^{max} = 797.4 \text{ GeV}$  expected from Eq. (7.10) using a weighted averaged squark mass scale  $m_{\tilde{q}} = 965.1 \text{ GeV}$ , where the weights are given by the production fractions of the individual squark flavors.<sup>10)</sup> The value for the gluino contribution differs by around  $2\sigma$  from the expected value of  $M_{llq}^{max} = 595.0 \text{ GeV}$ , which shows that the assumption of a pure contribution from gluino decays is oversimplifying.

2) + 3) The jet used for the reconstruction of the  $l^+l^-q$  invariant mass can also be combined with only

<sup>9)</sup>This assumption may probably produce a shift to lower values in the distribution, if the other of the two jets arises from the initial squark/gluino decay. This can be seen in what is called the *gluino contribution* in the distribution. Since this contribution has a smaller invariant mass than the squark contribution due to the lower gluino mass, the gluino contribution is contaminated with *wrong*  $l^+l^-q$  combinations.

<sup>10)</sup>The weights  $w$  are given by  $w(\tilde{u}_{L,R}) = \frac{1}{3}$  and  $w(\tilde{d}_{L,R}) = \frac{1}{6}$  from the generator information.

one of the two leptons. The corresponding two results for the invariant  $lq$  mass are denoted  $m_{lq}^{\text{low}}$  and  $m_{lq}^{\text{high}}$  depending on their values (*i.e.*  $m_{lq}^{\text{low}} < m_{lq}^{\text{high}}$ ). For the invariant  $lq$  mass distributions endpoints are expected at [123]

$$M_{lq}^{\text{high,max}} = \max \left[ (M_{l_{\text{near}q}}^{\text{max}})^2, (M_{l_{\text{far}q}}^{\text{max}})^2 \right]^{\frac{1}{2}}, \quad (7.10)$$

$$M_{lq}^{\text{low,max}} = \min \left[ (M_{l_{\text{near}q}}^{\text{max}})^2, \frac{(m_{\tilde{q}/\tilde{g}}^2 - m_{\tilde{\chi}_2^0}^2) \cdot (m_{\tilde{l}_R}^2 - m_{\tilde{\chi}_1^0}^2)}{2 \cdot m_{\tilde{l}_R}^2 - m_{\tilde{\chi}_1^0}^2} \right]^{\frac{1}{2}}, \quad (7.11)$$

with

$$(M_{l_{\text{near}q}}^{\text{max}})^2 = \frac{(m_{\tilde{q}/\tilde{g}}^2 - m_{\tilde{\chi}_2^0}^2) \cdot (m_{\tilde{\chi}_2^0}^2 - m_{\tilde{l}_R}^2)}{m_{\tilde{\chi}_2^0}^2}, \quad (7.12)$$

$$(M_{l_{\text{far}q}}^{\text{max}})^2 = \frac{(m_{\tilde{q}/\tilde{g}}^2 - m_{\tilde{\chi}_2^0}^2) \cdot (m_{\tilde{l}_R}^2 - m_{\tilde{\chi}_1^0}^2)}{m_{\tilde{l}_R}^2}. \quad (7.13)$$

Figure 7.5(a) shows the expected  $m_{lq}^{\text{low}}$  distribution (black data points) for the GMSB1 scenario for  $100 \text{ fb}^{-1}$  of data simulated with a fast simulation together with the flavor background (red data points). As in the case of the  $m_{llq}$  distribution, two contributions are visible. The long tail is expected to come from jets arising from squark decays (using the averaged mass scale the endpoint is expected at  $M_{lq}^{\text{low,max}} = 523.5 \text{ GeV}$ ), while the endpoint at lower values of the invariant mass is assumed to come from gluino decays (expected for the GMSB2 scenario at  $M_{lq}^{\text{low,max}} = 390.6 \text{ GeV}$ ). The flavor-subtracted distribution for the GMSB2 scenario for  $7.5 \text{ fb}^{-1}$  is shown in Fig. 7.5(b) together with the fit result using the same fitting function as for Fig. 7.4(b). The gluino endpoint is determined to be  $(330 \pm 40) \text{ GeV}$ , while for the squark endpoint  $(480 \pm 50) \text{ GeV}$  is obtained. Again, the gluino value differs by about  $2\sigma$  from the expected value.

The expected  $m_{lq}^{\text{high}}$  distribution for the GMSB1 scenario is shown in Fig. 7.6(a) (black data points) for  $100 \text{ fb}^{-1}$  of data simulated with a fast simulation together with the flavor background (red data points). The situation is similar to the  $m_{lq}^{\text{low}}$  distribution and the gluino endpoint is expected at  $M_{lq}^{\text{high,max}} = 491.6 \text{ GeV}$ , while the average squark mass scale leads to  $M_{lq}^{\text{high,max}} = 658.9 \text{ GeV}$ . The fit result shown in Fig. 7.6(b) for the GMSB2 scenario for  $7.5 \text{ fb}^{-1}$  leads to endpoints for the gluino and squark contributions of  $(450 \pm 60) \text{ GeV}$  and  $(670 \pm 60) \text{ GeV}$ , respectively, which agree with the expected values.

Similar to the invariant mass measurements involving photons, the endpoints obtained from the distributions involving jets can be used to determine the gluino mass and the average squark mass scale in a  $\chi^2$  fit using Eq. (7.7). Since the theoretical endpoints also depend on the masses of the  $\tilde{\chi}_2^0$ , the  $\tilde{\chi}_1^0$  and the  $\tilde{l}_R$ , the photon endpoints also enter the fit. The squark mass scale is determined to be  $m_{\tilde{q}} = (950 \pm 50) \text{ GeV}$ , while for the gluino mass one obtains  $m_{\tilde{g}} = (650 \pm 50) \text{ GeV}$ . The measured squark mass scale is in good agreement with the theoretical value, while the gluino mass value differs by around  $2\sigma$  from the expectation, which again shows that the assumption of a pure gluino contribution to the endpoints at lower invariant masses is oversimplifying.

In summary, the measurement of kinematic endpoints involving leptons and jets can be used to determine an average mass scale of the initially produced supersymmetric particles. However, the uncertainties related to the assignment of the measured endpoints to the initially produced type of squark or gluino

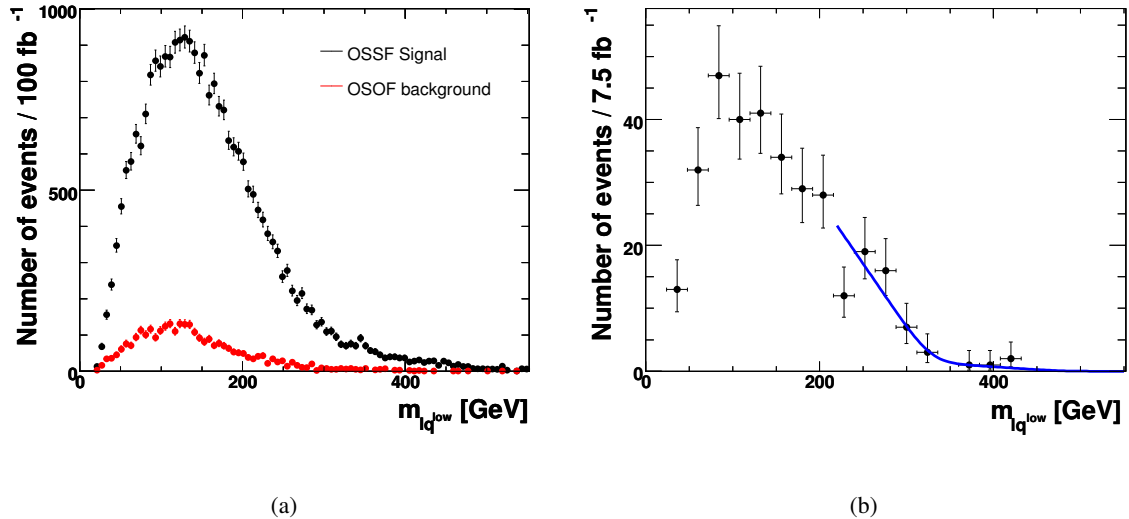


Figure 7.5: (a)  $lq^{\text{low}}$  invariant mass distribution in the GMSB1 scenario for  $100 \text{ fb}^{-1}$  of data simulated with a fast simulation. The flavor background from the signal is also shown. (b) Flavor-subtracted  $lq^{\text{low}}$  invariant mass distribution in the GMSB2 scenario for  $7.5 \text{ fb}^{-1}$ .

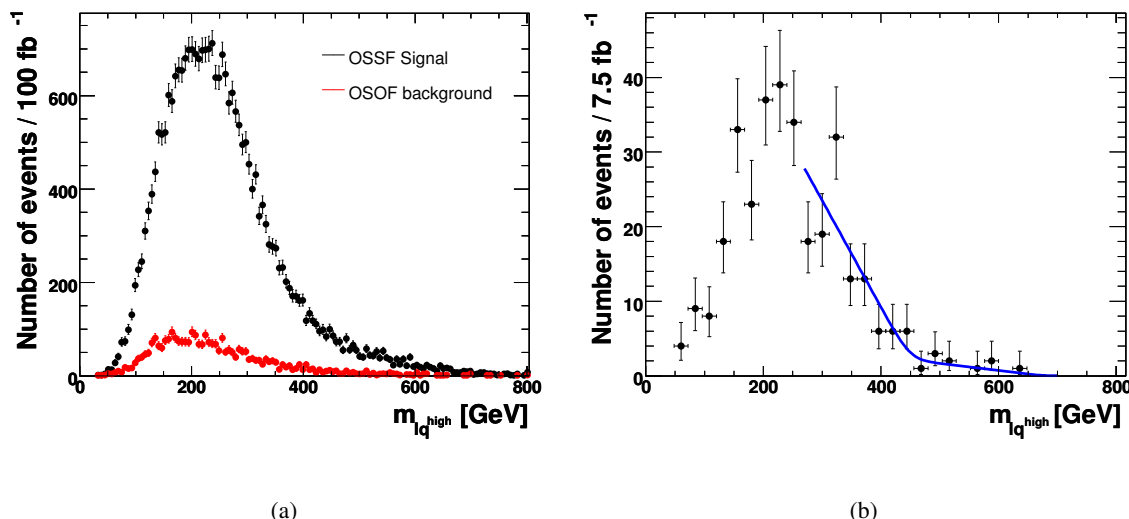


Figure 7.6: (a)  $lq^{\text{high}}$  invariant mass distribution in the GMSB1 scenario for  $100 \text{ fb}^{-1}$  of data simulated with a fast simulation. The flavor background from the signal is also shown. (b) Flavor-subtracted  $lq^{\text{high}}$  invariant mass distribution in the GMSB2 scenario for  $7.5 \text{ fb}^{-1}$ .

$C_{\text{grav}}$	1	10	20	30	40	55	70
$\tau_{\tilde{\chi}_1^0}$ [ns]	—	0.37	1.48	3.34	5.93	11.2	18.2

Table 7.2: Values of  $C_{\text{grav}}$  and the resulting  $\tilde{\chi}_1^0$  lifetime  $\tau_{\tilde{\chi}_1^0}$  as used in the generation of the signal samples for the measurement of the neutralino lifetime.

$C_{\text{grav}}$	10	20	30	40	55	70	Bgr.
Events	4132	3600	2842	2215	1441	1054	606

Table 7.3: Number of selected signal and background events for  $1 \text{ fb}^{-1}$ .

resulting from the smallness of the squark mass differences in the GMSB model, the small statistics and the limited experimental resolution, prevents a precise determination of the squark and gluino masses. The endpoints involving jets are therefore not used in the global GMSB fits of Chap. 8.

## 7.2 Neutralino lifetime determination

The parameters of the underlying GMSB model are not fully determined by the measurements of particle masses alone. As an example, the gravitino coupling  $C_{\text{grav}}$  determines the NLSP lifetime, while the particle masses (except the one from the gravitino) do not depend on  $C_{\text{grav}}$ . This lifetime can be determined using different experimental techniques. In this section a method based on the timing information of the ECal (see Sect. 5.3.2) is presented and its performance is tested in certain benchmark scenarios. Additionally, two alternative methods based on the reconstruction of the photon  $\eta$ -direction in the ECal and considering kinematic constraints in final states with additional leptons are studied.

### 7.2.1 Datasets

For the analysis of the determination of the neutralino lifetime additional GMSB1-like scenarios are investigated. They only differ in their values of  $C_{\text{grav}}$ , while the other parameters are again fixed to the GMSB1 values.<sup>11)</sup> According to Eq. (2.70) the different values of  $C_{\text{grav}}$  lead to different lifetimes of the neutralino. The values of  $C_{\text{grav}}$  and the corresponding lifetimes  $\tau_{\tilde{\chi}_1^0}$  for which event samples have been generated are listed in Tab. 7.2.<sup>12)</sup> The scenarios with  $C_{\text{grav}} = 1$ ,  $C_{\text{grav}} = 30$  and  $C_{\text{grav}} = 55$  correspond to the GMSB1, GMSB2 and GMSB3 scenarios used in the last sections, respectively. All scenarios except GMSB1 have non-pointing photons in the final state.

### 7.2.2 Method using the photon clustertime

As described in Sect. 6.3 a non-vanishing lifetime of the neutralino leads to a delayed signal of the photon cluster in the ECal as shown in Fig. 6.17(a) for the GMSB3 scenario. A determination of the size of the delay allows the measurement of the  $\tilde{\chi}_1^0$  lifetime  $\tau_{\tilde{\chi}_1^0}$  and  $C_{\text{grav}}$  assuming the other GMSB parameters to be known.<sup>13)</sup>

<sup>11)</sup>  $\Lambda = 90 \text{ TeV}$ ,  $M_{\text{mess}} = 500 \text{ TeV}$ ,  $\tan\beta = 5$ ,  $N_5 = 1$  and  $\text{sign}(\mu) = +$ .

<sup>12)</sup> For all samples 5000 events have been generated and passed through a full GEANT4 detector simulation.

<sup>13)</sup> The  $\tilde{\chi}_1^0$  lifetime cannot be measured directly, since only neutral particles are involved in the neutralino decay and no secondary vertices can be measured. Additionally, the initial state of the interaction is not known, such that *e.g.* the neutralino boost cannot directly be used in the calculation of a lifetime. This can only be done at a lepton collider for direct  $\tilde{\chi}_1^0$  production [124].

The same event preselection as for the estimation of the discovery potential for non-pointing photon scenarios (Sect. 6.3) is used for this lifetime measurement.<sup>14)</sup> The number of remaining background events as well as the number of selected signal events for the various benchmark scenarios from Tab. 7.2 are listed in Tab. 7.3 together with the corresponding  $C_{\text{grav}}$  values for  $1 \text{ fb}^{-1}$ . It can be observed that the number of selected signal events decreases with increasing  $C_{\text{grav}}$ . While the production cross section of supersymmetric particles is constant in these scenarios, the photon identification efficiency drops with increasing  $C_{\text{grav}}$  and an increasing number of  $\tilde{\chi}_1^0$  decay outside the inner detector volume also leading to a decreased number of identified photons.

A combined fit of the background and signal contribution in the distribution of the clustertime  $\tau_{\text{cluster}}$  of the leading photon (see Fig. 6.17(b) for the GMSB3 scenario) is then performed to determine the size of the delay of the photon cluster. Due to the different kinematics the shapes of the background and signal distributions are different: As shown in Fig. 7.7(a), the background is best modelled by the sum of two Gaussian functions. To reduce the number of free fit parameters the means of the Gaussians are chosen to be identical and the fit results for the widths of the Gaussians are  $(0.320 \pm 0.057) \text{ ns}$  for the Gaussian describing the tails of the distribution and  $(0.146 \pm 0.011) \text{ ns}$  for the Gaussian describing the peak.

The signal distribution is best described by a Landau distribution.<sup>15)</sup> Figure 7.7(b) shows the fit result for the GMSB3 scenario. The width of the distribution is determined to be  $(0.232 \pm 0.008) \text{ ns}$  from the fit. With the assumption that the  $\tau_{\text{cluster}}$  resolution is independent of the underlying background process<sup>16)</sup> the number of free fit parameters of the combined fit can be reduced by an independent data-driven determination of the shape of the background contribution using a clean sample of Standard Model events, *e.g.* data from the process  $Z^0 \rightarrow e^+ e^-$ .<sup>17)</sup> Figure 7.8(a) shows the  $\tau_{\text{cluster}}$  distribution of a sample of simulated  $Z^0 \rightarrow e^+ e^-$  events<sup>18)</sup> that is again described by the sum of two Gaussian functions with the widths determined to be  $(0.295 \pm 0.002) \text{ ns}$  for the Gaussian describing the tails of the distribution and  $(0.1527 \pm 0.0003) \text{ ns}$  for the Gaussian describing the peak. These values agree with the values obtained from the fit of the complete Standard Model background and are used in the following to fix the parameters for the Standard Model background contribution in the combined fit.

Once the parameters of the background contribution are fixed, four free parameters remain in the combined fit of signal and background. These are the mean and the width of the Landau contribution and the total number of signal and background events. As an example, Fig. 7.8(b) shows the clustertime distribution of the leading photon for the GMSB3 scenario and the background together with the fit result which nicely describes the combined distribution. The blue dashed line shows the fit result of the background contribution, while the red dashed line shows the fit result for the signal contribution. The Landau width is determined to be  $(0.241 \pm 0.013) \text{ ns}$  from the fit which agrees with the value obtained from fitting the GMSB3 signal distribution alone.<sup>19)</sup> Additionally, the number of signal and background

<sup>14)</sup> Again, the unbiased photon identification is used, see Sect. 5.3.

<sup>15)</sup> Possibly the exact signal distribution can be calculated from the complete matrix element of the initial squark/gluino decay and using a model of the detector geometry. Nevertheless, assumptions about the geometrical acceptance and thus about the underlying model would have to be made to determine the lifetime directly in a fit. This model dependent step is done via a calibration curve in the present analysis. Additionally, other parameterizations of the signal shape have been tested, such as convolutions of exponential functions with Gaussians or Crystal Ball functions. However, it turns out that the signal is best described by a Landau function.

<sup>16)</sup> This neglects the energy dependence of the clustertime resolution of the ECal, as shown in Fig. 5.11(b). Since the energy dependence for energies above  $\sim 50 \text{ GeV}$  is small, this assumption is justified.

<sup>17)</sup> In this process possible additional background from machine effects or soft interactions like beam-gas events have to be studied in detail.

<sup>18)</sup> The events have been selected using a medium electron identification (see Sect. 5.1.4) and a cut on the invariant mass  $m_{ee}$  of the electron pair of  $80 \text{ GeV} < m_{ee} < 100 \text{ GeV}$ . However, no dedicated  $Z^0 \rightarrow e^+ e^-$  analysis has been performed.

<sup>19)</sup> For the determination of the  $\tilde{\chi}_1^0$  lifetime both, the mean and the width of the Landau signal contribution could be used in principle. However, the performance of mean-based methods leads to larger uncertainties due to the closeness of the Landau

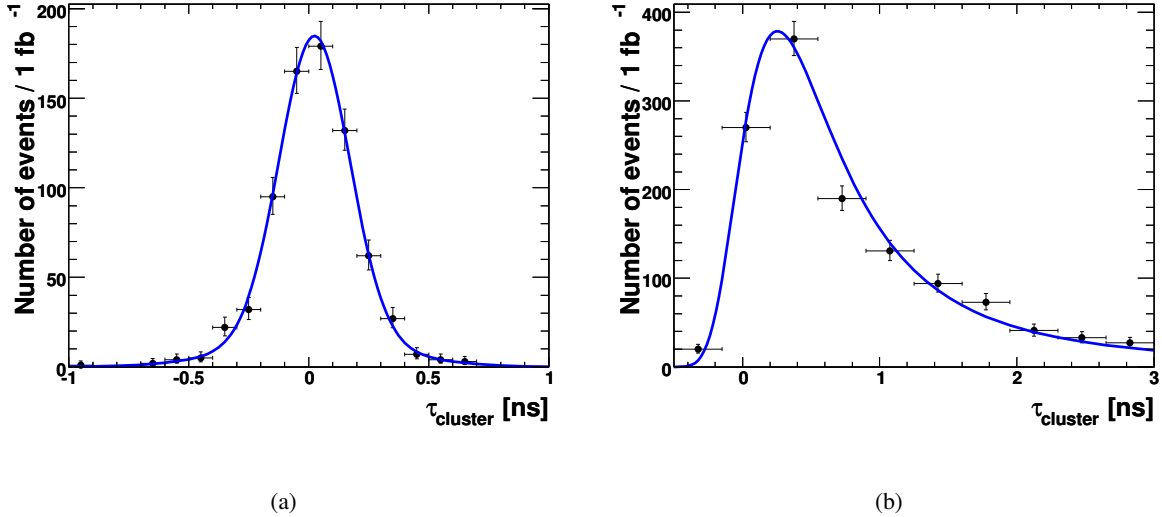


Figure 7.7: Distribution of the measured clustertime after the preselection for  $1 \text{ fb}^{-1}$  for (a) the Standard Model background and (b) the GMSB3 signal. The result of a fit to the MC data is also shown.

events can be determined in the fit and are given by  $1391 \pm 76$  and  $696 \pm 71$ , respectively. A comparison with the values given in Tab. 7.3 shows that the number of signal events is obtained accurately, while the number of fitted background events differs slightly more than  $1\sigma$  from the expectation.

Since the fitted Landau width has no direct functional relationship to the neutralino lifetime, a calibration curve derived from MC simulations of GMSB models with different neutralino lifetimes has to be used to determine the relationship between the Landau width and  $\tau_{\tilde{\chi}_1^0}$ . The scenarios listed in Tab. 7.2 are used and the fitting procedure described above is applied to each of the samples, *i.e.* a value for the Landau width is obtained for each  $C_{\text{grav}}$  value. Figure 7.9 shows the fit results as a function of  $C_{\text{grav}}$  and the decay length  $c\tau_{\tilde{\chi}_1^0}$ <sup>20)</sup> for the unbiased photon identification (closed symbols) and, for comparison, the ATLAS standard photon identification (open symbols). The error bars represent the fit uncertainties from the Landau fit to the individual samples. A calibration curve can be obtained by fitting the empirical function

$$y(x) = p_1 \cdot \left(1 - e^{-p_2 \cdot (x - p_3)}\right) \quad (7.14)$$

to these values, where  $p_1$ ,  $p_2$  and  $p_3$  are free fit parameters. They are given by  $p_1 = (0.284 \pm 0.017)$  ns,  $p_2 = 0.039 \pm 0.005$  and  $p_3 = 4.024 \pm 0.518$  for the unbiased photon identification. The resulting calibration curve is superimposed (solid line) in Fig. 7.9 together with its uncertainty<sup>21)</sup> (dashed lines) which, for a given measurement of the Landau width, results in an uncertainty for  $C_{\text{grav}}$  and  $c\tau_{\tilde{\chi}_1^0}$ . This uncertainty is called systematic uncertainty in the following.<sup>22)</sup> For illustration the inner radius of the ECal in the  $\tilde{\chi}_1^0$  rest frame is highlighted by the dashed line. After a steep increase of the calibration curve at small

mean to the background contribution and the stronger correlation of the Landau mean with the fitted total number of background events. For this reason only the width of the Landau distribution is exploited in the following for the determination of the  $\tilde{\chi}_1^0$  lifetime.

<sup>20)</sup>In the following only the  $C_{\text{grav}}$  value rather than  $c\tau_{\tilde{\chi}_1^0}$  will be investigated. The general parameter dependence of the method will be discussed in the next section.

<sup>21)</sup>The error bands are calculated by using the correlation matrix from the fit of the calibration curve to obtain new shifted data points. Two new calibration curves are fitted to the new data points using Eq. (7.14).

<sup>22)</sup>Note that this uncertainty can be reduced by simulating higher MC statistics that can be used in the production of the calibration curve.

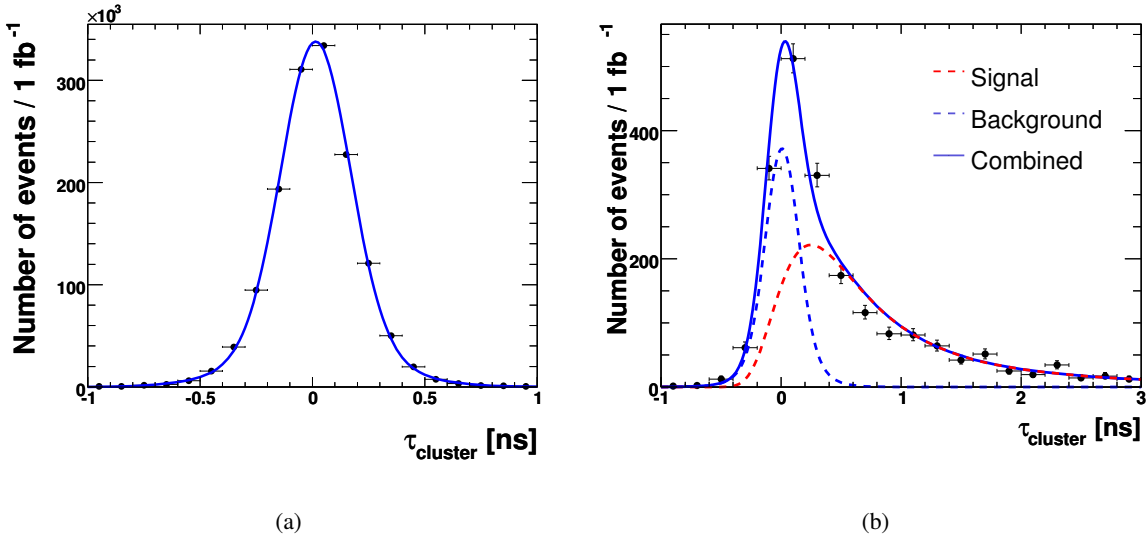


Figure 7.8: (a) Distribution of the measured clustertime for a sample of  $Z^0 \rightarrow e^+e^-$  events. The result of a fit of the sum of two Gaussian functions to the data is also shown. (b) Result of a combined signal and background fit of the clustertime distribution for the GMSB3 scenario.

values of  $C_{\text{grav}}$ , a saturation effect is visible for both photon identification methods, resulting from the decreasing photon identification efficiency and the increasing number of  $\tilde{\chi}_1^0$  decaying outside the inner detector volume. As expected, the unbiased photon identification yields a better performance as the saturation starts at larger values of  $C_{\text{grav}}$  leading to a larger range of possible lifetime measurements. Also the uncertainties in the projection of a possible Landau width measurement on the  $C_{\text{grav}}$  axis are smaller. It should be noted that one cannot trust the calibration curve for  $C_{\text{grav}} < 10$ , since in these regions it is very difficult to distinguish the signal from the background due to the smallness of the measured Landau width. Therefore the fit provides no reliable information about the lifetime in this region.

In addition, the uncertainties of possible measurements of the Landau width for two different example values of  $C_{\text{grav}}$  are indicated in Fig. 7.9, each for  $30\text{pb}^{-1}$ ,  $100\text{pb}^{-1}$  and  $1\text{fb}^{-1}$  of data. The upper value of the uncertainty on the corresponding  $C_{\text{grav}}$  value, resulting from the projection of the width measurement on the exponential fit function (called *statistical uncertainty* in the following), increases strongly for larger values of  $C_{\text{grav}}$  due to the saturation effect. In Fig. 7.10(a) the resulting statistical uncertainties on  $C_{\text{grav}}$  are shown as a function of the integrated luminosity for two example values of  $C_{\text{grav}}$ . The result of the saturation effect is clearly visible from the increased uncertainty at lower values of integrated luminosity for larger values of  $C_{\text{grav}}$ . Depending on the lifetime value realized in nature, this measurement might only be possible with at least  $1\text{fb}^{-1}$  of well understood data.

As a possible source of a systematic uncertainty, the influence of the size of the Standard Model background contribution on the fit result has been studied by artificially scaling the background contribution by scale factors  $x = 2$  and  $x = 0.5$ . Figure 7.10(b) shows the ratios of the determined values of the Landau widths with and without scaling factor and therefore indicates the stability of the width measurement. Since the measured widths with scaling factor differ only by around 1% from the widths measured without scaling factor, the resulting uncertainty on the  $C_{\text{grav}}$  determination is negligible.

The reconstructed  $C_{\text{grav}}$  values for the benchmark scenarios from Tab. 7.2 are compared to the true values in Tab. 7.4. The statistical uncertainties are estimated for  $1\text{fb}^{-1}$  of data and the systematic uncertainties are a result of the limited MC statistics and the uncertain theoretical description of the clustertime distribution used for the production of the calibration curve.<sup>23)</sup> It can be observed that the measured val-

<sup>23)</sup>Both sources of systematic uncertainties are implicitly given by the fit uncertainties of the Landau fits during production

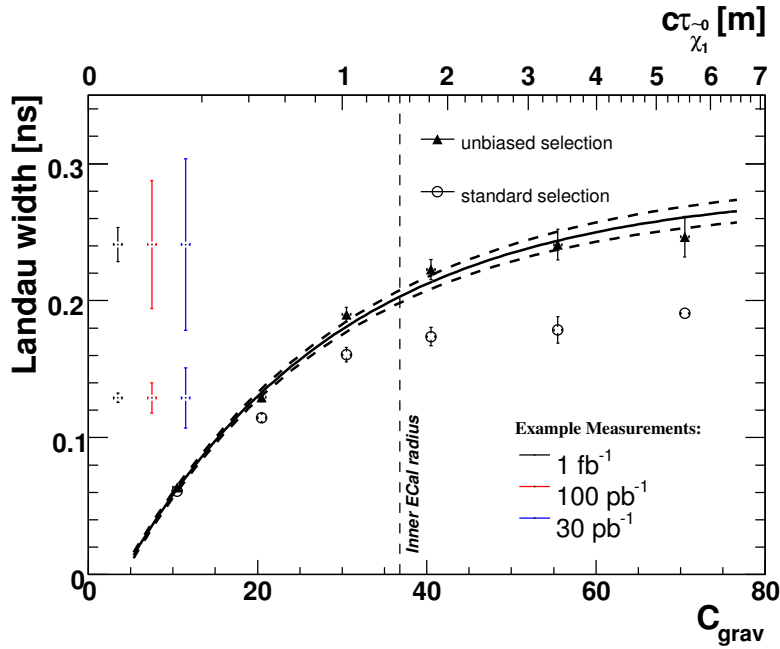


Figure 7.9: Fitted signal Landau widths as a function of  $C_{\text{grav}}$  and the decay length  $c\tau_{\tilde{\chi}_1^0}$  for the unbiased photon identification (closed symbols) and the ATLAS standard photon identification (open symbols). In addition, the expected uncertainties of two example width measurements are shown for different values of integrated luminosities.

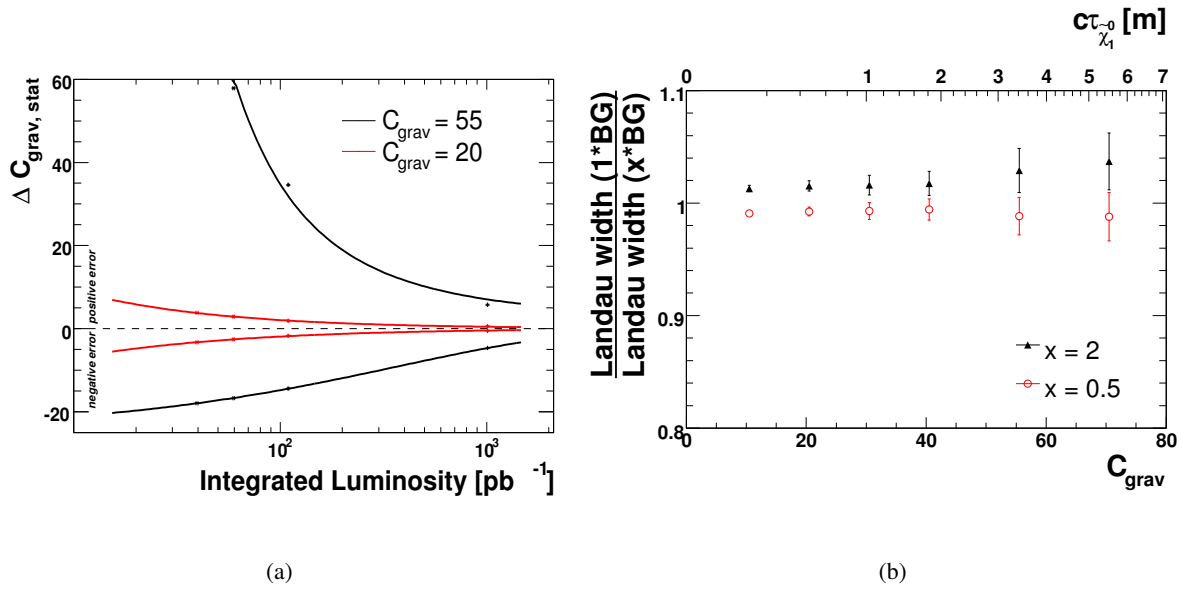


Figure 7.10: Method using the clustertime: (a) Statistical uncertainty of the  $C_{\text{grav}}$  measurement. (b) Influence of the background normalization on the determination of the Landau width.

$C_{\text{grav, theo}}$	$C_{\text{grav, meas}} \pm \text{stat.} \pm \text{sys.}$
10	$10.6 \pm^{0.2}_{0.2} \pm^{0.2}_{0.2}$
20	$19.9 \pm^{0.6}_{0.6} \pm^{0.5}_{0.4}$
30	$32.9 \pm^{1.6}_{1.5} \pm^{1.2}_{1.1}$
40	$44.2 \pm^{3.4}_{3.0} \pm^{2.6}_{2.2}$
55	$53.6 \pm^{8.2}_{6.2} \pm^{4.7}_{3.5}$
70	$57.5 \pm^{13.8}_{8.9} \pm^{5.9}_{4.3}$

Table 7.4: Method using the clustertime: Comparison of true and measured  $C_{\text{grav}}$  values for  $1 \text{ fb}^{-1}$ .

ues agree with their true values within the uncertainties. As expected, the relative uncertainties increase with increasing  $C_{\text{grav}}$  due to the saturation effect of the calibration curve.

### 7.2.3 Dependence of the clustertime method on GMSB parameters

The method using the clustertime described in the last section neglects that the neutralino lifetime is not only a function of  $C_{\text{grav}}$ , but depends also on other GMSB parameters, see Eq. (2.70). Therefore the  $C_{\text{grav}}$  value can in principle only be determined with the calibration curve in Fig. 7.9 when the other parameters are already known. Also the transformation between the  $C_{\text{grav}}$  value and the corresponding decay length, as shown in Figs. 7.9 and 7.10(b) is only valid for the special case of GMSB1-like scenarios. In addition, the other GMSB parameters influence the mass spectrum and therefore the kinematics of the decay chain. This could in turn alter the clustertime distribution, since  $\tau_{\text{cluster}}$  depends in principle on the boost and the angle distributions of the decaying neutralino.

These reasons result in two consequences: First, only the neutralino lifetime itself can be measured with a calibration curve when the other GMSB parameters are unknown. And second, it has to be investigated, if a general calibration curve independent of other GMSB parameters can be produced at all.

To study the parameter dependence of the calibration curve, additional samples of GMSB events have been produced<sup>24)</sup> in a wide range of the GMSB parameter space reasonable for this study considering experimental and theoretical constraints:

- $N_5 = 1$  and  $\tan \beta < 35$  ensure a neutralino NLSP.
- $\Lambda < 200 \text{ TeV}$  for having a reasonable cross section and to fulfil cosmological bounds [72].
- $\Lambda > 90 \text{ TeV}$  to fulfil Tevatron limits, as discussed in Sect. 2.3.4.
- $M_{\text{mess}} > \Lambda$  to fulfil theory constraints [23].
- $M_{\text{mess}} \leq 1000 \text{ TeV}$  to ensure that enough neutralinos decay inside the detector.

Table 7.5 summarizes the parameter values of the additional samples and the resulting lifetimes. For each sample only the parameters which differ from the GMSB3 scenario parameters are listed.

Following the procedure described above the signal Landau width has been determined in a fit of the clustertime distribution for each event sample. The results are shown in Fig. 7.11 as a function of

of the calibration curve.

<sup>24)</sup>For each scenario 5000 events have been generated and passed through a full GEANT4 detector simulation. A fast simulation cannot be used for a wide parameter scan, since a simulation of long-lived neutralinos is in principle not possible with ATLFAST.

Sample	$\tau_{\tilde{\chi}_1^0}$ [ns]	Sample	$\tau_{\tilde{\chi}_1^0}$ [ns]
$\text{sign}(\mu) = -$	9.47	$\tan \beta = 20, C_{\text{grav}} = 25$	2.19
$\Lambda = 120 \text{ TeV}$	4.31	$\Lambda = 120 \text{ TeV}, C_{\text{grav}} = 45$	2.87
$\Lambda = 180 \text{ TeV}$	1.11	$M_{\text{mess}} = 750 \text{ TeV}, C_{\text{grav}} = 15$	1.90
$\tan \beta = 20$	10.61	$M_{\text{mess}} = 1000 \text{ TeV}, C_{\text{grav}} = 13$	2.55
$M_{\text{mess}} = 300 \text{ TeV}$	3.85	$M_{\text{mess}} = 300 \text{ TeV}, C_{\text{grav}} = 50$	3.18
$M_{\text{mess}} = 350 \text{ TeV}$	5.35	$C_{\text{grav}} = 25$	2.32
$M_{\text{mess}} = 400 \text{ TeV}$	7.07	$C_{\text{grav}} = 35$	4.54
$M_{\text{mess}} = 450 \text{ TeV}$	9.03	$C_{\text{grav}} = 45$	7.51
$M_{\text{mess}} = 550 \text{ TeV}$	13.63	$C_{\text{grav}} = 50$	9.26
$M_{\text{mess}} = 750 \text{ TeV}$	25.57	$C_{\text{grav}} = 60$	13.34

Table 7.5: GMSB parameters and resulting  $\tilde{\chi}_1^0$  lifetimes of the event samples used to study the GMSB parameter dependence of the clustertime method. Only the listed parameters differ from the GMSB3 scenario.

$\tau_{\tilde{\chi}_1^0}^{\text{theo}}$ [ns]	$\tau_{\tilde{\chi}_1^0}^{\text{meas}} \pm \text{stat.} \pm \text{syst.}$ [ns]
0.37	$0.35 \pm^{0.03}_{0.03} \pm^{0.08}_{0.12}$
1.5	$1.6 \pm^{0.1}_{0.1} \pm^{0.1}_{0.1}$
3.3	$3.6 \pm^{0.3}_{0.2} \pm^{0.1}_{0.1}$
5.9	$5.7 \pm^{0.8}_{0.6} \pm^{0.3}_{0.2}$
11.2	$8.2 \pm^{5.4}_{1.8} \pm^{1.1}_{0.6}$

Table 7.6: Comparison of the expected and measured values of the  $\tilde{\chi}_1^0$  lifetime for  $1 \text{ fb}^{-1}$  using the clustertime method.

the  $\tilde{\chi}_1^0$  lifetime. The red data points represent the samples already used in Fig. 7.9. The same saturation effect is visible due to the decreasing photon identification efficiency and the increasing number of neutralinos decaying outside the inner detector volume. The data points can again be fitted with the empirical function (7.14) and the fit result is also shown in the figure.<sup>25)</sup> The fit parameters are given by  $p_1 = (0.254 \pm 0.006) \text{ ns}$ ,  $p_2 = 0.336 \pm 0.021$  and  $p_3 = -0.507 \pm 0.053$ . From the small spread of the measured Landau widths of the various scenarios in this figure it can be concluded that indeed  $\tau_{\tilde{\chi}_1^0}$  has the strongest effect on the Landau width and the dependence of the calibration curve on the particle masses is small. This result gives confidence that the determination of the signal Landau width of the clustertime distribution can indeed be used to determine the  $\tilde{\chi}_1^0$  lifetime in the studied GMSB parameter regions.

For the GMSB1-like scenarios used in the last section Tab. 7.6 summarizes the measured values of the  $\tilde{\chi}_1^0$  lifetime for  $1 \text{ fb}^{-1}$  using the calibration of Fig. 7.11 as well as the expected values. The systematic uncertainties again reflect the limited MC statistics and the uncertain theoretical description of the clustertime distribution used for the production of the calibration curve. It can be seen that the true values of the lifetime can be reproduced with good precision by the measurements. As expected, the relative uncertainties again increase with increasing lifetimes due to the saturation effect. The results obtained from this calibration curve are used in the global GMSB fit performed in Chap. 8 in order to constrain the underlying GMSB model.

<sup>25)</sup>Again, one cannot trust the calibration curve for  $\tau_{\tilde{\chi}_1^0} \leq 0.5 \text{ ns}$ , since the fit provides no reliable information in this region.

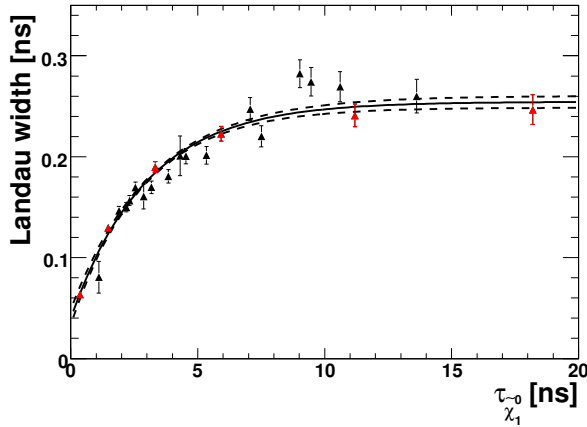


Figure 7.11: Method using the clustertime: Distribution of the fitted signal Landau widths as a function of  $\tau_{\chi_0^0}$  from event samples generated in a large part of the GMSB parameter space. The red points indicate the samples also used in Fig. 7.9.

#### 7.2.4 Method using the photon direction

The decay of neutralinos with a non-vanishing lifetime leads to photon clusters not pointing back to the primary interaction vertex. As detailed in Sect. 5.3.3, this leads to a displaced intersection point  $z_{\text{cluster}}$  of the z-axis with the projected photon path with respect to the primary interaction vertex. Alternatively to the delayed arrival time of the photon cluster, as described in Sect. 7.2.2, the reconstructed  $z_{\text{cluster}}$  can be used to determine the neutralino lifetime.

The  $z_{\text{cluster}}$  distributions of the leading photon for the example GMSB3 scenario and the main Standard Model backgrounds ( $t\bar{t}$  and  $W^\pm$  production) are shown in Fig. 7.12(a) after the preselection discussed in Sect. 6.3 for  $1 \text{ fb}^{-1}$ . As expected, the GMSB3 signal leads to larger values of  $|z_{\text{cluster}}|$ , while the Standard Model background events are distributed around zero with a width of  $\sim 75$  mm. Similarly to the method using the clustertime, the widths of the  $z_{\text{cluster}}$  distributions of various GMSB scenarios with differing neutralino lifetimes can be used to construct a calibration curve using a combined fit of the signal and background.

Again the different kinematics of signal and background processes lead to different distribution shapes: the background is best modelled by the sum of two Gaussian functions, while for the signal a Breit-Wigner function has been used.<sup>26)</sup> For a reduction of the number of free parameters in the fit, the  $z_{\text{cluster}}$  resolution can be measured from real data in clean Standard Model processes like  $Z^0 \rightarrow e^+e^-$  events.<sup>27)</sup> Once the parameters of the background contribution are fixed, four free parameters remain in the fit: the width and mean of the signal distribution as well as the number of signal and background events. Figure 7.12(b) shows the combined distribution which is nicely described by the fit result. The individual contributions of the fit function for the signal (red dashed line) and background (blue dashed line) are also shown. The Breit-Wigner width for the signal contribution is given by  $(682 \pm 35)$  mm. It

<sup>26)</sup>As in the case of the clustertime method the modelling of the signal distribution with a Breit-Wigner function is just empirically motivated. Possibly an exact function can be calculated from the full matrix element of the squark/gluino decay. In this case additional assumptions about the geometrical acceptance and the underlying model would have to be made and the possible advantages would have to be studied in detail.

<sup>27)</sup>In this process possible additional background from machine effects or soft interactions like beam-gas events have to be studied in detail.

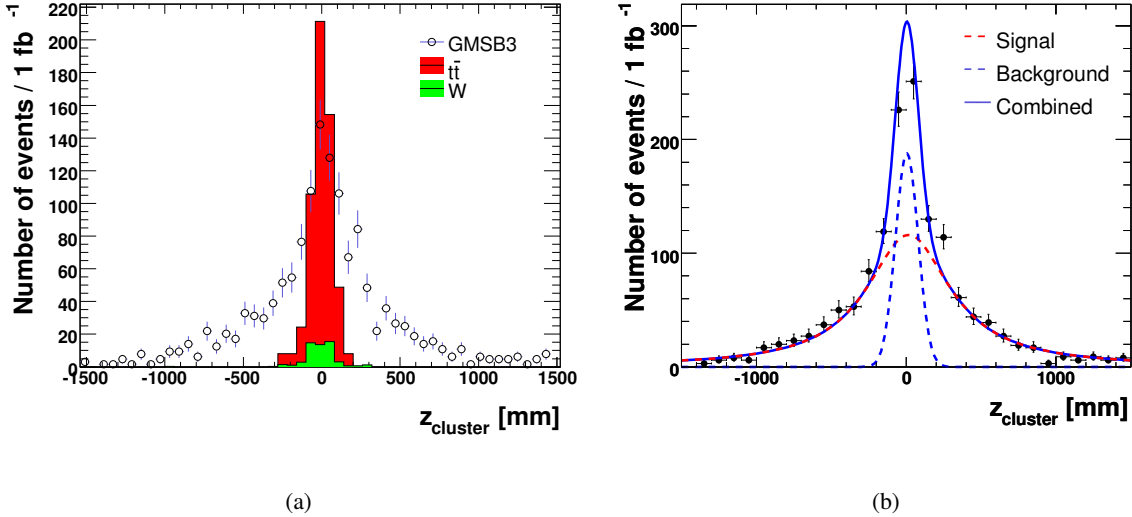


Figure 7.12: Method using the photon direction: (a)  $z_{\text{cluster}}$  distribution of the leading photon and (b) result of the combined signal and background fit of the  $z_{\text{cluster}}$  distribution for the GMSB3 scenario and the Standard Model background after the preselection for  $1 \text{ fb}^{-1}$ .

turns out that the relative normalization of the signal and background contributions cannot be reproduced as accurately as in the case of the clustertime method, since the two distributions have the same mean and a similar shape. For this reason, the  $z_{\text{cluster}}$  variable is not suited for a GMSB cross-section measurement with non-pointing photons. However, it can still be exploited for the determination of the neutralino lifetime, since similar to the method using the clustertime the procedure is stable against significant variations of the background contribution as discussed below.

To obtain a calibration curve using the Breit-Wigner width of the  $z_{\text{cluster}}$  distribution the combined fitting procedure is performed with the GMSB1-like scenarios listed in Tab. 7.2 and for each  $C_{\text{grav}}$  value a value for the signal width is determined. The results are shown in Fig. 7.13(a) as a function of  $C_{\text{grav}}$  and the decay length  $c\tau_{\tilde{\chi}_1^0}$ . Again, the empirical function (7.14) is used to fit the widths and the parameters are given by  $p_1 = (777 \pm 37) \text{ mm}$ ,  $p_2 = 0.056 \pm 0.007$  and  $p_3 = 6.40 \pm 0.35$ . The calibration curve shows the same behaviour as the one obtained from the clustertime method, including the saturation effect due to the decreasing photon identification efficiency and the increasing number of neutralinos decaying outside the inner detector volume.

As for the method using the clustertime, the influence of the size of the Standard Model background contribution on the fit result has been studied by artificially scaling the background contribution by scale factors  $x = 2$  and  $x = 0.5$ . The ratios of the fitted Breit-Wigner widths with and without scaling factor are shown in Fig. 7.13(b). Again, the measured widths depend only slightly on the scaling factor and therefore the resulting uncertainty on the  $C_{\text{grav}}$  determination is considered to be negligible.

With the calibration curve the  $C_{\text{grav}}$  values and the corresponding uncertainties can be calculated. Table 7.7 shows the results for some example scenarios. The  $z_{\text{cluster}}$  method is able to reproduce the true values of  $C_{\text{grav}}$  with statistical as well as systematic uncertainties slightly larger than the method using the clustertime (see Tab. 7.4).

Due to the reasons discussed in Sect. 7.2.3 the calibration curve in Fig. 7.13(a) is again only valid for the GMSB1-like scenarios under study. Therefore the same fitting procedure as described above has been applied to the GMSB scenarios listed in Tab. 7.5 covering a larger region of the parameter space. The resulting Breit-Wigner widths for all samples are shown in Fig. 7.14 (the samples used for the calibration curve in Fig. 7.13(a) are indicated with red data points). The data points can be fitted

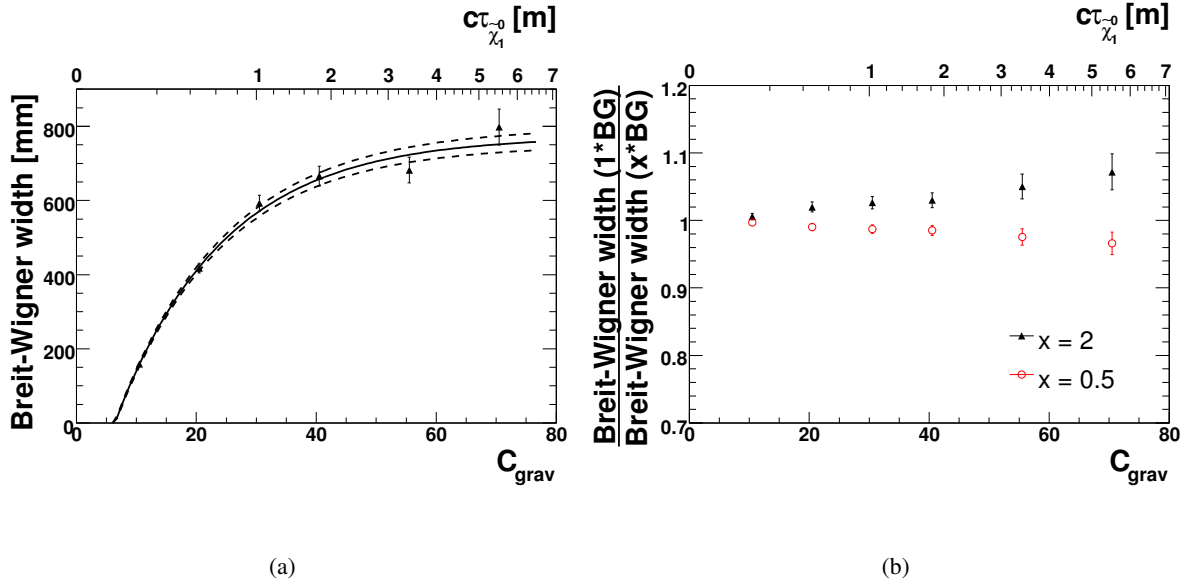


Figure 7.13: Method using the photon direction: (a) fitted signal Breit-Wigner width as a function of  $C_{\text{grav}}$  for the unbiased photon identification. (b) Influence of the background normalization on the determination of the Breit-Wigner width.

$C_{\text{grav, theo}}$	$C_{\text{grav, meas}} \pm \text{stat.} \pm \text{syst.}$
10	$10.6 \pm 0.1 \pm 0.2$
20	$20.4 \pm 0.7 \pm 0.5$
30	$32.5 \pm 2.3 \pm 1.6$
40	$41.9 \pm 5.1 \pm 3.4$
55	$44.7 \pm 8.6 \pm 4.2$

Table 7.7: Method using the photon direction: Comparison of true and measured  $C_{\text{grav}}$  values.

using the empirical function (7.14) and the resulting calibration curve shows the same behaviour as the one in Fig. 7.11, although the saturation sets in for smaller values of  $\tau_{\tilde{\chi}_1^0}$ .<sup>28)</sup> The fit parameters are given by  $p_1 = (704 \pm 14)$  mm,  $p_2 = 0.494 \pm 0.031$  and  $p_3 = -0.155 \pm 0.032$ . The spread of the measured Breit-Wigner widths is again small in this figure and it can be concluded that  $\tau_{\tilde{\chi}_1^0}$  has the strongest effect on the results and that the dependence of the calibration curve on the particle masses is small. Therefore the neutralino lifetime can be determined with the calibration method using the photon direction in the studied GMSB parameter regions.

Table 7.8 summarizes the reconstructed  $\tilde{\chi}_1^0$  lifetimes obtained from the calibration curve in Fig. 7.14 as well as the expected values for the GMSB1-like scenarios listed in Tab. 7.2. The statistical uncertainties are estimated for  $1 \text{ fb}^{-1}$ . The systematic uncertainties again reflect the limited MC statistics and the uncertain theoretical description of the  $z_{\text{cluster}}$  distribution used for the production of the calibration curve. The expected values can be reproduced with good precision by the measurement with uncertainties slightly larger than for the method using the clustertime. As expected, the relative uncertainties increase with increasing lifetimes due to the saturation effect. Since this method does not perform as well as the method using the clustertime, the obtained results are not used in the global GMSB fit in Chap. 8, but the  $z_{\text{cluster}}$  method is considered a possible way to cross check the results of the clustertime method.

<sup>28)</sup>Again, one cannot trust the calibration curve for  $\tau_{\tilde{\chi}_1^0} \leq 0.5$  ns, since the fit provides no reliable information in this region.

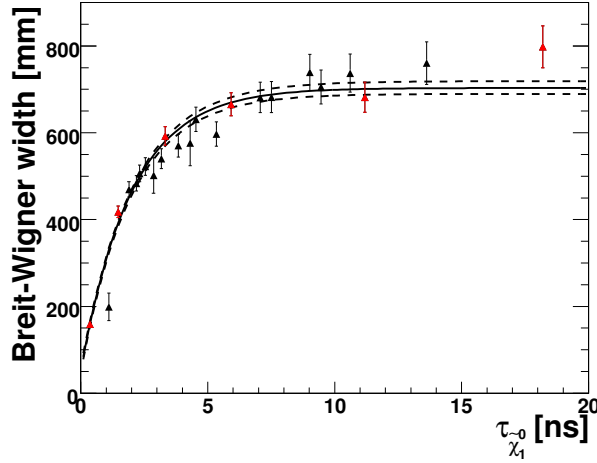


Figure 7.14: Method using the photon direction: Distribution of the fitted signal Breit-Wigner widths as a function of  $\tau_{\tilde{\chi}_1^0}$  from event samples generated in a large part of the GMSB parameter space. The red points indicate the samples also used in Fig. 7.13(a).

$\tau_{\tilde{\chi}_1^0}^{theo} [ns]$	$\tau_{\tilde{\chi}_1^0}^{meas} \pm \text{stat.} \pm \text{syst.} [ns]$
0.37	$0.36 \pm^{0.02}_{0.02} \pm^{0.02}_{0.02}$
1.5	$1.6 \pm^{0.1}_{0.1} \pm^{0.1}_{0.1}$
3.3	$3.5 \pm^{0.4}_{0.4} \pm^{0.2}_{0.1}$
5.9	$5.7 \pm^{2.5}_{1.1} \pm^{0.8}_{0.5}$
11.2	$6.8 \pm^{inf}_{1.9} \pm^{1.9}_{0.9}$

Table 7.8: Comparison of the expected and measured values of the  $\tilde{\chi}_1^0$  lifetime for  $1 \text{ fb}^{-1}$  using the  $z_{\text{cluster}}$  method.

### 7.2.5 Method using kinematic constraints in events with additional leptons

The decay time of the individual neutralinos can also be measured directly event by event in events with additional leptons in the final state [125]. Since the neutralino as well as its decay products leave no track information in the inner detector and the boost of the neutralino is unknown, additional information from the decay chain in Fig. 6.3(b) has to be used. As discussed in the following, the momentum of the second lepton in the decay chain as well as the masses of the lightest neutralino and the right-handed slepton are needed as information. For the decay of the lightest neutralino the following three equations hold:

$$\vec{v}_{\tilde{\chi}} t_D + \vec{v}_\gamma (\tau_{\text{cluster}} - t_D) = \vec{x}_\gamma, \quad (7.15)$$

where  $\vec{v}_{\tilde{\chi}}$  and  $\vec{v}_\gamma$  are the velocities of the neutralino and the photon, respectively (with  $|\vec{v}_\gamma| = c$ ).  $\tau_{\text{cluster}}$  and  $t_D$  are the measured clustertime in the calorimeter and the neutralino decay time in the laboratory frame, respectively.  $\vec{x}_\gamma$  are the coordinates of the barycenter of the photon cluster in the calorimeter. It can be seen that these equations describe the vector sum of the paths of the decaying neutralino and the final state photon by comparing these equations to Fig. 5.8. The equations contain five unknown parameters: the three components of the  $\tilde{\chi}_1^0$  velocity, the  $\tilde{\chi}_1^0$  decay time, as well as the  $\phi$ -direction of the photon momentum, which cannot be measured with the ATLAS calorimeter due to the coarse resolution in this

direction in the first compartment. Therefore, additional equations are needed in order to solve (7.15) for the neutralino decay time and to obtain the neutralino four-momentum to transform the decay time in the laboratory system to the decay time in the *neutralino rest frame*. The following kinematic constraints can be exploited:

$$p_{\tilde{G}}^2 = 0, \quad (7.16)$$

$$(p_{\tilde{G}} + p_\gamma)^2 = m_{\tilde{\chi}_1^0}^2, \quad (7.17)$$

$$(p_{\tilde{G}} + p_\gamma + p_l)^2 = m_{\tilde{l}_R}^2, \quad (7.18)$$

$$p_{\tilde{\chi}_1^0}^2 = m_{\tilde{\chi}_1^0}^2, \quad (7.19)$$

where  $p_{\tilde{G}}$  is the momentum of the gravitino (assumed to be massless),  $p_{\tilde{\chi}_1^0}$  is the neutralino momentum and  $m_{\tilde{l}_R}$  is the mass of the slepton which decays to the  $\tilde{\chi}_1^0$  and a lepton with the momentum  $p_l$ . In the following analysis it is assumed that  $m_{\tilde{l}_R}$  and  $m_{\tilde{\chi}_1^0}$  are known, *e.g.* from measurements following Sect. 7.1 (see Tab. 7.1 for the results). The Eqs. (7.16)- (7.18) are simply invariant mass constraints that can be derived by using the decay chain shown in Fig. 6.3(b). Equation (7.19) holds for on-shell particles, which is a good assumption for the long-lived neutralinos. Together with Eq. (7.15) these equations form effectively six equations with six unknowns: the  $\tilde{\chi}_1^0$  four-momentum, the  $\phi$ -direction of the photon and the  $\tilde{\chi}_1^0$  decay time in the laboratory frame. Solving these equations allows to calculate the decay time  $t'_D$  of the individual neutralinos in the neutralino rest frame.

The event preselection of Sect. 6.3 has been applied and additionally at least one reconstructed lepton (electron or muon) with  $p_{T,e} > 10$  GeV or  $p_{T,\mu} > 5$  GeV, respectively, and  $|\eta| < 2.5$  has been required. In case of several leptons in the event, the lepton forming the smaller invariant mass with the leading photon is chosen, since this is more likely the lepton of the slepton decay, as discussed for the interpretation of Fig. 7.3(b). With this event selection the Standard Model background is negligible. Since this selection degrades the signal selection efficiency significantly compared to the selections used for the methods using the clustertime or the reconstructed photon direction in the last sections, additional GMSB1-like samples with 20 000 events each have been simulated with  $C_{\text{grav}} = 10, 20, 30, 40, 50, 60$  and 70, corresponding to  $\tau_{\tilde{\chi}_1^0} = 0.37$  ns, 1.5 ns, 3.3 ns, 5.9 ns, 9.3 ns, 13.3 ns and 18.2 ns, respectively.

To obtain a solution for the Eqs. (7.15)- (7.19) a  $\chi^2$  minimization approach has been developed<sup>29)</sup> where the observables on the right-hand sides of the equations are treated as the main sources of uncertainties:<sup>30)</sup>

$$\chi^2 = \sum_{k=1}^{n_{eq}} \frac{(rhs_k - lhs_k)^2}{\sigma_k^2}, \quad (7.20)$$

where  $n_{eq}$  is the number of equations,  $rhs_k$  and  $lhs_k$  are their right- and left-hand sides, respectively, and  $\sigma_k$  are the uncertainties on the neutralino and slepton masses as well as on the coordinates of the barycenter of the photon cluster in the ECal.<sup>31)</sup>

For a good fit performance a reasonable choice for the starting values of the free fit parameters is important, especially for the direction of the neutralino momentum and the  $\phi$ -direction of the photon. From Figs. 5.8 and 5.12 can be derived that the direction of the neutralino momentum can be estimated by the direction of the photon assuming that the photon originates from the primary interaction vertex and

<sup>29)</sup>The  $\chi^2$  minimization has been compared to other numerical procedures to solve the equations and has been found to perform best.

<sup>30)</sup>This assumption is justified, since the uncertainties on the neutralino and slepton masses are by far larger than the uncertainties on the lepton and photon momenta.

<sup>31)</sup>Since the masses are measured in GeV, *i.e.*  $c = 1$ , the coordinates of the barycenter are measured in ns, as is the clustertime. The uncertainty on the coordinates of the barycenter are then assumed to be 0.05 ns.

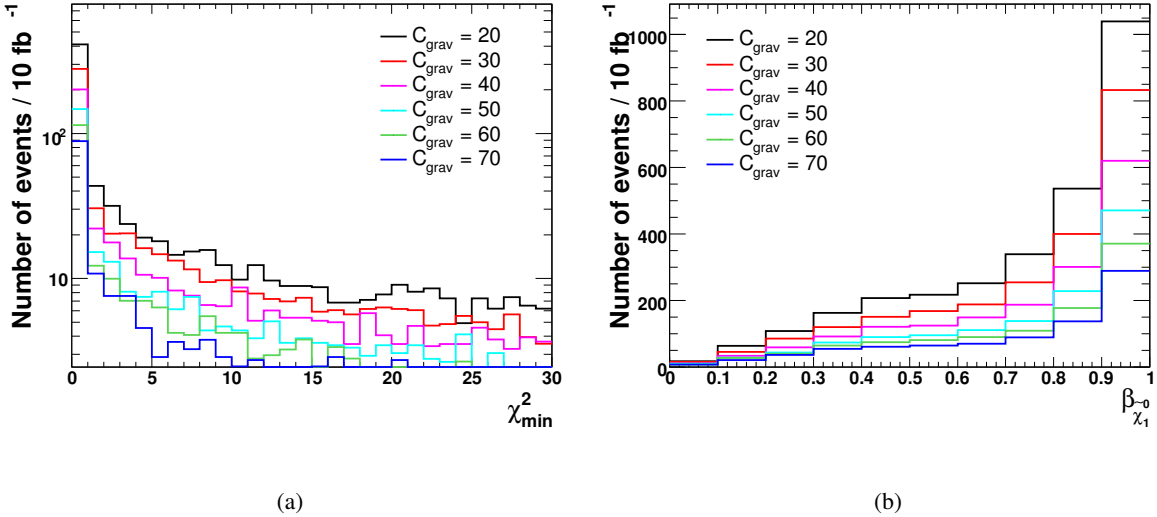


Figure 7.15: Method using kinematic constraints in events with additional leptons: (a) Distributions of the  $\chi^2_{\min}$  values and (b) distributions of the calculated neutralino  $\beta_{\tilde{\chi}_1^0}$  for  $10 \text{ fb}^{-1}$ .

the  $\phi$ -direction of the photon can be estimated by its  $\phi$ -direction again assuming the photon to originate from the primary interaction vertex.

Since the equations to solve are quadratic equations, but only a single solution can be found with a  $\chi^2$  minimization procedure, additional cuts on the quality of the fit have been imposed by rejecting unrealistic high reconstructed neutralino decay times ( $t_D > 20 \text{ ns}$ ) and large  $\chi^2_{\min}$  values ( $\chi^2_{\min} > 5$ ). The  $\chi^2_{\min}$  distributions for all samples are shown in Fig. 7.15(a) for  $10 \text{ fb}^{-1}$ . It can be observed that the distributions peak at small  $\chi^2_{\min}$  values, which shows that the fitting procedure works for most events. Figure 7.15(b) shows the distributions of the reconstructed  $\beta_{\tilde{\chi}_1^0}$  values of the neutralinos for all samples for  $10 \text{ fb}^{-1}$ . As expected, the distributions peak at 1 and the larger the  $C_{\text{grav}}$  value, the fewer neutralinos are reconstructed due to the limited detector size and the longer neutralino lifetime.

The distributions of the calculated neutralino decay time  $t'_D$  in the neutralino rest frame are shown in Fig. 7.16 for  $10 \text{ fb}^{-1}$ . As expected from the exponential decay law, the distributions for all values of  $C_{\text{grav}}$  decrease towards higher values of  $t'_D$ . Again, for larger  $C_{\text{grav}}$  values less neutralinos are reconstructed. It can be observed that the widths of the  $t'_D$  distributions increase with increasing neutralino lifetime.

Figure 7.17 shows the distributions of the ratios of the reconstructed values and the expected values for the variables  $E_{\tilde{\chi}_1^0}$ ,  $\beta_{\tilde{\chi}_1^0}$ ,  $\phi_\gamma$  and  $t'_D$  for the GMSB scenario with  $C_{\text{grav}} = 50$  to estimate the accuracy of the neutralino reconstruction. The maximum of the distributions is expected to be at 1. The expected values of the variables are obtained from the generator information by matching a reconstructed photon to a photon on generator level and this photon to the corresponding neutralino on generator level. It can be observed that all distributions have a maximum at a ratio of 1 and that  $E_{\tilde{\chi}_1^0}$ ,  $\beta_{\tilde{\chi}_1^0}$  and  $\phi_\gamma$  can be reconstructed quite accurately, while the uncertainty on  $t'_D$  is larger.

The widths of the  $t'_D$  distributions could in principle be exploited to determine  $\tau_{\tilde{\chi}_1^0}$  without any dependence on the other GMSB parameters. However, the shapes of the theoretical  $t'_D$  distributions are altered by detector efficiency and geometrical acceptance effects which cannot be calculated analytically. For this reason, a calibration procedure similar to those discussed before, relying on GEANT4-based simulated MC events, has been applied for the determination of  $\tau_{\tilde{\chi}_1^0}$ . A Landau function<sup>32)</sup> is fitted to the

<sup>32)</sup>Again, different functions to parameterize the shape of the distributions have been investigated and the Landau function has been found to describe the data best.

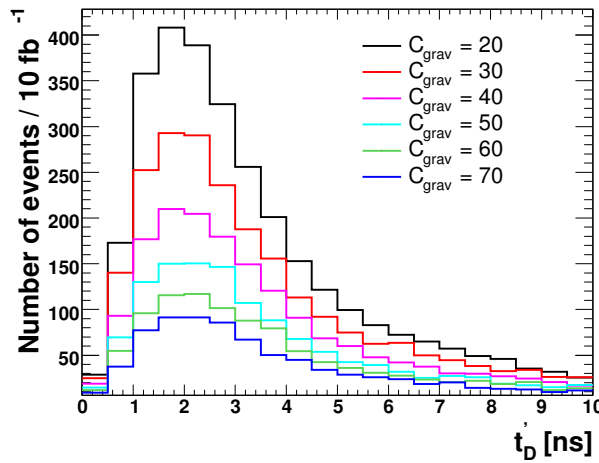


Figure 7.16: Distributions of the calculated neutralino decay time in the neutralino rest frame for  $10 \text{ fb}^{-1}$ .

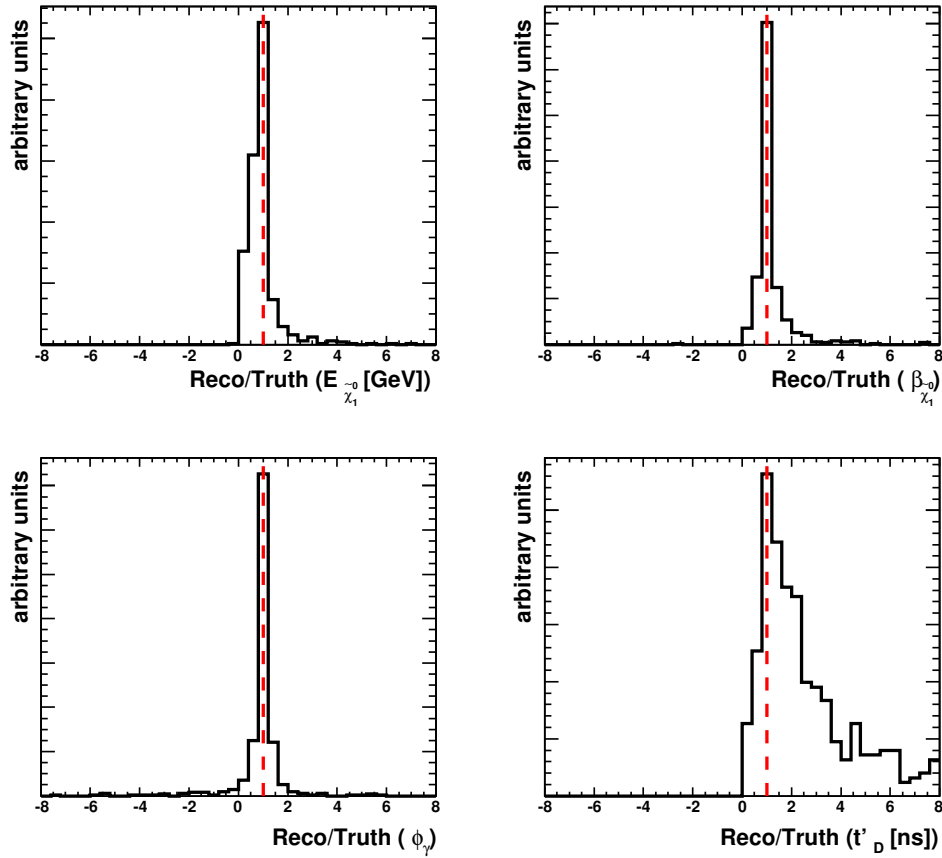


Figure 7.17: Accuracy of the numerical solution for the neutralino energy, boost, lifetime and photon azimuth angle  $\phi$ .

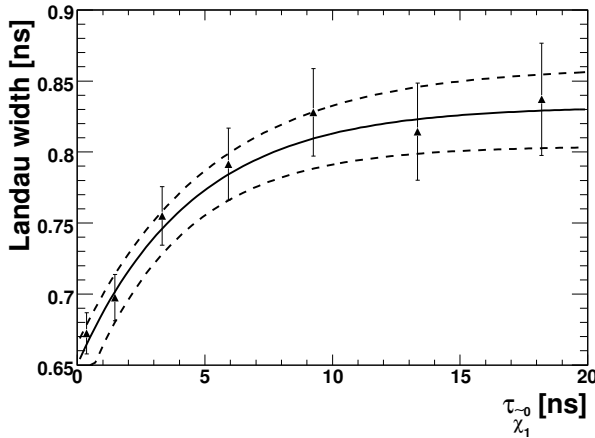


Figure 7.18: Method using kinematic constraints in events with additional leptons: Fitted signal Landau width as a function of  $\tau_{\tilde{\chi}_1^0}$ .

$\tau_{\tilde{\chi}_1^0}^{theo} [\text{ns}]$	$\tau_{\tilde{\chi}_1^0}^{meas} \pm \text{stat.} \pm \text{syst.} [\text{ns}]$
0.37	$0.58 \pm^{0.42}_{0.39} \pm^{0.67}_{0.38}$
1.5	$1.3 \pm^{0.6}_{0.5} \pm^{0.7}_{0.4}$
3.3	$3.8 \pm^{1.4}_{1.1} \pm^{1.2}_{0.7}$
5.9	$6.8 \pm^{4.4}_{2.2} \pm^{3.5}_{1.3}$
9.3	$16.7 \pm^{inf}_{5.4} \pm^{inf}_{7.5}$
13.3	$10.3 \pm^{inf}_{4.4} \pm^{inf}_{2.9}$

Table 7.9: Method using kinematic constraints: Comparison of true and measured values of  $\tau_{\tilde{\chi}_1^0}$  for  $10 \text{ fb}^{-1}$ .

distributions in Fig. 7.16 and the resulting Landau widths are shown in Fig. 7.18 as a function of  $\tau_{\tilde{\chi}_1^0}$ . Since the same behaviour of the shape of the distributions as for the other lifetime determination methods can be observed, the data points are fitted with the empirical function (7.14) and the resulting parameters are  $p_1 = 0.839 \pm 0.030$ ,  $p_2 = 0.222 \pm 0.095$  and  $p_3 = -6.81 \pm 2.77$ . Again a saturation effect is visible due to the effects discussed above. The fit uncertainties depend on the number of simulated events used in the production and on the uncertain modelling of the  $t'_D$  distribution by a Landau function.

The neutralino lifetime and its statistical and systematic uncertainties can be derived using the calibration curve and the results for the additionally produced MC samples are listed in Tab. 7.9 for  $10 \text{ fb}^{-1}$  together with the expected values. It can be observed that the method is able to reproduce the true values within the given uncertainties. Compared to the clustertime method the uncertainties are significantly enhanced. As a result, the range of possible  $\tau_{\tilde{\chi}_1^0}$  measurements is reduced. For this reason, these results are not used in the global fit of the GMSB model in Chap. 8. However, the method provides the opportunity of an additional cross-check of the results obtained from other methods.

# Chapter 8

## Determination of underlying GMSB parameters

Once a signature has been discovered at the LHC that could potentially be described by an underlying supersymmetric model, it is important to study its parameters and its compatibility with the data. Both aspects can be investigated by a global fit of the model to all observables measured in the experiment. In such a fit one obtains an estimate of the compatibility of the model in the form of a p-value and at the same time one obtains the values for the free parameters of the model that describe the data best. Especially for the study of supersymmetric models like mSUGRA or GMSB the fitting package Fittino [126, 127] has been developed. The basic ideas and functionalities of Fittino will be introduced in the following. The observables measured in Chap. 7 will then be used as input for a fit of the GMSB model in order to investigate to what extend the underlying parameters of the model used in the simulation of the events can be recovered. In addition, it will be analyzed, if the correct interpretation of the measurements in terms of the types of the involved particles can be distinguished from alternative interpretations.

### 8.1 The fitting package Fittino

Fittino is a program implemented in C++ written for comparing supersymmetric models with measured observables and for extracting the parameters of the Lagrangian. No *a priori* knowledge of the parameters is assumed, but can be used if desired. During the fitting procedure all correlations among parameters and all influences of loop-induced effects are taken into account. The theory predictions for the observables are obtained by using an independent theory code, which is interfaced to Fittino via the Les Houches Accord [95]. In this analysis the program SPheno [128] is used, but in principle also other theory codes can be implemented. SPheno allows the computation of all relevant particle masses, cross sections, branching ratios and widths, especially for the GMSB model. The formulas for the calculation of the observables (*e.g.* the endpoints of invariant mass distributions as discussed in Sect. 7.1) using these SPheno quantities are implemented in the Fittino code.<sup>1)</sup>

For the fitting procedure different algorithms are implemented in Fittino and the user can choose among them depending on the type of analysis to be performed. As an example, the  $\chi^2$  surface in the parameter space can be scanned using Markov Chains that can be used in a Bayesian or in a frequentist interpretation. In this analysis a Simulated Annealing approach has been chosen. In this method the  $\chi^2$  surface in the parameter space is treated as a potential. Once a starting point in the parameter space is

<sup>1)</sup>The formulas used for the endpoint predictions are functions of the particle masses and therefore depend on the type of the particles, *e.g.* the prediction of the di-lepton edge assumes that a  $\tilde{\chi}_2^0$  decays to a  $\tilde{l}$  and a lepton. It is not known *a priori*, if this is really the case in the measured events. Therefore the fit always assumes a certain *interpretation* of the measured observables and it has to be tested, if alternative interpretations can be distinguished (see Sect. 8.2.3).

Observable	theoretical value (ISAJET)	measured value	$\nu_{\text{ISAJET}} - \nu_{\text{SPheno}}$
$M_{l^+ l^-}^{\max}$	106.4 GeV	$108.0 \pm 4.3$ GeV	-2.0 GeV
$M_{l^+ l^- \gamma}^{\max}$	191.6 GeV	$189.6 \pm 3.8$ GeV	-2.1 GeV
$M_{l^\pm \gamma}^{\text{near,max}}$	107.9 GeV	$104.4 \pm 3.7$ GeV	-7.2 GeV
$M_{l^\pm \gamma}^{\text{far,max}}$	158.3 GeV	$161.9 \pm 3.9$ GeV	2.5 GeV
$\tau_{\tilde{\chi}_1^0}$	3.3 ns	$3.6 \pm 0.3$ ns	0.6 ns

Table 8.1: Measured and predicted values of the observables used in the global GMSB fit.

chosen, a temperature is defined, which sets the probability of a movement upwards in the potential using a Boltzmann distribution. Such a movement results in a  $\chi^2$  larger than for the parameter setting in the step before. In the process of Simulated Annealing the temperature is reduced step by step, where the reduction factor can be chosen by the user. This allows to escape from local minima in the  $\chi^2$  surface in early stages of the annealing process.

The Simulated Annealing procedure with the following MINUIT fit is repeated several times with varied values of the input observables obtained from the measurements. The variations are done within the uncertainties of each measurement. With this procedure one obtains a distribution of each free fit parameter as well as a distribution of the minimal  $\chi^2$  values. If a given parameter is *e.g.* Gaussian distributed one can obtain the mean value by a fit that coincides with the  $\chi^2$  value obtained from the MINUIT minimization for the central values of the input observables. In addition, the uncertainty on the parameter estimation can be taken from the width of the Gaussian distribution, such that all correlations between the parameters are taken into account correctly. The  $\chi^2_{\min}$  distribution has to be investigated in order to validate that the model describes the data at all.<sup>2)</sup> The number of degrees of freedom in the global fit can be obtained from a fit to this  $\chi^2_{\min}$  distribution.

## 8.2 Fitting a GMSB model to observables

The Simulated Annealing procedure as described above is used to fit a GMSB model to the observables investigated in Chap. 7 for the GMSB2 scenario: the invariant mass edges involving photons and leptons, as described in Sect. 7.1.2, and the measurement of the neutralino lifetime using the clustertime method, as described in Sect. 7.2.3. The kinematic endpoints in the invariant mass distributions involving jets are not used in the fit, since the uncertainties on their measurement are found to be too large and the interpretation of the results is too uncertain (see the discussion in Sect. 7.1.3). All input observables of the fit are summarized in Tab. 8.1. In total, five observables are used in the fit.

### 8.2.1 Expectations and fitting performance

Before using the measured values of the observables listed in Tab. 8.1 for a global GMSB fit, the fit is performed with the theoretical values of the observables as input to investigate the principal functionality and performance of the fit and the expectations for every single free fit parameter. The SPheno predictions have been used as input and an uncertainty of 1% for each observable has been assumed. The  $\chi^2_{\min}$  distribution and the central values of the GMSB parameters and their uncertainties are obtained using 400 repeated toy fits. For each toy fit, the  $\chi^2$  is minimized and the resulting distributions of the GMSB parameter values at the  $\chi^2$  minimum are used to determine the central values and the corresponding

<sup>2)</sup>This is of course more important in studies of real data where the underlying model is not *a priori* known and the p-value of the model has to be calculated. In the present MC analysis this step only serves to validate that the fitting procedure works.

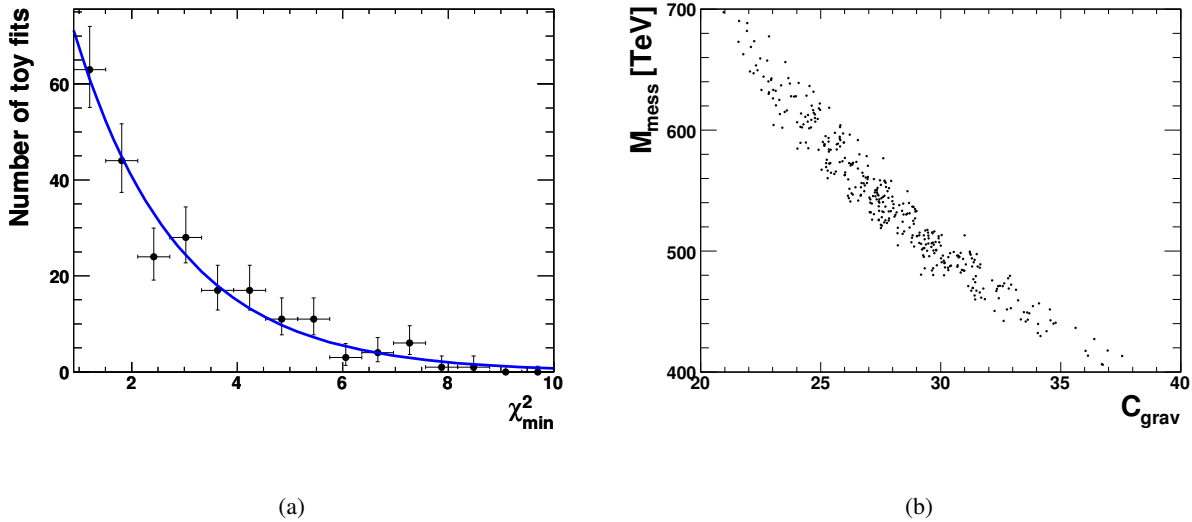


Figure 8.1: (a)  $\chi^2_{\min}$  distribution and (b) correlation between the  $M_{\text{mess}}$  and  $C_{\text{grav}}$  parameters as obtained from the toy fits of a GMSB model to the theoretical values of the input observables assuming an uncertainty on the observables of 1%.

uncertainty. The starting values of the fit have been chosen to be the expected values of the GMSB2 parameters.<sup>3)</sup>

Since the sparticle masses depend linearly on  $\Lambda$ , it is expected that this parameter can be determined accurately in the fit. On the other hand,  $M_{\text{mess}}$  enters only logarithmically in the calculation of the masses, such that the measurement of the masses alone are not able to constrain  $M_{\text{mess}}$ . In addition,  $C_{\text{grav}}$  cannot be constrained with the mass measurements. However, due to the quadratic dependence, the measurement of the neutralino lifetime can be used to constrain the product  $M_{\text{mess}} \cdot C_{\text{grav}}$ , but not the individual parameters alone (see Eq. (2.70)). In addition, no constraint on  $\tan\beta$  is expected from the fit since all measured observables depend only weakly on it. The parameters  $N_5$  and  $\text{sign}(\mu)$  are fixed to  $N_5 = 1$  and  $\text{sign}(\mu) = +$ .<sup>4)</sup> In summary the fit has four free model parameters:  $\Lambda$ ,  $M_{\text{mess}}$ ,  $\tan\beta$  and  $C_{\text{grav}}$ . Since  $M_{\text{mess}}$  and  $C_{\text{grav}}$  enter the lifetime as a product and are otherwise not constrained (apart from the logarithmic dependence of the masses on  $M_{\text{mess}}$ ), one expects a strong correlation between these parameters and a  $\chi^2$  distribution in the fit with more than one degree of freedom assuming five input observables.

The distribution of the  $\chi^2_{\min}$  values as obtained from the toy fits is shown in Fig. 8.1(a) together with a fitted  $\chi^2$  distribution. The number of degrees of freedom as given by the fit is  $1.98 \pm 0.23$ . This shows that the free fit parameters are not all completely uncorrelated, since five observables and four free fit parameters are used. Figure 8.1(b) shows the correlation between  $M_{\text{mess}}$  and  $C_{\text{grav}}$ , which is almost 100% and which explains the observed  $\chi^2$  distribution.

The distribution of the  $\Lambda$  parameter as obtained in the toy fits is shown in Fig. 8.2(a) for two choices of the starting values for the toy fit parameters. The blue curve shows the resulting Gaussian fitted to the  $\Lambda$  distribution obtained from setting the starting values to the theoretical values ( $\Lambda = 90$  TeV,  $M_{\text{mess}} = 500$  TeV and  $C_{\text{grav}} = 30$  in the case of GMSB2). One obtains  $\Lambda = (89.72 \pm 0.55)$  TeV, which

<sup>3)</sup>The parameters of the Simulated Annealing procedure, such as the temperature and its reduction factor, have been optimized in order to guarantee a smooth scanning of the parameter space independent of the starting values of the fit.

<sup>4)</sup>It has been found in [127] that  $\text{sign}(\mu) = +$  is preferred over  $\text{sign}(\mu) = -$  in many supersymmetric models by fitting the model to the existing electroweak precision observables and low-energy observables.  $N_5$  is set to 1, since in large regions of the parameter space this is necessary to have photons in the final state.

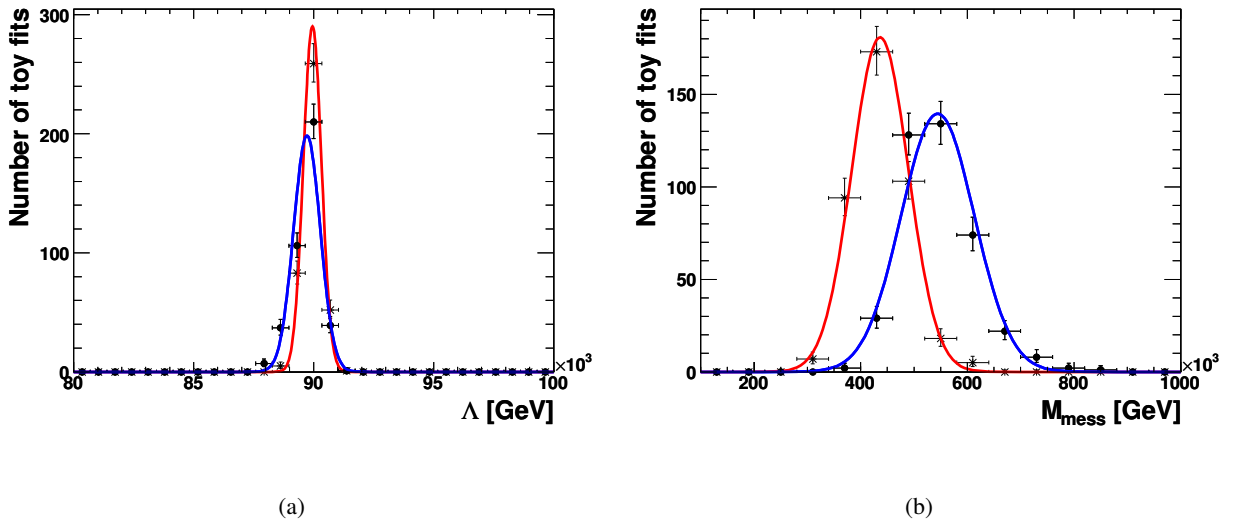


Figure 8.2: (a)  $\Lambda$  distribution and (b)  $M_{\text{mess}}$  distribution as obtained from the toy fits of a GMSB model to the theoretical values of the input observables assuming an uncertainty on the observables of 1%. Two different sets of starting values have been used for the toy fits.

shows that  $\Lambda$  can be recovered precisely as expected, since the true value is given by  $\Lambda = 90$  TeV. The red curve displays the resulting Gaussian fitted to the  $\Lambda$  distribution obtained from arbitrarily changing the starting values to  $\Lambda = 130$  TeV,  $M_{\text{mess}} = 300$  TeV and  $C_{\text{grav}} = 60$ . One can observe, that the resulting  $\Lambda$  values are stable against such variations. One obtains  $\Lambda = (89.95 \pm 0.38)$  TeV from the red curve.

The toy fit results for the  $M_{\text{mess}}$  parameter are shown in Fig. 8.2(b) for the same two choices of the starting values for the fit parameters. It can be observed from the blue curve that  $M_{\text{mess}}$  is recovered in the toy fits with the given uncertainty. However, the red curve shows that the results strongly depend on the choice for the starting values, *i.e.*  $M_{\text{mess}}$  cannot be constrained by the measured observables, as expected. Figure 8.3(a) shows the same situation for the  $C_{\text{grav}}$  parameter with the same starting value settings. Again, the results obtained from the toy fits depend on the starting values, as expected. However, due to the quadratic dependence of the neutralino lifetime, the product  $M_{\text{mess}} \cdot C_{\text{grav}}$  can be constrained. Figure 8.3(b) shows the distributions of  $M_{\text{mess}} \cdot C_{\text{grav}}$  obtained from the toy fits with both settings of the starting values and it can be observed that the result is stable. One obtains  $M_{\text{mess}} \cdot C_{\text{grav}} = (1.494 \pm 0.020) \cdot 10^7$  GeV from the blue Gaussian and  $C_{\text{grav}} = (1.501 \pm 0.020) \cdot 10^7$  GeV from the red Gaussian. These values agree well with the theoretical expectation given by  $M_{\text{mess}} \cdot C_{\text{grav}} = 1.5 \cdot 10^7$  GeV.

Finally, no constraint on  $\tan \beta$  can be derived (the expected value is  $\tan \beta = 5$ ). Figure 8.4 shows the distribution of the  $\tan \beta$  values obtained from setting the starting values of the toy fits to the true values. One can clearly observe that the distribution has no Gaussian shape and that the determination of a most probable value for  $\tan \beta$  is not possible.

### 8.2.2 Determination of GMSB parameters from realistic measurements

When using the observables listed in Tab. 8.1 with the measured values and uncertainties as input for the toy fits, one has to avoid certain sources of biases in the results. Due to the different treatment of some theoretical effects, the programs ISAJET and SPheno slightly differ in the theoretical calculation of the observables, leading to different results. Since ISAJET was used to generate the corresponding MC events in the GMSB2 scenario, while SPheno is used in the global fit, the measured observables have to be shifted towards their SPheno prediction. These differences in the predictions of both programs,

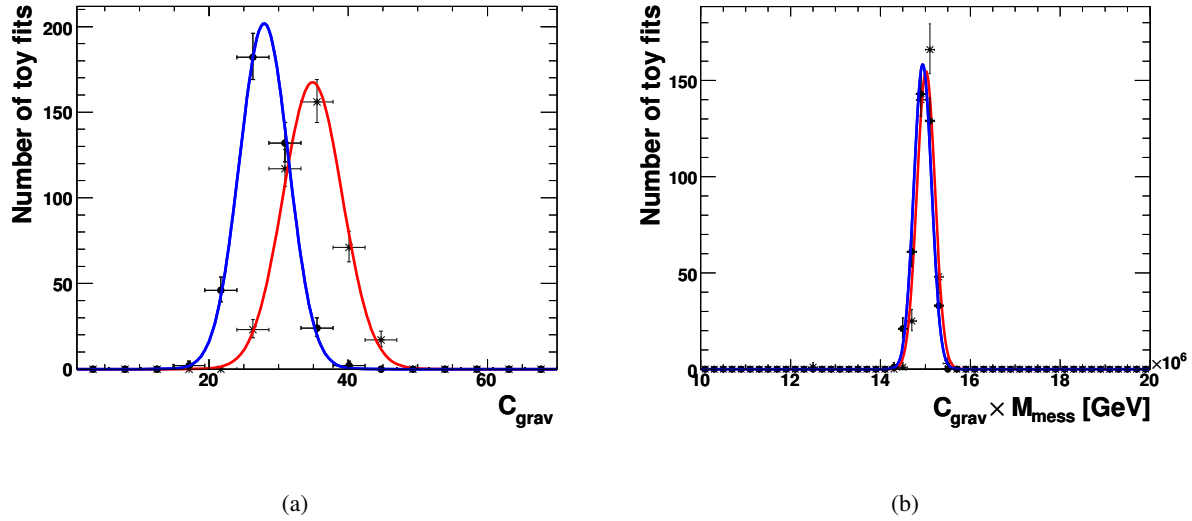


Figure 8.3: (a)  $C_{\text{grav}}$  distribution and (b)  $M_{\text{mess}} \cdot C_{\text{grav}}$  distribution as obtained from the toy fits of a GMSB model to the theoretical values of the input observables assuming an uncertainty on the observables of 1%. Two different sets of starting values have been used for the toy fits.

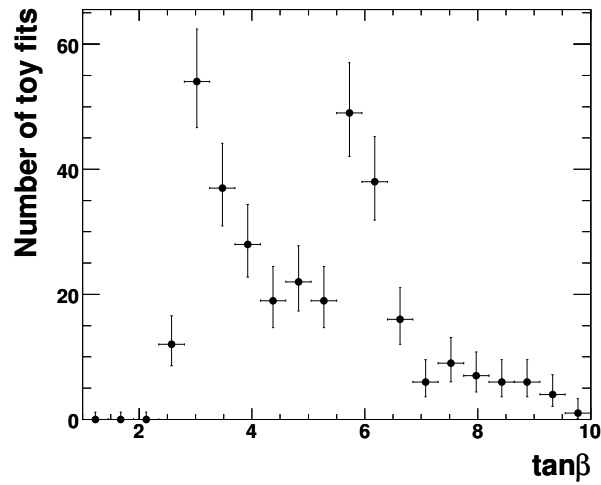


Figure 8.4:  $\tan \beta$  distribution as obtained from the toy fits of a GMSB model to the theoretical values of the input observables assuming an uncertainty on the observables of 1%.

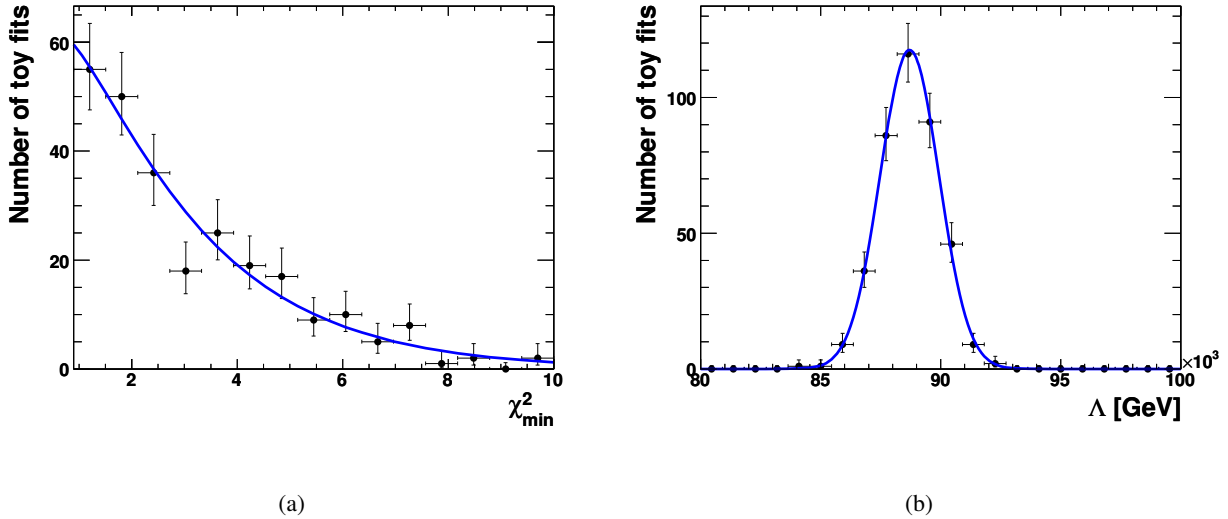


Figure 8.5: (a)  $\chi^2_{\min}$  distribution and (b)  $\Lambda$  distribution as obtained from the toy fits of a GMSB model to the measured values of the input observables and their uncertainties.

$v_{\text{SPheno}} - v_{\text{ISAJET}}$ , are also listed in Tab. 8.1 and can additionally be used as an estimate for the theoretical uncertainties of the observables.

The  $\chi^2_{\min}$  distribution as obtained from the toy fits using the measured values for the observables is shown in Fig. 8.5(a). The number of degrees of freedom as given by a fit of a  $\chi^2$  function to the data points is  $2.55 \pm 0.21$  again reflecting the strong correlation of  $M_{\text{mess}}$  and  $C_{\text{grav}}$ . The distribution of the  $\Lambda$  values obtained from the toy fits is shown in Fig. 8.5(b). It can be observed that the uncertainty on the  $\Lambda$  value is larger compared to the fit results from the last section, which is due to the larger uncertainties on the measured observables. The fit of a Gaussian to the distribution leads to  $\Lambda = (88.70 \pm 1.23)$  TeV agreeing with the expected value of  $\Lambda = 90$  TeV. Since only  $M_{\text{mess}} \cdot C_{\text{grav}}$  can be constrained in the fit, the distribution for this product is shown in Fig. 8.6(a) together with a fitted Gaussian. Again, the width of the Gaussian is larger than the one obtained in the last section due to the larger uncertainties on the measured input observables. The fit result is  $M_{\text{mess}} \cdot C_{\text{grav}} = (1.522 \pm 0.094) \cdot 10^7$  GeV agreeing with the expected value of  $M_{\text{mess}} \cdot C_{\text{grav}} = 1.5 \cdot 10^7$  GeV.

As discussed in Sect. 2.3.3, the order parameter of spontaneous supersymmetry breaking  $F$  is given by  $F = \Lambda \cdot M_{\text{mess}} \cdot C_{\text{grav}}$ . This value can easily be obtained from the fit results of each toy fit. Figure 8.6(b) shows the corresponding distribution together with a fit of a Gaussian. The central value and its uncertainty are given by  $F = (1.350 \pm 0.091) \cdot 10^{12}$  GeV $^2$  and agree well with the true value of  $F = 1.35 \cdot 10^{12}$  GeV $^2$ . This result shows that from the measurement of the neutralino lifetime, *i.e.* the determination of  $M_{\text{mess}} \cdot C_{\text{grav}}$ , together with the determination of  $\Lambda$  from the measurement of observables depending on supersymmetric particle masses the fundamental supersymmetry breaking scale can be explored in a global GMSB fit.

The GMSB parameter space can already be constrained with the existing electroweak precision observables, as well as with the low-energy observables. This has been shown in [127]. For the present study the same toy fits as described above have been performed including the observables listed in Tab. A.3<sup>5)</sup> as in [127] to check, if they have any influence on the results. The corresponding values have been shifted to their theoretical GMSB predictions in order to avoid a bias in the fit results. The

<sup>5)</sup>In total 22 additional observables have been used in the fit. The observables giving just lower or upper bounds on their values have been excluded as well as the constraint on the cosmological parameter  $\Omega$ . The Standard Model parameters  $\alpha_{\text{em}}$ ,  $G_F$ ,  $\alpha_s$ ,  $m_Z$ ,  $m_t$ ,  $m_b$  and  $m_\tau$  have been fixed to their current experimental values [9].

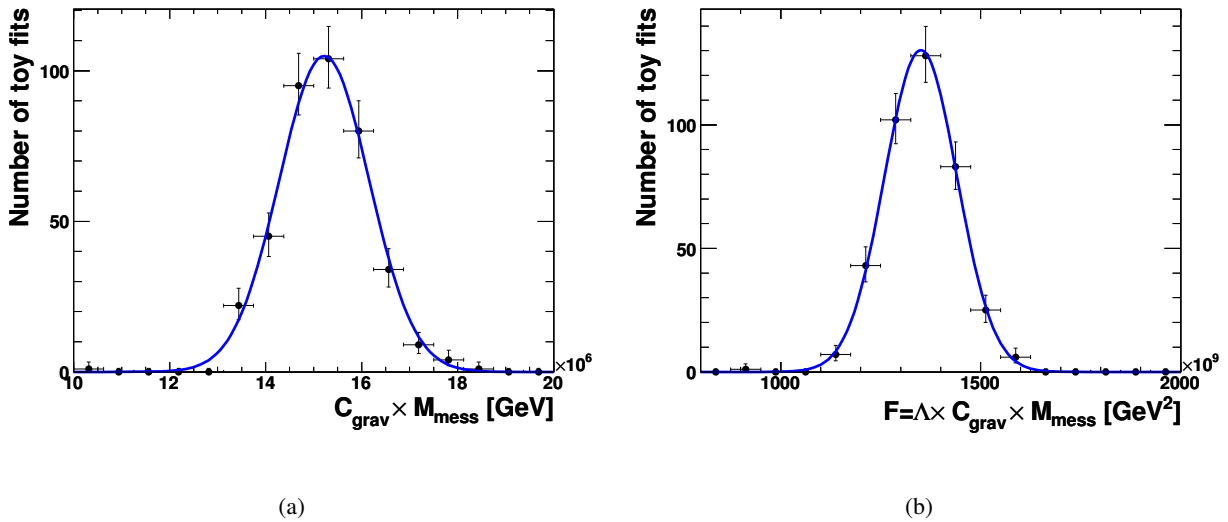


Figure 8.6: (a)  $M_{\text{mess}} \cdot C_{\text{grav}}$  distribution and (b)  $F$  distribution as obtained from the toy fits of a GMSB model to the measured values of the input observables and their uncertainties.

calculations in the toy fits have been performed by the so-called *Mastercode* [129, 130]. Figure 8.7(a) shows the distribution of the  $\chi^2_{\min}$  values as obtained from the toy fits. A  $\chi^2$  function has been fitted to the distribution and the number of degrees of freedom in the fit is determined to be  $27.86 \pm 0.41$  agreeing roughly with the expectation for 27 observables. For the determination of the GMSB parameters it has been found that the uncertainties on the parameter determination cannot be decreased by including the additional observables. As an example, Fig. 8.7(b) shows the distribution of the  $\Lambda$  values as obtained from the toy fits together with a fitted Gaussian function. The central value and its uncertainty are determined to be  $\Lambda = (88.64 \pm 1.35)$  TeV agreeing with the expected value of  $\Lambda = 90$  TeV.

### 8.2.3 Alternative data interpretations

During the fit of the GMSB model to the observables listed in Tab. 8.1 it has been assumed implicitly that the decay chain depicted in Fig. 6.3(b) leads to the measured observables event by event (this is called the *standard interpretation* in the following). *A priori* it is not known, if this is correct. There could be regions in the GMSB parameter space where a slightly different decay chain leads to a similar final state and to values for the observables that are the same as those listed in Tab. 8.1. Therefore alternative interpretations of the data have to be investigated and it has to be tested, if these lead to acceptable interpretations of the data in terms of a certain set of parameters in the GMSB parameter space.

In principal, there can be a large number of alternative interpretations and they can be constructed by changing the supersymmetric particle type in the theoretical formulas for the observables, *e.g.* in the formulas for the endpoints in invariant mass distributions as discussed in Sect. 7.1. However, the number of interpretations to be investigated can be reduced by checking whether a certain interpretation leads to the measured observables. As an example, the mass hierarchy cannot be changed arbitrarily, since this would lead to different shapes of the invariant mass distributions [18] or even to different final states. In this analysis two example interpretations are considered:

1.  $\tilde{\chi}_3^0$  **interpretation:** In the decay chain shown in Fig. 6.3(b) the  $\tilde{\chi}_2^0$  is replaced by the  $\tilde{\chi}_3^0$ , *i.e.* the decay chain

$$\tilde{q} \rightarrow \tilde{\chi}_3^0 q \rightarrow \tilde{l}_R^\pm l^\mp q \rightarrow \tilde{\chi}_1^0 l^+ l^- q \rightarrow \tilde{G} \gamma l^+ l^- q, \quad l = e, \mu \quad (8.1)$$

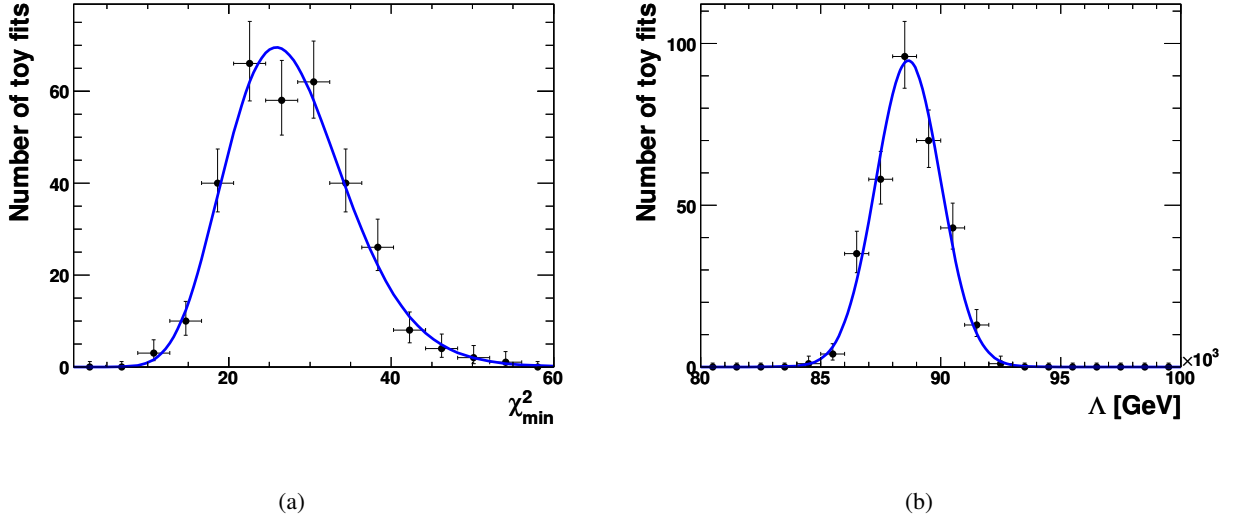


Figure 8.7: (a)  $\chi^2_{\min}$  distribution and (b)  $\Lambda$  distribution as obtained from the toy fits of a GMSB model to the measured values of the input GMSB observables and the existing electroweak precision observables and low-energy observables as listed in Tab. A.3.

is used to calculate the endpoint of the invariant mass distributions in the toy fits. In this interpretation it is assumed that the  $\tilde{\chi}_3^0$  is produced by squark or gluino decays and that its decay to the  $\tilde{\chi}_2^0$  is suppressed in a certain region of the GMSB parameter space such that the leptons used for the construction of the invariant mass distributions couple to the  $\tilde{\chi}_3^0$ . All other features of the decay chain stay the same as in Fig. 6.3(b), *e.g.* the  $\tilde{\chi}_1^0$  is the NLSP and has a non-vanishing lifetime.

During the toy fits of the  $\tilde{\chi}_3^0$  interpretation the same random seeds as for the fit in the *standard interpretation* as discussed above have been used in order to allow the comparison of the resulting  $\chi^2$  distributions and to determine which interpretation describes the data best. Figure 8.8(a) shows the correlation between the  $\chi^2_{\min}$  values for each toy fit for both interpretations. It can be observed that the  $\chi^2_{\min}$  values for the  $\tilde{\chi}_3^0$  interpretation are much larger for every toy fit than in the *standard interpretation*. Therefore this alternative can be excluded easily.

2.  $\tilde{\chi}_3^0, \tilde{l}_L$  interpretation: The interpretation of the observables as discussed above can be extended by substituting the right-handed slepton by a left-handed slepton. In the special case of the GMSB1 benchmark scenario the  $\tilde{\chi}_3^0$  has a larger mass than the left-handed sleptons (see Tab. 6.1) and therefore the decay chain

$$\tilde{q} \rightarrow \tilde{\chi}_3^0 q \rightarrow \tilde{l}_L^\pm l^\mp q \rightarrow \tilde{\chi}_1^0 l^+ l^- q \rightarrow \tilde{G} \gamma l^+ l^- q, \quad l = e, \mu \quad (8.2)$$

is possible, although largely suppressed. Nevertheless, there could be regions in the parameter space where this leads to measured values of the observables as listed in Tab. 8.1. Again, all other features of the final state are assumed to stay the same as in the *standard interpretation*. The same random seeds are used in the  $\tilde{\chi}_3^0, \tilde{l}_L$  interpretation and the resulting correlation between the  $\chi^2_{\min}$  values are shown in Fig. 8.8(b). Again, the alternative interpretation can be excluded easily, since its  $\chi^2_{\min}$  values are much larger for every toy fit.

The results obtained from the two alternative interpretations analysed here give confidence that wrong interpretations of the observables can be excluded in the case of GMSB models with photons in the final state. Nevertheless, a scan over all possible interpretations would be desireable, although this would require an enormous amount of CPU time with the current setup of Fittino.

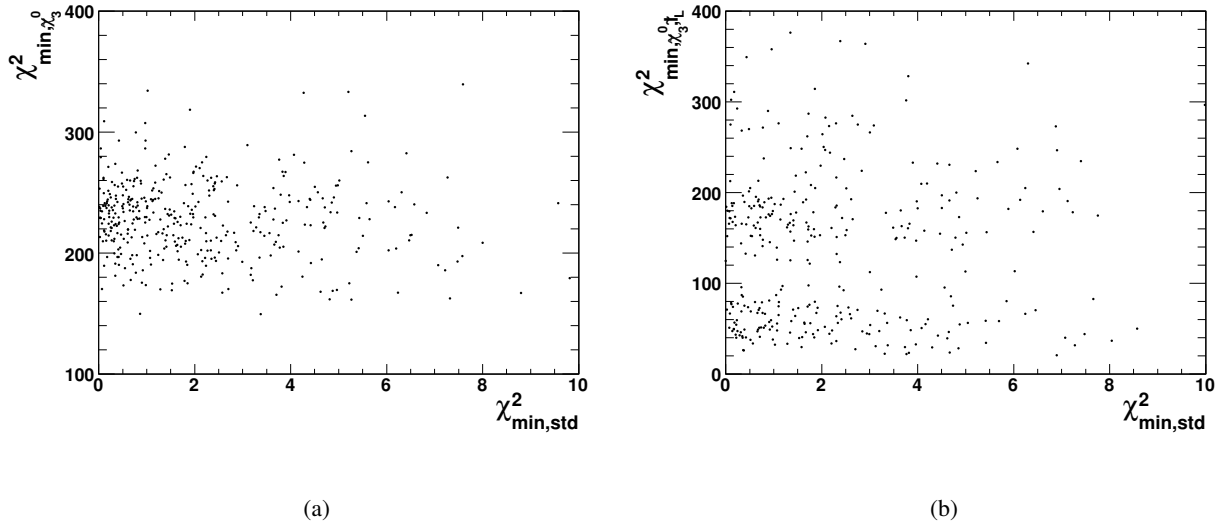


Figure 8.8: Correlations of the  $\chi^2_{\min}$  values of the *standard interpretation* of the measured observables and (a) the  $\tilde{\chi}_3^0$  interpretation and (b) the  $\tilde{\chi}_3^0, \tilde{l}_L$  interpretation as described in the text.

It should be noted that in all toy fits discussed above it has been assumed that the observables can be described by a GMSB model in *at least one interpretation*. Also this is *a priori* unknown. There could be another probably yet unknown theory which features the same final states as the GMSB model. If the data cannot be described by a GMSB model, the resulting  $\chi^2_{\text{min}}$  distributions would be unacceptable for *all possible interpretations* in terms of a GMSB model.



# Chapter 9

## Summary, conclusions and outlook

### 9.1 Summary and conclusions

With the foreseen start of LHC operation in 2009 a new energy frontier in high energy physics will be explored in  $pp$  collisions. Besides precise tests of the Standard Model and the possible investigation of the mechanism of electroweak symmetry breaking, the discovery of physics beyond the Standard Model will be among the most interesting and also most challenging tasks for the LHC experiments. As has been pointed out in this thesis, the Standard Model can not be the final theory of nature as it comprises fundamental problems of experimental as well as theoretical character. One of the most intensely investigated (and probably also most promising) candidates of a theory beyond the Standard Model is the idea of supersymmetry that predicts new particles that could directly be produced at the LHC, if their masses are on the TeV scale. Since there exist many different realizations of supersymmetric theories, measurements of the particle properties are necessary in order to constrain the possible supersymmetric parameter space.

Gauge mediated supersymmetry breaking provides a possible way to mediate supersymmetry breaking that occurs at a high scale to the electroweak scale. These models naturally feature a gravitino LSP, while the phenomenology is largely determined by the NLSP. This can *e.g.* be the lightest neutralino as well as a right-handed slepton or the lightest stau. GMSB models with a neutralino NLSP decaying to a gravitino and a photon have been investigated in this thesis. Benchmark scenarios have been studied that feature a neutralino NLSP with vanishing lifetime resulting in final states with photons coming from the primary interaction vertex as well as scenarios in which the NLSP has a non-vanishing lifetime and leads to photons being produced at a certain distance to the primary interaction vertex.

In addition to the photons in the final state, large missing transverse energy and multiple high energetic jets are expected in the  $pp$  collisions at the LHC. These final states extend the variety of supersymmetric final state topologies of mSUGRA-like models studied extensively in the past. The additional photons provide a handle to reduce the Standard Model background very efficiently leading to an almost background-free channel for early discoveries of GMSB events at the LHC. In addition, the photons can be used to measure certain properties of supersymmetric particles, like endpoints in invariant mass distributions as well as the possibly non-vanishing NLSP lifetime. These measurements can be exploited in global fits to determine the underlying GMSB parameters.

In this thesis it has been shown that the ATLAS detector has the ability to discover GMSB events with high significance in large parts of the parameter space covering both prompt and non-pointing final state photons. For both possibilities selection strategies have been optimized in order to cope with the different kinematical properties of prompt and non-pointing photons. By using an example benchmark scenario, it has been demonstrated that the measurement of kinematic endpoints in invariant mass distributions involving photons and leptons allows the determination of the masses of the two lightest neutralinos as

well as the mass of the intermediate right-handed slepton with good precision using a small data set. The measurement and the interpretation of endpoints in invariant mass distributions involving jets is more involved, but a rough estimate of the squark mass scale as well as of the gluino mass can be obtained.

The topology of the non-pointing photons in the final state can also be used to determine the NLSP lifetime. Methods have been presented that make use of different variables and approaches. It has been demonstrated that the delayed arrival time of the electromagnetic cluster of a photon in the calorimeter as well as its directional information can be exploited. If additional leptons are present in the event, kinematic constraints can be utilized that incorporate the mass measurements of the supersymmetric particles. The unbiased non-pointing photon selection provides advantages for this purpose, since it allows a more efficient identification of photons coming from late decaying neutralinos.

Finally, the mass measurements together with the measurement of the neutralino lifetime have been used as important input to global fits of the GMSB model. A Simulated Annealing approach has been applied and the possibility of determining the underlying GMSB parameters has been explored. The effective supersymmetry breaking scale  $\Lambda$  and the order parameter for spontaneous supersymmetry breaking  $F$  can be determined precisely, while for the measurement of  $\tan\beta$ , as well as for the disentanglement of  $M_{\text{mess}}$  and  $C_{\text{grav}}$  additional observables have to be taken into account. In addition it has been tested, if the measured observables interpreted in an alternative way might lead to a false parameter determination. It has been shown for two example scenarios that a wrong assignment of the decay chains leads to unacceptable  $\chi^2_{\text{min}}$  distributions showing the incompatibility of the interpretation with the data.

## 9.2 Outlook

The most important issue for first data analysis is to obtain a profound detector understanding. Especially analyses of supersymmetric scenarios make use of a variety of reconstructed objects like missing transverse energy, jets, leptons and photons. All aspects of the reconstruction of these objects have to be understood in order to perform a successful search for supersymmetric events. This includes a detailed understanding of the Standard Model background that is especially important for the search for GMSB events. The rates with which jets are misidentified as photons have to be measured and the photon identification criteria have to be optimized for a GMSB analysis with (non-pointing) photons in the final state.

For the measurement of the masses of supersymmetric particles it is essential to study the identification and reconstruction performance of the ATLAS detector for electrons, muons and photons with first data. This includes the energy resolutions and scales to obtain reliable results for the invariant mass distributions. Additionally, studies are needed in order to develop methods to determine the masses of the charginos, staus and other particles not covered in this thesis. One (possibly very complicated) method is to completely reconstruct the supersymmetric decay chain with kinematic constraints. As input for a fit additional observables such as lepton and jet momenta can be used. Due to the large jet multiplicities in supersymmetric events it might be complicated to cope with the large combinatorics in such a method. On the other hand, one could again profit from the final state photons in GMSB models with a neutralino NLSP.

For the determination of the neutralino lifetime it is important to study the timing resolution of the ECal with first data. This includes the measurement of the resolution with  $Z^0 \rightarrow e^+e^-$  events to investigate the Standard Model background contribution in the signal sample, as outlined in this thesis. Furthermore, the reconstruction of the neutralino lifetime can potentially profit from photon conversions. As an example, the direction of the photon can be measured much more precisely if it converts and the resulting electron tracks can be reconstructed. Especially the  $\phi$  direction of the photon can be determined in this way and the solution of the kinematic constraints equations used in the lifetime measurement would become much easier. Nevertheless, this might only be possible with larger datasets. Another interesting

question is, whether the neutralino decay to  $Z^0$  bosons can be exploited in order to determine the NLSP lifetime. If the decay vertex of the lepton pair resulting from the  $Z^0$  decay can be reconstructed efficiently, the decay length of every individual neutralino could be measured directly. Since the branching ratio of the neutralino decay to  $Z^0$  bosons is in general very small in the minimal GMSB model, this is again only possible with larger datasets.

It has been pointed out that the measurement of  $\tan\beta$  and the disentanglement of  $M_{\text{mess}}$  and  $C_{\text{grav}}$  is not possible with the measured observables presented in this thesis. Therefore, additional work has to be done to identify observables that depend stronger on  $\tan\beta$  and  $M_{\text{mess}}$  or  $C_{\text{grav}}$ . In the GMSB1-like scenarios the intermediate slepton can also be a stau that potentially could be exploited to get closer constraints on  $\tan\beta$ , since this parameter enters the stau mixing matrix on tree level.

It might be impossible to measure some of the properties of supersymmetric particles at the LHC. However, a lepton collider at high energies provides a much cleaner environment and the great advantage of a known initial state of the particle collisions. Especially the neutralino lifetime determination would profit from a known initial state and could be determined directly without the need of calibration curves as discussed in this thesis.



## Appendix A

# Additional tables

Table A.1 lists the Standard Model background samples used in this thesis. The generator codes, as described in Sect. 4.1, are indicated as well as the integrated luminosity for each sample. During the official ATLAS production process cuts on generator level have been applied in order to allow for a faster simulation of the relevant processes. The details are listed in Tab. A.2.

Process	Generator	$L [pb^{-1}]$
multiple jet production	PYTHIA	$\sim 10^{-5} - 30$
semi-leptonic $t\bar{t}$	HERWIG	597
full-hadronic $t\bar{t}$	HERWIG	256
$Z \rightarrow e^+e^-$	PYTHIA	331
$Z \rightarrow \mu^+\mu^-$	PYTHIA	331
$Z \rightarrow \tau^+\tau^-$	ALPGEN	465
$W \rightarrow e\nu + 2$ partons	ALPGEN	873
$W \rightarrow e\nu + 3$ partons	ALPGEN	5543
$W \rightarrow e\nu + 4$ partons	ALPGEN	14056
$W \rightarrow e\nu + 5$ partons	ALPGEN	8500
$W \rightarrow \mu\nu + 2$ partons	ALPGEN	1871
$W \rightarrow \mu\nu + 3$ partons	ALPGEN	48791
$W \rightarrow \mu\nu + 4$ partons	ALPGEN	143219
$W \rightarrow \mu\nu + 5$ partons	ALPGEN	8434
$W \rightarrow \tau\nu + 0$ parton	ALPGEN	1410
$W \rightarrow \tau\nu + 1$ parton	ALPGEN	176
$W \rightarrow \tau\nu + 2$ partons	ALPGEN	882
$W \rightarrow \tau\nu + 3$ partons	ALPGEN	704
$W \rightarrow \tau\nu + 4$ partons	ALPGEN	5321
$W \rightarrow \tau\nu + 5$ partons	ALPGEN	7874
$W\gamma$	PYTHIA	2066
$Z\gamma$	PYTHIA	3875
direct $\gamma\gamma$ production	PYTHIA	454
$WW$	HERWIG	2040
$ZZ$	HERWIG	23827
$WZ$	HERWIG	6117

Table A.1: Event samples of Standard Model background processes used in this thesis.

The electroweak precision observables and the low-energy observables measured by the  $B$ -factories,

Process	Generator cuts
$t\bar{t}$	$N_{\text{lepton}} > 0$
$Z \rightarrow e^+e^-, \mu^+\mu^-$	$p_{T,\text{lepton}} > 10 \text{ GeV},  \eta_{\text{lepton}}  < 2.7$
$Z \rightarrow \tau^+\tau^-$	$ \eta_{\text{lepton}}  < 2.7$
$W \rightarrow e\nu, \mu\nu$	$N_{\text{jet}} > 0, p_{T,\text{jet}_1} > 80 \text{ GeV},  \eta_{\text{jet}_1}  < 5, E_{\text{T}}^{\text{miss}} > 50 \text{ GeV}$
$W \rightarrow \tau\nu$	$N_{\text{jet}} > 0, p_{T,\text{jet}_1} > 80 \text{ GeV},  \eta_{\text{jet}_1}  < 5, E_{\text{T}}^{\text{miss}} > 50 \text{ GeV}, N_{\text{lepton}} > 0, p_{T,\text{lepton}} > 10 \text{ GeV},  \eta_{\text{lepton}}  < 2.7$
$W\gamma, Z\gamma$	$N_\gamma > 0, p_{T,\gamma} > 25 \text{ GeV},  \eta_\gamma  < 2.7$
$\gamma\gamma$	$N_\gamma > 1, p_{T,\gamma} > 20 \text{ GeV},  \eta_\gamma  < 2.7$
$WW, ZZ, WZ$	$N_{\text{lepton}} > 0, p_{T,\text{lepton}} > 10 \text{ GeV},  \eta_{\text{lepton}}  < 2.8$

Table A.2: Cuts on generator level imposed during the MC production procedure for the datasets used in this thesis.

kaon experiments, LEP, SLC and the TeVatron, as well as the measurement of  $(g - 2)_\mu$  as used in the toy fits in Sect. 8.2.2 are listed in Tab. A.3 with their current experimental values and uncertainties.

Observable	Experimental Value	Uncertainty		Exp. Reference
		stat	syst	
$\text{BR}(B \rightarrow s\gamma)/\text{BR}(B \rightarrow s\gamma)_{\text{SM}}$	1.117	0.076	0.096	[131]
$\text{BR}(B \rightarrow \tau\nu)/\text{BR}(B \rightarrow \tau\nu)_{\text{SM}}$	1.15	0.40		[132, 133, 134]
$\text{BR}(B_s \rightarrow X_s\ell\ell)/\text{BR}(B_s \rightarrow X_s\ell\ell)_{\text{SM}}$	0.99	0.32		[131]
$\Delta m_{B_s}/\Delta m_{B_s}^{\text{SM}}$	1.11	0.01	0.32	[135]
$\frac{\Delta m_{B_s}/\Delta m_{B_s}^{\text{SM}}}{\Delta m_{B_d}/\Delta m_{B_d}^{\text{SM}}}$	1.09	0.01	0.16	[131, 135]
$\Delta \varepsilon_K/\Delta \varepsilon_K^{\text{SM}}$	0.92	0.14		[135]
$\text{BR}(K \rightarrow \mu\nu)/\text{BR}(K \rightarrow \mu\nu)_{\text{SM}}$	1.008	0.014		[136]
$a_\mu^{\text{exp}} - a_\mu^{\text{SM}}$	$30.2 \times 10^{-10}$	$8.8 \times 10^{-10}$	$2.0 \times 10^{-10}$	[137, 138, 139, 140, 141]
$\sin^2 \theta_{\text{eff}}$	0.2324	0.0012		[9]
$\Gamma_Z$	2.4952 GeV	0.0023 GeV	0.001 GeV	[9]
$R_l$	20.767	0.025		[9]
$R_b$	0.21629	0.00066		[9]
$R_c$	0.1721	0.003		[9]
$A_{\text{fb}}(b)$	0.0992	0.0016		[9]
$A_{\text{fb}}(c)$	0.0707	0.0035		[9]
$A_b$	0.923	0.020		[9]
$A_c$	0.670	0.027		[9]
$A_l$	0.1513	0.0021		[9]
$A_\tau$	0.1465	0.0032		[9]
$A_{\text{fb}}(l)$	0.01714	0.00095		[9]
$\sigma_{\text{had}}$	41.540 nb	0.037 nb		[9]
$m_W$	80.399 GeV	0.025 GeV	0.010 GeV	[4]

Table A.3: Measurements from  $B$ -factories, kaon experiments, LEP, SLC and the TeVatron, as well as the measurement of  $(g - 2)_\mu$  as used in the toy fits.

# Bibliography

- [1] S. L. Glashow, *Partial-symmetries of weak interactions*, Nucl. Phys. **22** (1961) no. 4, 579.
- [2] S. Weinberg, *A Model of Leptons*, Phys. Rev. Lett. **19** (1967) no. 21, 1264.
- [3] A. Salam, *Elementary Particle Theory*, Almquist and Wiksell (1968) 367.
- [4] Particle Data Group Collaboration, C. Amsler *et al.*, *Review of particle physics*, Phys. Lett. **B667** (2008) 1.
- [5] M. Kobayashi and T. Maskawa, *CP violation in the renormalizable theory of weak interactions*, Prog. Theo. Phys. **49** (1973) 652.
- [6] SNO Collaboration, Q. R. Ahmad *et al.*, *Direct evidence for neutrino flavor transformation from neutral-current interactions in the Sudbury Neutrino Observatory*, Phys. Rev. Lett. **89** (2002) 011301, nucl-ex/0204008.
- [7] LEP Working Group for Higgs boson searches, R. Barate *et al.*, *Search for the standard model Higgs boson at LEP*, Phys. Lett. **B565** (2003) 61, hep-ex/0306033.
- [8] TeVatron Higgs working group, *Combined CDF and DZero Upper Limits on Standard Model Higgs-Boson Production with up to  $4.2\text{fb}^{-1}$  of Data*, arXiv:0903.4001.
- [9] ALEPH Collaboration and DELPHI Collaboration and L3 Collaboration and OPAL Collaboration and SLD Collaboration, *Precision electroweak measurements on the Z resonance*, Phys. Rept. **427** (2006) 257, hep-ex/0509008.
- [10] H. Flächer *et al.*, *Gfitter - Revisiting the Global Electroweak Fit of the Standard Model and Beyond*, Eur. Phys. J. **C60** (2009) 543, arXiv:0811.0009.
- [11] M. Goebel, *Global Fits of the electroweak Standard Model and beyond with Gfitter*, arXiv:0905.2488.
- [12] G. 't Hooft, *Renormalization of massless Yang-Mills fields*, Nucl. Phys. (1971) 173.
- [13] G. 't Hooft, *Renormalizable Lagrangians for massive Yang-Mills fields*, Nucl. Phys. (1971) 167.
- [14] H. Fritzsch, M. Gell-Mann, and H. Leutwyler, *Advantages of the Color Octet Gluon Picture*, Phys. Lett. **B47** (1973) 365.
- [15] D. J. Gross and F. Wilczek, *Ultraviolet behaviour of non-abelian gauge theories*, Phys. Rev. Lett. **30** (1973) 1343.
- [16] H. D. Politzer, *Reliable perturbative results for strong interactions?*, Phys. Rev. Lett. **30** (1973) 1346.

- [17] ZEUS Collaboration, A. M. Cooper-Sarkar, *Extraction of the proton parton density functions using a NLO-QCD fit of the combined H1 and ZEUS inclusive DIS cross sections*, arXiv:0808.1854.
- [18] The ATLAS Collaboration, G. Aad *et al.*, *Expected Performance of the ATLAS Experiment - Detector, Trigger and Physics*, arXiv:0901.0512.
- [19] S. Catani *et al.*, *QCD*, hep-ph/0005025.
- [20] H. Georgi and S. L. Glashow, *Unity of All Elementary-Particle Forces*, Phys. Rev. Lett. **32** (1974) no. 8, 438.
- [21] H. Nilles, *Supersymmetry, Supergravity and Particle Physics*, Phys. Rept. **110** (1984) 1.
- [22] H. E. Haber and G. L. Kane, *The Search for Supersymmetry: Probing Physics Beyond the Standard Model*, Phys. Rept. **117** (1985) 75.
- [23] S. Martin, *A supersymmetry primer*, hep-ph/9709356.
- [24] A. D. Sakharov, *Violation of CP invariance, C asymmetry, and baryon asymmetry in the universe*, JETP Lett. **5** (1967) 24.
- [25] A. G. Cohen, D. B. Kaplan, and A. E. Nelson, *Progress in electroweak baryogenesis*, Ann. Rev. Nucl. Part. Sci. **43** (1993) 27, hep-ph/9302210.
- [26] M. B. Gavela, P. Hernandez, J. Orloff, O. Pene, and C. Quimbay, *Standard model CP violation and baryon asymmetry. Part 2: Finite temperature*, Nucl. Phys. **B430** (1994) 382, hep-ph/9406289.
- [27] H. E. Haber, *The status of the minimal supersymmetric standard model and beyond*, Nucl. Phys. Proc. Suppl. **62** (1998) 469, hep-ph/9709450.
- [28] WMAP Collaboration, E. Komatsu *et al.*, *Five-Year Wilkinson Microwave Anisotropy Probe (WMAP) Observations: Cosmological Interpretation*, Astrophys. J. Suppl. **180** (2009) 330, arXiv:0803.0547.
- [29] S. Weinberg, *Implications of Dynamical Symmetry Breaking*, Phys. Rev. **D13** (1976) 974.
- [30] S. Weinberg, *Implications of Dynamical Symmetry Breaking: An Addendum*, Phys. Rev. **D19** (1979) 1277.
- [31] E. Gildener, *Gauge Symmetry Hierarchies*, Phys. Rev. **D14** (1976) 1667.
- [32] L. Susskind, *Dynamics of Spontaneous Symmetry Breaking in the Weinberg- Salam Theory*, Phys. Rev. **D20** (1979) 2619.
- [33] Z. Bern, L. J. Dixon, and R. Roiban, *Is  $N = 8$  Supergravity Ultraviolet Finite?*, Phys. Lett. **B644** (2007) 265, hep-th/0611086.
- [34] S. Coleman and J. Mandula, *All Possible Symmetries of the S Matrix*, Phys. Rev. **159** (1967) no. 5, 1251.
- [35] R. Haag, J. T. Lopuszanski, and M. Sohnius, *All Possible Generators of Supersymmetries of the S Matrix*, Nucl. Phys. **B88** (1975) 257.

- [36] W. Pauli, *The Connection Between Spin and Statistics*, Phys. Rev. **58** (1940) no. 8, 716.
- [37] R. Barbier *et al.*, *R-parity violating supersymmetry*, Phys. Rept. **420** (2005) 1, hep-ph/0406039.
- [38] H. K. Dreiner, *An introduction to explicit R-parity violation*, hep-ph/9707435.
- [39] G. R. Farrar and P. Fayet, *Phenomenology of the production, decay, and detection of new hadronic states associated with supersymmetry*, Phys. Lett. **B76** (1978) no. 5, 575.
- [40] A. Masiero and J. W. F. Valle, *A model for spontaneous R parity breaking*, Phys. Lett. **B251** (1990) no. 2, 273.
- [41] P. Fileviez Perez and S. Spinner, *Spontaneous R-Parity Breaking in SUSY Models*, arXiv:0904.2213.
- [42] M. Kuroda, *Complete Lagrangian of MSSM*, hep-ph/9902340.
- [43] L. O'Raifeartaigh, *Spontaneous symmetry breaking for chiral scalar superfields*, Nucl. Phys. **B96** (1975) no. 2, 331.
- [44] W. Rarita and J. Schwinger, *On a Theory of Particles with Half-Integral Spin*, Phys. Rev. **60** (1941) no. 1, 61.
- [45] E. Cremmer *et al.*, *Spontaneous symmetry breaking and Higgs effect in supergravity without cosmological constant*, Nucl. Phys. **B147** (1979) no. 1, 105.
- [46] E. Cremmer *et al.*, *Yang-Mills theories with local supersymmetry: Lagrangian, transformation laws and super-Higgs effect*, Nucl. Phys. **B212** (1983) no. 3, 413.
- [47] L. Alvarez-Gaume, J. Polchinski, and M. Wise, *Minimal Low-Energy Supergravity*, Nucl. Phys. **B221** (1983) 495.
- [48] L. Ibanez, *Locally Supersymmetric SU(5) Grand Unification*, Phys. Lett. **B118** (1982) 73.
- [49] J. Ellis, D. Nanopoulos, and K. Tamvakis, *Grand Unification in Simple Supergravity*, Phys. Lett. **B121** (1983) 123.
- [50] K. Inoue, A. Kakuto, H. Komatsu, and S. Takeshita, *Aspects of Grand Unified Models with Softly Broken Supersymmetry*, Prog. Theor. Phys. **68** (1982) 927.
- [51] A. Chamseddine, R. Arnowitt, and P. Nath, *Locally Supersymmetric Grand Unification*, Phys. Rev. Lett. **49** (1982) 970.
- [52] L. Alvarez-Gaume, M. Claudson, and M. Wise, *Low-Energy Supersymmetry*, Nucl. Phys. **B207** (1982) 96.
- [53] M. Dine and A. Nelson, *Dynamical supersymmetry breaking at low-energies*, Phys. Rev. **D48** (1993) 1277, hep-ph/9303230.
- [54] M. Dine, A. Nelson, and Y. Shirman, *Low-energy dynamical supersymmetry breaking simplified*, Phys. Rev. **D51** (1995) 1362, hep-ph/9408384.
- [55] M. Dine, A. Nelson, Y. Nir, and Y. Shirman, *New tools for low-energy dynamical supersymmetry breaking*, Phys. Rev. **D53** (1996) 2658, hep-ph/9507378.

- [56] S. P. Martin, *Generalized messengers of supersymmetry breaking and the sparticle mass spectrum*, Phys. Rev. **D55** (1997) 3177, hep-ph/9608224.
- [57] J. A. Bagger, K. T. Matchev, D. M. Pierce, and R.-J. Zhang, *Gauge and Yukawa unification in models with gauge-mediated supersymmetry breaking*, Phys. Rev. Lett. **78** (1997) 1002, hep-ph/9611229.
- [58] D0 Collaboration, V. M. Abazov *et al.*, *Search for charged massive stable particles with the D0 detector*, arXiv:0809.4472.
- [59] J. L. Feng, J.-F. Grivaz, and J. Nachtman, *Searches for Supersymmetry at High-Energy Colliders*, arXiv:0903.0046.
- [60] ALEPH Collaboration, A. Heister *et al.*, *Search for gauge mediated SUSY breaking topologies in  $e^+e^-$  collisions at center-of-mass energies up to 209 GeV*, Eur. Phys. J. **C25** (2002) 339, hep-ex/0203024.
- [61] M. Gataullin, S. Rosier, L. Xia, and H. Yang, *Searches for Gauge-Mediated SUSY Breaking Topologies with the L3 Detector at LEP*, AIP Conf. Proc. **903** (2007) 217, hep-ex/0611010.
- [62] DELPHI Collaboration, *Photon Events with Missing Energy at  $\sqrt{s} = 130$  to 209 GeV*, DELPHI 2002-077 CONF 611 .
- [63] OPAL Collaboration, G. Abbiendi *et al.*, *Searches for gauge-mediated supersymmetry breaking topologies in  $e^+ e^-$  collisions at LEP2*, Eur. Phys. J. **C46** (2006) 307, hep-ex/0507048.
- [64] D0 Collaboration, V. M. Abazov *et al.*, *Search for supersymmetry with gauge-mediated breaking in diphoton events at D $\emptyset$* , Phys. Rev. Lett. **94** (2005) 041801, hep-ex/0408146.
- [65] D0 Collaboration, V. M. Abazov *et al.*, *Search for supersymmetry in di-photon final states at  $\sqrt{s} = 1.96$  TeV*, arXiv:0710.3946.
- [66] D0 Collaboration, V. M. Abazov *et al.*, *Search for long-lived particles decaying into electron or photon pairs with the D0 detector*, Phys. Rev. Lett. **101** (2008) 111802, arXiv:0806.2223.
- [67] CDF Collaboration, D.E. Acosta *et al.*, *Search for anomalous production of diphoton events with missing transverse energy at CDF and limits on gauge- mediated supersymmetry-breaking models*, Phys. Rev. **D71** (2005) 031104, hep-ex/0410053.
- [68] CDF Collaboration, T. Aaltonen *et al.*, *Search for Heavy, Long-Lived Neutralinos that Decay to Photons at CDF II Using Photon Timing*, Phys. Rev. **D78** (2008) 032015, arXiv:0804.1043.
- [69] TeVatron SUSY Working Group, R. L. Culbertson *et al.*, *Low scale and gauge mediated supersymmetry breaking at the Fermilab Tevatron Run II*, hep-ph/0008070.
- [70] CDF and D0 Collaboration, V. Buescher *et al.*, *Combination of CDF and D0 limits on a gauge mediated SUSY model using diphoton and missing transverse energy channel*, hep-ex/0504004.
- [71] CDF and D0 Collaboration, S. S. Yu, *Searches for New Physics at the Tevatron in Photon and Jet Final States*, arXiv:0905.2285.
- [72] M. Viel *et al.*, *Constraining warm dark matter candidates including sterile neutrinos and light gravitinos with WMAP and the Lyman- alpha forest*, Phys. Rev. **D71** (2005) 063534, astro-ph/0501562.

- [73] K. Ichikawa *et al.*, *Constraining Light Gravitino Mass from Cosmic Microwave Background*, arXiv:0905.2237.
- [74] D. G. Cerdeno, Y. Mambrini, and A. Romagnoni, *Gravitino dark matter in hybrid gauge-gravity models*, arXiv:0907.4985.
- [75] J. Kersten and O. Lebedev, *Gravitino Dark Matter in Gravity Mediation*, arXiv:0905.3711.
- [76] E. A. Baltz and H. Murayama, *Gravitino warm dark matter with entropy production*, JHEP **05** (2003) 067, astro-ph/0108172.
- [77] M. Fujii and T. Yanagida, *Natural gravitino dark matter and thermal leptogenesis in gauge-mediated supersymmetry-breaking models*, Phys. Lett. **B549** (2002) no. 3-4, 273.
- [78] A. de Gouvea, T. Moroi, and H. Murayama, *Cosmology of supersymmetric models with low-energy gauge mediation*, Phys. Rev. **D56** (1997) 1281, hep-ph/9701244.
- [79] O. S. Bruening *et al.*, *LHC Design Report*. CERN, Geneva, 2004.
- [80] ATLAS Collaboration, G. Aad *et al.*, *The ATLAS Experiment at the CERN Large Hadron Collider*, JINST **3** (2008) S08003.
- [81] M. Aharouche *et al.*, *Energy linearity and resolution of the ATLAS electromagnetic barrel calorimeter in an electron test-beam*, Nucl. Instrum. Meth. **568** (2006) no. 2, 601.
- [82] ATLAS Collaboration, *ATLAS first-level trigger: Technical design report*, CERN-LHCC-98-14 .
- [83] C. Arnault *et al.*, *The ATLAS Computing Workbook*, 2007.
- [84] T. Sjostrand, *Monte Carlo Generators*, hep-ph/0611247.
- [85] M. A. Dobbs *et al.*, *Les Houches guidebook to Monte Carlo generators for hadron collider physics*, hep-ph/0403045.
- [86] D. Costanzo *et al.*, *ATLAS detector simulation: status and outlook*, ATL-SOFT-PUB-2005-004 (2005) .
- [87] ATLAS Collaboration, G. Duckeck *et al.*, *ATLAS computing: Technical design report*, CERN-LHCC-2005-022 .
- [88] E. Richter-Was, D. Froidevaux, and L. Poggioli, *ATLFAST 2.0, a fast simulation package for ATLAS*, ATL-PHYS-98-131 .
- [89] B. Andersson *et al.*, *Parton fragmentation and string dynamics*, Phys. Rept. **97** (1983) no. 2-3, 31.
- [90] T. Sjostrand, S. Mrenna, and P. Skands, *PYTHIA 6.4 physics and manual*, JHEP **05** (2006) 026, hep-ph/0603175.
- [91] G. Corcella *et al.*, *HERWIG 6: An event generator for hadron emission reactions with interfering gluons (including supersymmetric processes)*, JHEP **01** (2001) 010, hep-ph/0011363.
- [92] M. Mangano *et al.*, *ALPGEN, a generator for hard multiparton processes in hadronic collisions*, JHEP **07** (2003) 001, hep-ph/0206293.

- [93] S. Frixione and B. R. Webber, *Matching NLO QCD computations and parton shower simulations*, JHEP **06** (2002) 029, hep-ph/0204244.
- [94] B. Allanach, S. Kraml, and W. Porod, *Comparison of SUSY mass spectrum calculations*, hep-ph/0207314.
- [95] P. Skands *et al.*, *SUSY Les Houches accord: Interfacing SUSY spectrum calculators, decay packages, and event generators*, JHEP **07** (2004) 036, hep-ph/0311123.
- [96] M. Dobbs and J. B. Hansen, *The HepMC C++ Monte Carlo event record for High Energy Physics*, Computer Physics Communications **134** (2001) no. 1, 41.
- [97] M. R. Whalley, D. Bourilkov, and R. C. Group, *The Les Houches Accord PDFs (LHAPDF) and Lhaglue*, hep-ph/0508110.
- [98] T. Sjostrand, S. Mrenna, and P. Skands, *A Brief Introduction to PYTHIA 8.1*, Comput. Phys. Commun. **178** (2008) 852, arXiv:0710.3820.
- [99] F. Paige, S. Protopopescu, H. Baer, and X. Tata, *ISAJET 7.69: A Monte Carlo event generator for p p, anti-p p, and e+ e- reactions*, hep-ph/0312045.
- [100] S. Moretti *et al.*, *Implementation of supersymmetric processes in the HERWIG event generator*, JHEP **04** (2002) 028, hep-ph/0204123.
- [101] M. Bahr *et al.*, *Herwig++ Physics and Manual*, Eur. Phys. J. **C58** (2008) 639, arXiv:0803.0883.
- [102] J. Butterworth, J. Forshaw, and M. Seymour, *Multiparton interactions in photoproduction at HERA*, Z. Phys. **C72** (1996) 637, hep-ph/9601371.
- [103] S. Agostinelli *et al.*, *G4—a simulation toolkit*, Nucl. Instrum. Meth. **506** (2003) no. 3, 250.
- [104] A. Dellacqua *et al.*, *GEANT-4: An Object oriented toolkit for simulation in HEP*, CERN-DRDC-94-29 .
- [105] *ATLAS: Detector and physics performance technical design report. Vol. 1*, CERN-LHCC-99-14 .
- [106] *ATLAS detector and physics performance. Technical design report. Vol. 2*, CERN-LHCC-99-15 .
- [107] The ATLAS Validation Task Force, *Performance of the ATLAS Fast Simulation ATLFAST*, ATL-PHYS-INT-2007-005 (2007) .
- [108] ATLAS Collaboration, K. S. Cranmer, *The ATLAS analysis architecture*, Nucl. Phys. Proc. Suppl. **177-178** (2008) 126.
- [109] The POOL Project, <http://pool.cern.ch/>.
- [110] R. Brun and F. Rademakers, *ROOT: An object oriented data analysis framework*, Nucl. Instrum. Meth. **A389** (1997) 81.
- [111] K. Cranmer, A. Farbin, and A. Shibata, *EventView - The Design Behind an Analysis Framework*, ATL-SOFT-PUB-2007-008 (2007) .
- [112] W. Lampl *et al.*, *Calorimeter clustering algorithms: Description and performance*, ATL-LARG-PUB-2008-002 .

- [113] W. Cleland and E. Stern, *Signal processing considerations for liquid ionization calorimeters in a high rate environment*, Nucl. Instrum. Meth. **A338** (1994) no. 2-3, 467.
- [114] N. Konstantinidis *et al.*, *The Atlantis event visualisation program for the ATLAS experiment*, .
- [115] M. Aharrouche *et al.*, *Time resolution of the ATLAS barrel liquid argon electromagnetic calorimeter*, Nucl. Instrum. Meth. **A597** (2008) 178.
- [116] J. Colas *et al.*, *Crosstalk in the ATLAS Electromagnetic Calorimeter*, ATL-LARG-2000-004 (1999) .
- [117] S. Catani, Y. L. Dokshitzer, M. H. Seymour, and B. R. Webber, *Longitudinally invariant  $K_t$  clustering algorithms for hadron hadron collisions*, Nucl. Phys. **B406** (1993) 187.
- [118] S. D. Ellis and D. E. Soper, *Successive combination jet algorithm for hadron collisions*, Phys. Rev. **D48** (1993) 3160, hep-ph/9305266.
- [119] I. Abt *et al.*, *The tracking, calorimeter and muon detectors of the H1 experiment at HERA*, Nucl. Instrum. Meth. **386** (1997) no. 2-3, 348.
- [120] W. Ehrenfeld, J. Haller, and D. Ludwig, *Study of  $\tau$  final states in Gauge Mediated Supersymmetry Breaking models at ATLAS*, internal ATLAS note .
- [121] I. Hinchliffe and F. E. Paige, *Measurements in gauge mediated SUSY breaking models at LHC*, Phys. Rev. **D60** (1999) 095002, hep-ph/9812233.
- [122] B. C. Allanach, C. G. Lester, M. A. Parker, and B. R. Webber, *Measuring sparticle masses in non-universal string inspired models at the LHC*, JHEP **09** (2000) 004, hep-ph/0007009.
- [123] D. J. Miller, P. Osland, and A. R. Raklev, *Invariant mass distributions in cascade decays*, JHEP **03** (2006) 034, hep-ph/0510356.
- [124] ILC collaboration, ILD Concept Group, *International Large Detector: Letter of Intent*, 2009.
- [125] K. Kawagoe, T. Kobayashi, M. M. Nojiri, and A. Ochi, *Study of the gauge mediation signal with non-pointing photons at the CERN LHC*, Phys. Rev. **D69** (2004) 035003, hep-ph/0309031.
- [126] P. Bechtle, K. Desch, and P. Wienemann, *Fittino, a program for determining MSSM parameters from collider observables using an iterative method*, Comput. Phys. Commun. **174** (2006) 47, hep-ph/0412012.
- [127] P. Bechtle, K. Desch, M. Uhlenbrock, and P. Wienemann, *Constraining SUSY models with Fittino using measurements before, with and beyond the LHC*, arXiv:0907.2589.
- [128] W. Porod, *SPheno, a program for calculating supersymmetric spectra, SUSY particle decays and SUSY particle production at e+ e- colliders*, Comput. Phys. Commun. **153** (2003) 275, hep-ph/0301101.
- [129] O. Buchmueller *et al.*, *Predictions for Supersymmetric Particle Masses in the CMSSM using Indirect Experimental and Cosmological Constraints*, JHEP **09** (2008) 117, arXiv:0808.4128.
- [130] O. Buchmueller *et al.*, *Prediction for the Lightest Higgs Boson Mass in the CMSSM using Indirect Experimental Constraints*, Phys. Lett. **B657** (2007) 87, arXiv:0707.3447.

- [131] Heavy Flavor Averaging Group (HFAG), E. Barberio *et al.*, *Averages of  $b$ -hadron properties at the end of 2005*, [hep-ex/0603003](#).
- [132] BABAR Collaboration, B. Aubert *et al.*, *Search for the rare leptonic decay  $B^- \rightarrow \tau^- \bar{\nu}_\tau$* , Phys. Rev. Lett. **95** (2005) 041804, [hep-ex/0407038](#).
- [133] HPQCD Collaboration, A. Gray *et al.*, *The  $B$  Meson Decay Constant from Unquenched Lattice QCD*, Phys. Rev. Lett. **95** (2005) 212001, [arXiv:hep-lat/0507015](#).
- [134] Belle Collaboration, I. Adachi *et al.*, *Measurement of  $B^- \rightarrow \tau^- \bar{\nu}_\tau$  Decay With a Semileptonic Tagging Method*, [arXiv:0809.3834](#).
- [135] UTfit Collaboration, M. Bona *et al.*, *Model-independent constraints on  $\Delta F=2$  operators and the scale of new physics*, JHEP **03** (2008) 049, [arXiv:0707.0636](#).
- [136] FlaviaNet Working Group on Kaon Decays, M. Antonelli *et al.*, *Precision tests of the Standard Model with leptonic and semileptonic kaon decays*, [arXiv:0801.1817](#).
- [137] Muon g-2 Collaboration, G. W. Bennett *et al.*, *Measurement of the negative muon anomalous magnetic moment to 0.7 ppm*, Phys. Rev. Lett. **92** (2004) 161802, [hep-ex/0401008](#).
- [138] T. Moroi, *The Muon Anomalous Magnetic Dipole Moment in the Minimal Supersymmetric Standard Model*, Phys. Rev. **D53** (1996) 6565, [hep-ph/9512396](#).
- [139] G. Degrassi and G. F. Giudice, *QED logarithms in the electroweak corrections to the muon anomalous magnetic moment*, Phys. Rev. **D58** (1998) 053007, [hep-ph/9803384](#).
- [140] S. Heinemeyer, D. Stockinger, and G. Weiglein, *Two-loop SUSY corrections to the anomalous magnetic moment of the muon*, Nucl. Phys. **B690** (2004) 62, [hep-ph/0312264](#).
- [141] S. Heinemeyer, D. Stockinger, and G. Weiglein, *Electroweak and supersymmetric two-loop corrections to  $(g-2)_\mu$* , Nucl. Phys. **B699** (2004) 103, [hep-ph/0405255](#).

# Danksagung

An dieser Stelle möchte ich mich bei allen bedanken, die diese Arbeit möglich gemacht haben:

- JProf. Dr. Johannes Haller, der diese Arbeit betreut hat und mich immer wieder motiviert hat.
- Prof. Dr. Peter Schleper, der diese Arbeit als Zweitgutachter beurteilt hat.
- Dr. Philip Bechtle, Dr. Wolfgang Ehrenfeld und Dr. Karsten Köneke, die mir immer geduldig meine Fragen beantwortet haben und für Diskussionen immer Zeit hatten.
- Meinen Doktoranden- und Diplomandenkollegen (ATLAS, CMS und ILC), ohne die alles langweilig wäre und mit denen die Zusammenarbeit immer angenehm ist. Insbesondere danke ich Michael Böhler, Martin Goebel, Dörthe Ludwig und Martin Wildt für regen Gedankenaustausch aller Art und viel Spaß im Büro. Außerdem möchte ich Dr. Christoph Rosemann für unermüdliche Motivation und Unterstützung danken.
- Allen Mitgliedern der DESY-ATLAS Gruppe und der ATLAS-SUSY Gruppe, von denen ich viel gelernt und profitiert habe.
- Meinen Eltern und meinem Bruder, die immer für mich da sind.
- Meiner Freundin Kristin, die es nicht immer leicht mit mir hat, die mich aber immer unterstützt und die ich sehr lieb habe.